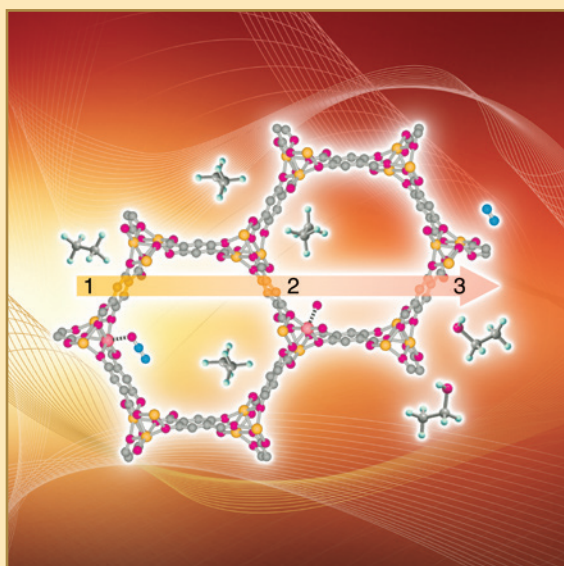


2014

Accomplishments and Opportunities

NIST CENTER FOR NEUTRON RESEARCH



ON THE COVER

Conversion of light alkanes into value-added chemicals remains an outstanding scientific challenge. The oxidation of ethane to ethanol on an iron(II) metal-organic framework is described in the highlight article by Hudson *et al.* on p.18.

2014 NIST Center for Neutron Research Accomplishments and Opportunities

NIST Special Publication 1177

Robert M. Dimeo, Director

Steven R. Kline, Editor

December 2014

U.S. Department of Commerce

Penny Pritzker, Secretary

National Institute of Standards and Technology

*Willie May, Acting Under Secretary of Commerce for
Standards and Technology and Acting Director*



DISCLAIMER

Certain commercial entities, equipment, or materials may be identified in this document in order to describe an experimental procedure or concept adequately. Such identification is not intended to imply recommendation or endorsement by the National Institute of Standards and Technology, nor is it intended to imply that the entities, materials, or equipment are necessarily the best available for the purpose. Error bars in figures represent one standard deviation unless otherwise stated.

National Institute of Standards and Technology
Special Publication 1177

Natl. Inst. Stand. Technol. Spec. Publ. 1177, 88 pages
(December 2014)

CODEN: NSPUE2

This publication is available free of charge from:
<http://dx.doi.org/10.6028/NIST.SP.1177>

Table of Contents

FOREWORD	iii
THE NIST CENTER FOR NEUTRON RESEARCH	1
NIST CENTER FOR NEUTRON RESEARCH INSTRUMENTS	2
NCNR IMAGES 2014	4

HIGHLIGHTS

BIOLOGY

Revealing protein complexes at the lipid membrane, J. C. Lee <i>et al.</i> ,	6
A sticky situation: antibody adsorption, desorption and aggregation at solid-liquid interfaces, H. Nanda <i>et al.</i> , (nSoft)	8
Determination of monoclonal antibody conformation using SANS and refined using free energy constraints, N. J. Clark <i>et al.</i> , (CHRNS)	10

CHEMICAL PHYSICS

Tunable CO/H ₂ and CO/N ₂ separations in metal-organic frameworks with exposed divalent metal cations via reversible CO binding, M. R. Hudson <i>et al.</i> ,	12
Crystal and magnetic stripes coupled to cooperative Jahn-Teller effects in Na _{5/8} MnO ₂ , X. Li <i>et al.</i> ,	14
Anion reorientations, sodium mobility, and superionic conduction in Na ₂ B ₁₂ H ₁₂ , N. Verdál <i>et al.</i> , (CHRNS)	16
Oxidation of ethane to ethanol by N ₂ O in an iron(II) metal-organic framework, M. R. Hudson <i>et al.</i> ,	18
Dynamic origin of the anomalous odd-even glass transition temperature in an ionic glass, K. Yang <i>et al.</i> , (CHRNS)	20

CONDENSED MATTER

TiAu: the first itinerant antiferromagnet with no magnetic elements, E. Svanidze <i>et al.</i> ,	22
The fluctuating magnetism of triangular molecules on a triangular lattice, M. Mourigal <i>et al.</i> , (CHRNS).	24
Giant charge fluctuations with Se-height and Fe-vacancy formation in M _x Fe _{2-y} Se ₂ , X. Luo <i>et al.</i> ,	26
Phonon localization drives polar nanoregions in a relaxor ferroelectric, M. E. Manley <i>et al.</i> ,	28
Effect of interfacial octahedral behavior in ultrathin manganite films, E. J. Moon <i>et al.</i> ,	30

ENGINEERING PHYSICS

Comparison of methods for the measurement of deformation induced martensite formation, K. S. Raghavan <i>et al.</i> ,	32
---	----

NEUTRON PHYSICS

Determining the effective transverse coherence of a neutron wave packet, C. F. Majkrzak <i>et al.</i> ,	34
Improved determination of the neutron lifetime, A. T. Yue <i>et al.</i> ,	36

SOFT MATTER

Shaken or stirred? It matters when addressing the dynamics and stability of macromolecular nanocarriers in aqueous solution, T. H. Epps, III <i>et al.</i> ,	38
Universal scaling of polymer diffusion in nanocomposites, J. Choi <i>et al.</i> , (CHRRNS)	40
Probing the relationship between water content and chain dynamics in fuel cell membranes, K. A. Page <i>et al.</i> , (nSoft) (CHRRNS)	42
Observation of spatially dependent heterogeneity of constrained local motions of rubber in carbon black nanocomposites, J. H. Roh <i>et al.</i> , (CHRRNS)	44

ADVANCES IN MEASUREMENT

Development of a neutron microscope, D. S. Hussey <i>et al.</i> ,	46
A scaling law to describe the average local structure of biomolecules, M. Watson <i>et al.</i> ,	47
Comparison of INAA and LC-ICP-MS for the determination of As species in marine tissues, R. Zeisler <i>et al.</i> ,	48
Wide-angle polarization analysis with neutron spin filters, T. R. Gentile <i>et al.</i> ,	49
Advances in measuring time-resolved neutron scattering from flowing complex fluids, S. A. Rogers <i>et al.</i> ,	50
Development of a scintillator-based proportional counter for use in a chromatically analyzing neutron detector, N. C. Maliszewskyj <i>et al.</i> ,	51
SLDMOL: A tool for the structural characterization of thermally disordered membrane proteins, H. Nanda <i>et al.</i> ,	52

NEUTRON SOURCE OPERATIONS	53
FACILITY DEVELOPMENT	54
SERVING THE SCIENCE AND TECHNOLOGY COMMUNITY	56
NEUTRON WORKSHOP	59
THE CENTER FOR HIGH RESOLUTION NEUTRON SCATTERING (CHRRNS)	61
2014 AWARDS	64
PUBLICATIONS: AUGUST 1, 2013 TO JULY 31, 2014	66
INSTRUMENTS AND CONTACTS	82
NIST CENTER FOR NEUTRON RESEARCH CONTACTS	inside back cover

Foreword

I am delighted to present this year's Accomplishments and Opportunities for the NIST Center for Neutron Research.

The reactor was scheduled to operate for 235 days during the reporting period (factoring in the loss of days due to the government shutdown in October) and did operate for 218 days yielding 93 % operations reliability. Both cold sources operated with greater than 99 % reliability, i.e. the cold sources held the reactor from operating for one day during the year. There were many noteworthy facility developments this year. In order to ensure robust, long-term source operations, NCNR continued to pursue an active reactor lifetime extension program. Details of this past year's progress can be found in the pages of this report. Users returned to the Neutron Spin-Echo instrument following its relocation to a dedicated neutron guide in the guide hall extension. The move included installation of a new polarizer and new power supplies resulting in higher performance and improved instrument availability and reliability. One of the 30m SANS instruments was relocated to an endstation in the guide hall extension where the beam is tailored for SANS instrumentation, resulting in a performance improvement. Design and procurements continued on the VSANS and CANDoR instruments as well as planning for the installation of the Cold Neutron Imaging station on NG-6. In addition, the first wide-angle polarized beam measurements were carried out on MACS. This is a significant development in our polarized beam program, marking yet another important capability that NCNR makes available to its users. Finally, design work commenced for a significant upgrade of the engineering diffractometer as part of a targeted NIST initiative on Advanced Neutron Technologies.

After VSANS, CANDoR, and the Cold Neutron Imaging instruments are commissioned (≈ 2018), we will have completed the major neutron instruments and user capabilities that the scientific community requested in the NCNR Expansion Workshop held in 2006. In order to plan for the next 5 to 10 years, we held a workshop on August 21-22 in Potomac,



MD, titled "Neutron Measurements for Materials Design & Characterization." This two-day event featured speakers who described many exciting opportunities in science driving the needs for new, innovative neutron scattering instruments and sample environment. As of this writing we are awaiting the final report from the topical break-out groups but it was clear from the close-out presentations at the workshop that there is no shortage of new, great ideas. Stay tuned for more details as the results of this workshop will shape the future of NCNR developments.

Amidst these many developments and planning for the future, the scientific community produced a wealth of first-class research using the NCNR instruments. In this report you will find a collection of short highlights of some of that research. I think that you will find that they exemplify the high quality of work that the community is carrying out here at the NCNR throughout the year.



The guide hall extension as seen in April 2014, was quickly becoming populated with new and relocated instruments. The new 10m Small Angle Neutron Scattering (SANS) instrument was operational in January 2013 and is the primary neutron instrument for the nSOFT consortium. The move of the 30m SANS from NG3 to NGB started in March 2014, and the instrument returned to full operation in May 2014. The Neutron Spin Echo instrument (NSE) formerly at NG5 was relocated starting in fall 2013, and after upgrading many components, returned to operation in August 2014. In addition, the MAGIK and PBR reflectometers are located on the new guides and have been operational since 2012.

The NIST Center for Neutron Research

Neutrons provide a uniquely effective probe of the structure and dynamics of materials ranging from water moving near the surface of proteins to magnetic domains in memory storage materials. The properties of neutrons (outlined at right) can be exploited using a variety of measurement techniques to provide information not otherwise available. The positions of atomic nuclei in crystals, especially of those of light atoms, can be determined precisely. Atomic motion can be directly measured and monitored as a function of temperature or pressure. Neutrons are especially sensitive to hydrogen, so that hydrogen motion can be followed in H-storage materials and water flow in fuel cells can be imaged. Residual stresses such as those deep within oil pipelines or in highway trusses can be mapped. Neutron-based measurements contribute to a broad spectrum of activities including engineering, materials development, polymer dynamics, chemical technology, medicine, and physics.

The NCNR's neutron source provides the intense, conditioned beams of neutrons required for these types of measurements. In addition to the thermal neutron beams from the heavy water or graphite moderators, the NCNR has two large area liquid hydrogen moderators, or cold sources, that provide long wavelength guided neutron beams for industrial, government, and academic researchers.

There are currently 28 experiment stations: 12 provide high neutron flux positions for neutron physics, analytical chemistry, or imaging, and 16 are beam facilities for neutron scattering research. The subsequent pages provide a schematic description of our instruments. More complete descriptions can be found at www.ncnr.nist.gov/instruments/. The second guide hall is currently populated with seven instruments. Three new cold neutron instruments are under development, including a very small angle neutron scattering instrument, a quasi-white beam neutron reflectometer and a cold neutron imaging station.

The Center supports important NIST measurement needs, but is also operated as a major national user facility with merit-based access made available to the entire U.S. technological community. Each year, about 2000 research participants from government, industry, and academia from all areas of the country are served by the facility (see pp. 56). Beam time for research to be published in the open literature is without cost to the user, but full operating costs are recovered for proprietary research. Access is gained mainly through a web-based, peer-reviewed proposal system with user time allotted by a beamtime allocation committee twice a year. For details see www.ncnr.nist.gov/beamtime.html. The National Science Foundation and NIST co-fund the Center for High Resolution Neutron Scattering (CHRNS) that currently operates six of the world's most advanced instruments (see pp. 61). Time on CHRNS instruments is made available through the proposal system. Some access to beam time for collaborative measurements with the NIST science staff can also be arranged on other instruments.

Why Neutrons?

Neutrons reveal properties not readily probed by photons or electrons. They are electrically neutral and therefore easily penetrate ordinary matter. They behave like microscopic magnets, propagate as waves, can set particles into motion, losing or gaining energy and momentum in the process, and they can be absorbed with subsequent emission of radiation to uniquely fingerprint chemical elements.

WAVELENGTHS – in practice range from ≈ 0.01 nm (thermal) to ≈ 1.5 nm (cold) ($1 \text{ nm} = 10 \text{ \AA}$), allowing the formation of observable interference patterns when scattered from structures as small as atoms to as large as biological cells.

ENERGIES – of millielectronvolts, the same magnitude as atomic motions. Exchanges of energy as small as nano-electronvolts and as large as tenths of electronvolts can be detected between samples and neutrons, allowing motions in folding proteins, melting glasses and diffusing hydrogen to be measured.


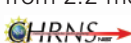

SELECTIVITY – in scattering power varies from nucleus to nucleus somewhat randomly. Specific isotopes can stand out from other isotopes of the same kind of atom. Specific light atoms, difficult to observe with X-rays, are revealed by neutrons. Hydrogen, especially, can be distinguished from chemically equivalent deuterium, allowing a variety of powerful contrast techniques.

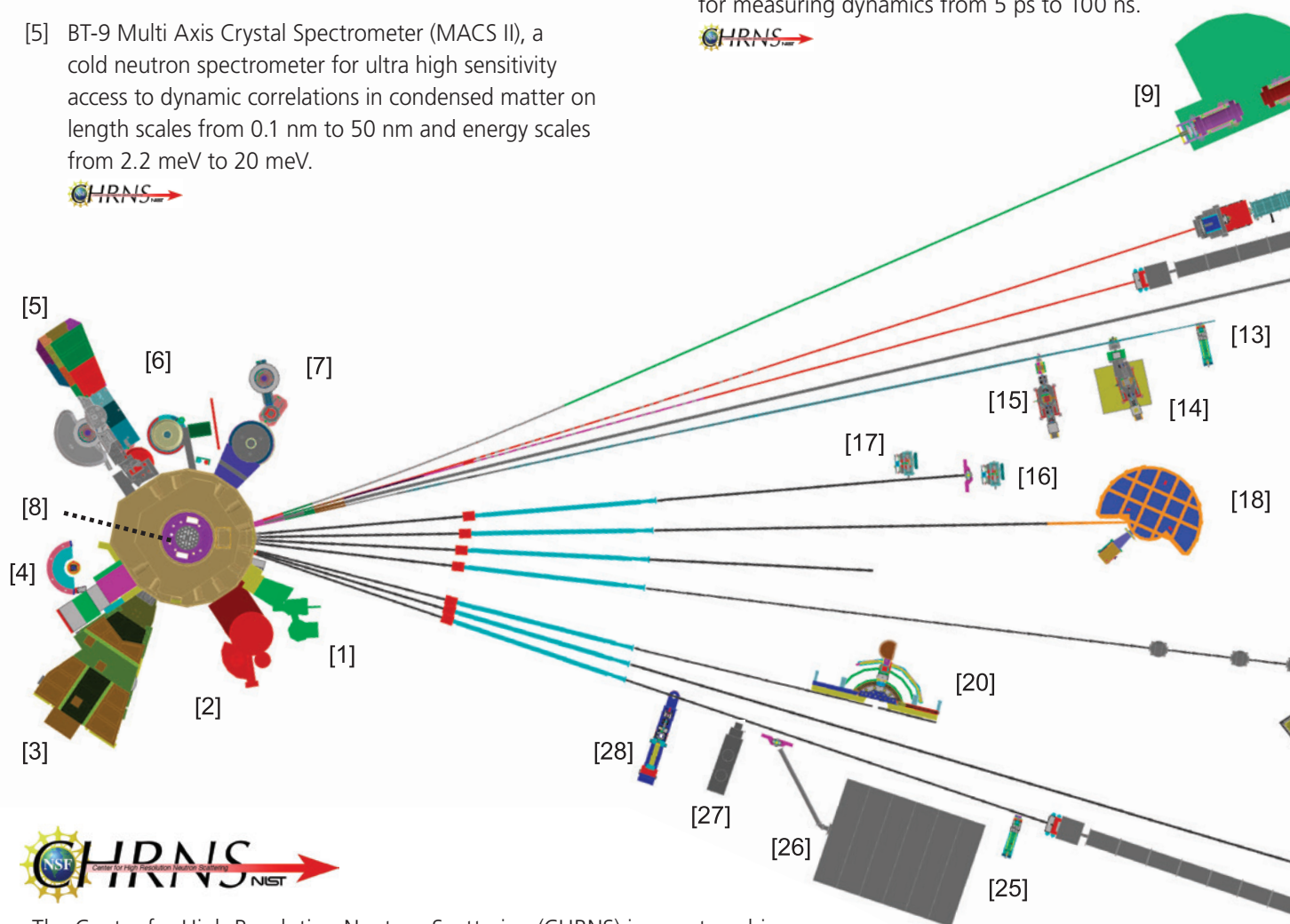
MAGNETISM – makes the neutron sensitive to the magnetic moments of both nuclei and electrons, allowing the structure and behavior of ordinary and exotic magnetic materials to be detailed precisely.

NEUTRALITY – of the uncharged neutrons allows them to penetrate deeply without destroying samples, passing through walls that condition a sample's environment, permitting measurements under extreme conditions of temperature and pressure.


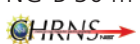
CAPTURE – characteristic radiation emanating from specific nuclei capturing incident neutrons can be used to identify and quantify minute amounts of elements in samples as diverse as ancient pottery shards and lake water pollutants.

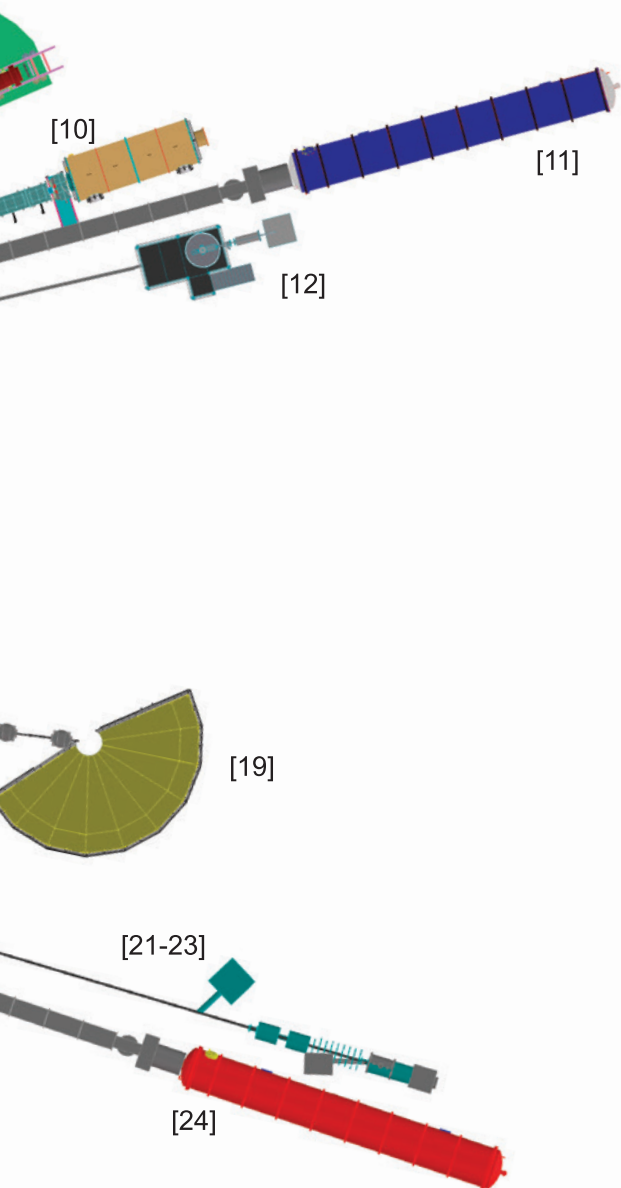
NIST Center for Neutron Research Instruments *(as of December 2014)*

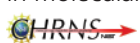

- [1] BT-5 Perfect Crystal Ultra-Small Angle Neutron Scattering (USANS) Diffractometer for microstructure up to 10^4 nm. 
- [2] BT-4 Filter Analyzer Neutron Spectrometer with cooled Be/Graphite filter analyzer for chemical spectroscopy and thermal triple axis spectrometer.
- [3] BT-2 Neutron Imaging Facility for imaging hydrogenous matter in large components such as water in fuel cells and lubricants in engines, in partnership with General Motors and DOE.
- [4] BT-1 Powder Diffractometer with 32 detectors; incident wavelengths of 0.208 nm, 0.154 nm, and 0.159 nm, with resolution up to $\Delta d/d \cong 8 \times 10^{-4}$.
- [5] BT-9 Multi Axis Crystal Spectrometer (MACS II), a cold neutron spectrometer for ultra high sensitivity access to dynamic correlations in condensed matter on length scales from 0.1 nm to 50 nm and energy scales from 2.2 meV to 20 meV. 
- [6] BT-8 Residual Stress Diffractometer optimized for depth profiling of residual stresses in large components.
- [7] BT-7 Thermal Triple Axis Spectrometer with large double focusing monochromator and interchangeable analyzer/detectors systems.
- [8] VT-5 Thermal Neutron Capture Prompt Gamma-ray Activation Analysis Instrument with a neutron fluence rate of $3 \times 10^8 \text{ cm}^{-2} \text{ s}^{-1}$ used for quantitative elemental analysis of bulk materials. Generally used for the analysis of highly hydrogenous materials ($\cong 1 \% \text{ H}$) such as foods, oils, and biological materials.
- [9] NG-A Neutron Spin-Echo Spectrometer (NSE) for measuring dynamics from 5 ps to 100 ns. 



The Center for High Resolution Neutron Scattering (CHRNS) is a partnership between NIST and the National Science Foundation that develops and operates neutron scattering instrumentation for use by the scientific community. The following instruments are part of the Center: 1 (USANS), 5 (MACS II), 9 (NSE), 11 (NG-B SANS), 18 (HFBS), and 19 (DCS).

- [10] NG-B 10 m SANS for macromolecular structure measurements. 
- [11] NG-B 30 m SANS for microstructure measurements. 
- [12] NG-C aCORN Neutron physics station for measurement of the correlation parameter between the electron and anti-neutrino in neutron beta decay.
- [13] NG-D Cold neutron capture Prompt Gamma Activation Analysis, for quantitative elemental analysis of bulk materials, especially of hydrogenous ones.
- [14] NG-D MAGIK off-specular reflectometer for studies of thin-film samples with in-plane structure.

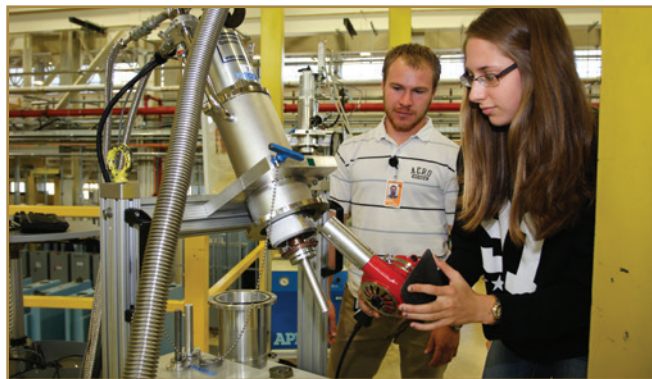


- [15] NG-D Polarized Beam Reflectometer (PBR) for measuring reflectivities as low as 10^{-8} to determine subsurface structure.
- [16] NG-1 Cold Neutron Depth Profiling for profiling of subsurface elemental composition.
- [17] NG-1 Detector development station.
- [18] NG-2 Backscattering Spectrometer (HFBS) high intensity inelastic scattering instrument with energy resolution $< 1 \mu\text{eV}$, for studies of motion in molecular and biological systems. 
- [19] NG-4 Disk Chopper Time-of-Flight Spectrometer for diffusive motions and low energy dynamics. Wavelengths from $\approx 0.18 \text{ nm}$ to 2.0 nm and energy resolutions from $\approx 2 \text{ meV}$ to $< 10 \mu\text{eV}$. 
- [20] NG-5 Spin-Polarized Triple Axis Spectrometer (SPINS) using cold neutrons with position sensitive detector capability for high-resolution studies.
- [21-23] NG-6A Neutron Physics Station for precise measurement of the neutron magnetic dipole moment, neutron flux, and neutron lifetime.
- [24] NG-7 30 m SANS for microstructure measurements, in partnership with ExxonMobil and University of Minnesota's IPrime.
- [25] NG-7 Cold neutron capture Prompt Gamma Activation Analysis, for quantitative elemental analysis of bulk materials.
- [26] NG-7 Neutron Interferometry and Optics Station with perfect crystal silicon interferometer. A vibration isolation system provides exceptional phase stability and fringe visibility.
- [27] NG-7 Neutron Physics Interferometry Test Bed for developing novel interferometry techniques.
- [28] NG-7 Horizontal Sample Reflectometer allows reflectivity measurements of free surfaces, liquid/vapor interfaces, as well as polymer coatings.

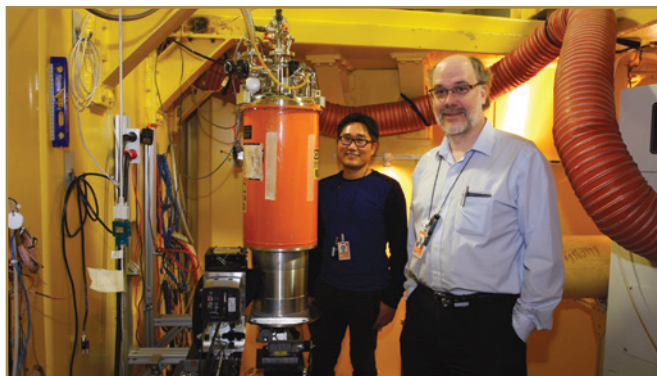
NCNR Images 2014



Students from Takoma Park Middle School (Silver Spring, MD) are wowed by a chain reaction as they learn about neutron science.



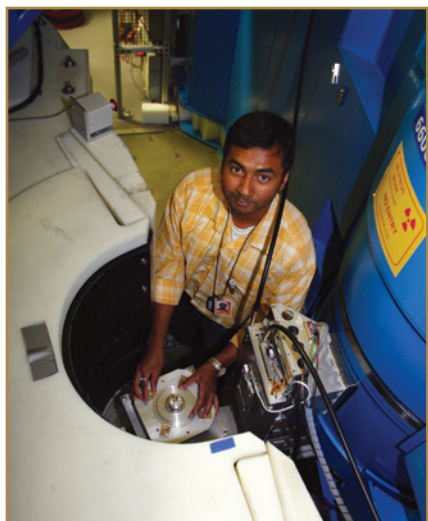
Clinton Wiener and Melanie Longanecker (U Akron) prepare a new hydrogel sample for measurement at DCS.



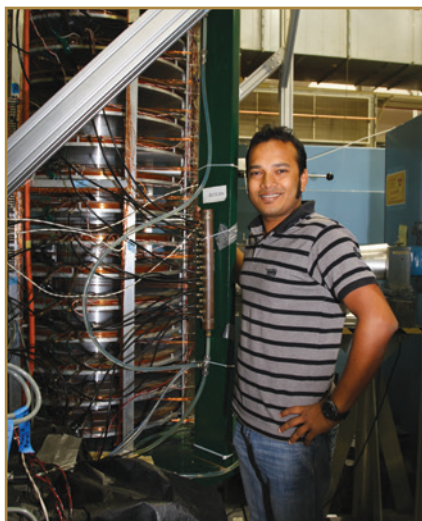
Chang Kyoung Choi and Jeffrey Allen (Michigan Technological U) after a successful experiment at the BT2 Neutron Imaging Facility.



Natasha Khatri (Georgetown U) is mounting her molecular magnet sample for a polarized beam experiment at the NGD reflectometer.



Pinaki Das (LANL) prepares the sample stage for his investigation of spin waves at MACS.



Md Taufique Hassan (Tulane U) at the NG6 Physics station conducting an aCORN experiment.



Mike Rinehart (bottom) and Doug Ogg of the NCNR carefully remove the neutron guides from the NG3 SANS instrument in preparation for its move to NGB.



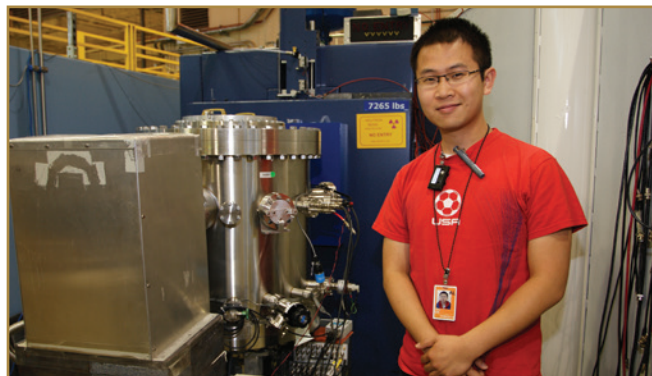
Dan Sunday (NIST MSed) carefully loads his samples into the sample chamber at NGB 10m SANS.



Zhijun Xu (UC Berkeley) makes some final adjustments to the sample environment at BT7 before he starts his experiment.



Three generations of NCNR directors: Mike Rowe, Pat Gallagher, and Rob Dimeo (L-R) together at Pat's farewell cookout.



Danny Liu (Ohio State U) is ready to take some data at the cold neutron depth profiling instrument.



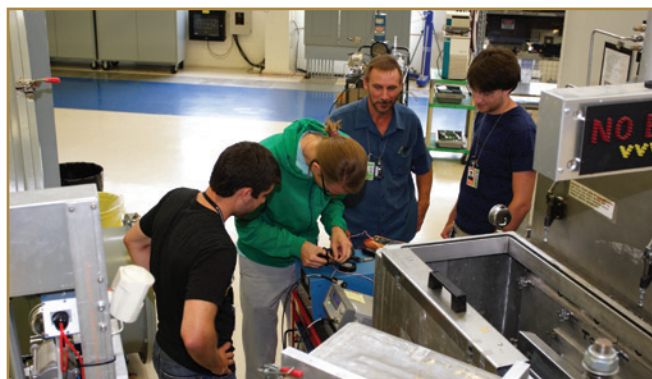
Jason Rich (ORNL) is all smiles at NG7 30m SANS, especially when the 1-2 shear cell is working.



At NSE, Koji Yoshida (L, Fukuoka U) is getting some help from Michihiro Nagao (NCNR) to set up his experiment scans.



Jeff Lynn (NCNR) explains to an interested group of students from Springbrook High School (Silver Spring, MD) how scientists use neutrons to "see" materials.



Doug Godfrin (U Delaware), Chris Bertrand (NCNR), Richard Menendez (Northwest HS), and Koty McAllister (U Delaware) (L-R) at the NGB 30m SANS. The three supervisors are making sure that Chris is connecting the electrodes correctly.

Revealing protein complexes at the lipid membrane

J. C. Lee¹ and F. Heinrich^{2,3}

Neutron reflectometry is uniquely positioned within the available techniques in structural biology in that it allows the characterization of membrane-associated proteins close to their native cellular environment, even though it is of lower resolution than the dominant structural methods like protein crystallography, nuclear magnetic resonance, or cryo-electron microscopy. Neutron reflectometry allows routine studies of physiologically relevant, fluid phospholipid bilayers of complex structure and composition with full control of the aqueous buffer surrounding the membrane such as pH and the presence of other relevant biomolecules [1-3]. Structural responses such as protein conformational changes or the formation of a protein-co-factor complex at the membrane interface can be investigated in-situ. Recent improvements in reflectometry methods have enabled more detailed studies of membrane-bound protein-protein complexes and have been successfully applied to a biomedically relevant complex involving α -synuclein and glucocerebrosidase, proteins that are related to Parkinson and Gaucher diseases, respectively.

Several parallel developments at the NCNR have transformed neutron reflectometry into a powerful tool for structural biology over the last 5 years [4]. The introduction of a rigorous uncertainty analysis based on Monte Carlo methods paved the way for using complex molecular models for data analysis, ensuring that the information content of the experimental data is utilized to its maximum without over-fitting the data. For biological neutron reflectometry, this has led to the retirement of the traditional box model and its replacement by a composition-space model (see Fig. 1) that directly models distributions of molecular groups while fully utilizing a maximum of prior information, such as known molecular volumes, scattering lengths, and chemical connectivity.

The Monte Carlo uncertainty methods also enables a new way of modeling protein envelopes using free-form spline functions (see Fig. 2). By itself, a fit to the data using a spline function is not very convincing because the uniqueness of the solution cannot be assessed. In combination with a rigorous uncertainty method, however, accurate confidence intervals on the spline envelope can be determined, transforming the spline fitting into a useful tool to describe unknown or disordered structural features of a protein. A recent advance is the extension of the spline fitting

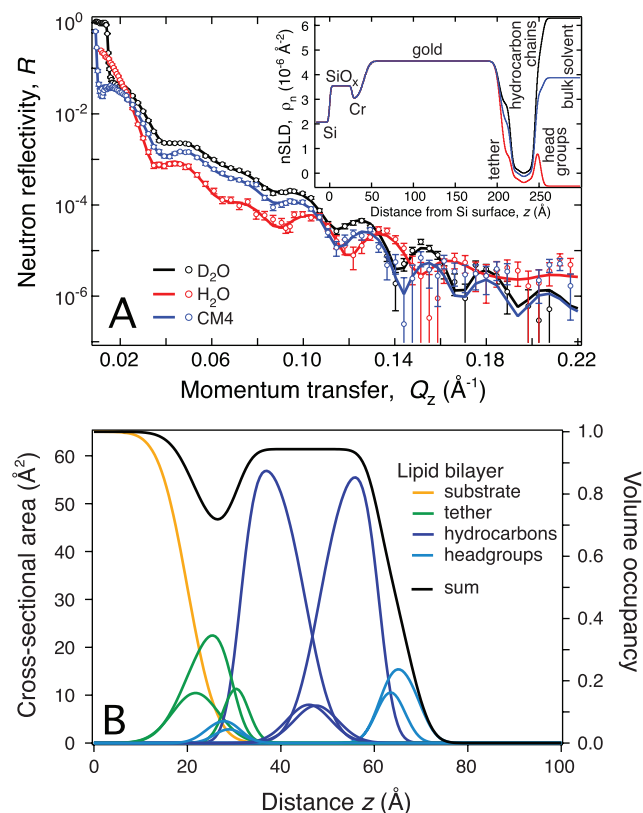


FIGURE 1: (A) Neutron reflectometry data and best-fit for a tethered lipid bilayer of palmitoyl oleoyl phosphatidylcholine (POPC) and palmitoyl oleoyl phosphatidic acid (POPA) at a composition of 50:50 POPC:POPA. The inset shows a scattering length density profile as it could be obtained using a box model. (B) Composition space model that describes the spatial distributions of molecular constituents of the tethered lipid bilayer by pairs of error functions; each POPC and POPA headgroups are modeled separately, as well as methylene and central methyl contributions from the hydrocarbon chains of the lipids. The tether is modeled using three chemically distinct distributions. Solvent occupies volume not filled by bilayer material.

method to reveal envelopes of protein complexes, in which different molecular constituents have a different scattering length density, for example, due to a different degree of perdeuteration. This is implemented by adding an additional parameterization to the spline, not only describing the volume filling of the protein at every position, but also its scattering length density. The free-form

¹ Biochemistry and Biophysics Center, National Heart, Lung, and Blood Institute, NIH, Bethesda, MD 20892

² Carnegie Mellon University, Pittsburgh, PA 15213

³ NIST Center for Neutron Research, National Institute of Standards and Technology, Gaithersburg, MD 20899

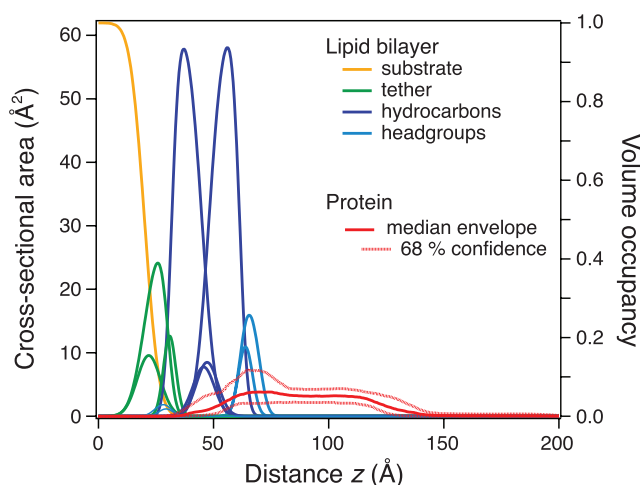


FIGURE 2: The structural envelope of the time and ensemble average of α -synuclein at a solution concentration of 3 $\mu\text{mol/L}$ associated with a tethered lipid membrane composed of 50:50 POPC:POPA lipids at pH 7. The envelope has been modeled using a free-form monotonic Hermite spline defined by 11 control points, originally spaced apart by 20 Å. In addition to being free to assume any volume occupancy, each control point is allowed to deviate from its original position by ± 7 Å during the fit. 68 % confidence limits are shown for the protein envelope. The median envelope peaks in the headgroup region and extends approximately 60 Å into the bulk solvent phase. A significant penetration of the protein into the hydrocarbon region of the bilayer is observed.

scattering length density that has been obtained in this way can be mathematically decomposed into contributions from each constituent, thus obtaining individual envelopes.

The first biological application of this method was to elucidate the membrane-bound complex of α -synuclein, an intrinsically disordered neuronal protein implicated in Parkinson disease, and glucocerebrosidase, a lysosomal enzyme that causes Gaucher disease and is associated with a higher risk for the development of Parkinson disease. Current research is focused on defining the underlying mechanism for the genetic relationship between glucocerebrosidase and Parkinson disease in the search of a new therapeutic approach for this devastating ailment. The complex formation between the two proteins within the lysosome offers one such molecular connection. In recent work, we have confirmed that, indeed, the two proteins form a complex at the membrane, and we were able to derive a structural model for the complex that is in agreement with the neutron reflectometry data and additional fluorescence data (see Fig. 3) [5]. Although our data do not preclude protein-protein interactions in other cellular milieus, we suggest that the α -synuclein–glucocerebrosidase association is favored in the lysosome both on and off intralysosomal membranes, and that this noncovalent interaction provides the groundwork to explore molecular mechanisms linking Parkinson disease with mutant glucocerebrosidase.

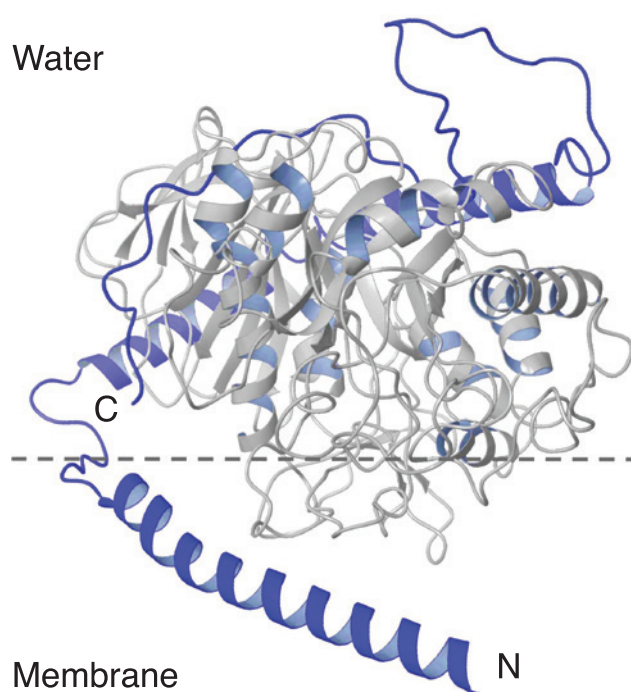


FIGURE 3: A structural model of α -synuclein and glucocerebrosidase-based neutron reflectivity data of perdeuterated α -synuclein and protated glucocerebrosidase associated with a tethered lipid membrane composed POPC and palmitoyl oleoyl phosphatidylserine (POPS) at a composition of 50:50 POPC:POPS at pH 5.5. Both protein concentrations were at 300 nmol/L. The orientation of glucocerebrosidase at the membrane was determined using a rigid-body model based on X-ray crystal structure as previously described for other systems [1]. The placement of α -synuclein with respect to the enzyme and the bilayer was based on best fit to the measured neutron density distribution for the complex.

References

- [1] F. Heinrich, H. Nanda, H. Z. Goh, C. Bachert, M. Lösche, A. D. Linstedt, *J. Bio. Chem.* **289**, 9683 (2014).
- [2] C. M. Pfefferkorn, F. Heinrich, A. J. Sodt, A. S. Maltsev, R. W. Pastor, J. C. Lee, *Biophys. J.* **102**, 613 (2012).
- [3] S. Shenoy, P. Shekhar, F. Heinrich, M.-C. Daou, A. Gericke, A. H. Ross, M. Lösche, *PLoS ONE* **7**, e32591 (2012).
- [4] F. Heinrich, M. Lösche, *Biochim Biophys. Acta* **1838**, 2341 (2014).
- [5] T. L. Yap, Z. Jiang, F. Heinrich, J. M. Gruschus, M. Barros, C. M. Pfefferkorn, J. E. Curtis, E. Sidransky, J. C. Lee, (submitted to *EMBO Reports*, 2014).

A sticky situation: antibody adsorption, desorption and aggregation at solid-liquid interfaces

H. Nanda,^{1,2} T. V. Nanda,^{3,4} D. P. Nesta,³ and C. J. Roberts⁴

Protein based therapeutics, especially those centered on monoclonal antibodies, are a fast growing area of drug development due to their high target-specificity and therefore generally lower toxicity. However, aggregation of proteins is a common issue during product development and manufacturing, as well as during subsequent transportation and storage [1]. Protein aggregation mediated by partial unfolding can be accelerated by inadvertent stresses, such as agitation, exposure to elevated temperatures, chemical degradation, and even exposure to solid-liquid and liquid-water interfaces (e.g. the inside surface of a glass vial or at the air-water interface of trapped bubbles in a tube) [2]. Large aggregate formation is a concern not only due to the potential loss in efficacy and shelf life of a drug but also due to the potential triggering of unwanted and possibly life-threatening immunogenic responses in patients [3].

Association of proteins at bulk interfaces has been empirically implicated in aggregate formation for some proteins but the mechanistic details of the process are not fully known, at least in part, because a majority of characterization techniques measure protein structure and aggregation state only in bulk solution. Therefore the nature of the protein layer at the surface, how its structure changes due to desorption and the correlation with aggregate particle formation in solution are all poorly understood. To target these questions, the interaction of a monoclonal antibody IgG1 with a hydrophilic SiO_x surface has been studied using the unique surface characterization technique of neutron reflectivity (NR). Solution-based methods such as micro flow imaging (MFI) were then used to connect protein surface structure to aggregate particle formation in the aqueous phase.

A schematic of the experimental setup and procedure is shown in Fig. 1. Interpretation of the NR data provides a 1-D profile of the protein density distributed along the surface normal (z-axis) direction from the SiO_x layer. To take advantage of the sensitivity of neutrons to the isotopic state of hydrogen, all measurements were repeated in both H_2O and D_2O buffer solution and the data were fit simultaneously to a single protein profile structure.

IgG structure at the SiO_x surface was measured at two different pH values, 4.5 and 6.2 and two salt concentrations, 0 mmol/L and 100 mmol/L NaCl resulting in four buffer conditions. Fig. 2

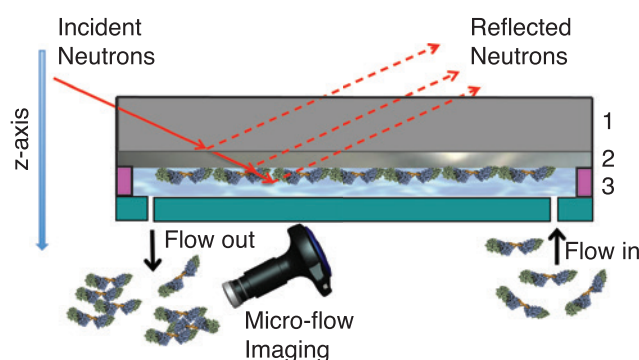


FIGURE 1: Schematic of the flow cell used for protein adsorption/desorption experiments and the scattering geometry for neutron reflectivity (NR) measurements. Stock solutions of mAb flow over the surface of a thin SiO_x film (layer 2) that forms natively on the underlying Si wafer substrates (layer 1). Adsorption of mAb occurs on the hydrophilic SiO_x surface forming a protein film (layer 3) and is structurally characterized by NR. Desorption of the protein layer was performed by a subsequent rinse with pure buffer. The protein film structure was also studied by NR after desorption. The collected rinse fractions are analyzed for aggregate particle formation on a Micro-flow Imaging (MFI) instrument.

shows the resulting protein layers derived from the NR measurements. At pH 4.5, for both salt conditions, the IgG1 molecules form a narrow single-peak distribution on the SiO_x surface with dimensions consistent with a 'flat-on' orientation as depicted in Fig. 2A, insert. At pH 6.2 an alternate layer structure is observed for the low salt condition (Fig. 2B). The broad distribution with a secondary peak can be interpreted as a protrusion of a protein lobe from the surface (Fig. 2B, inset). However the profile could also be due to multiple protein orientations and further measurements are required to distinguish between these cases.

During the desorption steps, the structure is unchanged and very little of the protein layer is removed at pH 4.5, indicating a strong surface interaction. Conversely, at pH 6.2, desorption resulted in 20 % to 30 % of the protein layer removed. This IgG1 molecule was shown to carry a +15e charge at low pH and a greater than 3-fold reduction in surface charge at high pH, [4] suggesting electrostatics play a significant role in promoting surface interactions

¹ NIST Center for Neutron Research, National Institute of Standards and Technology, Gaithersburg, MD 20899

² Carnegie Mellon University, Pittsburgh, PA 15213

³ Department of Biopharmaceutical Technologies, GlaxoSmithKline, King of Prussia, PA 19406

⁴ Department of Chemical & Biomolecular Engineering, and Center for Molecular and Engineering Thermodynamics, University of Delaware, Newark, DE 197116

of the IgG1 protein with the negative surface charge density of the SiO_x layer. On the other hand, the maximum surface coverage at pH 6.2 was comparable or higher than for the lower pH despite the weaker adsorption. The reduced net charge on IgG1 at pH 6.2 would allow for closer packing on the surface despite the low surface interaction energy.

The morphology of large particle aggregates was assessed by MFI. At pH 6.2 the formation of soluble aggregates were not detected. In previous work it was shown for this molecule in solution that thermally accelerated aggregation resulted in macroscopic, insoluble particles at pH values greater than 5.5 [4]. Therefore these aggregates are not expected to be detectable by MFI. At pH 4.5 soluble aggregate formations did occur and was monitored by MFI as shown in Fig. 3 for the 0 mmol/L NaCl sample. The stock solution showed < 0.03 % particle formation by mass and those particles detected were all found to be < 10 μm in diameter and spherical in morphology (Fig. 3A). After exposure to the SiO_x surface, the particle number increased by an order of magnitude and was significantly more asymmetric although sizes remained small (Fig. 3B). The second rinse fractions showed another increase in particle number as well as the formation of large elongated particle aggregates, > 30 μm in diameter (Fig. 3C). Images of the large particles indicated fibrillar-like shapes (Fig. 3D). Thioflavin T fluorescence assays found strong dye binding suggesting high beta sheet amyloid content in the second rinse solutions (data not shown).

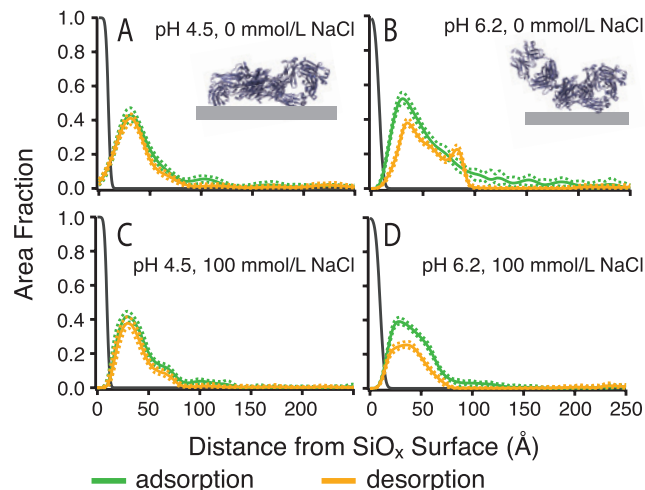


FIGURE 2: Area profiles derived from NR experiments show the pH and salt dependence of the IgG1 layer structure on SiO_x surfaces. All protein solutions consisted of 30 mmol/L citrate buffer and 15 mg/mL IgG. A 1-D protein density along the surface normal direction is given in terms of an area fraction for both the adsorption step (green) and the desorption step (yellow), dashed lines represent 2σ confidence intervals. An illustrative molecular model of the protein profiles are depicted as insets in (A) and (B).

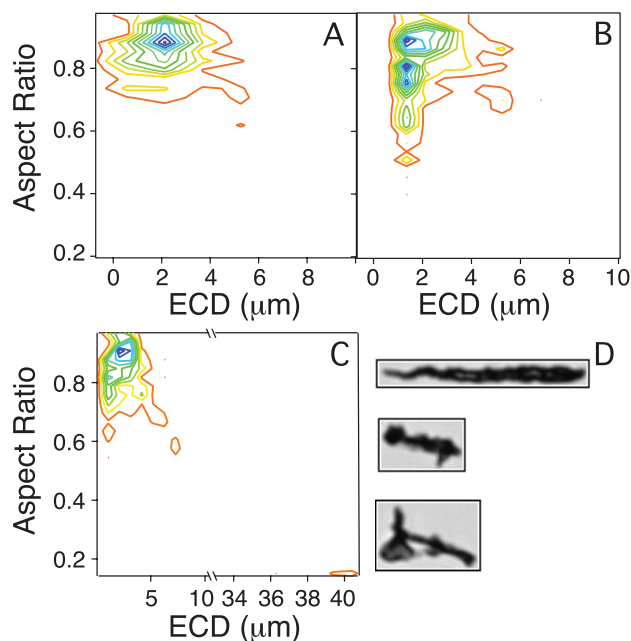


FIGURE 3: Particle size and shape analysis from MFI measurements of IgG1 solutions before and after exposure to the SiO_x surface. (buffer: pH 4.5 30 mmol/L citrate, 0 mmol/L NaCl). Contour plots indicate the frequency particles were counted with a certain equivalent circular diameter (ECD) and aspect ratio. Samples taken from the stock solution, first buffer rinse after SiO_x exposure and the second buffer rinse are shown in panels (A), (B), and (C) respectively. (D) shows characteristic images of the large (> 30 μm ECD) particles observed in the second buffer rinse sample.

Combining neutron reflectivity with solution-based techniques has allowed the correlation between protein layer structure and aggregate formation to be investigated. The results of this work clearly indicate that exposure to the SiO_x surface accelerated particle aggregate formation similar to thermally induced aggregation of IgG1 previously reported [4]. The surface density of proteins, the layer structure and the amount of desorption are highly dependent on pH and salt conditions of the buffer and likely stem from the interplay of protein-protein and protein-surface interactions. The balance of these factors as a function of surface properties and protein sequence provides valuable information in guiding formulation strategies for manufacturing and storage of protein based therapeutics.

References

- [1] E. Y. Chi *et al.*, *Pharm. Res.* **20**, 1325 (2003).
- [2] W. Norde *et al.*, *Adv. Colloid. Interface Sci.* **179-182**, 5 (2012).
- [3] S. K. Singh, *J. Pharm. Sci.*, **100**, 354 (2011).
- [4] R. K. Brummitt *et al.*, *J. Pharm. Sci.*, **100**, 2087 (2011).

Determination of monoclonal antibody conformation using SANS and refined using free energy constraints

N. J. Clark,¹ H. Zhang,¹ S. Krueger,¹ H. J. Lee,² R. R. Ketchem,² B. Kerwin,² S. R. Kanapuram,² M. J. Treuheit,² A. McAuley,² and J. E. Curtis¹

Over the past 30-plus years the biotechnology industry has mastered protein engineering, cloning and cell culture techniques that make designing and producing therapeutic antibodies with a singular, monoclonal, specificity an exciting reality. To date, many antibody therapeutics have been or are in the process of being approved by the FDA and they represent one of the fastest growing classes of pharmaceutical drug products. The use of therapeutic antibodies for the treatment of many cancers, allergy conditions and autoimmune diseases are underway and they represent a promising form of treatment to patients everywhere.

Biotechnology companies are striving to produce highly concentrated (> 100 mg/mL) patient-injectable antibody solutions. Occasionally, certain formulations of antibody solutions fail due to gradual formation of large potentially immunogenic aggregates, spontaneous crystallization and even phase separation. A greater understanding of the processes that lead to the above-mentioned phenomena would insure safety and increase shelf life for protein therapeutics.

Structurally, an antibody is a dynamic protein best described as having three distinct lobes, which can move independent of each other and yet are held in a Y-shape arrangement by a hinge-like junction (two identical Fab-lobes connected to an Fc-lobe). The built-in flexibility and the size of monoclonal antibodies, both of which are necessary for function, represent a challenge for structural studies. Here we have combined small-angle scattering with atomistic modeling to better define the possible conformations or lobe orientations that exist in solution [1]. Using simulation software developed at the NCNR [2], we have generated a full-atom ensemble of antibody orientations to compare to small angle neutron scattering (SANS) and X-ray scattering (SAXS) data of dilute antibody solutions.

Monoclonal Anti-Streptavidin Immunoglobulin G2 (ASA-IgG2) antibody was obtained from Amgen as a highly purified concentrated solution (30 mg/mL). ASA-IgG2 was shown to be unaggregated monomer (98 % monomer) by size-exclusion coupled multi-angle light scattering (SEC-MALS) over several concentrations ranging from (1 to 5) mg/mL. The average solution conformation of ASA-IgG2 was then evaluated using SANS at a concentration of 2.0 mg/mL, which was determined to be free

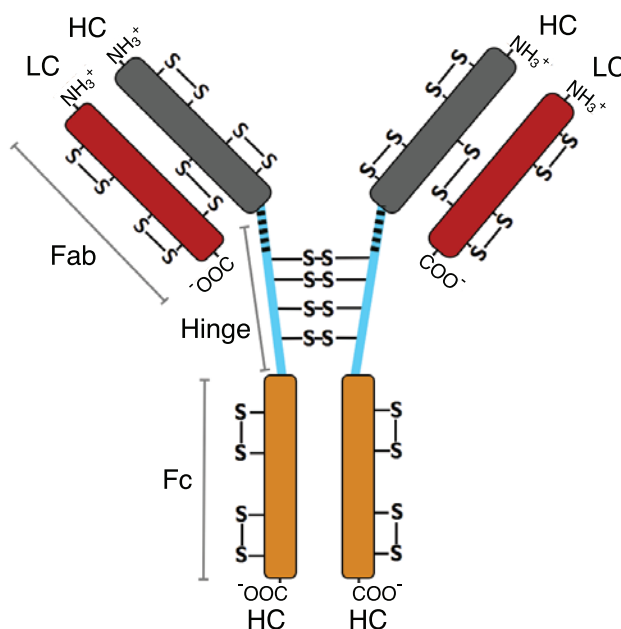


FIGURE 1: Schematic representation of an immunoglobulin G (IgG) subclass 2, isotype A protein. IgG is composed of two light chains (LC) and two heavy chains (HC) that are held together through several inter- and intrachain disulfide bonds (S-S) and non-bonding interactions. The LC and part of the HC form two identical Fab domains. Part of each HC also forms a single Fc domain. The Fab and Fc domains are connected via a flexible hinge region (blue) that has four interchain disulfide bonds. The parts of the hinge regions varied in Monte Carlo simulations are represented by heavy dashed black lines.

from interparticle interactions. For the 2.0 mg/mL ASA-IgG2 the radius of gyration was measured using SANS to be 47.5(6) Å. The pair distribution, $P(r)$, plot of ASA-IgG2 gave a maximum dimension of the average ASA-IgG2 molecule of 155 Å. The resulting real-space R_g was 48 Å and is in agreement with that found using the Guinier approximation.

Molecular simulations were performed using an atomistic coordinate model based on the ASA-IgG2 amino acid sequence. The program SASSIE [2] was used to generate 56,511 unique, non-overlapping structures. To do so, SASSIE sampled backbone dihedral angles, Ψ or ϕ , of three amino acids within the hinge

¹ NIST Center for Neutron Research, National Institute of Standards and Technology, Gaithersburg, MD 20899

² Amgen Inc., Process and Product Development, Thousand Oaks, CA 91320

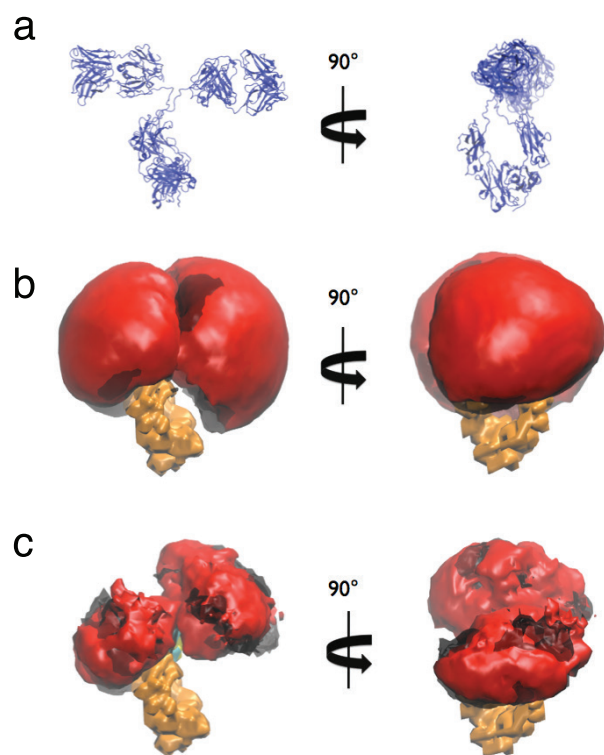


FIGURE 2: Iso-density plots of ASA-IgG2 from molecular Monte Carlo simulation. (a) Starting structure. (b) The solid surface representation of all structures. (c) The solid surface representation for structures with $\chi^2 < 2.0$. Structures were aligned on their Fc region (brown) in order to demonstrate the configuration space covered by the flexible Fab arms (Fab light chain, red; Fab heavy chain, gray).

region adjacent to each Fab lobe (see Fig. 1). Theoretical scattering profiles for each structure were calculated [3] and the resulting $I(q)$ -plots were compared with the 2 mg/mL SANS data.

Even though only three amino acids were used for dihedral angle sampling for both Fab-lobes, the relative configurations between the Fab to Fc domains varied quite drastically. The resulting orientations had R_g -values that spanned from ≈ 39 Å to ≈ 55 Å. However, the best-fit structures, those with $\chi^2 \leq 2$, had an R_g that were confined to a range of ≈ 46.5 Å to ≈ 50.5 Å. Overlaying the atomistic density, occupied for all the structures in the full ensemble and the sub-ensemble (those with $\chi^2 \leq 2$) allows a visual inspection of the conformational space available to ASA-IgG2. Density-plots for the full- and sub-ensemble are represented in Fig. 2.

The “best-fit” structures contained within the sub-ensemble number approximately 1200 of the $> 56,000$ structures. Constraints from additional experimentation offer a means to further refine the possible conformations and to further clarify structure function relationships. Orthogonal biophysical

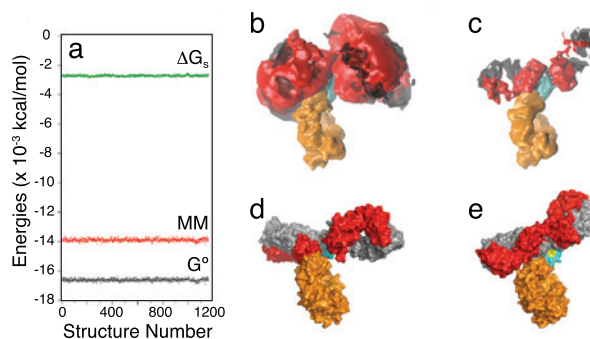


FIGURE 3: Relative configurational free-energy analysis of structures with $\chi^2 < 2$. (a) Molecular mechanical energy (MM), non-polar solvation energy (ΔG_s), and total free energy (G°) for 1160 structures. (b) Iso-density plot of ASA-IgG2 (reproduced from Fig. 2c). (c) Iso-density plot of structures of lowest free energy within one standard deviation of the lowest single free-energy value in the ensemble. Parts (d) and (e) show structures with the single highest and lowest free energy, respectively.

techniques like analytical ultracentrifugation (AUC), nuclear magnetic resonance (NMR) and Förster Resonance Energy Transfer (FRET) provide those constraints.

Another approach is to apply a free-energy analysis to evaluate the relative configurational energies of the sub-ensemble of ASA-IgG2. As shown in Fig. 3a, the relative free energy, ΔG° , of the sub-ensemble (structures with $\chi^2 < 2$) shows that fewer configurations may be energetically favorable. Evaluation of structures near the energetic minimum could allow a substantial reduction of the number of plausible, and hence representative, structures. Alternatively, evaluation of structures near the energetic maximum may help to evaluate regions that lead to undesirable intramolecular interactions.

The energetic analysis, while computationally demanding and inherently limited, includes thermodynamic constraints that have the potential to improve upon the results of conservative linear combinations of scattering profiles used to calculate the ensemble of structures depicted in density-plots in Fig. 2. Evaluation of molecular conformations present in dilute antibody solutions is an important prerequisite step for understanding how antibodies behave in more complicated concentrated solutions. The methods developed for this study are currently being applied to solutions with concentrations as high as 200 mg/mL. In conjunction with orthogonal experiments our goal is to better describe the types of interactions present in solution in order to better design safe, effective therapeutic proteins.

References

- [1] N. C. Clark *et al.*, J. Phys. Chem. B **117**, 14029 (2013).
- [2] J. E. Curtis *et al.*, Comput. Phys. Commun. **183**, 382 (2012).
- [3] S. Krueger *et al.*, J. Biol. Chem. **273**, 20001 (1998).

Tunable CO/H₂ and CO/N₂ separations in metal-organic frameworks with exposed divalent metal cations via reversible CO binding

M. R. Hudson,¹ C. M. Brown,^{1,2} E. D. Bloch,³ J. A. Mason,³ S. Chavan,⁴ V. Crocellà,⁴ J. D. Howe,^{5,6} K. Lee,^{5,6} A. L. Dzubak,⁷ W. L. Queen,⁶ J. M. Zadrozny,³ S. J. Geier,³ L.-C. Lin,⁵ L. Gagliardi,⁷ B. Smit,^{3,5,8} J. B. Neaton,^{6,8} S. Bordiga,⁴ and J. R. Long^{3,8}

Carbon monoxide has become an increasingly important chemical for the synthesis of a variety of chemical commodities, including many monomers and polymers, ethanol and other alcohols, and acetic acid. There are currently a number of competing technologies for its synthesis, the main products of which are carbon monoxide and hydrogen (syngas), typically present in H₂:CO ratios between 1 and 3. To use carbon monoxide as a feedstock, the ratio must be reduced. Although energy-intensive cryogenic distillation is currently employed to separate these mixtures, a number of alternative methods, including membrane and adsorptive separations, have recently been investigated for use in the production of pure carbon monoxide. Given their high density of coordinatively-unsaturated metal cation sites, metal-organic frameworks of the M₂(dobdc) structure type (M = Mg, Mn, Fe, Co, Ni, Zn; dobdc⁴⁻ = 2,5-dioxido-1,4-benzenedicarboxylate) hold considerable promise for the adsorptive separation of gas streams, including mixtures of CO₂/N₂, CO₂/H₂, O₂/N₂, CH₄/N₂, paraffins/olefins, and stand poised for the separation of gas mixtures containing CO [1-3].

The coordination of carbon monoxide to transition metals has been rigorously investigated for over a century, and has played an essential role in the development of our understanding of chemical bonding. Carbonyl complexes have been isolated and characterized for nearly every transition metal, in varying oxidation states and overall coordination numbers. The vast majority of these species feature CO irreversibly bound to low-valent, low-spin transition metal centers that are able to engage in the metal-to-CO π -backbonding required for strong binding. For systems in which π -backbonding is absent or diminished, carbonyl complexes remain elusive. With this work, we show that CO can reversibly bind to the coordinatively-unsaturated M²⁺ cations lining the surfaces within the metal-organic frameworks M₂(dobdc), providing the first crystallographically characterized magnesium and zinc carbonyl compounds and the first high-spin Mn(II), Fe(II), Co(II), and Ni(II) carbonyl species. The metal-organic framework lattice likely helps to maintain a high-spin state, as these materials would have to undergo significant structural changes to accommodate the smaller low-spin M²⁺ ions. As a result, these materials can be anticipated to display weak to moderate CO binding and complete reversibility,

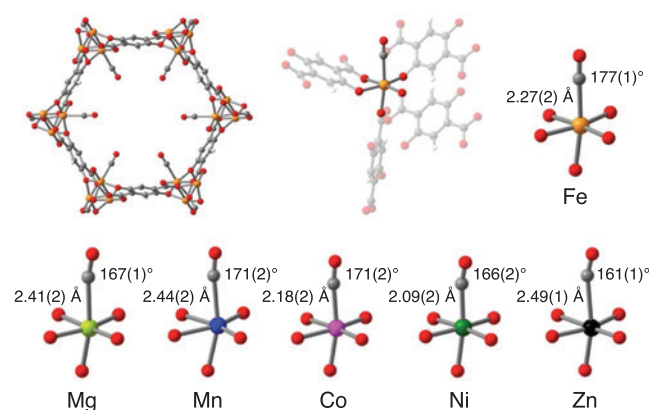


FIGURE 1: A channel view (c-axis) of Fe₂(dobdc)·1.5CO as determined by Rietveld analysis of powder neutron diffraction data (grey, carbon and red, oxygen) and coordination environment for a single Fe²⁺ site in Fe₂(dobdc)·1.5CO. First coordination sphere for the M²⁺ ions in M₂(dobdc)·1.5CO, with M–CO distances and M–C–O angles indicated.

a property that could potentially be exploited for removing CO from various gas mixtures.

As an initial probe of the interaction of CO with the square pyramidal M²⁺ cations lining the ≈ 12 Å wide channels in M₂(dobdc), we turned to *in-situ* infrared (IR) spectroscopy. For all 6 frameworks, a single adsorption band is observed at low coverage between 2160 cm⁻¹ and 2178 cm⁻¹, which is blue-shifted with respect to the stretching mode of free CO (2143 cm⁻¹). For classical transition metal carbonyl complexes, the average ν (CO) is red-shifted, because the M→CO π back-donation is the dominant effect, significantly weakening the C–O bond compared to that of free CO. When back-donation is absent or diminished, ν (CO) is blue-shifted in a phenomenon that is termed non-classical CO adsorption. Of the more than 20,000 reported M–CO stretching frequencies, only 250-300 can be considered non-classical.

Given our prior success in elucidating crystal structures of a number of adsorbent molecules in M₂(dobdc) [1,2], we turned to neutron

¹ NIST Center for Neutron Research, National Institute of Standards and Technology, Gaithersburg, MD 20899

² University of Delaware, Newark, DE 19716

³ Department of Chemistry, University of California, Berkeley, CA 94720

⁴ Department of Chemistry, NIS and INSTM Reference Centres, University of Turin, I-10135 Torino, Italy

⁵ Department of Chemical and Biomolecular Engineering, University of California, Berkeley, CA 94720

⁶ The Molecular Foundry, Lawrence Berkeley National Laboratory, Berkeley, CA 94720

⁷ Chemical Theory Center and Supercomputing Institute, University of Minnesota, Minneapolis, MN 55455

⁸ Materials Sciences Division, Lawrence Berkeley National Laboratory, Berkeley, CA 94720

powder diffraction experiments to further characterize the carbonyl adducts $M_2(\text{dobdc}) \cdot 1.5\text{CO}$ (Fig. 1). X-ray diffraction would be unable to distinguish the orientation of a CO molecule, but the difference in scattering cross sections are sufficient to allow this with neutrons. Consistent with the large range in CO IR stretching frequencies, we see a range of M-C-O angles, from $161.2(7)^\circ$ for Zn to $176.9(6)^\circ$ for Fe, with a strong correlation observed between $\nu(\text{CO})$ and the M-C-O angle (Fig. 2). In the Fe and Co, where a greater degree of π -backbonding is observed via IR spectra, more linear carbonyl adducts are formed, while in the cases where electrostatic effects play a major role, bent structures are observed. The structures also display a large range in M-C bond distances, ranging from $2.09(2) \text{ \AA}$ for Ni to $2.49(1) \text{ \AA}$ for Zn, with excellent correlation between adsorption enthalpy and M-C distance (Fig. 2). Both Ni(II)- and Co(II)-carbonyl are rare and feature low-spin metal cations and short M-C distances. $Mg_2(\text{dobdc}) \cdot 1.5\text{CO}$ and $Zn_2(\text{dobdc}) \cdot 1.5\text{CO}$, $d_{(\text{M-CO})} = 2.41(2)$ and $2.49(1) \text{ \AA}$, respectively, represent the first crystallographically characterized Mg and Zn carbonyl complexes, regardless of oxidation state.

Magnetic susceptibility data were also collected to confirm the high-spin character of the iron(II) centers in the CO-adsorbed phase $\text{Fe}_2(\text{dobdc}) \cdot 2\text{CO}$. Mössbauer spectra further confirm the assignments of high-spin Fe(II). The result for $\text{Fe}_2(\text{dobdc}) \cdot 2\text{CO}$ is without precedent. Of the nearly 9,000 iron-carbonyl structures reported in the Cambridge Crystal Structure Database, only three are paramagnetic, all featuring intermediate-spin ($S = 1$) Fe(II) centers in a trigonal bipyramidal coordination environment, for which an $S = 0$ spin state is generally not possible. Thus, $\text{Fe}_2(\text{dobdc}) \cdot 2\text{CO}$ represents the first

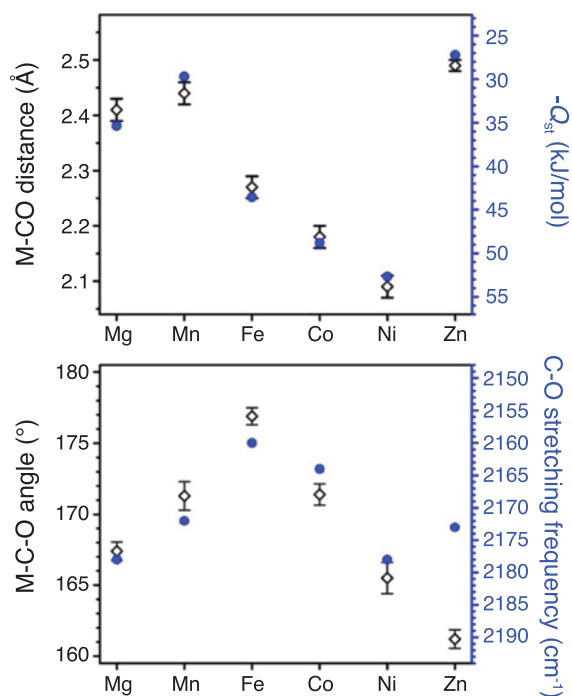


FIGURE 2: Variations of M-CO distance (neutron diffraction, black diamonds) and isosteric heat of CO adsorption (Q_{st} , blue circles) and of M-C-O angle (neutron diffraction, black diamonds) and C-O stretching frequency (FTIR, blue circles) with M^{2+} in $M_2(\text{dobdc})$. Error bars indicate the one standard deviation in the diffraction refinements.

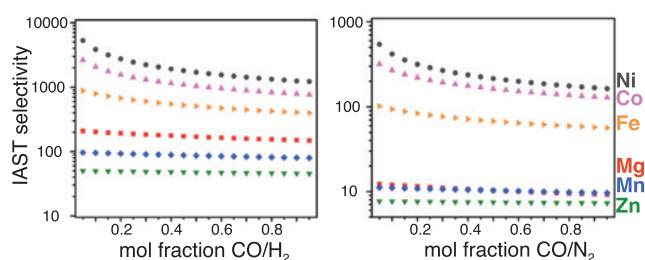


FIGURE 3: IAST selectivities for CO/H_2 and CO/N_2 mixtures (298 K, 1 bar) for 6 different M^{2+} species.

example of a paramagnetic octahedral iron carbonyl compound and, to our knowledge, the first reported $S = 2$ iron carbonyl.

To probe the ability of these compounds to separate gases and purify CO, we measured pure component CO adsorption isotherms at 298 K, 308 K, and 318 K, and isosteric heats of adsorption were calculated for each metal. At 298 K, the CO adsorption isotherms for the Fe, Co and Ni frameworks approach the value expected for one CO molecule per open metal site. Importantly, in all cases, the bound CO could be completely desorbed upon application of dynamic vacuum and/or heat, and subsequent CO adsorption isotherms showed no loss of uptake capacity. The isosteric heats of adsorption calculated from the data vary widely with metal; the CO binding strength following the order $\text{Ni} > \text{Co} > \text{Fe} > \text{Mg} > \text{Mn} > \text{Zn}$ (Fig. 2). The extraordinary ability of these materials to bind CO reversibly and at high capacity does suggest their potential application in removing CO from gas mixtures, such as CO/N_2 and CO/CH_4 , and, in particular, for the purification of CO from syngas. In order to determine the CO/H_2 selectivities, we employed ideal adsorbed solution theory (IAST). To reflect the varying $\text{H}_2:\text{CO}$ ratios found in syngas, IAST selectivities were calculated over a range of compositions (Fig. 3), and were found to vary widely, from a minimum of 45 in the case of $\text{Zn}_2(\text{dobdc})$ to over 5200 for $\text{Ni}_2(\text{dobdc})$ at low CO concentrations. The high CO/N_2 selectivities of these materials also bodes particularly well for use in separating CO from syngas contaminated with N_2 .

$M_2(\text{dobdc})$ type metal-organic frameworks provide an excellent platform for the investigation of new coordination chemistry via gaseous substrate binding at coordinatively-unsaturated metal sites. The fully reversible CO binding at high capacity and moderate adsorption enthalpies further make these materials outstanding candidates for the efficient separation of CO gases such as H_2 and N_2 . The rigidity of the evacuated materials, together with their highly crystalline nature, has thus enabled the generation and crystallographic characterization of the first high-spin Mn(II), Fe(II), Co(II), and Ni(II) carbonyl species, as well as the first magnesium and zinc carbonyls. Neutron diffraction, and the ability to fully differentiate C and O atoms, is critical to making this possible.

References

- [1] S. J. Geier *et al.*, Chem. Sci. **4**, 2054 (2013).
- [2] E. D. Bloch *et al.*, Science **335**, 1606 (2012).
- [3] E. D. Bloch *et al.*, J. Am. Chem. Soc. ASAP, DOI: 10.1021/ja505318p.

Crystal and magnetic stripes coupled to cooperative Jahn-Teller effects in $\text{Na}_{5/8}\text{MnO}_2$

X. Li,¹ X. Ma,¹ D. Su,² L. Liu,¹ R. Chisnell,³ S. P. Ong,¹ H. Chen,¹ A. Toumar,¹ J.-C. Idrobo,⁴ Y. Lei,¹ J. Bai,⁵ F. Wang,⁶ J. W. Lynn,⁷ Y. S. Lee,³ and G. Ceder¹

Layered oxides with alternating Na and transition metal layers have been studied extensively to understand their fundamental properties as well as for their potential application in rechargeable batteries, thermoelectrics, and as the parent materials of the superconductive cobaltates. Na can be electrochemically and reversibly removed from these materials in a process called de-intercalation, which can precisely control the Na concentration in the compound. The ordering of the unoccupied Na sites, or vacancies, is controlled by electrostatic interactions in the non-Jahn-Teller active systems. However, Na_xMnO_2 is expected to be more complicated as it mixes Mn^{3+} ions, which display one of the largest Jahn-Teller distortions in transition metal compounds and prefer nearest neighbor antiferromagnetic (AF) coupling, with Mn^{4+} ions, which are not Jahn-Teller active and can form either ferromagnetic or AF nearest neighbor couplings depending on the competition between different direct and indirect exchange mechanisms. The well-ordered $\text{Na}_{5/8}\text{MnO}_2$ material is a prototype for this class of systems, and we have carried out combined neutron, X-ray, and electron scattering measurements together with electronic calculations to unravel these intertwined interactions and provide a foundation to understand the important properties of this interesting and useful class of systems [1].

The Jahn-Teller (JT) effect refers to the local distortion of the chemical bonds around the Mn^{3+} transition metal ions, which lifts the degeneracy of the electronic configuration and lowers the energy of the system. The JT distortions can become correlated, resulting in the cooperative Jahn-Teller effect (CJTE) in complex (typically oxide) materials. The effect usually induces strong coupling between the charge, orbital and magnetic interactions, which control many important phenomena such as colossal magnetoresistance and superconductivity. For $\text{Na}_{5/8}\text{MnO}_2$, we find an unexpected superstructure with a pronounced static CJTE that is coupled to an unusual Na vacancy ordering. X-ray and electron scattering, plus the addition of neutron scattering measurements to elucidate the magnetic bonding were required to unravel the complex interactions in this prototype material. In particular, the magnetic order was found to consist of Mn interwoven magnetic stripes with different moments and magnetic couplings. This work demonstrates the strong

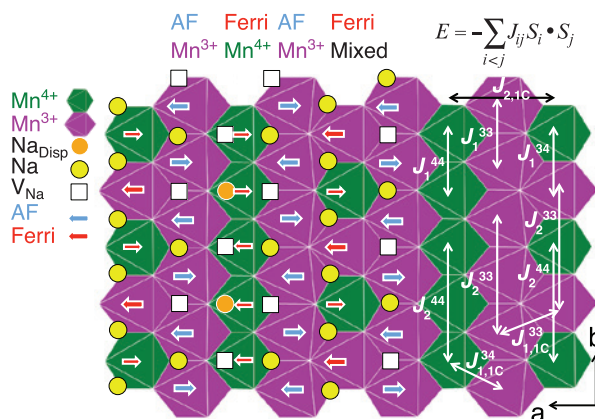


FIGURE 1: $\text{Na}_{5/8}\text{MnO}_2$ superstructure shows V_{Na} ordering, Mn charge and magnetic stripe orderings. The magnetic spin-stripe ordering includes ferrimagnetic stripes (Ferri) and antiferromagnetic stripes (AF). The spin exchange parameters J_{ij} between different Mn sites were calculated by density functional theory.

interaction between alkali ordering, electronic structure, and magnetic interactions, and underlines the essential role that structural details play in determining electronic behavior.

Electrochemical Na de-intercalation from NaMnO_2 initially occurs through a two-phase reaction, forming a new phase $\text{Na}_{5/8}\text{MnO}_2$ as illustrated in Fig. 1. The Na ordering was solved by a combination of different techniques including electron diffraction, scanning transmission electron microscopy (STEM) imaging, synchrotron X-ray diffraction (SXRD) and density functional theory (DFT) simulation. The Na layer of $\text{Na}_{5/8}\text{MnO}_2$ is formed by one full Na atomic stripe parallel to three half-full Na stripes in which Na and V_{Na} (vacancies) alternate, with the Mn charge ordering reflecting the modulation of the Na ordering. There are three types of Mn stripes identified through magnetic neutron diffraction, electron energy loss spectroscopy in STEM mode and DFT simulation: a pure Mn^{3+} stripe, a pure Mn^{4+} stripe and a stripe of alternating Mn^{3+} and Mn^{4+} ions. As the Mn^{3+}O_6 octahedron is JT distorted and the Mn^{4+}O_6 is not, the periodic arrangement of these different stripes gives a CJTE, which can be directly

¹ Department of Materials Science and Engineering, Massachusetts Institute of Technology, Cambridge, MA 02139

² Center for Functional Nanomaterials, Brookhaven National Laboratory, Upton, NY 11973

³ Department of Physics, Massachusetts Institute of Technology, Cambridge, MA 02139

⁴ Oak Ridge National Laboratory, Oak Ridge, TN 37831

⁵ National Synchrotron Light Source, Brookhaven National Laboratory, Upton, NY 11973

⁶ Sustainable Energy Technologies Department, Brookhaven National Laboratory, Upton, NY 11973

⁷ NIST Center for Neutron Research, National Institute of Standards and Technology, Gaithersburg, MD 20899

visualized by the rippling of the Mn layers from STEM imaging. It is worth noting that in the DFT-calculated structure, the Na ions in one of the three half-full Na stripes are displaced along the stripe direction by about 1.4 Å from their normal octahedral site location, into a new site. This stripe is labeled as Na_{Disp} in Fig. 1. The local environment of the displaced Na ions is a highly distorted octahedral site face-sharing with both Mn⁴⁺O₆ octahedra. The other Na sites in Na_{5/8}MnO₂ are normally slightly distorted octahedral sites that edge-share with both TM layers. The origin of the Na_{Disp} displacement is that the relaxed Na ions to the highly distorted octahedral site can share the symmetric attraction of the two neighboring JT distorted -O-Mn³⁺-O-Na configurations.

One of the interesting consequences of the electronic and alkali ordering in Na_{5/8}MnO₂ is that it leads to a new and intriguing magnetic ordering. Based on neutron powder diffraction, magnetic susceptibility measurements and DFT calculations, we proposed the magnetic-stripe-sandwich structure shown in Fig. 1. The DFT total energies for different collinear magnetic spin orderings in Na_{5/8}MnO₂ were calculated and mapped onto a spin Hamiltonian, $-\sum_{i,j} J_{ij} \mathbf{S}_i \cdot \mathbf{S}_j$ to extract the nearest-neighbor and next-nearest-neighbor spin exchange parameters J_{ij} between site i and j , as defined in Fig. 1. \mathbf{S}_i and \mathbf{S}_j are the spin angular momentum operators. The result predicts the Mn³⁺ stripes to be AF, Mn⁴⁺ stripes to be ferrimagnetic, and mixed valence Mn³⁺/Mn⁴⁺ stripes to be ferrimagnetic with AF nearest-neighbor coupling.

Neutron diffraction measurements were performed on 5 g of chemically de-intercalated Na_{5/8}MnO₂ powder using the triple axis spectrometer BT-7 at the NIST Center for Neutron Research [2]. The diffraction pattern taken at $T = 2.5$ K reveals additional magnetic Bragg peaks compared with the diffraction pattern at $T = 100$ K (consisting of nuclear Bragg peaks from the crystal structure), demonstrating that the material exhibits long-range magnetic order. The inset in Fig. 2 shows the temperature dependence of the integrated intensity of the lowest angle magnetic Bragg peak, indicating an ordering temperature of $T \approx 60$ K, consistent with the temperature of the upturn in the magnetic susceptibility. The DFT calculated coupling constant of -61.5 K (negative value corresponds to AF interaction) for the Mn³⁺ AF stripe is in good agreement with the temperature scale of the observed ordering.

The intensities of the magnetic Bragg peaks can be described by a pattern of magnetic stripes of ordered moments on the Mn sites. The simplest model of ordered moments consistent with the data involves AF stripes of Mn³⁺ with an AF coupling between stripes, as indicated by the blue arrows in Fig. 1. When only these moments are taken into account, the fits yield an ordered moment of 3.2(4) μ_B per Mn³⁺. Other magnetic ordering patterns which have the same periodicity as these AF Mn³⁺ stripes would also be consistent with the data. For example, AF stripes of Mn⁴⁺ and mixed Mn³⁺/Mn⁴⁺ coexisting with the AF stripes of Mn³⁺ would yield a similar magnetic diffraction pattern, but the average moment would have a smaller value of 2.2(3) μ_B per Mn. Further details of the magnetic structure will likely require measurements on single crystals. Interestingly, the divergence of the field-cooled and zero-field-cooled susceptibility curves around $T = 12$ K may indicate

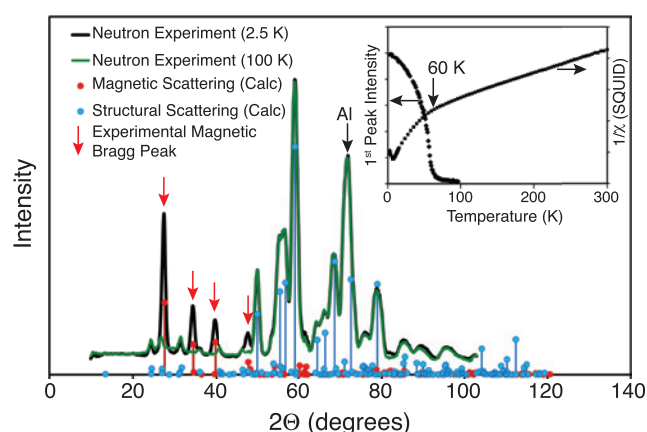


FIGURE 2: Neutron diffraction and magnetic susceptibility measurement indicating magnetic stripe ordering. Magnetic Bragg peaks labeled by red arrows are seen in the 2.5 K spectrum compared to the 100 K spectrum. The inset shows the integrated intensity of the strongest magnetic peak in the neutron spectrum (left scale) and also the inverse magnetic susceptibility (right scale) versus temperature.

the presence of weakly coupled ferrimagnetic components and agrees quantitatively with the calculated nearest-neighbor coupling constant of 11.9 K for the Mn⁴⁺ ferrimagnetic stripes. Overall, the general pattern predicted by DFT of AF Mn³⁺ stripes interwoven with the Mn⁴⁺ and Mn⁴⁺/Mn³⁺ stripes is fully supported by the experiments. This new magnetic-stripe-sandwich structure may have potential application in magnetic storage or spin electronics as the 1D analogy to the sandwich structure of 2D magnetic thin films, from which abundant magnetic phenomena have been engineered. It is also worth noting that the dynamic version of the hole-segregated magnetic stripes has been proposed to be important for high temperature cuprate superconductors [3].

In summary, we have found Na_{5/8}MnO₂ to be a model system to visualize the complex interactions between Na ion/vacancy ordering, charge ordering, magnetic ordering and cooperative Jahn-Teller distortions. We find that in contrast to other alkali-vacancy systems, the Na ordering in Na_xMnO₂ is controlled by the underlying combination of electrostatic and electronic structure interactions through the Jahn-Teller effect, which enables some Na to occupy the highly distorted octahedral site. This leads to Na and Mn charge-ordered stripes, which in turn yields a fascinating low temperature magnetic ordering to develop. DFT and experimental observations are in excellent agreement, providing confidence in the proposed ground state and in the explanation for the physical origin of its stability. The understanding of the CJTE here may have general implications for understanding complex compounds where the Jahn-Teller effect is prominent, including intercalation energy storage materials and high temperature superconductors, and illustrates the fascinating physics of mixed Mn valence systems.

References

- [1] X. Li *et al.*, Nat. Mater. **13**, 586 (2014).
- [2] J. W. Lynn *et al.*, J. Res. NIST **117**, 61 (2012).
- [3] M. Vojta, Adv. Phys. **58**, 699 (2009).

Anion reorientations, sodium mobility, and superionic conduction in $\text{Na}_2\text{B}_{12}\text{H}_{12}$

N. Verdal,^{1,2} T. J. Udovic,¹ J. J. Rush,^{1,2} W. S. Tang,^{1,2} J.-H. Her,³ A. V. Skripov,⁴ V. Stavila,⁵ M. Matsuo,⁶ and S. Orimo⁶

Light-metal dodecahydro-*closo*-dodecaborate ($\text{B}_{12}\text{H}_{12}^{2-}$) salts have received increased scrutiny in recent years because they are byproducts during the dehydrogenation of corresponding tetrahydroborates, such as LiBH_4 and NaBH_4 , which are potential hydrogen-storage materials. More recently, we have discovered that thermal stability of $\text{B}_{12}\text{H}_{12}^{2-}$ and its large size and quasispherical shape, which enable larger intralattice pathways for cation diffusion, are desirable qualities for its use in fast-ion conductor materials. Moreover, we have found that the lighter-alkali-metal compounds, $\text{Li}_2\text{B}_{12}\text{H}_{12}$ and $\text{Na}_2\text{B}_{12}\text{H}_{12}$, undergo entropy-driven transformations to disordered cubic phases exhibiting orientational disorder of the $\text{B}_{12}\text{H}_{12}^{2-}$ anions and vacancy-rich cation sublattices that lend themselves to unusually facile cation diffusion. The unit cells of the low-temperature, ordered monoclinic ($P2_1/n$) and the high-temperature bcc ($Im\bar{3}m$) structures of $\text{Na}_2\text{B}_{12}\text{H}_{12}$ determined by neutron powder diffraction [1] are shown in Fig. 1. (It should be noted that $\text{Na}_2\text{B}_{12}\text{H}_{12}$ passes through a partially disordered $Pm\bar{3}n$ phase at ≈ 529 K before achieving “full” $Im\bar{3}m$ disorder.) The orientational disorder of the anions is represented in Fig. 1b by a number of superimposed orientations. Also, in contrast to the ordered cation sites in Fig. 1a, the Na^+ cations in the bcc phase are disordered among

a complex array of off-center sites within the large interstices formed by the anions. This suggests the possibility of highly mobile Na^+ cations capable of superionic conduction.

To probe the detailed nature of the dynamical disorder indicated by the diffraction results, we measured the reorientational behavior of the $\text{B}_{12}\text{H}_{12}^{2-}$ anions and Na^+ cation diffusion by combined quasielastic neutron scattering (QENS) [2] and NMR [3]. The QENS data were obtained using the DCS spectrometer at the NCNR at $\lambda = 4.8$ Å with 56 μeV FWHM resolution and a Q range up to 2.4 Å⁻¹. In Fig. 2, we show the elastic incoherent structure factors derived from the QENS results at 580 K compared to a number of reorientational models, a representative QENS spectrum, and the schematics of two uniaxial jump models. A major conclusion of the model comparisons in Fig. 2 is that the $\text{B}_{12}\text{H}_{12}^{2-}$ anions undergo predominantly uniaxial, small-angle,

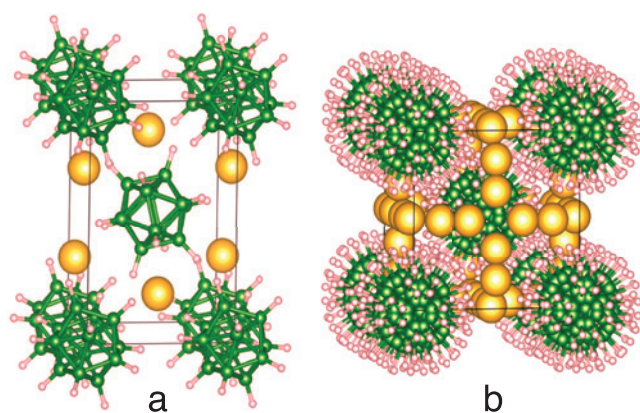


FIGURE 1: Unit cells of the (a) low-temperature, ordered monoclinic and (b) high-temperature, disordered cubic $\text{Na}_2\text{B}_{12}\text{H}_{12}$ structures. Yellow, green, and pink spheres denote Na, B, and H, respectively.

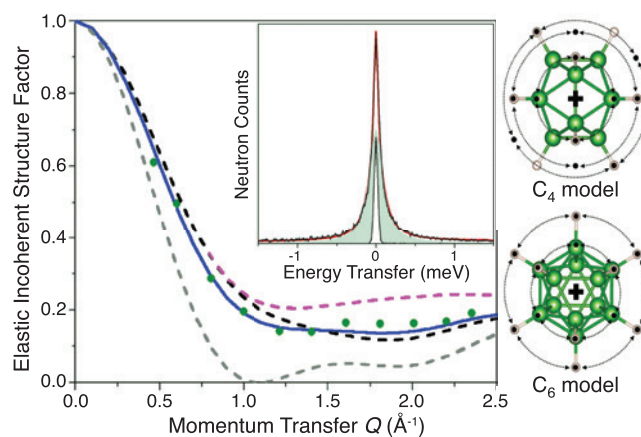


FIGURE 2: The elastic incoherent structure factor (green symbols) measured at 580 K compared to several reorientational models. The uniaxial C_4 (magenta dashes) and C_6 (black dashes) jump reorientation models are shown schematically at the right. The 3-D tumbling model (gray dashes) mimics isotropic rotational diffusion. The solid blue line is a composite model of 50 % uniaxial C_6 jumps, 30 % uniaxial C_4 jumps, and 20 % 3-D tumbling. The inset shows a corresponding QENS spectrum at 1.2 Å⁻¹. The fit (red) to the data (black) is comprised of elastic (white) and quasielastic (gray) contributions.

¹ NIST Center for Neutron Research, National Institute of Standards and Technology, Gaithersburg, MD 20899

² University of Maryland, College Park, MD 20742

³ GE Global Research, Niskayuna, NY 12309

⁴ Institute of Metal Physics, Ural Branch of the Russian Academy of Sciences, Ekaterinburg, Russia

⁵ Sandia National Laboratories, Livermore, CA 94551

⁶ Institute for Materials Research, Tohoku University, Sendai, Japan

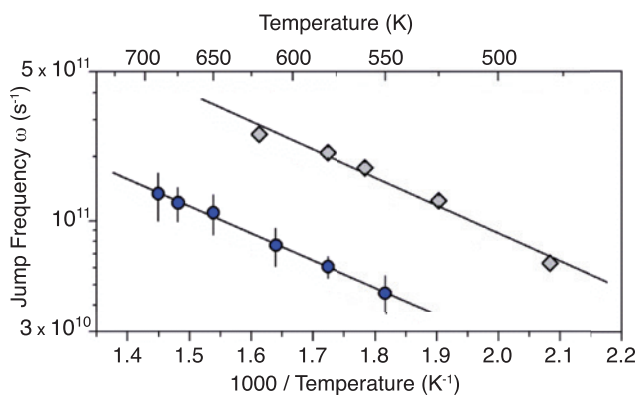


FIGURE 3: Arrhenius plots for $\text{Na}_2\text{B}_{12}\text{H}_{12}$ (gray diamonds) and $\text{Na}_2\text{B}_{12}\text{D}_{12}$ (blue circles) from which the activation energies for the reorientational motion were determined. Calculated jump frequencies are based on the C_6 model.

reorientational jumps rather than 3-D tumbling motions, with 6-fold jump reorientations around the anion 3-fold symmetry axes giving the best overall fit at 580 K. An even better fit can be achieved in Fig. 2 by assuming a small admixture of occasional 3-D tumbling to the predominantly uniaxial reorientations, acknowledging that there will be a distribution of rotational potentials within this highly disordered structure.

Additional information about the anion dynamical behavior was obtained by analyzing the quasielastic widths vs. temperature. The results, which are shown in Fig. 3 for both $\text{Na}_2\text{B}_{12}\text{H}_{12}$ and $\text{Na}_2\text{B}_{12}\text{D}_{12}$ (87 % deuterated), provide activation energies for reorientation of 259(22) meV and 252(7) meV, respectively. In a complementary study by ^1H , ^{11}B , and ^{23}Na NMR spectroscopy, we have probed the $\text{B}_{12}\text{H}_{12}^{2-}$ reorientational motions and Na^+ diffusion in both the ordered and disordered phases. From proton spin-lattice relaxation data, respective activation energies of 770(20) meV and 270(40) meV were derived. NMR data confirmed a hundred-fold increase in reorientational jump rate ($\approx 10^9 \text{ s}^{-1}$ to $\approx 10^{11} \text{ s}^{-1}$) at the phase transition. The analysis of the ^{23}Na spin-lattice relaxation data revealed a striking increase in Na^+ diffusion jump rate at the order-disorder transition to a value of at least $2 \times 10^8 \text{ s}^{-1}$, indicating the possible onset of superionic conduction. See Refs. [2] and [3] for a complete analysis of the anion and cation dynamics in this compound.

To examine the implications of the great increase of anion reorientational and cation diffusional jump rates at the order-disorder transition in $\text{Na}_2\text{B}_{12}\text{H}_{12}$, AC impedance measurements were carried out over a temperature range from 300 K to 575 K, including both cooling and heating scans [4]. The results are shown in Fig. 4, compared to other complex hydride materials. Hysteretic behavior is evident upon cooling, but the results clearly show a dramatic, nearly thousand-fold enhancement in conductivity upon transformation to the cubic phases. A conductivity of $\approx 0.1 \text{ S cm}^{-1}$ near 550 K greatly exceeds that of all other complex-hydride

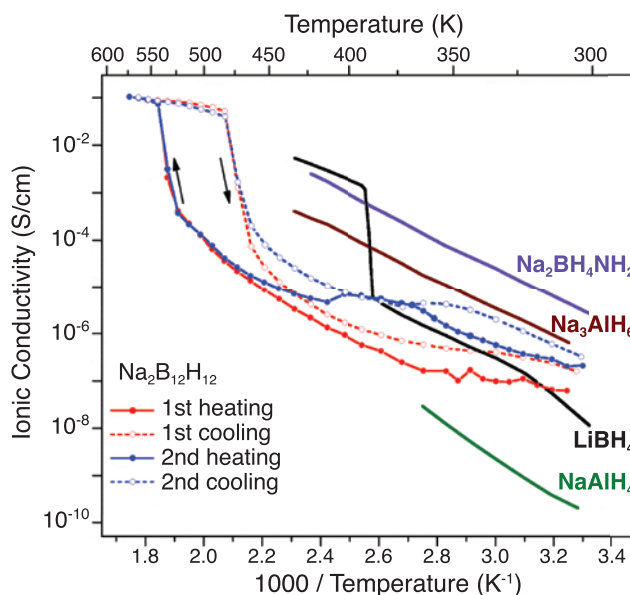


FIGURE 4: Temperature dependence of the ionic conductivity of $\text{Na}_2\text{B}_{12}\text{H}_{12}$ compared with that for other complex hydride materials (see Refs. in [4]).

materials to date. In fact, the conductivity of $\text{Na}_2\text{B}_{12}\text{H}_{12}$ rivals that of sodium beta alumina, the current commercial electrolyte for Na-ion batteries operating in this temperature region. Aside from favorable conductivity, this material's relative insensitivity to air, high-temperature stability, low cost, and simplicity of preparation make it worthy of further investigation.

Finally, as the research continues for analogous superionic electrolytes with improved properties, further work is required to reveal the mechanisms for fast cation diffusion. A direct comparison between different complex hydrides is clouded by differences in structures, anion valence numbers, anion/cation stoichiometric ratios, and the possible presence of mixed phases. Nonetheless, it is probable that the large, quasispherical $\text{B}_{12}\text{H}_{12}^{2-}$ anions, and perhaps their reorientational mobility, provide for more facile cation pathways with lower barriers for diffusion.

References

- [1] N. Verdal, J.-H. Her, V. Stavila, A. V. Soloninin, O. A. Babanova, A. V. Skripov, T. J. Udovic, J. J. Rush, *J. Solid State Chem.* **212**, 81 (2014).
- [2] N. Verdal, T. J. Udovic, V. Stavila, W. S. Tang, J. J. Rush, A. V. Skripov, *J. Phys. Chem. C* **118**, 17483 (2014).
- [3] A. V. Skripov, O. A. Babanova, A. V. Soloninin, V. Stavila, N. Verdal, T. J. Udovic, J. J. Rush, *J. Phys. Chem. C* **117**, 25961 (2013).
- [4] T. J. Udovic, M. Matsuo, A. Unemoto, N. Verdal, V. Stavila, A. V. Skripov, J. J. Rush, H. Takamura, S. Orimo, *Chem. Commun.* **50**, 3750 (2014).

Oxidation of ethane to ethanol by N₂O in an iron(II) metal-organic framework

M. R. Hudson,¹ C. M. Brown,^{1,2} D. J. Xiao,³ E. D. Bloch,³ J. A. Mason,³ W. L. Queen,⁴ N. Planas,⁵ J. Borycz,⁵ A. L. Dzubak,⁵ P. Verma,⁵ K. Lee,⁴ F. Bonino,⁶ V. Crocellà,⁶ J. Yano,⁷ S. Bordiga,⁶ D. G. Truhlar,⁵ L. Gagliardi,⁵ and J. R. Long^{3,8}

The selective and efficient conversion of light alkanes into value-added chemicals remains an outstanding challenge with tremendous economic and environmental impacts, especially given the recent worldwide increase in natural gas reserves. In nature, C–H functionalization is carried out by copper and iron metalloenzymes, which activate dioxygen and facilitate two- or four-electron oxidations of organic substrates through metal-oxo intermediates. Duplicating this impressive reactivity in synthetic systems has been the focus of intense research. Fe(IV)–oxo complexes have now been characterized structurally in various geometries (octahedral, trigonal bipyramidal) and spin states ($S = 1$, $S = 2$), and have proved to be competent catalysts for a variety of oxygenation reactions. In the absence of a protective protein superstructure, terminal iron–oxo species are highly susceptible to a variety of decomposition pathways. Tethering a molecular iron species to a porous solid support could potentially prevent many of these side-reactions. However, complexes heterogenized in this manner are difficult to characterize, and have problems with steric crowding, site inaccessibility and metal leaching. Iron cations can also be incorporated into zeolites to produce reactive iron centers. Fe-ZSM-5, for example, has been shown to oxidize methane to methanol stoichiometrically when pretreated with nitrous oxide. Characterization of these materials is nontrivial because of the presence of multiple iron species, and the nature of the active sites in Fe-ZSM-5 remains largely speculation.

The use of a metal–organic framework (MOF) to support isolated terminal iron–oxo moieties is a highly promising area of research [1,2]. The high surface area, permanent porosity, chemical and thermal stability, and synthetic tunability displayed by many of these materials makes them appealing in this regard. Additionally, MOFs are typically highly crystalline with well-defined metal centers suited for characterization by single-crystal and/or powder-diffraction techniques. Of the 3-dimensional Fe(II)-containing MOFs shown to be stable to desolvation, few possess coordinatively unsaturated metal centers in a single, well-defined environment. The compound Fe₂(dobdc) (dobdc⁴⁻ = 2,5-dioxido-1,4-benzenedicarboxylate) is rare in this regard, as the hexagonal channels of the framework are lined with a high density of a single type of square pyramidal, redox-active Fe(II) site (Fig. 1).

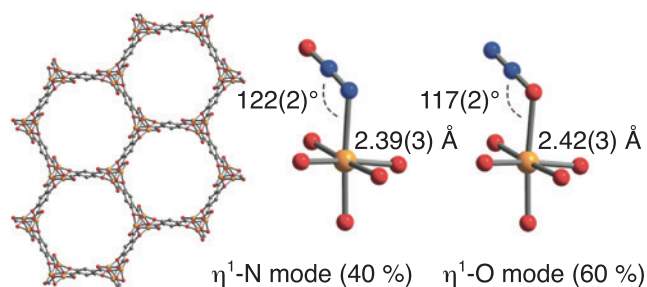


FIGURE 1: (Left) Structure of Fe₂(dobdc), showing hexagonal channels lined with five-coordinate Fe(II) sites. (Right) N₂O binding in Fe₂(dobdc) solved from powder neutron diffraction data (10 K). Orange, grey, dark blue and red spheres: Fe, C, N, O respectively.

We embarked on a study of its reactivity towards nitrous oxide (N₂O, molecular structure N≡N–O), a gaseous two-electron oxidant and O-atom transfer agent that is widely employed in industry, anticipating the generation of a highly reactive Fe(IV)–oxo species capable of oxidizing strong C–H bonds [1].

Experimental studies on the coordination chemistry of N₂O are scarce, as metal–N₂O adducts are challenging to synthesize because of the poor σ -donating and π -accepting properties of the molecule. Indeed, of the several proposed binding modes, only one (end-on, η^1 -N) has been structurally characterized in a molecular complex. To establish the coordination mode of N₂O in Fe₂(dobdc), powder neutron-diffraction data, which are very sensitive to the atomic assignment of O and N, were collected on a sample dosed with various loadings of N₂O. At low loadings, the best fit was an average of approximately 60 % η^1 -O and 40 % η^1 -N coordination, with Fe–N₂O distances of 2.42(3) and 2.39(3) Å, respectively (Fig. 1). In both cases, a bent Fe–N₂O angle close to 120° was observed. Density functional theory (DFT) studies of N₂O-bound Fe₂(dobdc) show excellent agreement with experiment, predicting the η^1 -O mode to be favored over the η^1 -N mode by just 1.1 kJ mol^{–1}. Although η^1 -O coordination with a bent Fe–O–N angle has been proposed in a variety of systems ranging from isolated metal atoms to iron zeolites, η^1 -N coordination with a bent Fe–N–N angle is much more unusual. The bent

¹ NIST Center for Neutron Research, National Institute of Standards and Technology, Gaithersburg, MD 20899

² University of Delaware, Newark, DE 19716

³ University of California, Berkeley, CA 94720

⁴ The Molecular Foundry, Lawrence Berkeley National Laboratory, Berkeley, CA 94720

⁵ Chemical Theory Center and Supercomputing Institute, University of Minnesota, Minneapolis, MN 55455

⁶ NIS and INSTM Reference Centres, University of Turin, I-10135 Torino, Italy

⁷ Physical Biosciences Division, Lawrence Berkeley National Laboratory, Berkeley, CA 94720

⁸ Materials Sciences Division, Lawrence Berkeley National Laboratory, Berkeley, CA 94720

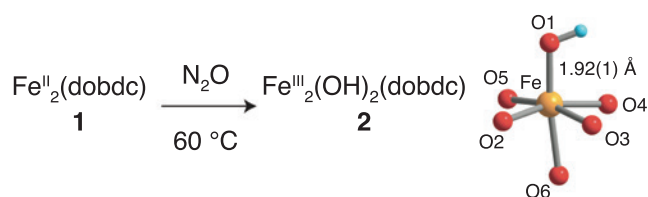


FIGURE 2: (Left) Reaction scheme for the preparation of $\text{Fe}_2(\text{OH})_2(\text{dobdc})$ from $\text{Fe}_2(\text{dobdc})$. (Right) The structure of $\text{Fe}_2(\text{OH})_2(\text{dobdc})$ obtained from powder diffraction data (100 K). The Fe–OH bond distance of 1.92(1) Å is consistent with reported Fe(III)–OH compounds. Orange, red and blue spheres represent Fe, O and H, respectively.

geometry, long Fe– N_2O bond length and mixed N and O coordination indicate that N_2O is bound only weakly to the Fe(II) centers in the framework suggesting a physically adsorbed phase with little to no perturbation of the N_2O molecule. As expected, this interaction is fully reversible under an applied vacuum.

On heating the N_2O -dosed framework to 60 °C, the material undergoes a drastic color change from bright green to dark red–brown, suggestive of oxidation. Characterization of the resulting product is consistent with the formulation $\text{Fe}_2(\text{OH})_2(\text{dobdc})$, in which each iron center is in the +3 oxidation state and bound to a terminal hydroxide anion (Fig. 2). $\text{Fe}_2(\text{OH})_2(\text{dobdc})$ is likely to be formed via a fleeting iron–oxo intermediate, which rapidly undergoes hydrogen-atom abstraction. Mössbauer spectroscopy was used to probe the local environment of the iron centers in the oxidized material, and is consistent with other high-spin haem and non-haem Fe(III) species. Rietveld analysis of powder diffraction data collected at 100 K on $\text{Fe}_2(\text{OH})_2(\text{dobdc})$ firmly established the presence of a new Fe–O bond at a distance of 1.92(1) Å, consistent with the bond lengths of previously reported octahedral Fe(III)–hydroxide complexes (Fig. 2) [1]. Extended X-ray absorption fine structure (EXAFS) analysis and periodic DFT calculations provided bond lengths that are consistent with those obtained from the diffraction data. Surprisingly, the Fe(III)–hydroxide species is capable of activating weak C–H bonds. When the partially oxidized sample $\text{Fe}_2(\text{OH})_{0.6}(\text{dobdc})$ was exposed to 1,4-cyclohexadiene at room temperature, benzene was produced as the sole product in quantitative yield. In the process, the framework converted entirely back to Fe(II), as determined by Mössbauer spectroscopy. Such reactivity is rare, but not unprecedented, for Fe(III)–hydroxide compounds. However, the oxidizing power of $\text{Fe}_2(\text{OH})_2(\text{dobdc})$ and $\text{Fe}_2(\text{OH})_{0.6}(\text{dobdc})$ is limited, and no reaction was observed with less-activated C–H bonds.

As the isolation of an Fe(III)–hydroxide product from a reaction that employs a two-electron oxidant strongly suggests the intermediacy of an Fe(IV)–oxo species, we next carried out the oxidation in the presence of a hydrocarbon substrate that contained stronger C–H bonds, specifically ethane, hoping to intercept the oxo species before its decay. Indeed, flowing an N_2O :ethane:Ar mixture (10:25:65) over the framework at 75 °C led to the formation of various ethane-derived oxygenates, which included ethanol, acetaldehyde, diethyl ether and other ether oligomers. We hypothesized that the complex mixture of products was related to the close

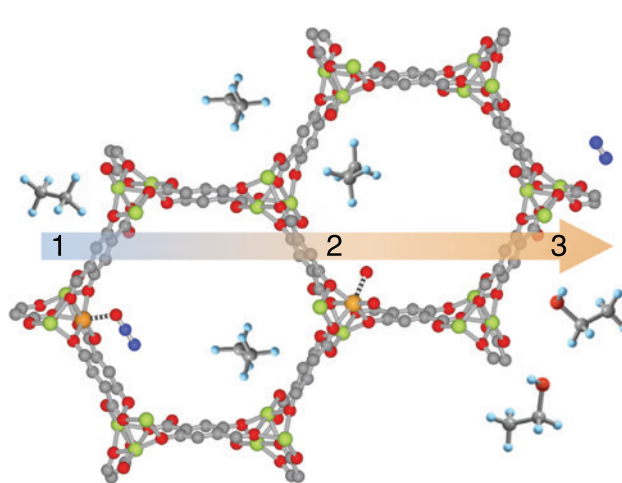


FIGURE 3: Heating of N_2O -bound $\text{Fe}_{0.1}\text{Mg}_{1.9}(\text{dobdc})$ (1) results in the formation of a transient high-spin Fe(IV)–oxo species (2), which can react with the strong ethane C–H bonds converting it to ethanol (3). Orange, Fe; green, Mg; grey, C; dark blue, N; red, O.

proximity of reactive iron centers, which are 8.13(2) Å and 6.84(1) Å apart across and along a channel, respectively. To avoid oligomerization and overoxidation, a mixed-metal MOF, $\text{Fe}_{0.1}\text{Mg}_{1.9}(\text{dobdc})$, in which the Fe(II) sites are diluted with redox-inactive magnesium(II) centers, was synthesized. Although determining the exact distribution of metal centers in heterometallic MOFs is challenging, the unit-cell parameters of $\text{Fe}_{0.1}\text{Mg}_{1.9}(\text{dobdc})$ are between those of $\text{Fe}_2(\text{dobdc})$ and $\text{Mg}_2(\text{dobdc})$, which suggests the formation of a solid solution rather than a mixture of two separate phases. Exposure of $\text{Fe}_{0.1}\text{Mg}_{1.9}(\text{dobdc})$ to N_2O and ethane under the same flow-through conditions yielded the exclusive formation of ethanol and acetaldehyde in a 10:1 ratio, albeit in low yield; 60 % with respect to iron (Fig. 3).

Although spectroscopic and theoretical studies have long attributed the reactivity of non-haem enzymatic and synthetic Fe(IV)–oxo complexes to a quintet spin state, only a handful of mononuclear high-spin Fe(IV)–oxo species have been characterized, and all but one exhibit a trigonal bipyramidal coordination geometry. In these systems, the oxo moiety is either extremely unstable ($[\text{Fe}(\text{O})(\text{H}_2\text{O})_5]^{2+}$, for example, has a half-life of roughly ten seconds) or inaccessible to substrates because of bulky ligand scaffolds, which lead to sluggish reactivity. However, the $\text{Fe}_2(\text{dobdc})$ framework features sterically accessible, site-isolated metal centers entrenched in a weak-field ligand environment. Utilizing these two properties, it is possible not only to generate such a species, albeit fleetingly, but also to direct it towards the facile activation of one of the strongest C–H bonds known. With this, $\text{Fe}_2(\text{dobdc})$ has now been shown to stabilize iron–superoxo, –peroxo, –hydroxo and –oxo intermediates, which highlights the promise of MOFs both as catalysts and as scaffolds for interrogating reactive metal species [1,2].

References

- [1] D. J. Xiao *et al.*, *Nature Chemistry* **6**, 590 (2014).
- [2] E. D. Bloch *et al.*, *J. Am. Chem. Soc.* **133**, 14814 (2011).

Dynamic origin of the anomalous odd-even glass transition temperature in an ionic glass

K. Yang,^{1,2} M. Tyagi,^{3,4} J. S. Moore,^{1,2,5} Y. Zhang^{1,2,6}

Odd-even effects are the non-monotonic dependency of physical properties on molecular odd-even structural units. These effects are widely observed in homologous series of crystalline materials with the most well known example being the n-alkane series, in which even-membered species have a higher melting point (T_m) than odd-membered ones. In general, packing effects are used to explain this alternating trend in crystalline materials. However, the lack of periodic packing makes the odd-even effect unexpected for amorphous materials. We have recently found that the odd-even effect also exists in the fully amorphous state in a homologous series of network-forming ionic glasses (IGs) where organic multivalent cations and anions are connected primarily by electrostatic interactions [1]. To understand the phenomenon's molecular origin, we studied the physical and dynamic properties a homologous series of IGs.

Organic molecular glasses are a class of organic molecules that do not crystallize readily upon cooling [2]. Structural features can be introduced to frustrate crystallization in these materials such as including nonpolar molecules and introducing conformers. Additionally, among ionic liquids, we can choose from a library of ionic interactions in terms of types and strength. By combining the design principles of these two types of materials, we construct a new kind of material that we call a network-forming ionic glass. These glasses include structural frustration from alkyl side chains (existence of conformers) and a variety of ionic interactions. Organic multivalent cations and anions are paired to form a network that possesses reversibility and tunability.

Network-forming IGs were synthesized using diammonium cations and citrate anions (Fig. 1). These materials were prepared by reacting an α,ω -dibromoalkane with a trialkylamine. The bromide counter anion was then replaced with hydroxide using an anion exchange column. In situ reaction with citric acid (or other polyacids) produced the desired products and water. We name the series of IGs with the form IG A-B where A is the backbone spacer length and B is the side chain length (Fig. 1). The amorphous nature of IGs was determined by X-ray diffraction (XRD) and differential scanning calorimetry (DSC). By changing the side chain length, B, the material can be tuned from semi-crystalline to amorphous glass. Increasing the side chain length decreases the glass transition

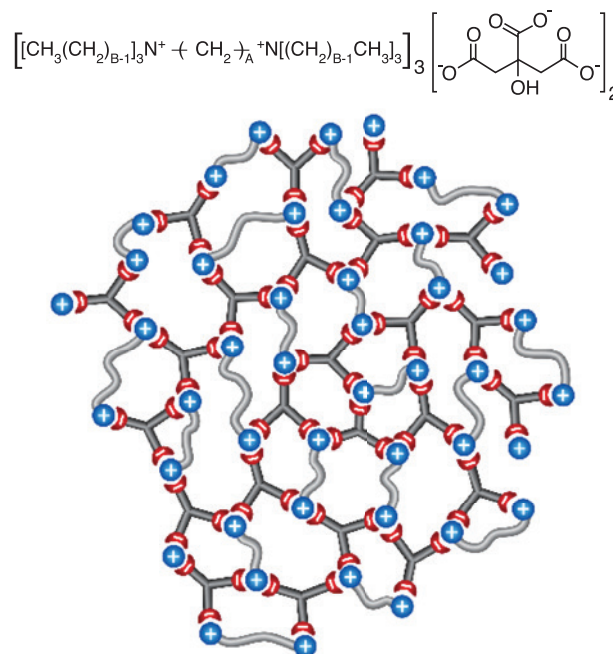


FIGURE 1: Chemical formula and simplified 2-D schematic depiction of interconnected network-forming ionic glass (side chains in cations are not shown).

temperature. Both electrostatic and van der Waals forces influence the phase behavior of ionic glasses. Since the electrostatic force is inversely proportional to the square of the separation distance, increasing the length of side chains enhances the steric hindrance between positive and negative charges. As a result, even though the van der Waals forces between segments may increase, the glass transition temperature drops due to weaker electrostatic interactions. In this way, we can fine-tune the ionic interaction strength by tailoring the structure of the building blocks.

The glass transition temperatures of various IGs were measured using two independent methods: direct measurement by DSC and the crossover point of the storage modulus (G') and loss modulus (G'') under dynamic loading (1 Hz) by rheology. Investigating the dependence of T_g on spacer length, the overall trend exhibits a

¹ Beckman Institute for Advanced Science and Technology, University of Illinois at Urbana-Champaign, Urbana, IL 61801

² Department of Materials Science and Engineering, University of Illinois at Urbana-Champaign, Urbana, IL 61801

³ NIST Center for Neutron Research, National Institute for Standards and Technology, Gaithersburg, MD 20899

⁴ University of Maryland, College Park, MD 20742

⁵ Department of Chemistry, University of Illinois at Urbana-Champaign, Urbana, IL 61801

⁶ Department of Nuclear, Plasma, and Radiological Engineering, University of Illinois at Urbana-Champaign, Urbana, IL 61801

peaked shape (Fig. 2a). The drop in T_g for long spacer lengths is explained by the competition between the electrostatic and van der Waals forces. An unexpected odd-even effect was observed in the spacer length study. IGs with an even number of methylene groups consistently have higher T_g than the odd-numbered IGs. The alternation amplitude decreases with longer chains, which is similar to n-alkanes and their derivatives. For spacer length $A > 9$, the odd-even effect was not observed, suggesting the effect from weaker ionic interaction per molecular volume becomes more prominent.

To understand the odd-even phenomenon, we measured the atomistic dynamics of IGs using incoherent elastic neutron scattering (IENS). IENS probes the effective Debye-Waller factor, $\exp[-\langle r^2 \rangle Q^2/6]$, averaged over a nano-second time resolution window, which directly yields the hydrogen mean-squared displacement (MSD). For our IG system, most of the hydrogen atoms are in the cations, so the MSD reflects the cation behavior. Three samples (IG 4-4, IG 5-4 and IG 5-6) were chosen in order to decouple the contributions to the MSD from the side chains and backbone. As shown in Fig. 2b, the MSD as a function of temperature can be divided into three regimes: (i) below 100 K, MSD shows pure harmonic behavior, almost all relaxational degrees of freedom freeze; (ii) From 100 K to 250 K, anharmonic motions start contributing. IG 4-4 and IG 5-4 with the same side chain length show similar temperature dependence, while IG 5-6 with longer hexyl side chain exhibits slower motions. This contrast suggests that the motion of the IG alkyl side chain dominates in this temperature range. In comparison, the backbone is largely immobile in this regime as the ionic cross-links behave like anchors and restrict the backbone diffusional movement; (iii) above 250 K, which is close to the glass transition temperature, the hydrogen MSD increases dramatically. IG 5-4 and IG 5-6 with the same backbone length behave almost identically while IG 4-4 moves much slower. Therefore we can reasonably conclude that in this temperature range, the backbone spacer rather than the side chain determines the nanosecond molecular motions of IG.

Comparing IG 4-4 and IG 5-4, which have the same length of side chain but different number of spacer groups, the main difference of their MSD lies in regime (iii) ($T > T_g$), where IG 4-4 molecules exhibit considerably slower motions compared to IG 5-4. This measurement of the molecular mobility explains why IG 4-4 has a higher T_g than its odd membered counterparts. Indeed, the mobility of the molecules is influenced by their structural symmetry, central symmetry for even membered IG and mirror symmetry for odd membered IG, which ultimately determines the configurational entropy of the system and thus affects the glass transition temperature. Another interesting feature of the MSD plot is that all three curves seem to have a common crossover point around 300 K, which is under current investigation.

This organic ionic glass system, with all its versatility, is a model system for the study of glasses and liquids. We have discovered an intriguing dynamic-related odd-even effect in the amorphous

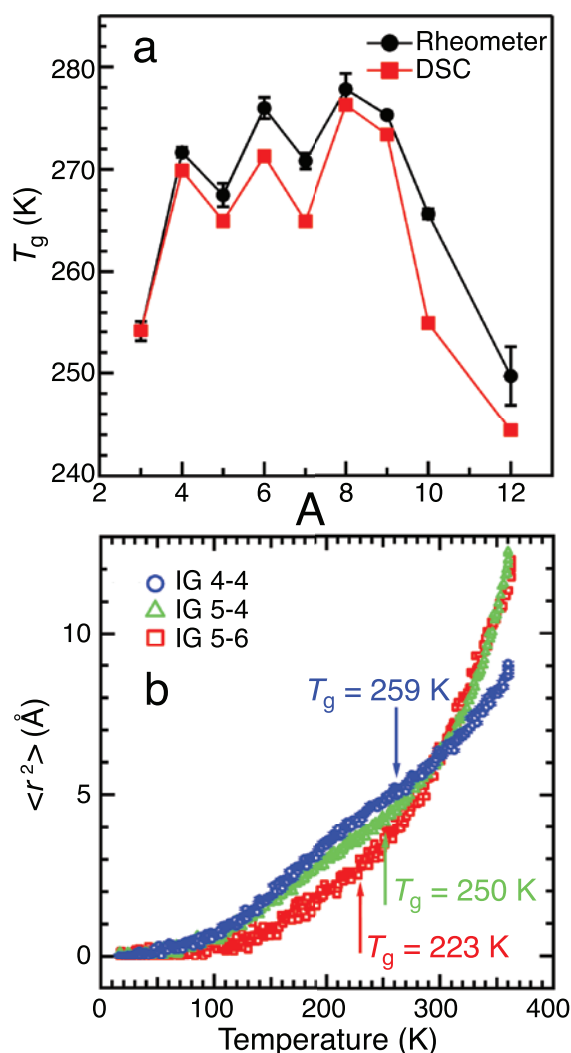


FIGURE 2: (a) Odd-even dependence of the glass transition temperatures (determined by both rheology and DSC) of IGs by varying spacer alkyl chain length (IG A-3); (b) Nanosecond hydrogen mean squared displacement (MSD) of three selective IGs extracted from elastic incoherent neutron scattering experiments. The glass transition temperatures in panel (b) are determined by DSC.

state. Measurements of mean squared displacement (MSD) reveal the discrete mobility of the side chain and backbone at different temperatures. Comparison of odd and even membered MSD plots shows the effect is associated with differences in molecular mobility. The understanding of such structure-dynamics-property relationships can provide guiding principles for the design and construction of next-generation adaptive and self-responding molecular ionic materials.

References

- [1] K. Yang, M. Tyagi, J. S. Moore, Y. Zhang, *J. Am. Chem. Soc.* **136**, 1268 (2014).
- [2] Y. Shirota and H. Kageyama, *Chem. Rev.* **107**, 953 (2007).

TiAu: the first itinerant antiferromagnet with no magnetic elements

E. Svanidze,¹ J. K. Wang,¹ T. Besara,² L. Liu,³ Q. Huang,⁴ T. Siegrist,² B. Frandsen,³ J. W. Lynn,⁴ A. H. Nevidomskyy,¹ M. B. Gamza,^{5,6} M. C. Aronson,^{5,7} Y. J. Uemura³ and E. Morosan¹

The theoretical description of magnetic materials has been a challenge since the inception of quantum mechanics, with Heisenberg's perturbation theory to describe magnetic insulators and the Slater/Stoner description of metallic magnets. The distinction for these two types depends on whether the unpaired ("magnetic") electrons reside on a particular ion, or whether they form a polarized band that crosses the Fermi energy and are thus itinerant. A vast number of local-moment materials are known and very well described theoretically, while the description of highly correlated itinerant electron systems such as cuprate and iron-based superconductors systems remains a central challenge of condensed matter physics. One particularly important class of itinerant electron systems is where the constituents are nominally non-magnetic, meaning that the atoms generally do not develop a local moment. Such materials greatly simplify the theoretical considerations, but are very rare, with the only two known ferromagnetic systems being ZrZn_2 [1] and Sc_3In [2]. Here we present the magnetic properties of TiAu, which we find is the first example of an itinerant electron antiferromagnet material with no magnetic constituents. A complete theory of magnetism that unifies the itinerant and local moment regimes remains elusive, mainly due to the limited number of known simple itinerant magnetic systems, and it is anticipated that this new system will provide important theoretical guidance.

The first clear evidence for an antiferromagnetic ground state in TiAu is the identical zero-field cooled and field-cooled cusp in the temperature-dependent magnetic susceptibility $M(T)/H$ around 36 K, shown in Fig. 1 (left axis). This behavior is analogous to the phase transition behavior generally observed for local-moment antiferromagnets. Upon warming above the Néel temperature, the inverse susceptibility $H/(M - M_0)$ (right axis, Fig. 1) is linear in temperature over a very large range, up to 800 K [3]. Such *Curie-Weiss-like* temperature dependence of $H/M(T)$ has been long considered the hallmark of local moment magnetism, until the identical behavior was observed in the weak itinerant ferromagnets ZrZn_2 and Sc_3In . While self-consistent renormalization theory

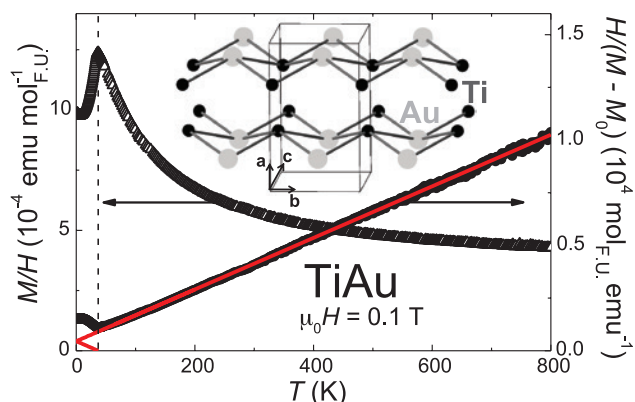


FIGURE 1: Left axis. Zero-field cooled magnetic susceptibility as a function of temperature for an applied field of $\mu_0 H = 0.1$ T. Right axis. Inverse susceptibility H/M along with a *Curie-Weiss-like* fit (solid line), with $\theta \approx -37$ K. Inset: the crystal structure of TiAu with Ti (small) and Au (large) atoms. (1 emu = 10 A/cm²).

has gone a long way to integrating the local and itinerant pictures of ferromagnetism [4], no existing theory accounts for an antiferromagnetic ground state if neither of the constituents is magnetic.

Distinguishing between local and itinerant moment magnetism is inherently difficult, especially in the nearly unexplored realm of itinerant antiferromagnets. It is therefore striking that in TiAu, abundant evidence points towards its itinerant magnetic character. The fact that the peak in the specific heat is not as strong as the local moment prediction is one such argument, with another being the very small magnetic entropy S_m associated with the transition, amounting to only $\approx 3\%$ of that expected ($R \ln 2$). Despite the remarkably large paramagnetic moment $\mu_{PM} \approx 0.8 \mu_B$, the maximum measured magnetization up to 7 T is only $0.01 \mu_B$, with no saturation observed in the field-dependent data $M(H)$. The small magnetic moment in the ordered state, as discussed below, compared to the paramagnetic moment, is another signature of itinerant magnetism.

¹ Rice University, Houston, TX 77005

² National High Magnetic Field Laboratory, Florida State University, Tallahassee, FL 32306

³ Columbia University, New York, NY 10027

⁴ NIST Center for Neutron Research, National Institute of Standards and Technology, Gaithersburg, MD 20899

⁵ Brookhaven National Laboratory, Upton, NY 11973

⁶ Department of Physics, Royal Holloway, University of London, Egham, TW20 0EX, UK

⁷ Stony Brook University, Stony Brook, NY 11794

To investigate the nature of the ordered magnetism, both neutron diffraction and muon spin relaxation data were measured. The muon spin relaxation technique provides a microscopic probe that determines the local magnetic fields throughout the inside of the material. The measurements on TiAu unambiguously show that essentially the whole volume of the sample orders magnetically, as shown in Fig. 2a. The muon spin relaxation data also indicate a very small ordered moment in TiAu, which is also confirmed by neutron diffraction measurements. High intensity neutron diffraction patterns were obtained both below ($T = 2$ K) and above ($T = 60$ K) the magnetic ordering temperature on BT-7 using the position-sensitive detector. These data reveal a magnetic peak that can be indexed as $(0, \pi/b, 0)$ (inset of Fig. 2(b)), indicating that commensurate long range magnetic order has developed. The ground state ordered moment is estimated to be $\approx 0.1 \mu_B$, and such a small moment is consistent with expectations for an itinerant electron system. The temperature dependence of the integrated intensity of the magnetic peak is shown in Fig. 2b. The solid curve is a simple mean-field fit to determine an ordering temperature of 36(2) K, in excellent agreement with the susceptibility, specific heat, and muon spin relaxation data. The neutron data therefore demonstrate that the magnetic order is associated with the TiAu lattice, which together with the muon data that the magnetic order exists in the entire sample, rules out any extrinsic origins for the magnetism such as an impurity phase or grain-boundary/surface effects. Thus the magnetic order is an intrinsic property of TiAu.

Overall our data convincingly show that TiAu is the first itinerant antiferromagnet with no magnetic constituents, analogous to the only two itinerant ferromagnets Sc_3In and ZrZn_2 . This new itinerant antiferromagnet challenges the currently limited understanding of weak itinerant antiferromagnetism while providing long sought-after insights into the effects of spin fluctuations in itinerant electron systems. The discovery of this itinerant electron antiferromagnet opens a promising avenue for developing a unified theory of magnetism that includes both local and itinerant electron systems and the complex magnetism that straddles these regimes.

References

- [1] B. T. Matthias, R. M. Bozorth, Phys. Rev. **109**, 604 (1958).
- [2] B. T. Matthias, A. M. Clogston, H. J. Williams, E. Corenzwit, R. C. Sherwood, Phys. Rev. Lett. **7**, 7 (1961).
- [3] E. Svanidze *et al.*, in preparation (2014).
- [4] T. Moriya, Spin Fluctuations in Itinerant Electron Magnetism, Springer - Verlag, Berlin (1985).

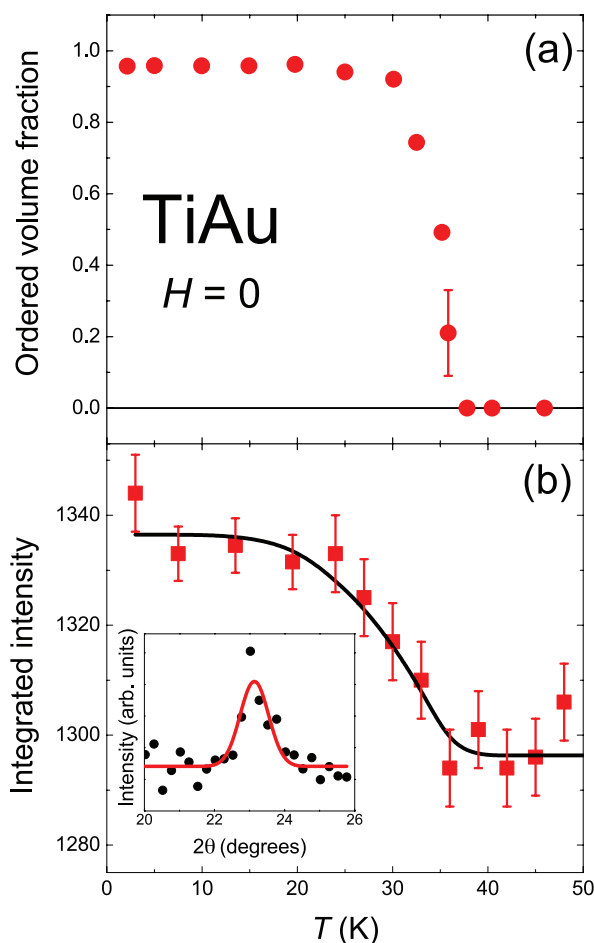


FIGURE 2: (a) Magnetic volume fraction, extracted from muon spin relaxation data, as a function of temperature, showing that the entire sample orders magnetically. (b) Neutron diffraction data of the integrated intensity of the TiAu magnetic Bragg peak as a function of temperature. The solid curve is a mean field fit to the powder data to obtain an ordering temperature of 36 K, in excellent agreement with the susceptibility, specific heat, and muon data. Inset: The $(0, \pi/b, 0)$ magnetic Bragg peak fit with a Gaussian (red line).

The fluctuating magnetism of triangular molecules on a triangular lattice

M. Mourigal,¹ W. T. Fuhrman,¹ J. P. Sheckelton,^{1,2} A. Wartelle,^{1,3} J. A. Rodriguez-Rivera,^{4,5} D. L. Abernathy,⁶ T. M. McQueen,^{1,2} and C. L. Broholm^{1,4,6}

Measured along any direction, the magnetic moment of an electron takes on one of two quantized values ($\pm\mu_B$). Correspondingly, the magnetic moments of a pair of electrons can be perpetually antiparallel in the so-called “singlet” state with no net moment, or they can conspire to form a twice-larger moment. In a compass needle or refrigerator magnet, a very large number of electrons combine in the latter fashion forming a classical magnetic moment. It is natural to ask whether a singlet-dominated state of matter is possible where the quantized nature of the electron transcends the atomic scale? In a seminal paper published forty years ago, Nobel Laureate P.W. Anderson suggested this might occur for electrons on a triangular lattice [1]. Now an experiment on the newly enhanced MACS spectrometer offers evidence of singlet formation among electrons confined to triangular molecules on a triangular lattice.

The curious “doubly triangular” structure of $\text{LiZn}_2\text{Mo}_3\text{O}_8$ is shown in Fig. 1a [2]. Susceptibility measurements show an intriguing transition from a high temperature regime ($T > 100$ K) with one active spin per triangular Mo_3O_{13} molecule to a low temperature regime with one electron spin per three molecules. This loss of moments already indicates some sort of quantum singlet formation. The absence of conventional magnetic ordering down to $T = 0.1$ K is a further indication of an anomalous electronic state.

While extending the magnetic orbital from an atom to a molecule may be key to realizing resonating valence bonds (singlets) in $\text{LiZn}_2\text{Mo}_3\text{O}_8$, an unfortunate consequence is that magnetic neutron scattering is weak and confined to wave vector transfer below 1 \AA^{-1} (Fig. 1b). Nonetheless, the high efficiency MACS spectrometer detected a broad, diffusive form of magnetic scattering from a powder sample of $\text{LiZn}_2\text{Mo}_3\text{O}_8$ (Fig. 2a). Conventional magnetism is excluded, as the momentum dependence of the data (open symbols, Fig. 2c) is broad at energy transfers far less than the Curie-Weiss temperature extracted from high temperature susceptibility data ($\Theta_{\text{CW}} = -339(12) \text{ K}$ [3,4]). Instead we compare the data to what would be expected for a singlet-dominated state of matter where electron spins fluctuate but remain antiparallel. The solid and dashed black lines in Fig. 2c show expectations for nearest and next nearest neighbor singlets, respectively, neither of which are consistent with the data. A superposition of the two

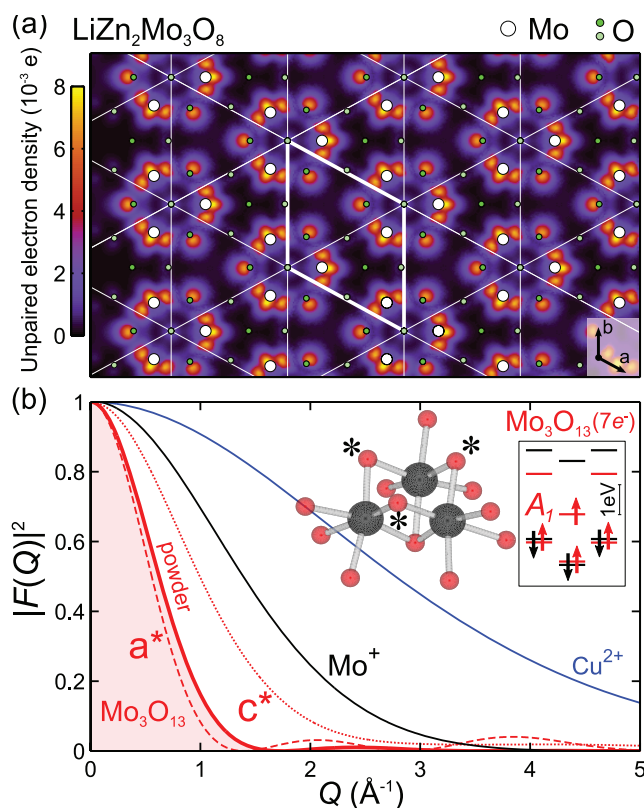


FIGURE 1: (a) The extended unpaired electron density associated with the triangular lattice of Mo_3O_{13} molecules in $\text{LiZn}_2\text{Mo}_3\text{O}_8$. (b) The square magnetic form factor of Mo_3O_{13} compared to that of Cu^{2+} . Magnetic neutron scattering from $\text{LiZn}_2\text{Mo}_3\text{O}_8$ is complicated because the form factor confines the signal to wave vector transfer below 1 \AA^{-1} .

(solid blue line in Fig. 2c), however, describes the data well. This is a further break with semi classical descriptions of magnetism in $\text{LiZn}_2\text{Mo}_3\text{O}_8$, implying that a ground state with a static or dynamic configuration of singlets is formed between electrons confined to Mo_3O_8 molecules.

The zero-field neutron data indicate a continuous and gapless spectrum of excitations associated with breaking singlets (open

¹ Institute for Quantum Matter and Department of Physics and Astronomy, Johns Hopkins University, Baltimore, MD 21218

² Department of Chemistry, Johns Hopkins University, Baltimore, MD 21218

³ École Normale Supérieure de Lyon, Université de Lyon, 46 Allée d'Italie, 69364 Lyon Cedex 07, France

⁴ NIST Center for Neutron Research, National Institute of Standards and Technology, Gaithersburg, MD 20899

⁵ University of Maryland, College Park, MD 20742

⁶ Oak Ridge National Laboratory, Oak Ridge, Tennessee 37831

symbols, Fig. 2d). This cannot be the result of a static, periodic arrangement of singlets on the triangular lattice. Applying a magnetic field on the other hand, induces a resonance in the spectrum of neutron scattering (Fig. 2b and filled symbols, Fig. 2d), the wave vector dependence of which shows it to be associated with individual magnetized Mo_3O_{13} molecules (red line in Fig. 2c). The data clearly identify $\text{LiZn}_2\text{Mo}_3\text{O}_8$ as a quantum dominated magnet but leave several questions unanswered: (1) Why do 2/3 of the spins all but vanish from view at low temperatures? Absolute normalization of the MACS data show the low energy scattering is associated with 1/3 of the Mo_3O_8 molecules. A higher energy experiment using ARCS at the SNS showed the remaining magnetic scattering must be distributed through a broad range of energies. This is consistent with susceptibility data and the apparent absence of translational symmetry breaking. (2) How is it possible for a gapless excitation spectrum to be associated with short-range singlet formation? The energy to convert an isolated pair of electronic magnetic moments from the singlet configuration to the magnetic configuration equals a finite antiferromagnetic exchange constant. Therefore a gap in the excitation spectrum is expected for a static short-range singlet configuration. A satisfactory answer to these questions may be found if the configuration of singlets itself undergoes quantum fluctuations as envisioned in Anderson's resonating valence bond state. Possible factors that have been proposed to drive the exotic magnetism of $\text{LiZn}_2\text{Mo}_3\text{O}_8$ are molecular distortions or rotations that influence inter-site interactions [5] and delocalization of electrons beyond their host Mo_3O_{13} molecules described by a Hubbard model on a distorted kagome lattice [6]. Neutron scattering from single crystalline samples will be required to distinguish such scenarios and to exclude a disorder dominated random singlet state. For now the important experimental finding is that singlet dominated quantum magnetism is possible on the triangular lattice when electrons occupy molecular rather than atomic orbitals.

References

- [1] P.W. Anderson, Mater. Res. Bull. **8**, 153 (1973).
- [2] J. P. Sheckelton, J. R. Neilson, D. G. Soltan, T. M. McQueen, Nat. Mater. **11**, 493 (2012).
- [3] M. Mourigal, W. T. Fuhrman, J. P. Sheckelton, A. Wartelle, J. A. Rodriguez-Rivera, D. L. Abernathy, T. M. McQueen, C. Broholm, Phys. Rev. Lett. **112**, 027202 (2014).
- [4] J. P. Sheckelton, F. R. Foronda, LiDong Pan, C. Moir, R. D. McDonald, T. Lancaster, P. J. Baker, N. P. Armitage, T. Imai, S. J. Blundell, T. M. McQueen, Phys. Rev. B **89**, 064407 (2014).
- [5] R. Flint, P. A. Lee, Phys. Rev. Lett. **111**, 217201 (2013).
- [6] G. Chen, H.-Y. Kee, Y. B. Kim, arXiv:1408.1963 (2014).

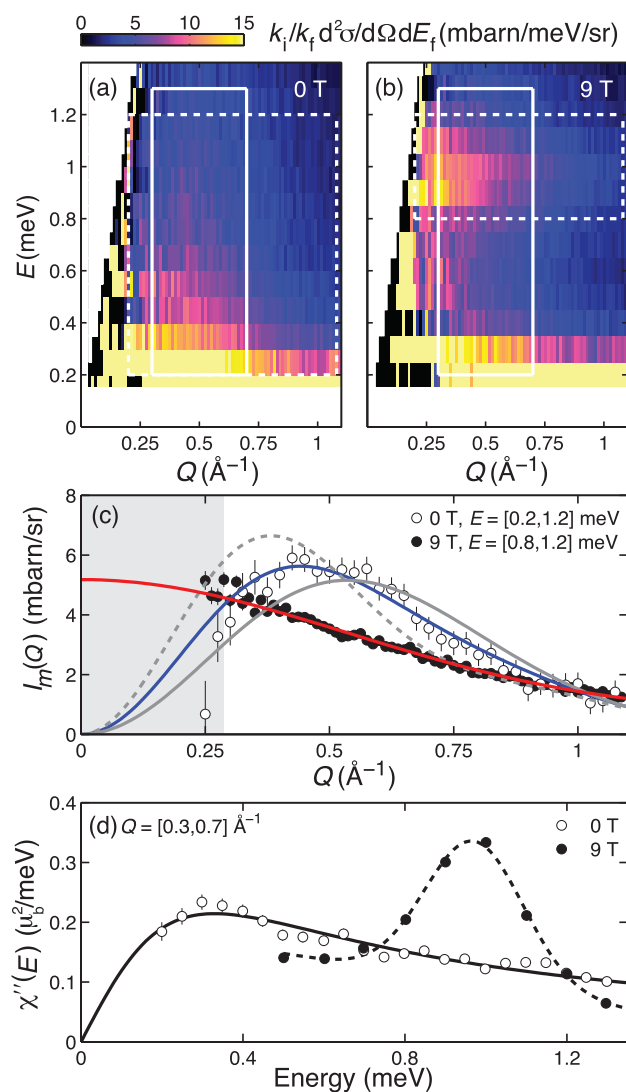


FIGURE 2: Color map of the magnetic neutron scattering intensity from $\text{LiZn}_2\text{Mo}_3\text{O}_8$ in (a) zero magnetic field and (b) 9 T magnetic field. The substantial field effect identified this scattering as magnetic. (c) Shows the wave vector dependence of the scattering integrated over the indicated energy ranges. The zero field data are consistent with a magnetic ground state consisting of a superposition (solid blue line) of quantum singlets between nearest (solid black line) and second nearest (dashed black line) neighboring Mo_3O_{13} molecules. The field induced resonance carries the wave vector dependence of the theoretical form factor of the Mo_3O_{13} molecule (solid red line). (d) The spectrum of magnetic neutron scattering from $\text{LiZn}_2\text{Mo}_3\text{O}_8$ in zero field (open symbols) and 9 T (closed symbols) showing the transition from a continuum of scattering to a well defined resonance associated with precession of the molecular magnetization.

Giant charge fluctuations with Se-height and Fe-vacancy formation in $M_x\text{Fe}_{2-y}\text{Se}_2$

X. Luo, S. Ögüt,¹ and T. Yildirim^{2,3}

Superconductivity was recently discovered in alkali-metal doped iron-selenide systems $M_x\text{Fe}_y\text{Se}_2$ at T_c 's up to 32 K [1,2]. One of the most important questions about this class of materials is related to the similarities and differences between the iron selenide and pnictide systems. In this work, we present important results from state-of-the-art first principles calculations that address this issue. We show that there is an intimate relationship between the Se height and the spin configuration of the underlying Fe-square in $M_x\text{Fe}_{2-y}\text{Se}_2$, where M denotes an alkali metal. A displacement of the Se atom by an amount as small as 0.2 Å is enough to change the amount of charge in the Fe-plane by as much as 0.7 electrons per Fe. The height of the Se atom above the Fe-square increases as the number of ferromagnetic Fe-Fe bonds increases, yielding an expansion of 2 Å in the c-axis for the fully ferromagnetic spin configuration. This suggests the presence of a giant magneto-elastic coupling in this system. We show that the formation of Fe vacancies is energetically favorable, and that their presence changes the ground state from double-stripe to block-antiferromagnetic ordering. The formation of K vacancies is found to be energetically unfavorable.

We first consider the ideal $122\text{ MFe}_2\text{Se}_2$ structure with non-magnetic (NM) as well as the following four magnetic configurations shown in Fig. 1: Anti-ferromagnetic stripe (AFs), anti-ferromagnetic checkerboard (AFc), anti-ferromagnetic double stripe (AFd), and ferromagnetic (FE) phases. We then consider the experimentally observed $\sqrt{5} \times \sqrt{5}$ supercell as determined by neutron scattering with and without Fe vacancies (Fig. 1e - 1f). Our first principles calculations are performed with a plane wave basis set within the framework of density functional theory using the Perdew-Burke Ernzerhof exchange-correlation functional as implemented in the VASP package.

To demonstrate the dependence of total energy and magnetization on the Se-height z_{Se} , we performed self-consistent calculations with different z_{Se} values in a fixed cell. Fig. 2 shows the results for five different spin configurations in the optimal AFs cell of KFe_2Se_2 and the FE-cell of NaFe_2Se_2 . For the case of K (Fig. 2, left panel), when z_{Se} is larger than 1.4 Å, the Fe magnetic moment increases linearly with z_{Se} . Once z_{Se} is below 1.4 Å, the magnetic moment drops quickly as z_{Se} decreases. The Fe atoms in the FE and AFs phase lose their magnetization when z_{Se} is smaller than 1.25 Å. We note that the energetic ordering of the five phases (with

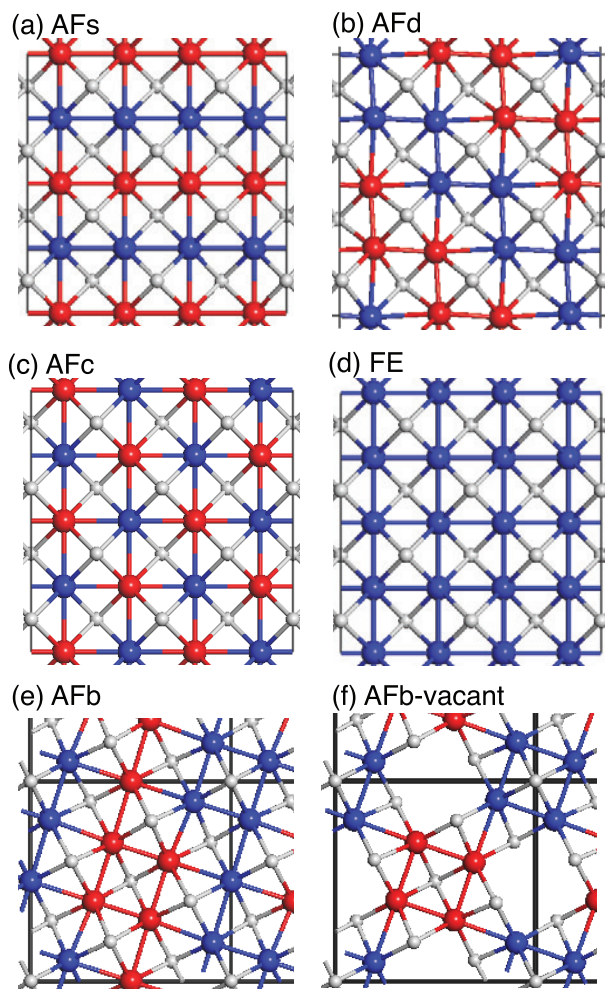


FIGURE 1: (a-d) Four different magnetic structures of MFe_2Se_2 . AFs, AFd, AFc, FE denote anti-ferromagnetic stripe, anti-ferromagnetic double-stripe, anti-ferromagnetic checkerboard, and ferromagnetic spin configurations, respectively. (e-f) The optimized structures of the anti-ferro block stripe phase within the $\sqrt{5} \times \sqrt{5}$ cell without (e) and with the Fe-vacancies (f).

respect to magnetic configuration) depends on z_{Se} . In KFe_2Se_2 , AFs competes with AFd to become the ground state with z_{Se} controlling the competition. When z_{Se} increases from 1.44 Å to 1.48 Å, the ground state switches from AFs to AFd. In NaFe_2Se_2 (Fig. 2, right panel), it is the AFd and FE phases that compete

¹ University of Illinois at Chicago, Chicago, IL 60607

² NIST Center for Neutron Research, National Institute of Standards and Technology, Gaithersburg, MD 20899

³ University of Pennsylvania, Philadelphia, PA 19104

for the ground state: When z_{Se} is less than 1.6 Å, the AFd spin configuration is the ground state. However, with a small increase in z_{Se} from 1.6 Å to 1.65 Å, the ground state changes to the FE spin configuration. Hence, for both K and Na, the ground state spin configuration is very sensitive to the height of the Se ion.

Next, we show that the charge distribution in Fe-selenides is also very sensitive to the Se-height. In order to demonstrate this, we first calculate the charge density as a function of the coordinate z along the c -axis, $\rho(z)$, by averaging the full charge density $\rho(x,y,z)$ in the x - y plane. We then plot the change $\Delta\rho(z)$ in the averaged charge density as Se ions are shifted along the z -direction by a small amount. Fig. 3 shows such a charge density difference plot for a Se-displacement of 0.2 Å. We see that there is a huge charge transfer from the Se-Fe-Se region to the Se-K-Se region upon a small Se-displacement. On average, the Se-Fe-Se region loses about 0.7 electrons per Fe with a 0.2 Å increase in the Se-height, suggesting that Fe-Se and Se-Se hybridizations are strongly coupled.

Recent neutron experiments indicate [3] that these systems possess significant Fe vacancies, which are ordered in a $\sqrt{5} \times \sqrt{5}$ cell as shown in Fig 1e - 1f. Hence, it is important to understand the energetics of Fe and K vacancy formation in these systems. We calculated the Fe and K vacancy formation energies in a $\sqrt{5} \times \sqrt{5}$ cell for both the AFd and NM phases. We considered three vacancy structures for the AFb phase: $\text{KFe}_{1.6}\text{Se}_2$ with only Fe vacancies, $\text{K}_{0.8}\text{Fe}_2\text{Se}_2$ with only K vacancies, and $\text{K}_{0.8}\text{Fe}_{1.6}\text{Se}_2$ with both Fe and K vacancies, and obtained the E_v values of

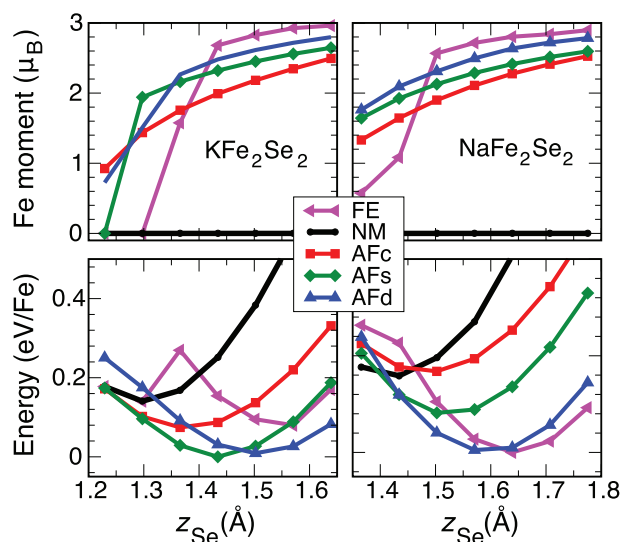


FIGURE 2: The dependence of Fe magnetic moment (top) and the total energy (bottom) on the z -position of Se (z_{Se}) in the optimized AFs-cell of KFe_2Se_2 (left) and the FE-cell of NaFe_2Se_2 (right).

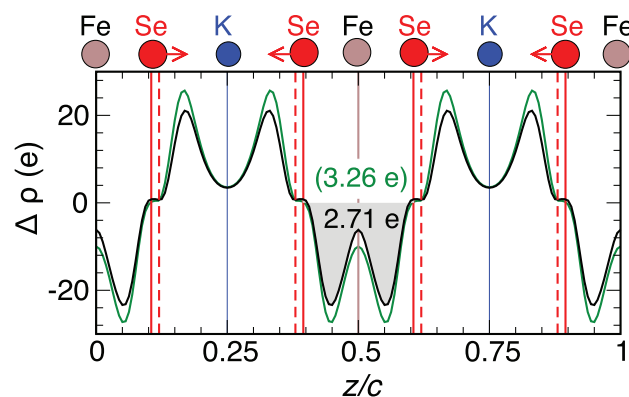


FIGURE 3: The plot of the charge density difference averaged over the x - y plane as the Se atoms z_{Se} are shifted away from the Fe-plane in the AFs optimal cell of KFe_2Se_2 . The shaded area indicates the large charge transfer of 2.71 e (per four Fe ions) from the Se-Fe-Se region to the Se-K-Se region with a small Se-displacement of 0.2 Å. Vertical solid and dashed lines shows the Se-position before and after the Se displacement. The solid green line shows the averaged charge density difference upon the same 0.2 Å Se-displacement for the $\sqrt{5} \times \sqrt{5}$ cell with Fe-vacancies shown in Fig. 1f.

-0.55 eV, 0.90 eV, and 1.24 eV, respectively. The negative energy for the structure with the Fe vacancy only indicates that Fe vacancies are energetically favorable. However, the large positive defect energies for K vacancies (with and without the Fe vacancies) suggest that K-vacancy formation is not energetically favorable. Hence, according to these results, the samples should always have Fe vacancies but the presence of K vacancies would depend on how fast the samples are quenched during the synthesis and may show variance from sample to sample.

In conclusion, we have examined the coupling of the Se-height to the spin configuration in the underlying Fe-squares in $\text{M}_x\text{Fe}_2\text{Se}_2$. We have shown that this coupling, while rather local, is so strong that a displacement of the Se atom by as little as 0.03 Å is enough to change the magnetic configuration of the Fe-square. This Se displacement works like a charge-valve; a displacement as small as 0.2 Å can transfer about 0.7 electrons per Fe from the Se-Fe-Se region to the Se-K-Se region. We believe that these results are likely to provide new research directions for experimentalists such as the possible observation of a collapsed non-magnetic phase under pressure when small alkali metals are doped into the Fe-selenides.

References

- [1] J. Guo *et al.*, Phys. Rev. B **82**, 180520 (2010).
- [2] X. Luo, S. Ögüt, T. Yildirim, Phys. Rev. B **89**, 054519 (2014).
- [3] J. Zhao, H. Cao, E. Bourret-Courchesne, D. -H. Lee, R. J. Birgeneau, Phys. Rev. Lett. **109**, 267003 (2012).

Phonon localization drives polar nanoregions in a relaxor ferroelectric

M. E. Manley,¹ J. W. Lynn,² D. L. Abernathy,¹ E. D. Specht,¹ O. Delaire,¹ A. R. Bishop,³ R. Sahul,⁴ and J. D. Budai¹

For over 50 years it has been known that conventional ferroelectrics form long-range polar order upon cooling by the gradual slowing (softening) of a zone center transverse optic (TO) phonon. Relaxor ferroelectrics, on the other hand, are chemically disordered ferroelectrics with technologically useful properties that are not well understood. The useful properties of relaxor ferroelectrics originate with polar nanoregions (PNRs), although there is no agreement on how PNRs form. Possible explanations range from analogs with frustration in magnetic spin glasses, to short-range chemical order, to the nonlinear localization and slowing of phonons at “dopant” sites (intrinsic localized modes) [1]. However, none of these models explain the size, shape, and distributions of the PNRs, nor do they explain the appearance of antiferroelectric nanoregions with zone-edge TO phonon displacements. In recent work, using neutron scattering to characterize the lattice dynamics of relaxor PMN-30%PT, we have discovered a new phonon localization mechanism that explains the size and shape of the PNRs as well as zone-edge antiferroelectric nanoregions in terms of the coherent trapping of the TO phonons by randomly distributed localized resonance modes [2].

Near the Burns temperature (T_d) a dispersionless mode forms in resonance with the TO phonon with a flat intensity profile, indicating a fully localized stationary mode (Fig. 1a). On cooling towards the ordering temperature, T_c , however, the intensity of the localized phonons becomes peaked at the crossing with the TO phonon (Fig. 1b). These localized phonons have a coherence length (size) that equals a single TO wavelength at the crossing (Fig. 1c), and this size matches the PNRs. Furthermore, near the zone edge high-symmetry M point (antiferroelectric), the intensity becomes enhanced at a 2nd crossing (Fig. 1d and Fig. 1e). The size of the localized modes is set by the wavelength of the TO phonon where the TO phonon dispersion surface crosses the resonance local mode. This relationship explains the evolution of the size, shape, and positions in reciprocal space of the PNR and antiferroelectric nanoregion diffuse scattering patterns in PMN-xPT for $x = 0\%$ to 30% [2]. As described below, these results are explained in terms of an Anderson-type localization mechanism, where constructive interference of the TO phonons interacting with randomly distributed localized resonance modes results in the localization of both the ferroelectric and antiferroelectric TO phonons.

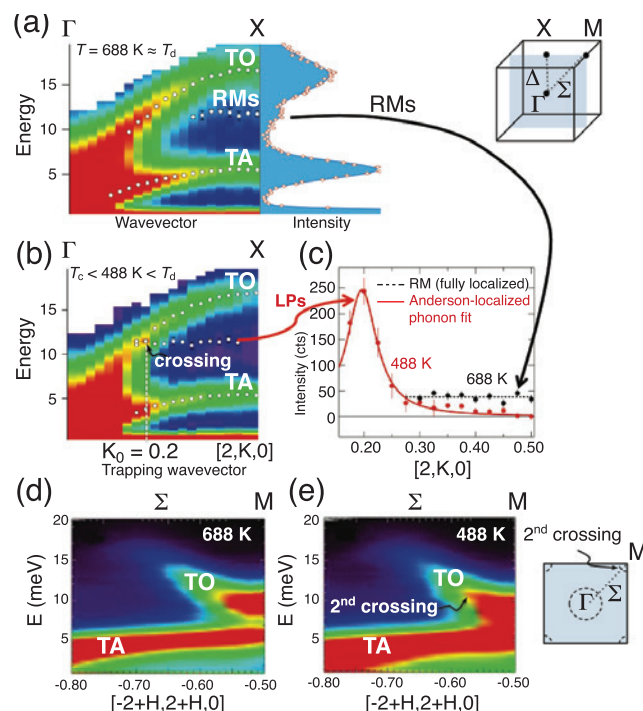


FIGURE 1: Inelastic neutron scattering measurements of phonons in PMN-30%PT. (a) and (b) are measured along Γ -X at 688 K and 488 K using BT7 at NIST. (c) Intensity profile and fits for the indicated local modes. At 688 K the mode intensity is flat, which implies well localized. At 488 K the profile indicates a coherence length of 2 nm, which matches the wavelength at the resonance crossing and the PNR size. (d) and (e) are measured along Γ -M at 688 K and 488 K using ARCS at SNS.

To understand these results, it is instructive to first consider the apparently paradoxical result that the localized mode becomes longer lived (sharper in energy) as it forms resonance crossings with the TO phonon [2]. As depicted in Fig. 2a, a localized mode in resonance with traveling phonons, in this case the TO phonons, is expected to radiate these phonons. The radiation of energy through the TO phonons is expected to quickly disperse the resonance mode energy, thereby relegating it to a short-lived fluctuation rather than a long-lived excitation. As depicted in Fig. 2b, however, it is possible to “trap” (localize) the radiating phonons between two resonance modes in 1D. The radiating phonons constructively interfere to form a standing wave

¹ Oak Ridge National Laboratory, Oak Ridge, TN 37831

² NIST Center for Neutron Research, National Institute of Standards and Technology, Gaithersburg, MD 20899

³ Los Alamos National Laboratory, Los Alamos, NM 87545

⁴ TRS Technologies, State College, PA 16801

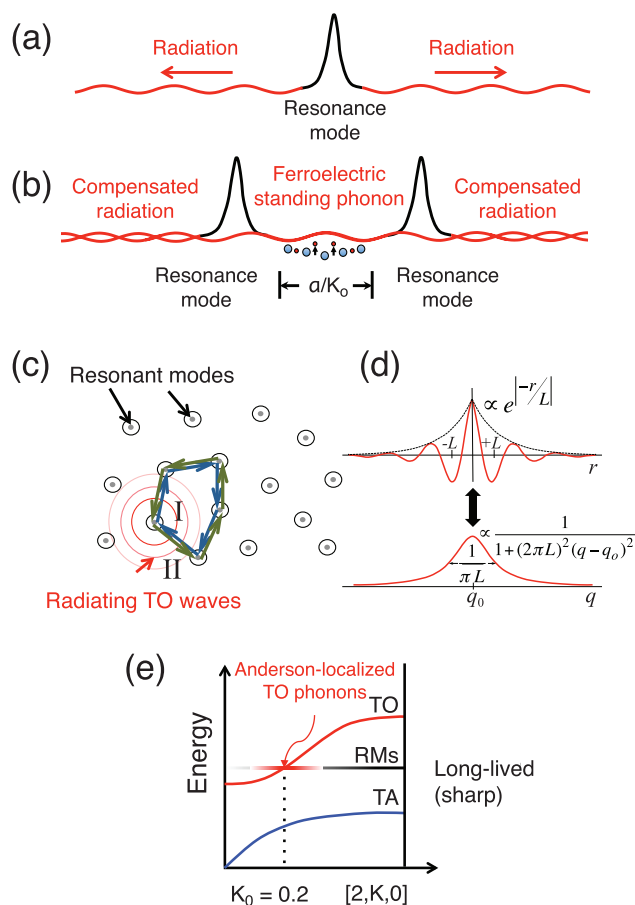


FIGURE 2: Trapping ferroelectric modes with resonance modes. (a) Resonance mode radiating TO phonons. (b) Trapped TO phonon in 1D. (c) Anderson localization scheme. (d) Exponential localization transformation. (e) Modifications to the dispersion curves from an Anderson-localized standing TO phonon at the resonance wave vector.

between the pair while destructively interfering outside of the pair, resulting in a long-lived bound state. The problem of how radiating phonons become localized in a random 3D distribution of resonance modes is, in essence, Anderson localization [3]. The reason is illustrated in Fig. 2c: waves emanating from a single resonance mode and traveling in equal by opposite directions around the same random scattering path constructively interfere on returning. Anderson localization is exponential in real space, which transforms to Lorentzian in reciprocal space (Fig. 2d), and the characteristic length scale, L , is the wavelength of the trapped phonon. Invoking the convolution theorem, the localized TO phonon is as a q -broadened TO mode centered at the crossing and with a coherence length matching the wavelength (Fig. 2e). This explains the observed dynamical structure shown in Fig. 1b and Fig. 1e. The trapped wavelength of 2 nm matches the coherence length of the localized phonon and the size of the PNRs. Considering how the trapping wavevector maps with direction, Fig. 3a, explains why the anisotropy of the PNR

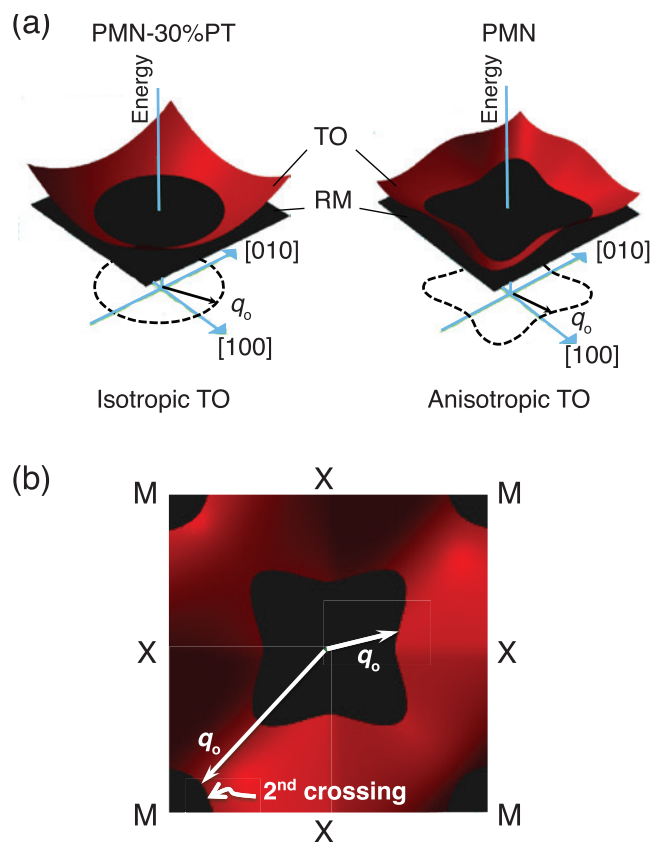


FIGURE 3: Trapping wavevectors expected for a single resonance mode frequency crossing the dispersion surface of the transverse optic (TO) phonon. (a) A comparison of the trapping wavevectors, q_0 , expected near the zone center for PMN-30%PT and PMN. The trapping wavevector loci map to the observed diffuse scattering anisotropy [4]. (b) Locations in reciprocal space where the 2nd crossing introduces trapping wavevectors near the M points. These are the wavevectors where antiferroelectric distortions were observed [5].

diffuse scattering follows the anisotropy of the TO phonon [4]. Furthermore, the trapping wavevectors at the zone edge M points, Fig. 3b, explains why antiferroelectric nanoregions of distortion develop at these points in reciprocal space [5]. This mechanism is generic and may apply to other disorder-frustrated ferroic materials, where function often originates with nanoregions.

References

- [1] R. A. Cowley *et al.*, Adv. Phys. **60**, 229 (2011).
- [2] M. E. Manley *et al.*, Nature Commun. **5**:3683 doi: 10.1038/ncomms4683 (2014).
- [3] A. Lagendijk, B. Tiggelen, D. S. Wiersma, Phys. Today **62**, 24 (2009).
- [4] M. Matsuura *et al.*, Phys. Rev. B **74**, 144107 (2006).
- [5] I. P. Swainson *et al.*, Phys. Rev. B **79**, 224301 (2009).

Effect of interfacial octahedral behavior in ultrathin manganite films

E. J. Moon,¹ P. V. Balachandran,¹ B. J. Kirby,² D. J. Keavney,³ R. J. Sischel-Tissot,¹ C. M. Schlepütz,³ E. Karapetrova,³ X. M. Cheng,⁴ J. M. Rondinelli,¹ and S. J. May¹

Transition metal oxides featuring strongly correlated electrons exhibit a host of fascinating and useful properties, such as ferromagnetism, ferroelectricity, and superconductivity. New and different properties can emerge at an abrupt interface between two such materials with differing ground states [1]. As such, novel materials featuring electronic and magnetic properties not found naturally can be artificially designed through precise epitaxial growth of oxide thin film heterostructures. For example, it is known that in bulk, altering the rotation angle of the constituent BO_6 octahedra can stabilize different electronic and magnetic phases in ABO_3 perovskites. In principle, it should therefore be possible to tune the properties of ABO_3 thin films via interfacing with a material exhibiting an appropriate degree of octahedral rotation. In practice however, for such a heterostructure it is difficult to distinguish the contributions of octahedral coupling from those of epitaxial strain.

To isolate the role of octahedral rotations, we have studied the electronic and magnetic properties of $\text{La}_{2/3}\text{Sr}_{1/3}\text{MnO}_3$ (LSMO) films epitaxially grown on different oxide substrates with similar lattice parameters, but that either do or do not exhibit octahedral rotation [2]. In bulk, 1/3 doped LSMO is ferromagnetic, has an $a^- a^- a^-$ tilt pattern, with a pseudocubic lattice parameter $a_{\text{pc}} = 3.873 \text{ \AA}$, and a uniform 166.3° B-O-B bond angle. Using molecular beam epitaxy, ultra-thin LSMO layers were grown on the (001) surface of $(\text{LaAlO}_3)_{0.3}(\text{Sr}_2\text{AlTaO}_6)_{0.7}$ (i.e. LSAT), the (001) surface of NdGaO_3 (NGO) and the (110) surface of NGO. LSAT is

cubic, with $a_{\text{pc}} = 3.868 \text{ \AA}$, and lacks octahedral rotations – i.e. it exhibits an $a^0 a^0 a^0$ tilt pattern and a uniform 180° B-O-B bond angle. Conversely, NGO is orthorhombic, with $a_{\text{pc}} = 3.862 \text{ \AA}$, and exhibits significant octahedral rotations – an $a^- a^- c^+$ tilt pattern with an average B-O-B bond angle of 154° . The LSMO / substrate interfacial structure is depicted in Fig. 1. In principle, rotations of the MnO_6 octahedra in LSMO (in pink) should be altered via coupling with the LSAT (blue) or NGO (green) substrates. For growth on the LSAT substrate, the lack of octahedral rotation should lead to larger LSMO bond angles near the substrate interface compared to films grown on NGO – an effect that could manifest itself in bandwidth related properties such as resistivity and magnetization.

X-ray diffraction measurements were performed at beamline 33-BM-C of the Advanced Photon Source. Fig. 2 shows scans of intensity vs. wavevector transfer (Q_z) about the pseudocubic LSMO (002) peak for films 11 unit cells (u.c.) thick grown on each of the three substrates. Pronounced LSMO Bragg peaks are observed indicating layered order along the growth axis, while the presence

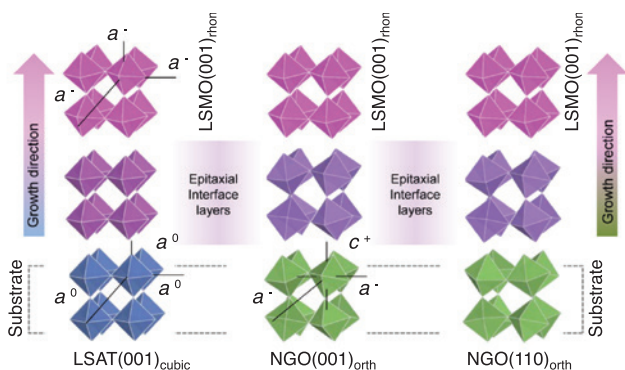


FIGURE 1: Schematic of the LSMO/LSAT and LSMO/NGO heterostructures.

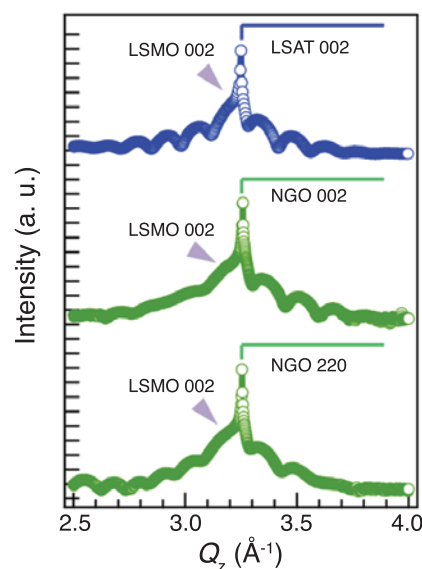


FIGURE 2: X-ray diffraction scans about the LSMO (002) for samples grown on (from top) LSAT (001), NGO (001), and NGO (110).

¹ Drexel University, Philadelphia, PA 19104

² NIST Center for Neutron Research, National Institute of Standards and Technology, Gaithersburg, MD 20899

³ X-ray Sciences Division, Advanced Photon Source, Argonne National Laboratory, Lemont, IL 60439

⁴ Bryn Mawr College, Bryn Mawr, PA 19010

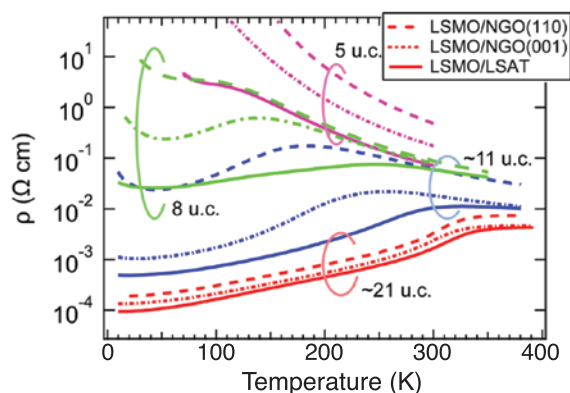


FIGURE 3: Resistivity (ρ) for samples of varying thickness.

of clear Kiesel fringes indicates good film quality. Most importantly, the LSMO (002) peaks are observed at effectively identical values of Q_z , indicating that the LSMO growth axis lattice parameters are also the same. This is evidence that the differences in substrate are not changing the strain state of the LSMO films, and that any observed variations in electronic or magnetic properties are attributable to changes in octahedral rotation.

Direct current transport measurements were used to characterize electronic properties of the samples. Fig. 3 shows the temperature-dependent resistivity for LSMO films of varying thickness grown on the different substrates. As expected, resistivity decreases with increasing thickness, but additionally, for a given thickness band, films grown on LSAT consistently exhibit the lowest resistivity. This demonstrates that by changing the substrate, we are indeed changing the electronic properties of the LSMO film.

Such changes in electronic structure make substrate-dependent variations in magnetic properties plausible as well. Given the interfacial nature of the substrate-dependent effects, it is desirable to use a depth-sensitive probe to characterize the magnetization. Thus, polarized beam reflectometry (PNR) measurements were performed using the PBR beamline at the NCNR. 18 u.c. thick LSMO samples were cooled to 100 K in a magnetic field $\mu_0 H = 0.5$ T applied parallel to the sample plane. The incident neutron beam was spin polarized such that the neutron magnetic moment was either parallel (+) or anti-parallel (-) to H , and the non spin-flip reflectivities R^{++} and R^{--} were measured as functions of Q_z . These data are shown in Fig. 4 (a-c), multiplied by Q_z^4 in order better simultaneously visualize features at low Q_z (where the reflected intensity is high) and high Q_z (where the reflected intensity is orders of magnitude lower). Pronounced spin-dependent oscillations are observed, indicating sensitivity to the nuclear and magnetic depth profiles. Model fitting of the data yields the profiles shown in Fig. 4(d).

Starting at the right of Fig. 4(d), we find significant differences in the magnetizations of the free LSMO surfaces of the samples. In particular, the free surface of the sample grown on NGO (001) has

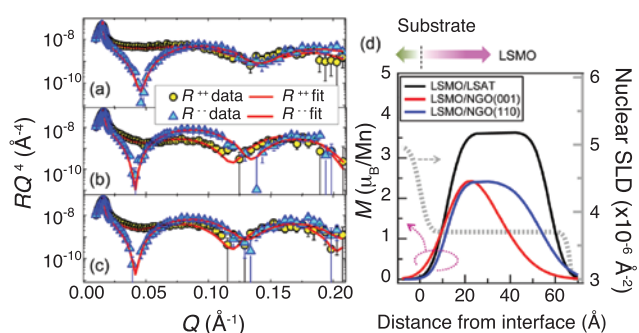


FIGURE 4: Fitted PNR data for (a) LSMO/LSAT, (b) LSMO/NGO (001), and (c) LSMO/NGO (110). (d) Nuclear (dotted line, shown for LSMO/LSAT) and magnetic (solid lines) depth profiles determined from the fits in (a-c).

a region of suppressed magnetic moment much larger than do the other two samples. However, X-ray absorption spectroscopy measurements (not shown) suggest that this difference arises from increased surface oxidation for the NGO (001) sample, and is likely independent of variations due to substrate.

On the other hand, there are features in the magnetic profiles that are indeed pertinent to this study. For all three samples, there is a region of LSMO approximately 5 u.c. thick at the substrate interface with significantly reduced magnetic moment. This region does not coincide with a change in the nuclear scattering length density profile, indicating that it does not arise from a local variation in composition. Instead, we conclude that this magnetic suppression corresponds to a region of LSMO with pronounced distortions in octahedral rotation in all three samples. Finally (and most importantly), the LSMO/LSAT sample exhibits a significantly higher maximum magnetic moment than LSMO grown on NGO.

It would be expected that “straightening out” the LSMO octahedral rotation should lead to increased electronic bandwidth, corresponding to increased conductivity and magnetization. Therefore, if our picture of octahedral coupling in Fig. 1 is correct, we would expect LSMO grown on LSAT to exhibit lower resistivity and higher magnetic moment than LSMO grown on NGO – and indeed that is what we observe.

In conclusion, we have shown pronounced changes in the electronic and magnetic properties of ultrathin LSMO films grown on cubic and orthorhombic substrates, despite the same strain state imposed by these substrates. This effect is attributed to interfacial structural coupling, leading to reduced MnO_6 rotations near the film / substrate interface in the LSMO / LSAT compared to LSMO / NGO. This work demonstrates the functional properties of oxide heterostructures can be controlled via interfacial BO_6 rotations.

References

- [1] H. Y. Hwang *et al.*, Nat. Mater. **11**, 103 (2012).
- [2] E. J. Moon *et al.*, Nano Letters **14**, 2509 (2014).

Comparison of methods for the measurement of deformation induced martensite formation

K. S. Raghavan,¹ G. Thomas,¹ J. Arnold,¹ and T. Gnaupel-Herold²

The current level of research in sheet metal development has delivered materials that exhibit extreme strength while retaining significant straining reserve and formability – properties that come at a premium in the automotive industry. Transformation induced plasticity is a significant source of strengthening in metastable austenitic stainless steels, in low carbon TRIP steels, and in third generation quenched and partitioned steels. All these steels rely on transformation of remaining austenite (face centered cubic iron) into martensites (body centered tetragonal and hexagonal forms of Fe-C-X compounds, with X being stabilizing alloy constituents) to increase strength level and ductility. Consequently, accurate evaluation of phase volume fractions of remaining austenite is of considerable interest, both in the context of alloy design and in the development of constitutive hardening models.

Several methods have been proposed to study the evolution of transformed martensite following straining. The more common measurement techniques are based on the ferromagnetic properties of α' and δ martensite: the FERITSCOPE instrument uses magnetic induction to determine the ferromagnetic constituents; a SATMAGAN analyzer uses a magnetic force balance method based on applying a saturating magnetic field to the specimen. Paramagnetic phases cannot be detected directly. Specific concerns include the dependence of the magnetic signal on specimen geometry, texture, magnetic permeability changes of α' martensite with strain and sensitivity to applied stress.

X-ray diffraction (XRD) methods have also been used extensively for phase volume fraction measurement. The principles of diffraction based phases analysis are well established; however, there are lingering concerns about the surface limit (interaction volume $\leq 0.01 \text{ mm}^3$), and the influence of crystallographic texture. In practice, using multiple reflections for each phase with specimen rotation/tilt for better averaging alleviates the effect of texture. In recent years neutron diffraction (ND) has emerged as a useful tool to study phase volume fractions on sheet metal samples. Some benefits of neutron diffraction over XRD include the orders of magnitude larger sample interaction volume, and a largely eliminated texture effect through complete orientation averaging.

Here, FERITSCOPE MP-30 measurements are compared with XRD and ND on a metastable austenitic stainless grade (UNS S20400 - NITRONIC 30) for a wide range of pre-strain conditions resulting

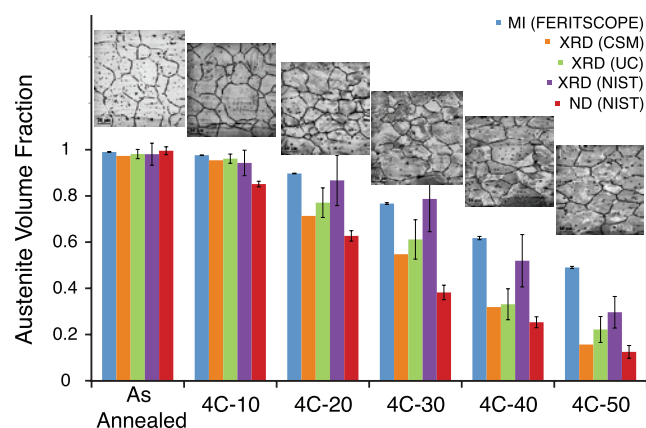


FIGURE 1: Comparison of austenite volume fraction by magnetic induction, X-ray diffraction and neutron diffraction for specimens deformed in uniaxial tension (0 % to 50 % engineering strain) at 4 °C. The accompanying microstructural changes are shown in the micrographs. Light colored regions indicate austenite; darker regions are martensites. Legend: University of Cincinnati (UC); Colorado School of Mines (CSM); NIST Center for Neutron Research (NIST).

in different states of preferred orientation (uniaxial tension, cold rolling, plane strain tension, balanced biaxial tension), with the focus on the functional correlation between the magnetic induction (MI) measurements and the diffraction measurements [1].

This multi-laboratory comparison shown in Fig. 1 is notable in several respects. The scatter among diffraction results is substantial, and there is no single identifiable reason responsible for the differences. Among the XRD measurements, CSM reports the smallest standard deviation (1 %) but it uses one sample orientation (< 1 % of orientation space), with ϵ -martensite identified and included. UC and NIST use some averaging over sample orientations (coverage of orientations space: UC ≈ 2.5 %; NIST-XRD ≈ 45 %) but the equipment used cannot resolve ϵ -martensite diffraction peaks.

Through complete orientation averaging (100 % of orientation space), neutron diffraction (ND) provides superior texture averaging and it uses the largest number of peaks in the analysis, with interaction volumes of the order of $\approx 100 \text{ mm}^3$, which is similar to FERITSCOPE. Most notable, however, is the increasing difference

¹ AK Steel Corporation, West Chester, OH 45069

² NIST Center for Neutron Research, National Institute of Standards and Technology, Gaithersburg MD 20899

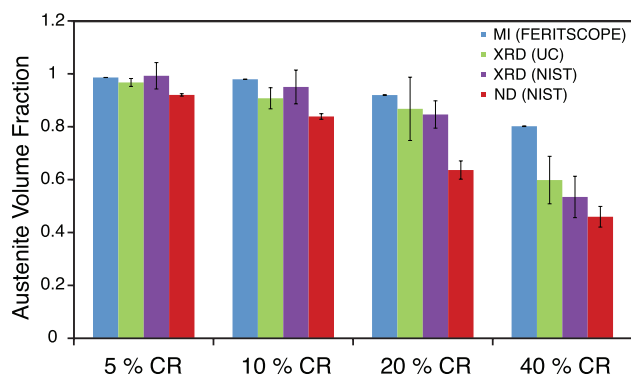


FIGURE 2: Comparison of austenite volume fraction measurement with magnetic induction, X-ray diffraction and neutron diffraction methods for specimens cold rolled (CR) up to 40 % at room temperature.

between diffraction results and MI measurements. This finding holds across different deformation paths as shown in Fig. 2 for cold rolled samples.

Folded into the results shown in Fig. 1 and Fig. 2 is not only the evolving texture but also the appearance of the hard-to-detect paramagnetic ϵ -martensite which tops out at a volume fraction of 11 % before nearly disappearing by 40 % strain (Fig. 3). The appearance of ϵ -martensite provides a partial answer to the question why neutron diffraction yields the lowest estimate of austenite content: the estimates from MI and XRD (Fig. 2) represent the sum of austenite and ϵ -martensite while neutron diffraction represents austenite only. The reason for the remaining difference between MI and diffraction methods cannot be conclusively discussed here; the purpose of this investigation was to elucidate the functional relationship between the estimates from FERITSCOPE and neutron diffraction. The result is shown in Fig. 4.

Dependence of deformation mode on the relationships between neutron diffraction and magnetic induction is shown in Fig. 4; it is apparent that the regression slopes vary substantially with deformation mode. Plane strain and balanced biaxial stretching slopes are lower than for uniaxial tension and cold rolling which creates concerns in using a single regression slope for converting magnetic induction measurements to neutron diffraction estimates in different deformation modes. The reasons for the observed differences in the relationship between different measurement techniques and deformation mode require further investigation beyond the scope of this work.

Reference

- [1] K. S. Raghavan, G. Thomas, J. Arnold, T. Gnaupel-Herold, Proc. of MS&T, Pittsburgh, PA, in press (2014).

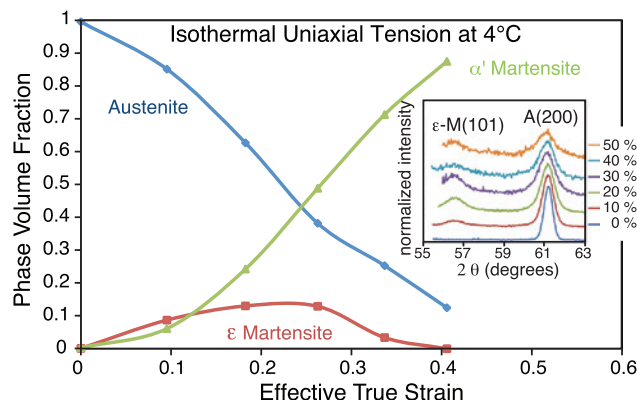


FIGURE 3: Phase volume fraction changes based on neutron diffraction measurements as a function of strain during isothermal tensile straining at 4 °C. One standard deviation is approximately 3 %.

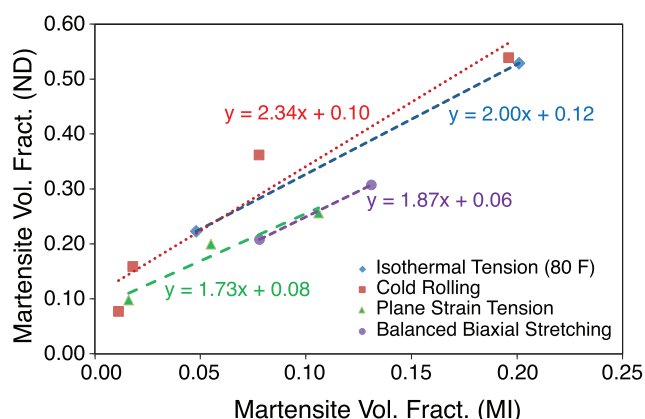


FIGURE 4: Comparison of neutron diffraction measurement with FERITSCOPE magnetic induction to study evolution of strain induced martensite in austenitic stainless steel under different strain paths.

Determining the effective transverse coherence of a neutron wave packet

C. F. Majkrzak,¹ C. Metting,^{1,2} B. Maranville,¹ J. A. Dura,¹ S. Satija,¹ T. Udovic,¹ and N. F. Berk^{1,2}

The goal of this investigation [1] was to determine the effective coherent extent of the neutron wave packet transverse to its mean propagation vector k , when it is prepared in a typical instrument used to study the structure of materials in thin film form via specular reflection. There are two principal reasons for doing so. One is the fundamental physical interest in the characteristics of a free neutron as a quantum object while the other is of a more practical nature, relating to the understanding of how to interpret elastic scattering data when the neutron is employed as a probe of condensed matter structure on an atomic or nanometer scale. Knowing such a basic physical characteristic as the neutron's effective transverse coherence can dictate how to properly analyze specular reflectivity data obtained for material film structures possessing some amount of in-plane inhomogeneity. We describe a means of measuring the effective transverse coherence length of the neutron wave packet by specular reflection from a series of diffraction gratings of different spacings.

The process of elastic, specular neutron reflection (SNR) (momentum transfer Q normal to the film surface) from layered film structures can be remarkably well described by plane wave solutions of a time-independent, one-dimensional Schrödinger wave equation. Nonetheless, it is unphysical, in principle, to describe the neutron wave function as a single plane wave composed of identical, parallel wave fronts of infinite lateral extent. In reality, the wavefronts representing an incident neutron are of finite size. Consequently, a theoretical analysis of SNR is valid only if the in-plane sample area illuminated by the projection of the transverse extent of the wave onto the surface is sufficient to effectively average over any existing in-plane inhomogeneities in scattering length density (SLD). Otherwise, an area-weighted, incoherent sum of independent reflectivities would be measured, necessitating a modified, more complicated analysis and interpretation of the data.

For neutrons produced at a source that is both temporally and spatially incoherent, the remark by Dirac [2] that "... a photon only interferes with itself ..." applies in this case to neutrons as well. To describe the wave-like behavior of a localized quantum object such as the neutron, the concept of a *wave packet* was originally conceived as a mathematical representation consisting of a continuous, coherent superposition of plane-wave momentum eigenstates. The wave packet construction effectively creates a probability distribution for finding a neutron in a finite, localized region of ordinary space while at the same time preserving the essential

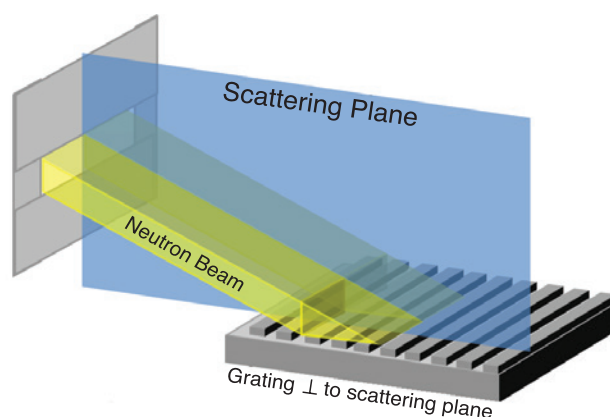


FIGURE 1: Grating stripes perpendicular to the scattering plane defined by incident and reflected nominal wavevectors. (In the actual instrumental configuration, the scattering plane is horizontal.)

wave property of coherence. Such a picture is consistent with, and is a natural consequence of, the Heisenberg uncertainty principle.

Now the very same optical elements in an experimental set-up, i.e., moderator, guides, monochromating crystal, and slits which impart a particular form and size to the neutron wave packet also define, at the same time, the incoherent distribution of mean wavevector values corresponding to each of the individual neutron wave packets that compose a beam and associated resolution. By analyzing the shape of the specular reflection curve for each of a set of uniform, rectangular gratings of incrementally differing periods – particularly in the region about the characteristic critical Q below which total external neutron reflection occurs – the effective transverse coherence length of the neutron wave packet can be determined within well-defined limits, almost independently of the angular divergence and wavelength spread of the beam.

In the experiments reported here, the conventional roles of the neutron and grating are interchanged – we use the gratings of “known” physical characteristics to probe an “unknown” wave property of the neutron. A comprehensive set of specular reflectivity measurements were performed for various neutron monochromators and sources (pyrolytic graphite, perfect single crystal silicon, vanadium) and different beam angular divergences and wavelength bandwidths. (The results of the specular measurements were corroborated by conventional non-specular, grating reflection width analysis.)

¹ NIST Center for Neutron Research, National Institute of Standards and Technology, Gaithersburg, MD 20899

² University of Maryland, College Park, MD 20742

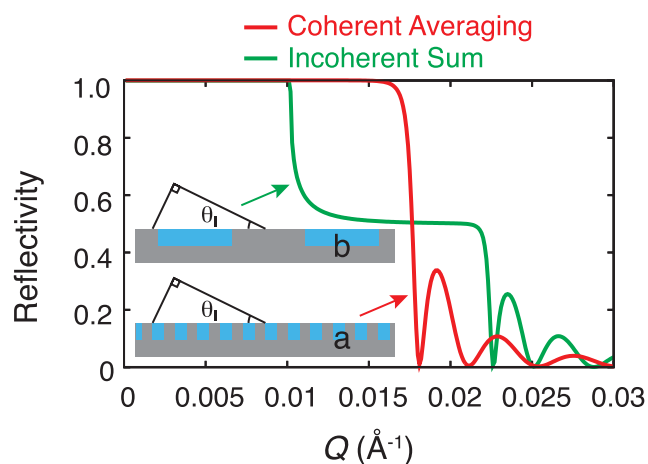


FIGURE 2: Reflectivity curves corresponding to coherent or incoherent averaging of two different SLDs, as described in the text. In the real space schematic of the grating structures, the material for the periodic rectangular structure is the same as the substrate and is taken to have the SLD of Si – the troughs in between, have the SLD of ordinary Ni. For the structure on the bottom (a), only a single critical Q is observed. Note that the real space figures are a highly schematic representation of the projection of the wave packet's transverse coherence length onto the grating. In reality, the wavefront structure of the packet is highly distorted in the vicinity of its interaction with the material. Grating (b) corresponds to an incoherent sum of two independent areas of in-plane SLD in the film, as described in the text. Note the appearance of two distinct critical Q values in the reflectivity curve.

The basic orientation of the grating structure used in the specular reflectivity measurements is shown in Fig. 1. If in-plane variations in SLD are present but of sufficiently small magnitude and/or spatial extent that the specular analysis remains a good approximation, then the effective SLD depth profile corresponds to the in-plane average SLD. A typical specular reflectivity model curve for a film (approximately 1000 Angstroms thick) composed of equal areas of two different constant SLDs (for Ni and Si on a semi-infinite substrate of Si) – and for which the dimensions of the in-plane areas of each of the two materials are sufficiently smaller than the projected length of the transverse dimension of the neutron wave packet (as depicted in the inset) – is shown in Fig. 2(a). In this case a single critical Q is observed which is related to a SLD that is the average of that for the two materials. In Fig. 2(b) is another real-space structure which has, again, equal net areas of the same pair of different constant SLDs but where now the areas of each material are divided into constituent sub-areas which have dimensions large enough that effective coherent averaging does not appreciably occur. In this latter case, the observed reflectivity is essentially an area-weighted incoherent sum of two distinct reflectivities, each for one of the two different SLDs. In this latter case, two critical Q values are observed, one corresponding to the material of lower SLD (Si) (below which the reflectivity is unity) and another determined by the SLD of the material of higher SLD (Ni). Between these two critical Q values the reflectivity is 50 percent, corresponding to the equal in-plane areas of the two materials. The differences between the reflectivity curves for the two cases shown in Fig. 2 are striking and clearly indicative of the length scale over which effective averaging takes place. Note that for glancing angles of incidence, the projected length of the transverse coherence length is greatly enhanced.

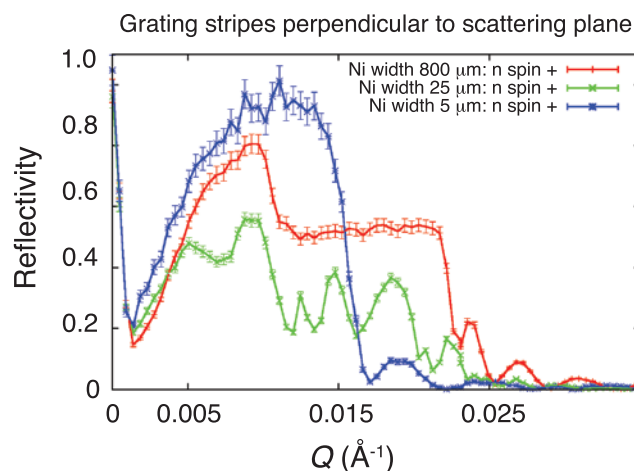


FIGURE 3: Summary of the specular reflectivity results, showing the reflectivity for a representative grating period in each of the three classes – incoherent, intermediate, and coherent. Error bars on the data points are statistical and represent one standard deviation.

Fig. 3 summarizes the specular reflectivity results, showing reflectivities for a representative grating period in each of three classes – incoherent, intermediate, and coherent. In the coherent limit, the neutron wave packet effectively averages over a sufficient number of periods in the grating structure. There is only a single critical Q – that corresponding to a film with half the SLD of Ni on a semi-infinite Si substrate. In the incoherent limit, on the other hand, the neutron wave packet effectively sees either a Ni stripe or an intervening Si area – so that for a sufficient number of incident neutrons in a beam, two distinct critical edges are observed, as discussed previously. In between these two limiting cases, a more complicated specular reflectivity curve is observed representing a cross-over region where the relatively large distortions observed are also a manifestation of the grating structure itself, as discussed in reference [3]. All of the specular and non-specular measurements performed in this work are consistent with a value of approximately one micron for the effective transverse coherence of the neutron packet.

In summary, by analyzing the specular reflectivity from a set of well-characterized diffraction gratings of different periods, we have obtained a measure of the effective transverse coherence length of a neutron wave packet – as prepared in a typical reflectometer configured for the study of the structure of condensed matter in thin film form – which is of the order of one micron. The particular measure of transverse coherence obtained in this manner is indicative of the ability of the packet to effectively average over in-plane variations of scattering density in specular reflectivity measurements.

References

- [1] C. F. Majkrzak, C. Metting, B. M. Maranville, J. A. Dura, S. Satija, T. Udovic, N. F. Berk, *Phys. Rev. A* **89**, 033851 (2014).
- [2] P. A. M. Dirac, *Quantum Mechanics*, 4th Ed., (Oxford University Press, London, 1958) p. 9.
- [3] N. F. Berk, *Phys. Rev. A* **89**, 033852 (2014).

Improved determination of the neutron lifetime

A. T. Yue,¹ M. S. Dewey,¹ D. M. Gilliam,¹ G. L. Greene,^{2,3} A. B. Laptev,⁴ J. S. Nico,¹ W. M. Snow,⁵ and F. E. Wietfeldt⁶

The accurate determination of the mean lifetime of the free neutron addresses important problems in physics [1]. The neutron lifetime is used in precision tests of the weak sector of the Standard Model, is an important input for models of light element formation following the Big Bang, and is required for comparisons between the measured and predicted antineutrino flux produced by nuclear reactors [2]. High-precision measurements (1 s to 5 s total uncertainty) have been performed with two distinct experimental strategies, yielding the Particle Data Group (PDG) world average neutron lifetime of $\tau_n = (880.0 \pm 0.9)$ s [3]. In the “beam” method, the absolute density of neutrons and the absolute decay rate are measured in a well-defined volume of a beam. In the “bottle” method, neutrons are confined to a storage vessel for varying times and the remaining neutrons are counted. As seen in Fig. 1, the beam and bottle measurements demonstrate reasonable internal consistency, but the weighted averages from the two methods differ by 2.6σ ($\Delta\tau_n \equiv \tau_{n\text{beam}} - \tau_{n\text{bottle}} = (887.3 \pm 2.8) \text{ s} - (879.6 \pm 0.8) \text{ s} = (7.7 \pm 2.9) \text{ s}$). This discrepancy casts doubt on the accuracy of the world average at the level of several seconds. The discrepancy is best addressed by reducing the uncertainty in the comparatively lower precision beam experiments. To that end, we have significantly improved the neutron flux measurement technique used in the NIST beam lifetime experiment. It has been used to retroactively improve the determination of the neutron lifetime [4] and it

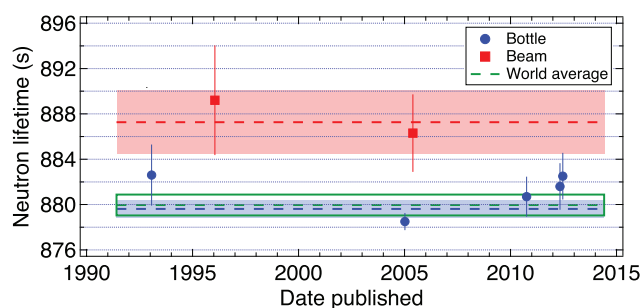


FIGURE 1: The neutron lifetime measurements used in the PDG 2013 world average. Three weighted averages (dashed lines) and their respective $1\text{-}\sigma$ uncertainties (rectangles) are shown: beam lifetimes (red), bottle lifetimes (blue), all lifetimes (green).

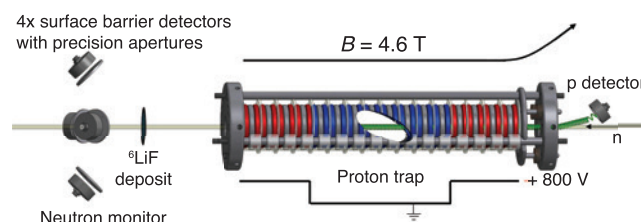


FIGURE 2: A schematic of the NIST beam neutron lifetime experiment. Protons produced by neutron decay are trapped radially by a 4.6 T magnetic field and axially by an electrostatic potential from voltage applied to the electrodes. The upstream electrodes are periodically grounded to flush protons out to the proton detector. Simultaneously, the neutron density in the trap is determined with a ^6Li -based neutron monitor.

provides a clear path to 1 s total uncertainty in a new run of the lifetime experiment [5].

The most precise beam neutron lifetime measurement was performed at the NCNR in 2000 [6, 7]. As shown in Fig. 2, the experiment uses an electromagnetic proton trap to determine the absolute rate of neutron decay in a well-defined volume of the beam, and a neutron monitor to measure the absolute density of neutrons in the trap. The neutron monitor operates by counting the charged particle products from the $^6\text{Li}(n,t)^4\text{He}$ reaction. The neutron beam passes through a thin deposit of ^6LiF and the reaction products are counted with surface barrier detectors masked by precision apertures. The detection efficiency for the monitor is determined from the evaluated nuclear data file value for the $^6\text{Li}(n,t)^4\text{He}$ cross section, and from measurements of the areal density of the ^6LiF deposit and the solid angle subtended by the detectors. The NIST experiment reported a lifetime of $\tau_n = (886.3 \pm 3.4) \text{ s}$ with the uncertainty dominated by the detection efficiency of the neutron monitor (2.7 s) [7]. Through the use of a totally absorbing neutron detector called the Alpha-Gamma (AG) device, we have directly measured the detection efficiency of the lifetime neutron monitor without reference to the $^6\text{Li}(n,t)^4\text{He}$ cross section and deposit density, circumventing the dominant sources of uncertainty in the prior efficiency determination.

¹ National Institute of Standards and Technology, Gaithersburg, MD 20899

² University of Tennessee, Knoxville, TN 37996

³ Oak Ridge National Laboratory, Oak Ridge, TN 37831

⁴ Los Alamos National Laboratory, Los Alamos, NM 87545

⁵ Indiana University, Bloomington, IN 47408

⁶ Tulane University, New Orleans, LA 70118

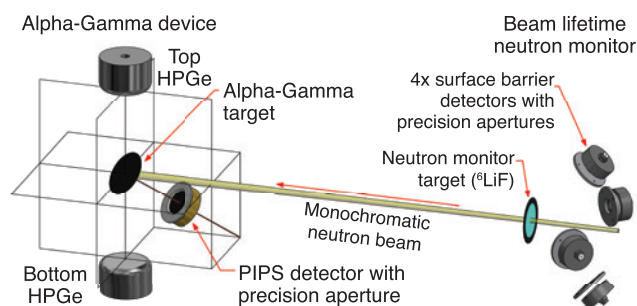


FIGURE 3: Schematic of the instrument setup on NG-6M.

The AG device determines the flux of neutrons impinging on a totally-absorbing ^{10}B -enriched boron carbide target by counting the 478 keV $^{10}\text{B}(n,\gamma)^7\text{Li}$ reaction gamma rays with high-purity germanium (HPGe) detectors. The flux is determined from the measured gamma rate and the absolute detection efficiency of the HPGe detectors for the capture gamma. The gamma detection efficiency is determined in a separate calibration procedure in which the precisely known activity of an alpha source is successively transferred through a series of intermediate steps [8].

The AG device and beam lifetime neutron monitor were operated simultaneously on NG-6M, a monochromatic cold neutron beam (as shown in Fig. 3). The measured flux from the AG device, the measured rate of $^6\text{Li}(n,t)^4\text{He}$ reaction products in the neutron monitor, and the measured wavelength of the beam are then used to determine the detection efficiency of the neutron monitor for thermal neutrons without reference to the $^6\text{Li}(n,t)^4\text{He}$ cross section or the target density. As shown in Fig. 4, data taken with three different beam collimations show good statistical consistency after correction for several systematic effects that may alter the efficiency. Including the uncertainties from systematic effects, the neutron monitor efficiency has been determined to 0.06 % with the AG device, a five-fold improvement [9].

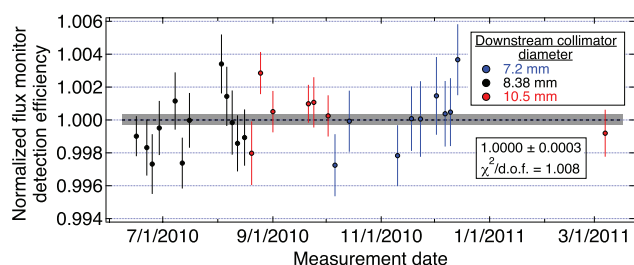


FIGURE 4: Normalized neutron monitor detection efficiency measurements with the AG device for three beam collimations. Corrections for systematic effects depending on beam collimation are included. The error bars are statistical only. The dashed black line is a weighted average of the data, and the grey bar represents the 1σ uncertainty on the fit.

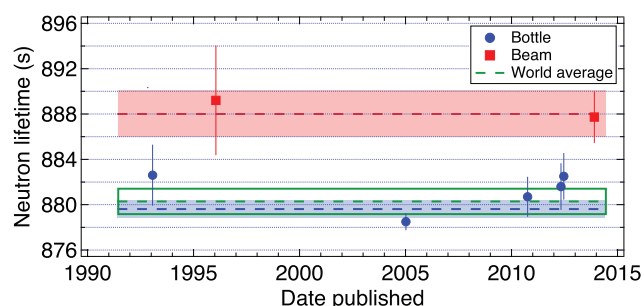


FIGURE 5: The neutron lifetime measurements used in the PDG 2013 world average after replacement of the 2005 NIST beam lifetime result with the 2013 result.

The measured detection efficiency is in good agreement with the value used in the prior work. We have verified the temporal stability of the neutron monitor (stability of the aperture frame and stability of the ^6LiF deposit density) through additional measurements. This allows us to use the newly measured detection efficiency to improve the neutron flux determination in the lifetime experiment, yielding an improved lifetime result of $\tau_n = (887.7 \pm 2.3) \text{ s}$ that replaces the prior result [4]. As seen in Fig. 5, this results in a new world average of $\tau_n = (880.3 \pm 1.1) \text{ s}$ and $(\Delta\tau_n = (888.0 \pm 2.1) \text{ s} - (879.6 \pm 0.8) \text{ s} = (8.4 \pm 2.2) \text{ s})$, increasing the significance of the discrepancy to 3.8σ . It is important that this discrepancy be resolved through measurements at higher precision. The NIST experiment will continue to play an important role, as the improvements in neutron flux determination reported here allow for the possibility to achieve 1 s total uncertainty with the existing apparatus in a new measurement.

References

- [1] D. Dubbers, M. G. Schmidt, *Rev. Mod. Phys.* **83**, 1111 (2011).
- [2] G. Mention *et al.*, *Phys. Rev. D* **83**, 073006 (2011).
- [3] J. Beringer *et al.*, *Phys. Rev. D* **86**, 010001 (2012).
- [4] A. T. Yue *et al.*, *Phys. Rev. Lett.* **111**, 222501 (2013).
- [5] M. S. Dewey *et al.*, *Nucl. Instr. and Meth. A* **611**, 189 (2009).
- [6] M. S. Dewey *et al.*, *Phys. Rev. Lett.* **91**, 152302 (2003).
- [7] J. S. Nico *et al.*, *Phys. Rev. C* **71**, 055502 (2005).
- [8] D. M. Gilliam, G. L. Greene, G. P. Lamaze, *Nucl. Instr. and Meth. A* **284**, 220 (1989).
- [9] A. T. Yue, Ph.D. thesis, University of Tennessee (2011).

Shaken or stirred? It matters when addressing the dynamics and stability of macromolecular nanocarriers in aqueous solution

T. H. Epps, III, M. O. Sullivan, R. P. Murphy, E. G. Kelley, J. E. Seppala, T. P. Smart, and S. D. Hann

The solution self-assembly of macromolecular amphiphiles, such as block copolymers, offers an efficient strategy for producing well-defined nanocarriers, with applications ranging from drug delivery and diagnostics to nanoreactors and reagent recovery. Typically, the formation of nanocarrier architectures is dictated by processing methods that employ cosolvent mixtures. These fabrication strategies rely on the assumption that polymeric solution nanostructures are kinetically stable following transfer from an organic/aqueous solution into an aqueous medium. We recently demonstrated that step-changes in polymer micelle populations could occur over days to weeks following transfer into a highly selective solvent, such as water [1]. This unexpected micelle growth was critically dependent on the method and rate of solution agitation (Fig. 1) and has a major impact on the assumed stability of polymer assemblies for therapeutic applications.

Amphiphilic macromolecules, such as block copolymers, are promising for many applications as molecular design offers enormous chemical versatility and exquisite control over the size and shape of solution assemblies. Of particular interest are the unique material properties conferred by the macromolecular nature of the hydrophobic block, such as exceptionally slow inter-aggregate chain exchange in highly selective solvents. These characteristics overcome key limitations of small molecule aggregates by improving the retention of encapsulated cargo for delivery and nanoreactor applications [2].

Many common preparation methods employ cosolvent mixtures to enable the loading of self-assembled morphologies with various hydrophobic cargoes such as dyes and therapeutic agents for diagnostics and drug delivery applications [2]. Cosolvent methods are essential to solubilize both the hydrophobic cargo and amphiphilic copolymer to facilitate efficient encapsulation. As nanocarriers are routinely used in aqueous solution, these preparation methods also hinge on the assumption that the assemblies are kinetically trapped (and nanostructure is preserved) following transfer from an organic/aqueous solution into water.

Although the effects of cosolvent introduction on the generation of block copolymer assemblies are well researched, the consequences of cosolvent removal on self-assembled structures typically are overlooked [1]. While some macromolecular assemblies are known to be kinetically trapped over time scales of days

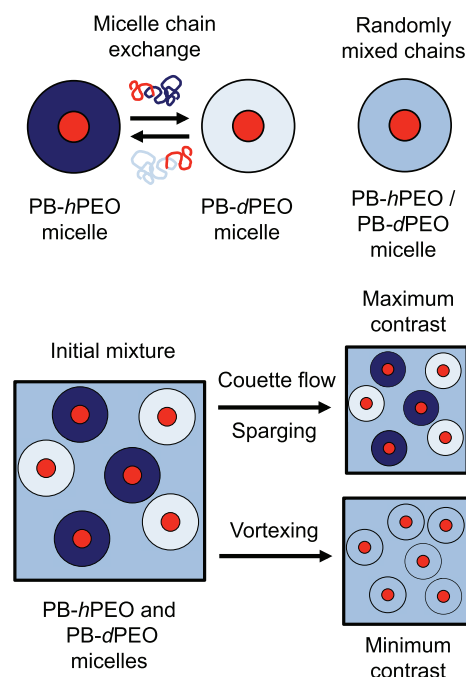


FIGURE 1: Schematic representation of contrast conditions used to study chain exchange as a result of solution agitation. Micelles containing protonated PB chains in the core and either non-deuterated or deuterated PEO chains in the corona (lower left panel) were agitated using rapid vortex mixing, Couette flow, or nitrogen gas sparging. SANS was used to measure the scattering intensity as a function of mix time and hence to quantify the extent of chain exchange (lower right panels). Chain exchange between micelles decreases the solvent-corona contrast and the scattered intensity, and under certain agitation conditions, the scattered intensity gradually approaches that of micelles with randomly mixed hPEO/dPEO corona chains.

or even months, a cohesive understanding of polymeric micelle dynamics is still lacking [1]. In the present work, it is shown that significant dynamic processes occur in block copolymer micelles following cosolvent removal, even in highly selective solvents. In the absence of agitation, the micelles are stable, consistent with scaling theories. However, gentle agitation, which is not considered in many scaling theories, leads to a marked increase in the micelle size. The micelle sizes evolve through a bimodal distribution, in which well-defined step-changes in size lead to a monodisperse final nanostructure population with an aggregation number much larger than that of the starting population.

The growth of poly(butadiene-*b*-ethylene oxide) [PB-PEO] micelles following solvent transfer (from tetrahydrofuran [THF]/water mixtures) into pure water was examined using small angle neutron scattering (SANS) and cryogenic transmission electron microscopy (cryo-TEM). Specifically, chain exchange in water was investigated using SANS by exploiting contrast variations and monitoring the temporal changes in the scattered intensity. Separate PB-PEO and PB-*d*PEO micelle solutions were prepared in an H₂O/D₂O mixture and mixed at time $t = 0$, giving rise to a maximum in scattered intensity due to contrast between the coronas and solvent. The lack of a temporal change in intensity in these mixed solutions indicated that single chain exchange was not prevalent in the highly amphiphilic PB-PEO systems [1].

Thus, fusion processes were examined as the other mechanism that could promote micelle reorganization. To visualize the micelle growth, cryo-TEM was employed to follow the temporal evolution of a micelle solution over a 21-day period following cosolvent removal. As one example, the data are illustrated for a solution that was initially in a solvent of volume fraction 43 % THF, prior to transfer into pure water at day 0. The core radii at day 0 were described by a single and nearly monodisperse distribution centered at (5 to 6) nm. Unexpectedly, a second distinct distribution of core radii centered at (10 to 11) nm appeared after 1 day. This second distribution represented an approximate eight-fold increase in core volume or aggregation number from the initial distribution. The distinct bimodal distribution persisted for ≈ 10 days, with the population weighting shifting from the smaller to the larger distribution over time. By day ≈ 16 , the core size distribution exhibited a single and nearly monodisperse population at (10 to 11) nm. Similar behavior was noted for samples prepared from solutions of volume fraction 30 % THF and 50 % THF, suggesting that specimens prepared at high THF contents grew through a fusion-controlled process.

The size evolution also was examined as a function of micelle concentration using cryo-TEM and SANS. The cryo-TEM images show that on day 10/11, 2 mg mL⁻¹ and 5 mg mL⁻¹ solutions still contained an appreciable bimodal population of micelles, while the 10 mg mL⁻¹ solution had transitioned to primarily larger micelles (Fig. 2). These micrographs suggested that the relative weighting of the larger population increased with micelle concentration and further supported that the micelles grew through fusion. For the SANS experiments, the micelle coronas were contrast-matched to the solvent (D₂O) by blending PB-PEO and PB-*d*PEO polymers, thereby probing only the PB core size distribution. The SANS data showed a marked difference in micelle populations for the 2 mg mL⁻¹ sample vs. the higher concentration samples (Fig. 2). However, the maxima and minima were located at approximately the same q -values, supporting that the larger micelles were the same size in all samples (Fig. 2). The bimodal core distribution centered at $R_c \approx 5$ nm and ≈ 10 nm was in good agreement with the cryo-TEM results, supporting the fusion mechanism for micelle growth.

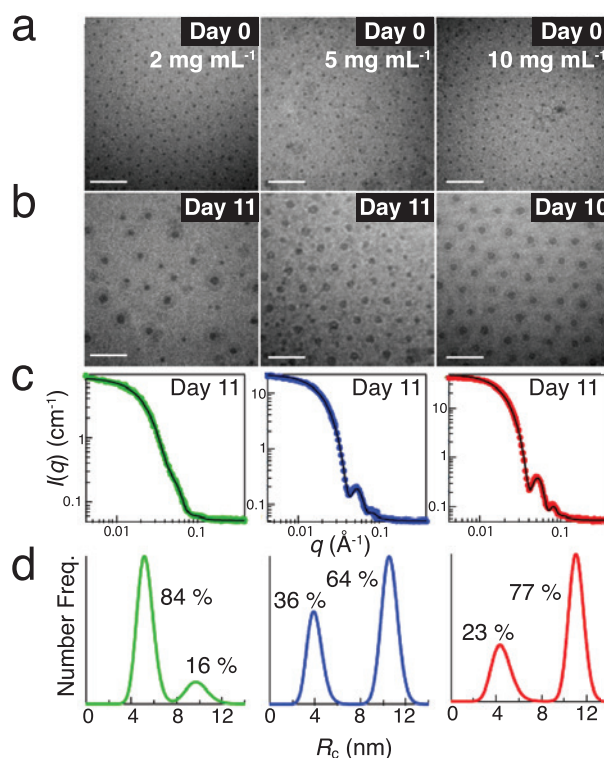


FIGURE 2: Cryo-TEM micrographs showing changes in micelle core radii between day 0 (a) and day 10 or day 11 (b) for several polymer concentrations. Scale bars are 100 nm. (c) SANS data (points) and fits (solid lines) for micelle solutions at different concentrations. (d) Corresponding number frequency distribution of core radii from fits to SANS data. Samples for the SANS experiments were prepared in a solvent of volume fraction 43 % THF and dialyzed against D₂O, and SANS experiments were performed at day 11 post dialysis to D₂O. The relative percentages of the smaller ($R_c < 8$ nm) and larger ($R_c \geq 8$ nm) core radii populations are shown on the frequency curves.

In summary, the distinct bimodal distribution found in the present work does not reflect standard predictions for micelle growth process [1]. Additionally, the micelle size evolution critically depended on solution agitation, suggesting that the growth may be an interfacial phenomenon. Hence, further quantitative studies are needed to distinguish the detailed mechanism and associated kinetics to fully understand the air-water interfacial effects on the long-term stability of macromolecular assemblies [3]. This relationship between processing conditions and subsequent dynamics has critical implications on the stability and overall “shelf-life” of solution nanostructures.

References

- [1] E.G. Kelley, R. P. Murphy, J. E. Seppala, T. P. Smart, S. D. Hann, M. O. Sullivan, T. H. Epps, III, *Nature Comm.* DOI:10.1038/ncomms4599 (2014).
- [2] E. G. Kelley, J. N. L. Albert, M. O. Sullivan, T. H. Epps, III, *Chemical Society Reviews* **42**, 7057 (2013).
- [3] R. P. Murphy, E. G. Kelley, S. A. Rogers, M. O. Sullivan, T. H. Epps, III, (2014) submitted to *ACS Macro Letters*.

Universal scaling of polymer diffusion in nanocomposites

J. Choi,¹ M. J. A. Hore,^{2,3} J. S. Meth,⁴ N. Clarke,⁵ K. I. Winey,¹ and R. J. Composto¹

Nanoparticles are added to polymers to form polymer nanocomposites (PNCs), which often exhibit enhanced physical properties due to the presence of the nanoparticle component. For example, PNCs possess properties that are attractive for biological, energy, and sensing applications, and have received growing interest due to the variety of functional nanoparticles that are available. In addition, advances in grafting polymers to surfaces have lead to powerful approaches for controlling nanoparticle dispersion by mediating the interactions between the nanoparticles and the free polymer. The processing of PNCs into bulk materials or films depends on the mobility of polymer chains in the presence of the nanoparticles, which can be grafted with small molecules or longer polymer chains. Unfortunately, while polymers with and without nanoparticles exhibit similar dynamics, a unified picture of polymer dynamics in the presence of nanoparticles is not available. Previous work [1] has demonstrated that polystyrene diffusion in PNCs containing bare nanoparticles obeys a universal rule, and is parameterized by a single confinement parameter $ID/2R_g$, where ID is the interparticle distance and R_g is the radius of gyration of the diffusing polymer chains. The confinement parameter characterizes the effective size of a diffusion pathway relative to the size of the diffusing polymer. In this way, if $ID/2R_g$ is small, the diffusion pathway near nanoparticles is small compared to the diffusing polymer, and the diffusing polymer is more strongly confined – leading to a slowing down of dynamics and a decrease in the diffusion constant. When bare nanoparticles are replaced with polystyrene-grafted nanoparticles, however, the diffusion constants do not follow this rule. Using a combination of self-consistent field theory (SCFT) and small-angle neutron scattering (SANS), we demonstrate that nanoparticles can appear larger or smaller to a diffusing polymer, depending on the molecular weight of that polymer, which in turn leads to an “effective” confinement parameter. When the polymer diffusion is instead parameterized by the *effective* confinement parameter, polymer diffusion in both systems collapses onto a single master curve [2].

The interparticle distance, ID , is a function of the nanoparticle volume fraction, which in turn depends on the nanoparticle size. To determine the effective interparticle distance, ID_{eff} , we performed SCFT calculations on a system consisting of a

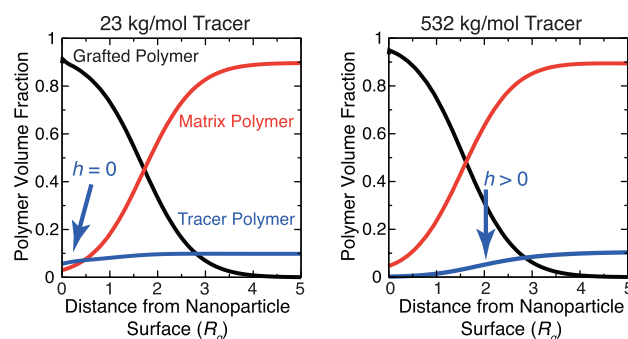


FIGURE 1: Self-consistent field theory (SCFT) calculations of the density of the grafted polymer (black), matrix polymer (red), and tracer polymer (blue) as a function of distance from the nanoparticle surface for two different tracer molecular weights. The arrow denotes the brush thickness h that the tracer polymer cannot penetrate. For example, $h = 0$ implies that the tracer polymer penetrates through the entire brush.

polymer-grafted nanospheres (molecular weight 87 kg/mol), embedded in a polymer matrix (molecular weight 160 kg/mol) that contains a volume fraction of 10 % of a diffusion tracer. As shown in Fig. 1, for a low molecular weight tracer, the volume fraction profile for the tracer polymer is fairly uniform as the distance to the nanoparticle surface decreases. In other words, the tracer polymer is not excluded from the grafted polymer region. On the other hand, for a larger tracer molecular weight (532 kg/mol, left) the tracer volume fraction falls off from 10 % to approximately 5 % at a distance $2R_g$ from the nanoparticle surface, as indicated by the blue arrow. In this situation, the tracer polymer cannot diffuse farther into the grafted polymer layer. Therefore, the size of the nanoparticle appears larger to a high molecular weight polymer, $R_{\text{eff}} = R_{\text{NP}} + h$, where R_{eff} is the effective nanoparticle radius, R_{NP} is the physical nanoparticle radius, and h is the brush height that the tracer polymer cannot penetrate into. Thus, nanoparticles appear larger or smaller to a diffusing polymer depending on the molecular weight of the tracer. If the molecular weight of the tracer is *larger* than that of the grafted polymer, $R_{\text{eff}} > R_{\text{NP}}$; otherwise, $R_{\text{eff}} \approx R_{\text{NP}}$. This behavior is entropic in nature, and due to autophobic dewetting between the two polymers. The effective confinement parameter ID_{eff} is obtained from the effective radius.

¹ University of Pennsylvania, Philadelphia, PA 19104

² NIST Center for Neutron Research, National Institute of Standards and Technology, Gaithersburg, MD 20899

³ Case Western Reserve University, Cleveland, OH 44106

⁴ E.I. DuPont de Nemours and Co., Inc., Wilmington, DE 19801

⁵ Sheffield University, Sheffield, S10 2TN United Kingdom

The SCFT results were validated by small-angle neutron scattering (SANS) measurements. PNCs were synthesized that matched the parameters of the SCFT calculations. Polystyrene (PS) grafted SiO_2 nanospheres ($R_{\text{NP}} = 25$ nm, PS molecular weight 87 kg/mol) were added to a hydrogenated polystyrene matrix (molecular weight 160 kg/mol) that contained a volume fraction of 10 % deuterated polystyrene (dPS, 23 kg/mol or 532 kg/mol). The dPS provided contrast in the system by changing the scattering length density of the polymer “shell” surrounding the nanoparticles. Shown on the left in Fig. 2 are the scattering length densities (SLDs) of the polymer shell around the nanoparticle, obtained from the tracer polymer volume fractions in Fig. 1. For the 23 kg/mol tracer, the ratio of deuterated polymer to hydrogenated polymer is very close to that in the bulk of the sample (*i.e.*, away from the nanoparticles). Thus, there is little contrast between the two components and only the bare nanoparticles can be observed in SANS (*i.e.*, the nanoparticles are “hard” nanoparticles). On the other hand, for larger tracer molecular weights, the deuterated tracer is excluded from a region of size h near the nanoparticle, which leads to a large contrast between these two regions. In this case, SANS sees the bare nanoparticles with a surrounding shell of hydrogenated polymer (*i.e.*, the nanoparticles are “soft” nanoparticles). When these values are used to fit the SANS intensities with a modified core/multi-shell model (Fig. 2, right), the fits reproduce the scattering data quite well, indicating the validity of the SCFT description of the system.

By using this ability to transform nanoparticles from hard to soft by varying the molecular weight of the diffusing polymer, we have uncovered a universal scaling rule for polymer diffusing in nanocomposites. Diffusion constants of deuterated polymers with varying molecular weights diffusing into PNCs containing a volume

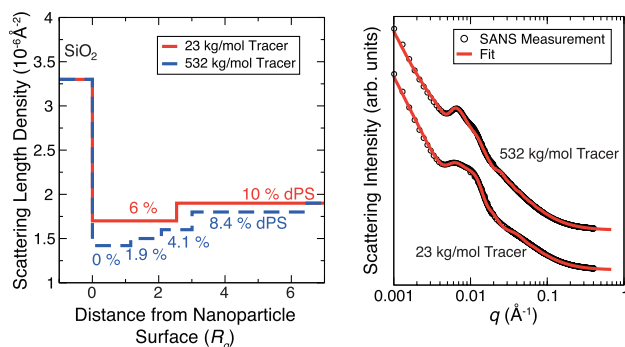


FIGURE 2: (Left) Calculated scattering length density (SLD) from SCFT in the grafted polymer layer as a function of distance from the nanoparticle surface. The red curve corresponds to a 23 kg/mol tracer polymer, and blue to a 532 kg/mol tracer polymer. The scattering length density is higher for the lower molecular weight tracer because more deuterated polymer is present within the brush. (Right) Small-angle neutron scattering (SANS) measurements and fits, according to a modified spherical core-shell model using the calculated SLDs.

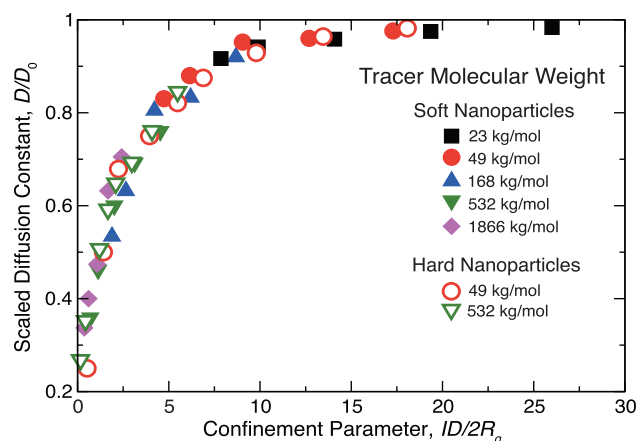


FIGURE 3: A plot of the scaled diffusion constant versus the confinement parameter yields a master curve. Closed and open symbols represent polystyrene diffusion in nanocomposites with soft and hard nanoparticles, respectively. The effective confinement parameter was determined using SCFT calculations, such as those shown in Fig. 1.

fraction of 5 % SiO_2 nanoparticles were measured using elastic recoil detection (ERD). The diffusion constants, D , were normalized by D_0 , the diffusion constant measured in the absence of nanoparticles. Fig. 3 shows the scaled diffusion constant as a function of the effective confinement parameter $ID_{\text{eff}}/2R_g$. As the confinement parameter decreases, the diffusion constant decreases substantially compared to D_0 due to the presence of entropic bottlenecks that hinder diffusion into the PNC. Remarkably, the scaled diffusion constants for both the hard and soft nanoparticle systems fall onto a single master curve, indicating a universal diffusion behavior in both classes of systems.

By combining self-consistent field theory and small-angle neutron scattering measurements, we have demonstrated that the effective size of a polymer-grafted nanoparticle can be larger than the physical size of the nanoparticle core, depending on the molecular weight of the diffusing polymer. For diffusing polymers with large molecular weights, relative to the brush, the grafted polymer exclude the diffusing polymers from the grafted layer, leading to a larger effective size, and a larger degree of confinement. Plotting the scaled diffusion constant D/D_0 as a function of $ID_{\text{eff}}/2R_g$ yields a single master curve that describes polymer diffusion into polymer nanocomposite systems [2].

References

- [1] S. Gam, J. S. Meth, S. G. Zane, C. Chi, B. A. Wood, M. Seitz, K. I. Winey, R. J. Composto, *Macromolecules* **44**, 3494 (2011).
- [2] J. Choi, M. J. A. Hore, J. S. Meth, N. Clarke, K. I. Winey, R. J. Composto, *ACS Macro Letters* **2**, 483 (2013).

Probing the relationship between water content and chain dynamics in fuel cell membranes

K. A. Page,¹ B. W. Rowe,¹ K. Masser,¹ and A. Faraone^{2,3}

Fuel cells based on polymer electrolyte membranes (PEM) show promise as a means of energy conversion for a wide range of applications both in the transportation sector and for stationary power production due to their high charge density and low operating temperatures. Perfluorosulfonate ionomers (PFSI's), particularly Nafion, are one of the most widely studied classes of materials for use as PEMs in fuel cell applications. In order to understand the performance of these membranes, it is necessary to understand the structure, water dynamics, and proton conductivity in these materials over a large range of relative humidity, temperatures, and processing conditions. Water and polymer dynamics play a critical role in the performance (i.e., proton conductivity) and durability of membrane materials in operating hydrogen fuel cells. Ultimately, researchers would like to find ways to reduce the amount of water necessary for high proton conductivity because the fuel cell could then be operated at higher temperatures, which improves the efficiency of the cell. Therefore, many studies have focused on understanding the bulk water transport with considerable effort to learn how this transport is related to the nanostructure of the membrane. Researchers have used neutron techniques to investigate the local water dynamics within the nanoscale structures present in the material and to correlate the motions of water at the nanoscale to the bulk transport of water, which is critical to the performance of these materials in electrochemical devices. While the focus has mainly been on water, the complex structural features of these materials as well as the relationship between the water (both local and macroscopic) and the polymer chain dynamics have received less attention. However, if any advances are to be made in the elucidation of the fundamental properties of water transport, one must develop a working knowledge of the interplay between water dynamics/transport and chain motions. One way to approach this problem is to measure the collective structural dynamics in hydrated PFSI materials at elevated temperatures and to relate those dynamics to the content and behavior of water. In this work, we have used neutron spin echo (NSE) spectroscopy and dielectric relaxation spectroscopy (DRS) to investigate the relationship between water content and chain dynamics in Nafion membranes [1, 2].

Figure 1 demonstrates typical results from the NSE measurement which is the normalized intermediate scattering function, $S(Q,t)/S(Q,0)$, as measured for dry ($\lambda \approx 0$) and hydrated ($\lambda \approx 16$)

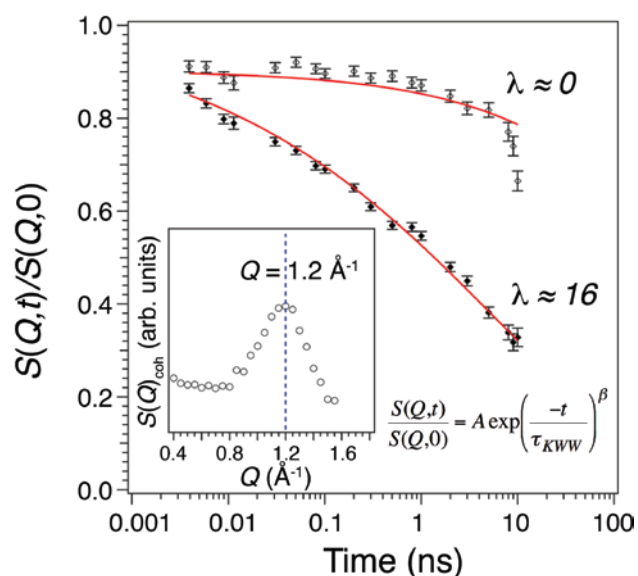


FIGURE 1: The normalized intermediate scattering function, $S(Q,t)/S(Q,0)$, for a nominally dry and hydrated ($\lambda = 16$) Nafion membrane at $Q = 1.2 \text{ \AA}^{-1}$. The Q value was chosen to coincide with the peak in the coherent structure factor associated with inter-chain scattering of the Nafion polymer backbone (inset). The $S(Q,t)/S(Q,0)$ was fit with the KWW equation as shown in the graph, where τ_{KWW} is the relaxation time of the polymer chains and β is related to the distribution of relaxation times observed. Notice the remarkable increase of the polymer chains' mobility as the water content increases. Error bars represent one standard deviation in the measured scattering intensity.

Nafion membranes at 335 K (where λ is the moles of water per mole of sulfonic acid groups in the polymer). The measured $S(Q,t)/S(Q,0)$ is associated with motions occurring on the length scale of the inter-chain distances (ca. 5 Å) of the polymer backbone as determined from the coherent structure-factor (inset, Fig. 1). The data was fit with a Kohlrausch-Williams-Watts (KWW) equation (inset, Fig. 1) to determine the time scale associated with the polymer chain motions both as a function of water content and temperature. Clearly, $S(Q,t)/S(Q,0)$ decays at a faster rate with the addition of water which indicates that the motions occurring on the length scale of the inter-chain distance are occurring at shorter time scales. Moreover, at a given water content a similar behavior is exhibited with increasing temperature. A summary of the quantitative analysis of the relaxation

¹ National Institute of Standards and Technology, Gaithersburg, MD 20899

² NIST Center for Neutron Research, National Institute of Standards and Technology, Gaithersburg, MD 20899

³ University of Maryland, College Park, MD 20742

process(es) can be found in Fig. 2. The time scale of the backbone dynamics, τ_{KWW} , undoubtedly has a strong dependence on both λ and temperature. Essentially, as the temperature and the water content, λ , increase; τ_{KWW} decreases accordingly, indicating that the chain motions are becoming faster, which is to be expected. With increasing levels of water, the electrostatic interactions are weakened and the polymer is effectively plasticized by the water molecules. Additionally, τ_{KWW} begins to decrease less significantly with λ for values greater than approximately 6. Interestingly, researchers have shown that the effective diffusivity of water through the membrane and the local water dynamics both seem to plateau at approximately the same water content ($\lambda \approx 6$). This is evidence that there is a strong inter-dependence of the dynamics of water and the polymer chains. As with the local water dynamics, at water contents greater than $\lambda \approx 6$, the chain dynamics seem to be approaching a plateau and the relaxation times of the chains are no longer, to a large degree, being plasticized by the presence of additional water molecules. The increased mobility in molecular relaxations induced by the presence of water points to the molecular origins of the temperature- and humidity-dependent softening mechanisms in Nafion and other perfluorinated sulfonic acid (PFSA) membrane materials. Moreover, we have determined the activation energy, E_a , for the segmental dynamics through an analysis of the temperature dependence of relaxation times measured and found a decrease in the activation energy for this process with increasing water content. This is a similar behavior that has been observed by Lingwood and coworkers [3] for the energetics of water transport in Nafion. Taking both studies into consideration, it is important to note that the activation energy for water transport at low water contents is comparable to that measured for the polymer chain motions as measured by both NSE and DRS [4]. This is strong evidence that the water/proton transport in these materials is strongly coupled to the polymer chain dynamics.

We have successfully measured the chain dynamics as a function of water content and temperature using NSE spectroscopy and have demonstrated that the chain dynamics become faster with increasing temperature and water content. And, more importantly, that the energetics of water transport and chain dynamics are quite comparable at relatively low water contents. These results provide evidence that there is a strong coupling between the water transport and the polymer segmental dynamics at low

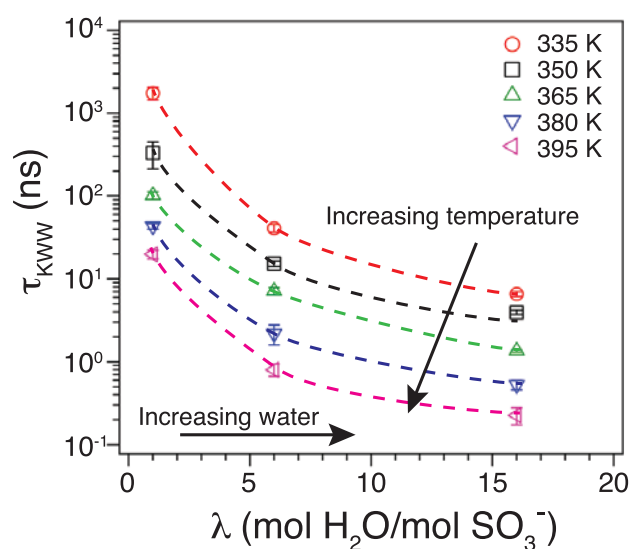


FIGURE 2: Time scale of backbone dynamics, τ_{KWW} , at various water contents (dry, $\lambda = 6$, and $\lambda = 16$) at (○) 335 K, (□) 350 K, (△) 365 K, (▽) 380 K, and (◀) 395 K. Error bars represent one standard deviation in the determination of τ_{KWW} from fitting of the KWW equation to the intermediate scattering $S(Q,t)/S(Q,0)$. Dashed lines are guides for the eye.

water contents in perfluorinated sulfonic acid (PFSA) membrane materials. These results have strong implications if materials capable of achieving high performance at low water content are to be engineered. Going forward, this information aids chemists in the design of polyelectrolyte membrane materials that have higher proton conductivity at low water contents by finding ways to incorporate acid groups with fast dynamics at low water contents or decoupling the water and polymer dynamics altogether.

References

- [1] Y. Wang, K. S. Chen, J. Mishler, S. C. Cho, X. C. Adroher, *Appl. Energ.* **88** (4), 981 (2011).
- [2] K. Mauritz, R. Moore, *Chem. Rev.* **104**, 4535 (2004).
- [3] M. D. Lingwood, Z. Y. Zhang, B. E. Kidd, K. B. McCreary, J. B. Hou, L. A. Madsen, *Chem. Comm.* **49**, 4283 (2013).
- [4] K. A. Page, B. R. Rowe, K. A. Masser, A. Faraone, *J. Polym. Sci. Part B Polym. Phys.* **52** (9), 624 (2014).

Observation of spatially dependent heterogeneity of constrained local motions of rubber in carbon black nanocomposites

J. H. Roh,¹ M. Tyagi,^{2,3} and C. M. Roland⁴

Understanding the molecular dynamics and vitrification transition of polymers at the interface with fillers remains a challenge for material scientists. The physical and chemical properties of polymers in proximity to substrates are directly coupled to the local dynamics at the interface. The binding affinity can give rise to dynamic heterogeneity of the motions, as reflected in spatial and temporal correlations, as well as a distribution of relaxation times [1].

However, the physical interactions between polymers and interfaces and their effect on dynamical properties remain poorly understood, with discordant conclusions from various experimental studies. It is more intuitive that binding of polymer segments to hard particles suppresses local motions, to increase both the relaxation time [2] and the length scale of the cooperativity [3]. Interestingly, a few quasielastic neutron scattering (QENS) studies showed *increased* librational mobility of the polymer chains in the glassy state due to the presence of carbon black (CB) nanoparticles. Accordingly, there is no clear distinction between backbone units adsorbed at the surface of a substrate and local segments immobilized by their spatial proximity to the interface.

Our quasielastic scattering studies aimed to investigate how dynamic heterogeneity and flexibility of 1,4-polybutadiene (PBD) is influenced by its physical interactions with CB particles. The initial composition of carbon (volume fraction) of 20.5 % in the composite increased to 60 % after extracting PBD chains that did not bond to CB particles. Quasielastic neutron scattering experiments were conducted using the High Flux Back-Scattering (HFBS, NG2) and Disk Chopper (DCS, NG4) spectrometers. The dynamic scattering function, $S(Q, E)$, was measured at HFBS with an energy resolution of 0.8 μeV up to 17 μeV ; the Q range was 0.31 \AA^{-1} to 1.71 \AA^{-1} . The boson peak of neat PBD and the nanocomposite was measured at DCS with energy resolution of about 25 μeV . The fraction of incoherent scattering cross section of H-atoms in the polymers was estimated to be 94 % of the total scattering for neat PBD and 82 % for the extracted nanocomposite, ensuring that the measured data represent dynamic scattering functions of PBD chains only. The wavevector (Q) dependent Kohlrausch-Williams-Watts (KWW) equation was

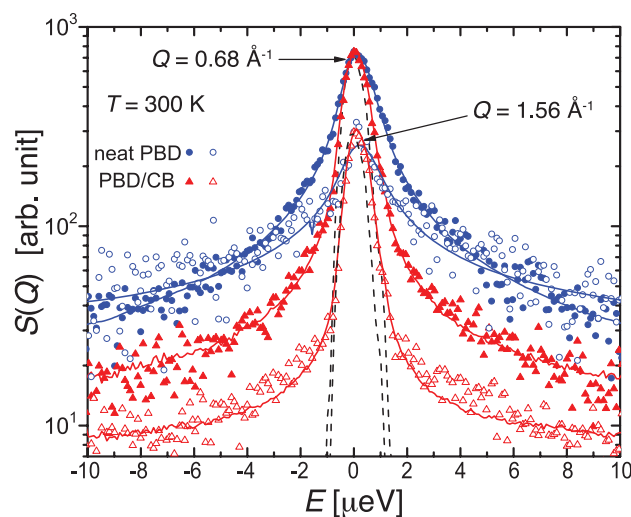


FIGURE 1: Incoherent dynamic structure factors at 300K at the indicated wavevectors for neat PBD (circles) and the nanocomposite (triangles). Dashed line is the resolution function measured at 4 K.

used to obtain the spatial dependence of the local segmental relaxation times (τ_α).

$$\Phi_{KWW}(Q, t) \propto \exp(-[t/\tau_\alpha(Q)]^{\beta(Q)})$$

Since the accessed dynamic range of neutron scattering is too narrow to determine the values of both the stretch exponent β and the relaxation time, the former was obtained from dielectric measurements on the same material.

The spatially dependent relaxation times from the quasielastic neutron scattering measurements show a transition from Gaussian to non-Gaussian behaviors. At small Q (below $\approx 1 \text{ \AA}^{-1}$) where the first maximum of the static structure factor emerges, the microscopic motions exhibit simple Gaussian diffusion, with $\tau_\alpha^\beta \sim Q^{-2}$. At larger Q , the spatial dependence is much weaker, and is referred to as sub-linear diffusion. Such behavior is predicted by various theoretical models, including mode-coupling theory (MCT), jump diffusion models, and caging-decaging fractals [4, 5].

¹ Center for Self-assembly and Complexity, Institute for Basic Science, Pohang, Republic of Korea, 790-784

² NIST Center for Neutron Research, National Institute of Standards and Technology, Gaithersburg MD 20899

³ University of Maryland, College Park, MD 20742

⁴ Chemistry Division, Code 6120, Naval Research Laboratory, Washington DC 20375

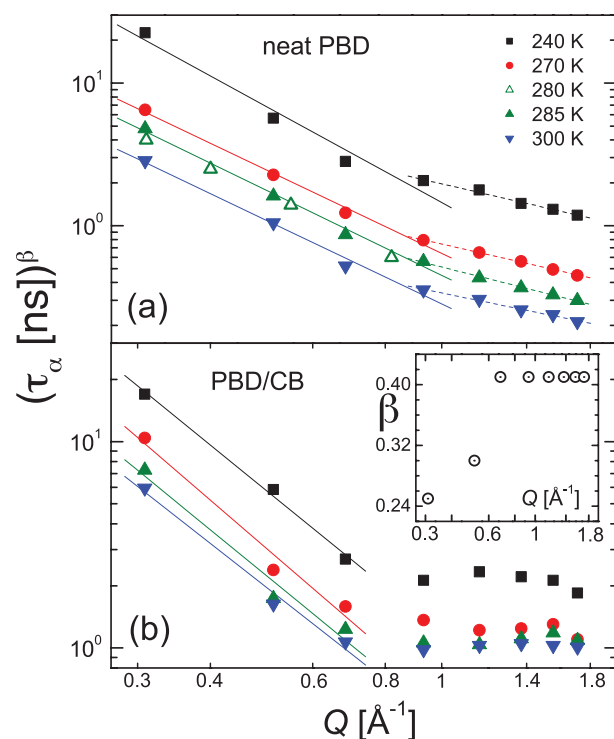


FIGURE 2: Local segmental relaxation times from QENS for (a) unfilled PBD with the value of the stretch exponent obtained from dielectric and mechanical spectroscopy. (b) extracted nanocomposite with the $\beta(Q)$ (plotted in the inset) taken to be the values giving conformance to the Gaussian approximation for $< 0.8 \text{ \AA}^{-1}$, and fixed at 0.41 for higher Q . Lines are least squares fits having a slope equal to -2 at small Q .

The stretch exponent for neat PBD was determined from its dielectric spectrum, yielding $\beta = 0.41$. For the filled polymer, $\beta = 0.38$ was found from the mechanical shear loss modulus (G'') peak, although there is some deviation at lower frequencies [6].

Fig. 1 clearly shows that the dynamic structure function, $S(E)$ for the nanocomposite is narrower than that for neat PBD, which is a consequence of greater constraints on the segmental motions [6]. For the neat PBD, the Q -dependence of the relaxation times is shown in Fig. 2a. For $Q < 1 \text{ \AA}^{-1}$ the Gaussian approximation holds, $\tau_{\alpha}^{0.41} \sim Q^{-2}$. At larger Q ranges, the behavior changes, with the Q -dependence becoming weaker, $\tau_{\alpha}^{0.41} \sim Q^{-0.9}$. This non-Fickian diffusion implies more local and/or isolated motions.

We calculated the β value using the expected $\tau_{\alpha}^{0.41} \sim Q^{-2/\beta}$ behavior for small Q 's (Fig. 2b). Similar to the Q -dependence of relaxation times for neat PBD, a transition to a weaker Q -dependence is observed for the nanocomposite at larger Q . The $\beta(Q)$ values for the nanocomposite are plotted against Q in the inset to Fig. 2b [6]. Fig. 3 shows the quasielastic incoherent structure factor (QISF), reflecting the more mobile fraction of the local motions at the accessed timescales [7]. QISF for the nanocomposites is less

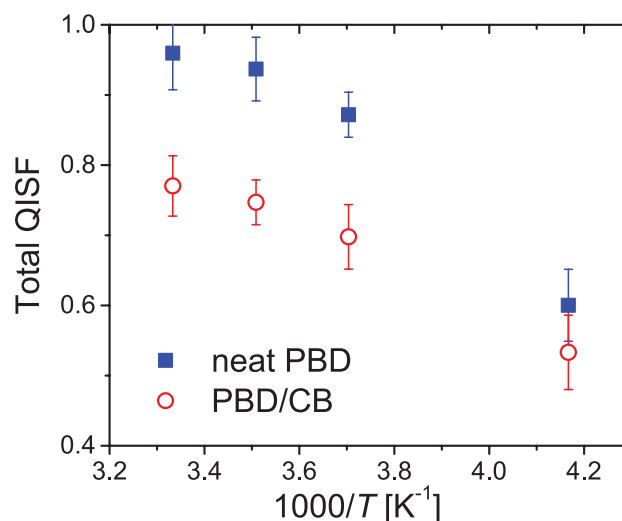


FIGURE 3: Quasielastic incoherent structure factor (QISF) for the nanocomposite and the neat PBD. These QISF values were averaged for $Q \geq 1.16 \text{ \AA}^{-1}$.

than that for the neat PBD at higher temperatures ($> 240 \text{ K}$). The difference is proportional to the amount of hydrogen atoms immobilized in the nanocomposite. Analysis of boson peaks at 60 K revealed that the number of mobile sites involving only the fast process and collective vibrations is essentially the same for the neat polymer and the nanocomposites. This shows clearly that only the segmental motions of polymers are affected by the binding affinity of the nanoparticle.

Our main result is that binding of PBD chains to the carbon particle surface slows the segmental motions and increases the heterogeneity of the dynamics. We also found that the spectral stretching and change in τ_{α} are spatially dependent. Both the breadth of the relaxation peak and the relaxation time are larger in the CB nanocomposite. The fact that this slowing down is observed primarily at shorter length scales implies that the constraints on the chains from the particles depend on the proximity of a segment to the particle surface.

References

- [1] M. D. Ediger, *Ann. Rev. Phys. Chem.* **51**, 99 (2000).
- [2] C. G. Robertson, C. M. Roland, *Rubber Chem. Technol.* **81**, 506 (2008).
- [3] F. W. Starr, J. F. Douglas, *Phys. Rev. Lett.* **106**, 115702 (2011).
- [4] R. Zorn, *Phys. Rev. B* **55**, 6249 (1997).
- [5] B. Vorselaars, A. V. Lyulin, K. Karatasos, M. A. J. Michels, *Phys. Rev. E* **75**, 011504 (2007).
- [6] J. H. Roh, M. Tyagi, T. E. Hogan, C. M. Roland, *Macromolecules* **46**, 6667 (2013).
- [7] J. H. Roh, M. Tyagi, T. E. Hogan, C. M. Roland, *J. Chem. Phys.* **139**, 134905 (2013).

Development of a neutron microscope

D. S. Hussey,¹ D.L. Jacobson,¹ D. Liu,² B. Khaykovich,² M.V. Gubarev,³ and M. Arif¹

An effective neutron lens is hard to find. To be a good lens for light, neutrons, X-rays, etc., a material must substantially change the path of the incoming wave. The refractive index of the material characterizes this change and the refractive index of vacuum is 1 (air is also close to vacuum). Many materials strongly bend visible light, for instance the refractive index of polycarbonate (used in reading glasses) is about 1.6, a 60 % relative change. The situation is completely different for neutrons, for which the refractive index for polycarbonate differs from air by only 0.001 %, and the focal length of such a lens is hundreds of meters. However, neutrons can be focused in a few meters by reflection from curved surfaces and recent efforts at NASA will enable the development of a truly effective neutron lens and lead to the world's first neutron microscope.

Lens materials for soft X-rays and cold neutrons have similar, small refractive indices. Astronomers have developed reflective optics in order to image faint X-ray sources with telescopes such as the CHANDRA X-ray observatory. This optics was first proposed by Hans Wolter and is based on reflection from two confocal conic sections [1]. The two reflections cancel coma, meaning that this optics possess good off-axis imaging properties. The advance in this technology that NASA has made is to create high resolution mirrors from thin nickel foils [2] rather than CHANDRA's mirrors which are thick, highly polished glass substrates coated with iridium. Nickel is an excellent neutron mirror and thin foils allow nesting several such mirrors in order to increase the solid angle of the optics. NASA continues to improve the resolution of these mirrors and believes that an angular resolution of 1 arcsec will be obtained in the very near future. With a focal length of 4 m, the spatial resolution of such a lens is about 15 μm ; further improvements in mirror quality will enable spatial resolution of about 1 μm [3].

Without a lens, neutron imaging uses pinhole optics geometry, where the pinhole diameter is on the order of a centimeter. With such a large aperture, the object must be placed as close to the detector as possible to obtain the best spatial resolution. This means that one cannot magnify the image and to improve the achievable spatial resolution one can only improve the detector; currently the best neutron imaging detector has a resolution of about 15 μm . To image a thick object at high spatial resolution requires the use of small apertures which in turn strongly reduces the neutron intensity and results in long exposure times – typical exposure times for a 15 μm image are about 20 minutes. On the other hand, a lens determines the image spatial resolution and does not require one to use such strong

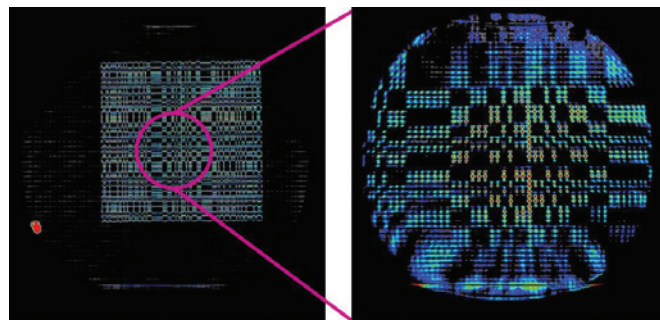


FIGURE 1: Images of a pinhole mask with conventional neutron imaging (left) and the prototype neutron microscope (right). The individual pinholes are clearly visible only with the neutron microscope.

collimation – for an image with 15 μm spatial resolution, the exposure time could be reduced by a factor of 100. As well, a lens can magnify the image which improves the resolution of the detector – a magnification of 10 will improve the resolution of the best detectors to about 1 μm . These dramatic improvements will enable neutron imaging to contribute to many new areas of materials science.

A prototype neutron microscope was built on the NG-1 beam line to demonstrate the concept [4]. The lens was designed for magnification of 4 with an overall focal length of 3.2 m. The measured spatial resolution of the images was about 75 μm which was in agreement with the angular resolution of about 110 μrad measured by X-rays. The effect of image magnification and increased intensity are shown in Figure 1 where images of a pinhole array with 100 μm wide holes on 200 μm spacing using conventional neutron imaging and microscope neutron imaging are compared. The intensity in the microscope is increased by 5 and the holes in the center of the array are clearly distinguished in the neutron microscope image whereas they are blurred in the conventional image. This proof of concept measurement has spurred the development of an optimized neutron microscope at the NCNR, and it is anticipated that user operation will begin by 2017.

References

- [1] H. Wolter, *Ann. Der Physik* **10**, 52 (1952).
- [2] M.V. Gubarev *et al.*, NASA, assignee. Patent 8,575,577 (2013).
- [3] K. Kilaru, B. D. Ramsey, M. V. Gubarev, D. A. Gregory, *Opt. Eng.* **50**, 106501 (2011).
- [4] D. Liu *et al.*, *Appl. Phys. Lett.* **102**, 183508 (2013).

¹ Physical Measurement Laboratory, National Institute of Standards and Technology, Gaithersburg, MD 20899

² Massachusetts Institute of Technology, Cambridge, MA 02139

³ NASA Marshall Space Flight Center, Huntsville, AL 35812

A scaling law to describe the average local structure of biomolecules

M. C. Watson and J. E. Curtis

Small-angle neutron and X-ray scattering have become invaluable tools for probing the nanostructure of molecules in solution. It was recently shown that the definite integral of the scattering profile exhibits a scaling (power-law) behavior with respect to molecular mass [1]. We have derived the origin of this relationship, and shown that the integrated scattering profile can be used to identify differing levels of disorder over local (3 nm) length scales [2].

Proteins and polymers in solution have many common features. Like a polymer chain, proteins are composed of a long chain of monomer units. The degree of folding for both polymers and proteins is strongly influenced by their interactions with the solvent. The global structure of many proteins is consistent with Flory's scaling law for polymers, $R_g = R_0 N^\nu$ where R_g is the radius of gyration, N is the number of chain segments, and R_0 is the length of each segment. The value of ν lies in the range $1/3 < \nu < 3/5$, and depends on the nature of the polymer chain. Experimental measurements have found that unfolded proteins exhibit the behavior of a self-avoiding random walk ($\nu = 0.588$). When interactions between the solvent and chain are sufficiently unfavorable, polymers collapse into a compact shape ($\nu = 1/3$). This prediction is in good agreement with measurements of globular proteins.

Unlike polymers, however, globular proteins adopt conformations specific to their amino-acid sequence and physiological role. Despite the overall scaling trend described by Flory, the spread in the experimental data is large. Two proteins with the same number of residues can have radii of gyration that differ by an order of magnitude. Although Flory's scaling law offers a qualitative model of protein size, it does not provide a structural description that is closely obeyed by all proteins. Calculating the definite integral of the small-angle scattering profile, $V_c(q_m)$, provides a quantity that shows clear differences depending on the degree of disorder of a protein. For a given q_m , $V_c(q_m)$ is larger as the protein becomes more disordered. This is shown clearly in Fig. 1 for three different protein structures. Then, constructing a scaling similar to Flory: $V_c(q_m) = aN^b$ and analyzing more than 9000 proteins provides a master scaling showing clear trends based on the amount of disorder in the protein [2].

Our analysis was applied to both globular and intrinsically disordered proteins. For nearly all cases, the integrated scattering profile scales with the number of chain segments, but exhibits much less

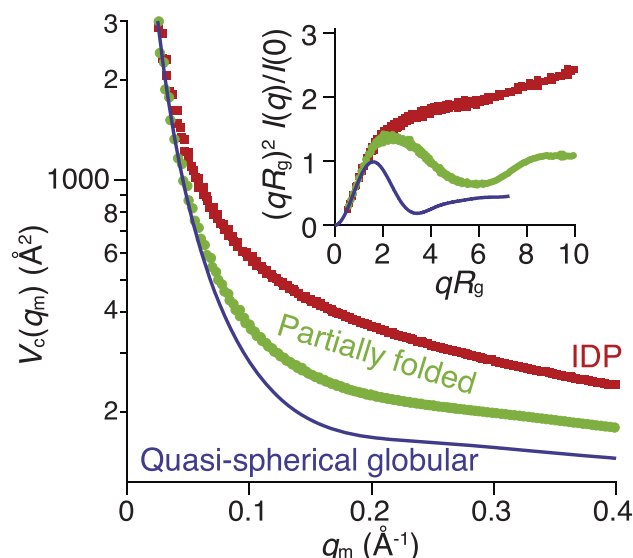


FIGURE 1: Degree of disorder as revealed by $V_c(q_m)$ and the unitless Kratky Plot for a compact quasi-spherical globular protein, a partially folded protein, and an intrinsically disordered protein IDP.

dispersion, reflecting similarities in density on length scales below 3 nm. Integrating to a finite q_m corresponds to scanning the entire particle with a probe of radius $2\pi/q_m$, providing structural information that cannot be directly obtained from the scattering profile itself. In addition, we have shown how an individual molecule's deviation from this scaling trend can be used to quantify its degree of disorder. For a given number of residues, the disorder and shape of any two molecules can be compared by measuring their respective $V_c(q_m)$. The integrated profile of a new molecule can therefore be compared with previous measurements to infer its degree of disorder and/or asphericity. This general framework for interpreting the integrated profile is not restricted to proteins, and may be applied to other macromolecules. The integrated profile can also be used in concert with other measurements to gain a deeper understanding of molecular form and function.

References

- [1] R. P. Rambo, J. A. Tanier, *Nature* **496**, 477 (2013).
- [2] M. C. Watson, J. E. Curtis, *Biophys. J.* **106** (11), 2474 (2014).

Comparison of INAA and LC-ICP-MS for the determination of As species in marine tissues

R. Zeisler,¹ L. L. Yu,¹ R. Oflaz,¹ V. M. O. Carioni,² and C. S. Nomura³

Arsenic (As), a well-known toxic element and proven human carcinogen, remains a major human health concern. It can occur in high concentrations in products used for human consumption, for example as arsenate of geological origin in some drinking waters and organic arsenicals in marine organisms. With the introduction of regulations for As species in foodstuffs and for environmental control, it has become more important to quantify the amount of arsenic species present. To address this concern, new reference materials (RMs) for validation and quality assurance of As speciation measurements are being developed. Initial studies involve a tuna tissue RM developed in Brazil (CRM 1101 Tecido de Atum) [1, 2], a candidate seaweed Standard Reference Material (SRM 3232 Kelp), and several marine certified RMs as controls. The aim of this work is to acquire traceable quantitative results for total As in whole samples and in extracts containing As species. Instrumental neutron activation analysis (INAA) is well suited for such measurements to validate the As mass fraction determined by liquid chromatography combined with inductively coupled plasma mass spectrometry (LC-ICP-MS).

For tuna tissue, INAA was used to determine total As and trace elements in original solids, extracted solids, and in extracts as well as LC fractions; LC-ICP-MS was limited to the determination of As species in extracts. Extracts were used for quantitative As species evaluation with LC-ICP-MS incorporating internal standards and single point standard addition, while the sum of all As fractions was monitored by INAA. Typical results are shown in Table 1 for three certified RMs where excellent agreement with certified values is achieved. Differences between the techniques may be explained by the substantial dilution required by LC-ICP-MS resulting in very low mass fractions of other species in the extracts not being detected, and/or inadvertent blank contributions in INAA.

TABLE 1: Results for certified RMs after ultrasonic bath extraction using acetone/methanol/H₂O (1:1:1). Mass fractions values are for As (not the compound); uncertainties are one standard deviation for DORM-3, DOLT-3 and BCR 627 ($n = 3$), and expanded uncertainties for certified values.

CRM	Extracted As (LC-ICP-MS) (mg/kg)	Extracted As (INAA) (mg/kg)	Remaining As (INAA) (mg/kg)	Total As Calculated (mg/kg)	Certified value for total As (mg/kg)
DORM-3	5.71 ± 1.01	5.58 ± 0.51	1.44 ± 0.01	7.02 ± 0.51	6.88 ± 0.30
DOLT-3	8.10 ± 0.36	8.93 ± 0.22	1.21 ± 0.18	10.13 ± 0.20	10.2 ± 0.5
BCR 627	4.15 ± 0.10*	4.28 ± 0.18	0.47 ± 0.11	4.75 ± 0.17 4.81 ± 0.11**	4.8 ± 0.3

*sum of AB + DMA, measured AB = 3.99 ± 0.08; DMA = 0.148 ± 0.010; certified values: AB = 3.91 ± 0.23; DMA = 0.15 ± 0.02.

**original solid measured by INAA.

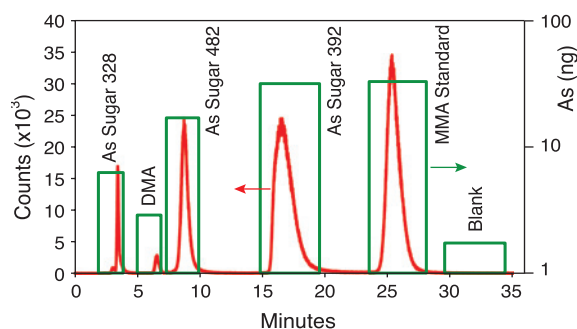


FIGURE 1: LC-ICP-MS chromatogram of kelp extract overlaid with columns indicating the amount of As determined by INAA. The column width represents the collection time from the chromatography column; the height is the mass of As (ng) including blank. Monomethylarsonic acid (MMA) was added as an internal standard.

The measurement of the aforementioned species, mainly the arsenobetaine (AB), plus the dimethyl arsenic acid (DMA) using LC-ICP-MS is widely used and can be considered reliable. Complementing these measurements with INAA for value assignment in an RM delivers validated results. Expanding these measurements to nutritional supplements like seaweed presents a challenge, in part identifying a traceable As species. We selected two widely consumed species of seaweed, laver and kelp, as candidates for the developmental work.

The As species in the seaweeds are assessed with anion exchange LC-ICP-MS. Three major un-identified arsenic species are found in kelp (Fig. 1) and subsequently identified by electrospray ion trap time-of-flight mass spectrometry (ESI-IT-TOF) as As-sugars. The individual fractions shown in the chromatogram are collected, concentrated, and determined by INAA. These INAA results are then used to calibrate the peaks in the LC-ICP-MS chromatogram.

The investigations have laid out a roadmap towards the value assignment and certification of As species in marine tissue and related RMs. Species, including those not available as standards, e.g., the arsenosugars found in kelp, can be accurately determined by INAA and used as calibrants. INAA and LC-ICP-MS thus were successfully used as comparable and complementary techniques for characterization and traceability studies related to the development of RMs for As species.

References

- [1] V. M. O. Carioni, R. Chelegao, J. Naozuka, C.S. Nomura, *Accred. Qual. Assur.* **16**, 453 (2011).
- [2] V. M. O. Carioni, C. S. Nomura, L. L. Yu, R. Zeisler, *J. Radioanal. Nucl. Chem.* **299**, 241 (2014).

¹ Chemical Sciences Division, National Institute of Standards and Technology, Gaithersburg, MD 20899

² Universidade Federal do ABC, Centro de Ciencias Naturais e Humanas, Santo Andre-SP, Brazil

³ Universidade de Sao Paulo, Instituto de Quimica, Sao Paulo-SP, Brazil

Wide-angle polarization analysis with neutron spin filters

T. R. Gentile,¹ Q. Ye,^{1,2} W. C. Chen,^{1,2} S. Watson,¹ J. Anderson,¹ J. Fuller,¹ A. Kirchhoff,¹ R. W. Erwin,¹ Y. Qiu,^{1,2} J. A. Rodriguez-Rivera,^{1,2} C. Broholm,^{1,3} and Y. Nambu⁴

Many neutron experiments would benefit from the capability to perform polarization analysis over a wide range of angles. However, polarization analysis generally yields an order of magnitude or more decrease in data collection rates, making such experiments highly demanding. The Multi-Axis Crystal Spectrometer (MACS) [1], was specifically designed for high neutron flux, but polarization analysis was not part of its original design scope. While neutron spin filters (NSFs) based on nuclear spin-polarized ^3He gas have been routinely applied at the NCNR [2] to small-angle neutron scattering (SANS) and thermal neutron triple-axis spectrometry (TAS) instruments, various technical developments were required to apply NSFs to MACS. Recently all the elements have come together, in particular the unique polarized ^3He cells needed for the 220-degree range of scattering angles on MACS. In April 2014 the first polarized neutron scattering experiment utilizing these wide-angle cells was performed, with the goal of establishing the direction of magnetism in the triangular lattice antiferromagnet NiGa_2S_4 . Here we describe the apparatus for wide-angle polarization analysis [3] and the performance in this first experiment.

Neutron spin filters are based on the spin dependence of the neutron absorption cross section of ^3He gas. An ideal NSF is a volume of ^3He gas in which all the nuclear spins are aligned. Neutrons with spin antiparallel to the ^3He nuclear spin are absorbed by the gas, and for a sufficient thickness of ^3He the transmitted neutron beam is highly polarized. Spin-polarized ^3He gas is produced by optical pumping, which effectively transfers angular momentum from circularly polarized laser light to the ^3He nuclei. An intermediary that absorbs the laser light is required for this transfer, which for our method of spin-exchange optical pumping is provided by an alkali-metal vapor contained within the glass ^3He cell heated to ≈ 490 K. Due to space constraints, the optical pumping is typically done off the beam line, hence the polarization storage time ("relaxation time") is a key parameter. The relaxation time is maximized by using carefully prepared blown glass cells in which depolarization of ^3He on the cell walls is minimized. In addition, a magnetic field with homogeneity of a few parts in 10^4 per cm or better is required to reduce relaxation due to spin flips from transit of ^3He atoms through magnetic field gradients.

Figure 1 shows the polarization analysis apparatus for MACS, with the sample cryostat removed. The neutron beam passes through an end-compensated aluminum-wire solenoid that contains the ^3He cells and the sample and provides a 3 mT uniform magnetic field. The beam passes through a cylindrical polarizer cell and is incident on a sample (not shown) at the center of the solenoid. The polarization of scattered neutrons is analyzed by two cells on either side of the incident beam, each of which covers an angular range of up to

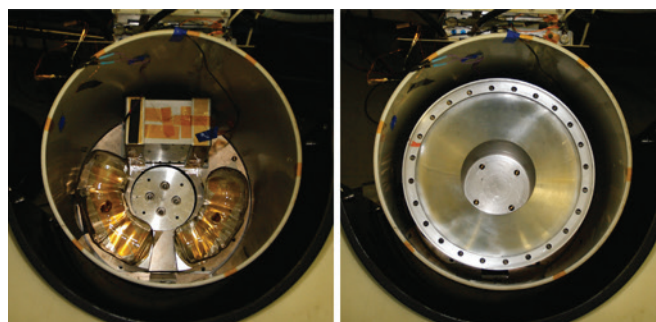


FIGURE 1: Top view of the MACS polarization analysis apparatus. The neutron beam enters from the top of the images, where the MACS pre-sample optics can be seen. The left photo shows the ^3He cells mounted within the 3 mT solenoid; the polarizer cell is contained in the aluminum box. The right photo shows the same view with an aluminum "thimble" that provides a mounting interface for the cryostat and protects the cells.

110 degrees. To control the direction of the incident beam polarization via nuclear magnetic resonance without affecting the analyzer cells, the polarizer cell is contained within a radio-frequency (RF) solenoid surrounded by an RF shielding box. After the polarized cells are installed, the "thimble" shown in the right photo is mounted to the MACS sample stage to receive the sample cryostat.

During the experiment, the typical initial ^3He polarization in both the polarizer and analyzer cells was between 70 % and 80 %. For the 3.7 meV energy of this elastic experiment the typical initial flipping ratio was nearly 30 with roughly an order of magnitude decrease in neutron flux for the desired spin state. Given the intense incident beam on MACS and high ^3He polarization the initial polarized beam flux on the sample was approximately $3 \times 10^7 \text{ cm}^{-2} \text{ s}^{-1}$. The relaxation times of the cells on MACS were between 90 h and 260 h. The polarization in the polarizer cell was routinely flipped with only 0.1 % loss per flip and essentially no effect on the analyzer cells. Measurements of non spin-flip scattering and spin-flip scattering were performed at various temperatures. This allowed separate determination of the components of the elastic magnetic scattering cross section parallel and perpendicular to the solenoid guide field. This successful experiment creates opportunities for a variety of high efficiency polarized inelastic magnetic scattering experiments on MACS.

References

- [1] J.A. Rodriguez-Rivera *et al.*, Meas. Sci. Technol. **19**, 034023 (2008).
- [2] W.C. Chen *et al.*, Journal of Physics: Conference Series **294**, 012003 (2011).
- [3] Q. Ye *et al.*, Physics Procedia **42**, 206-212 (2013).

¹ National Institute of Standards and Technology, Gaithersburg, MD 20899

² University of Maryland, College Park, MD 20742

³ Johns Hopkins University, Baltimore, MD 21218

⁴ Tohoku University, Sendai, Miyagi 980-8577 Japan

Advances in measuring time-resolved neutron scattering from flowing complex fluids

S. A. Rogers, M. A. Calabrese, and N. J. Wagner

Soft materials can undergo time-dependent flows during their production, processing and transportation, as well as during use. The microstructure of soft materials may be significantly different under flow than that at rest. Such flow-induced changes in microstructure may be beneficial, such as reducing the viscosity during the pouring of liquid detergents or transporting fluids while drilling oil and gas wells, or detrimental, such as the degradation of product stability during shipping. Therefore, there is a fundamental need for accurate, time-resolved measurements of microstructure under flow to aid in understanding and controlling the properties of flowing complex fluids.

This report presents new methods for probing microstructural changes on the nanoscale during dynamic deformations using time-resolved small-angle neutron scattering (SANS). Traditional SANS methods provide the necessary structural information on relevant length scales, but are typically averaged in time. With increases in neutron flux on the SANS instruments at the NCNR and through developing more efficient and accurate algorithms for analyzing data from temporally-resolved SANS experiments, we can now uncover previously unknown dynamic behaviors of materials whose static and steady-state flow properties may have been well-understood for decades.

As an example of the new information accessible using time-resolved SANS, we explore the effects of branching on the flow properties of self-assembled micellar solutions. The issue of branching in polymer science is a significant and long-standing scientific and technological challenge and worm-like, or polymer-like micelles are often used as model systems for understanding this class of complex fluids. Time dependent flows, such as flow startup and large amplitude oscillatory shear (LAOS), have been proposed as methods to characterize branching in such systems. We recently developed SANS techniques involving transient flows for the purpose of linking microstructural transitions to the macroscopic flow behavior [1-6].

The branched micellar solutions of interest are composed of the mixed cationic and anionic surfactant cetyltrimethylammonium tosylate (CTAT) and sodium dodecyl benzene sulfonate (SDBS) with sodium tosylate (NaTos) added to induce branching [7]. Under shear flow, segmental alignment of the micelles is observed in the flow direction and is quantified here by the scalar alignment factor, A_f , which varies from 0 for isotropic to 1 for full alignment. Material behavior is especially interesting under LAOS deformations [2, 4], where temporal resolution of ≈ 100 ms can be achieved.

Reported here is an example from our recent study of the alternating state of a branched WLM under LAOS (Fig. 1). Time stamping and triggering capabilities allow the alignment factor to be measured throughout the course of the applied oscillation [4]. A new analysis

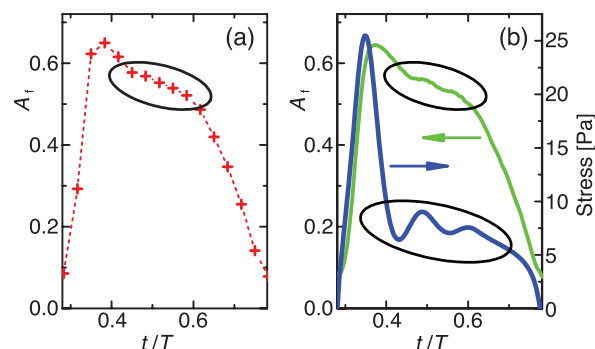


FIGURE 1: The alignment factor for a branched WLM during part of a LAOS cycle: (a) measured using standard binning methods and (b) using the new methods. The new technique (b) resolves features (circled regions) that are not apparent in (a) but that are evident in the rheological stress measurements during LAOS at 0.2 rad/s and 225 strain amplitude.

method that employs signal-processing techniques is applied to the neutron scattering data. We compare the values of A_f obtained from the standard stroboscopic method using binning techniques in Fig. 1a, where 15 discrete points were collected per half period against the same data but analyzed using the new procedure shown in (b). This new analysis provides a nearly continuous curve (b) revealing fine details in the time evolution of A_f (circled region) that closely mimic similar features observed in the rheology, overlaid in Fig 1(b). These microstructural changes are not evident in the data obtained using traditional binning (a). The method also decreases the total measurement time required to achieve a given level of precision as compared to binning methods. Ongoing and future work will use these techniques to quantify the effects of branching on WLM rheology and should find numerous applications in broader studies of the time-dependent behavior of complex fluids and soft materials.

References

- [1] A. P. R. Eberle, L. Porcar, *Curr. Opin. Colloid Int. Sci.* **17** (1), 33 (2012).
- [2] S. A. Rogers, J. Kohlbrecher, M. P. Lettinga, *Soft Matter* **8** (30), 7831 (2012).
- [3] A. K. Gurnon *et al.*, *J. Vis. Exp.* **1** (84), 51068 (2014).
- [4] A. K. Gurnon, C. R. Lopez-Barron, A. P. R. Eberle, L. Porcar, N. J. Wagner, *Soft Matter* **10** (16), 2889 (2014).
- [5] A. K. Gurnon, C. R. Lopez-Barron, M. J. Wasbrough, L. Porcar, N. J. Wagner, *ACS Macro Letters* **3** (3), 276 (2012).
- [6] C. R. Lopez-Barron *et al.*, *Phys. Rev. E* **89** (4), 042301 (2014).
- [7] B. A. Schubert, E. W. Kaler, N. J. Wagner, *Langmuir* **19** (10), 4079 (2003).

Development of a scintillator-based proportional counter for use in a chromatically analyzing neutron detector

N. C. Maliszewskyj,¹ A. N. Osovizky,^{2,3} K. Pritchard,¹ J. Ziegler,¹ Y. Yehuda-Zada,⁴ E. Binkley,¹ and C. F. Majkrzak¹

The Chromatic Analysis Neutron Diffractometer or Reflectometer

(CANDoR) will use a polychromatic incident beam of neutrons and an energy-analyzing bank of detectors to measure a complete reflectivity curve with only a few settings of the instrument. The detector bank consists of 30 independent channels, each consisting of an array of 54 HOPG monochromator crystals oriented at takeoff angles that Bragg diffract neutrons of discrete energies from 5.1 meV (4 Å) to 2.3 meV (6 Å) into corresponding neutron proportional counters. In order to maximize the number of energy analyzing channels and approximate the performance of a conventional ³He tube, the proportional counter must be exceedingly thin (≈ 1 mm), highly efficient (90 % for 3.3 meV (5 Å) neutrons), and have excellent gamma rejection (10^{-7}).

The proportional counter under development uses ⁶LiF:ZnS (Ag) plastic scintillator [1] into which wavelength shifting (WLS) fibers have been embedded. The WLS fibers conduct the scintillation light out of the scattering plane to a silicon photomultiplier (SiPM) for readout (Figs. 1 and 2). Although the photon yield from a neutron capture is quite large (nominally 160,000 photons/neutron capture), a number of factors (opacity of ZnS to its own scintillation light, losses encountered in photon transport, photodetection efficiency of the photosensor) conspire to reduce the signal to a tiny level. Further, the inherent gamma sensitivity of the scintillator and thermally induced avalanches in the photosensor makes neutron discrimination a challenging proposition.

GEANT4 [2] simulations of this system have already pointed to a number of important optimizations to be made in the grain size and stoichiometry of ⁶LiF and ZnS in the scintillator and the arrangement and placement of the WLS fibers in the scintillator.

SEM imaging of scintillator material indicates that LiF and ZnS grains will tend to cluster, effectively creating larger grains than expected. Additionally, optical transmission measurements indicate that adding a 50 % greater proportion of binder to the scintillator composition can result in a nearly fourfold increase in the transmission of scintillation light through the scintillator. We are working

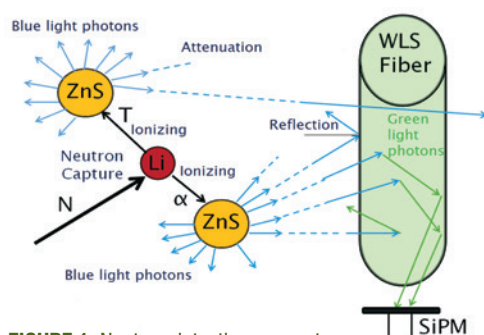


FIGURE 1: Neutron detection concept.

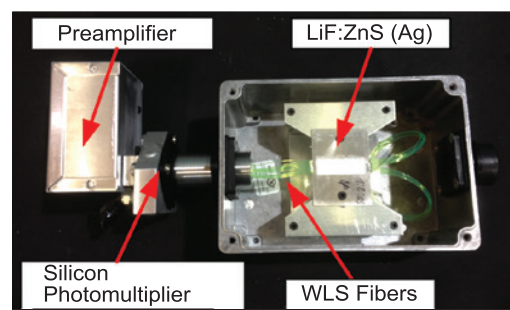


FIGURE 2: A working prototype detector.

actively with scintillator manufacturers to improve the light production and transmission within their product.

Although the ZnS in the scintillator is inherently sensitive to gamma rays, the duration of a burst of photons resulting from gamma capture is very short, on the order of 200 ns, while the duration of a burst of photons resulting from neutron capture is much longer, up to 2 μ s or more. Pulse shape discrimination techniques may then be applied to discard the short, intense bursts resulting from gamma capture or thermally induced noise. By integrating the SiPM in "prompt" (200 ns) and "delayed" (200 ns to 2 μ s) windows and setting thresholds on each it is possible to distinguish neutron capture events from other signals. In the current incarnation of the discriminator, a high speed analog-to-digital converter digitizes the raw signal from the SiPM, which is then processed by the firmware of a field programmable gate array.

Currently, the 1 mm thick prototypes we have tested exhibit 90 % stopping power and 46 % neutron sensitivity at 3.3 meV. The pulse shape discrimination has resulted in excellent gamma rejection (2×10^{-7}) measured using isotopic sources. Indications are that we may be able to increase the sensitivity by optimizing the scintillator composition and WLS configuration, actively cooling the SiPM, and tuning pulse shape discrimination parameters without compromising the geometry of the sensor. Next steps for the project include design and fabricating a prototype analyzer/detector array and scaling up the electronics to manage the signals from that array of 54 proportional counters.

References

- [1] L. A. Wraight *et al.*, Nucl. Instr. Meth. **33**, 181 (1965).
- [2] <http://geant4.web.cern.ch/geant4>

¹ NIST Center for Neutron Research, National Institute of Standards and Technology, Gaithersburg, MD 20899

² University of Maryland, College Park, MD 20742

³ ROTEM Industries Ltd, Beer Sheva, Israel

⁴ Ben Gurion University of the Negev, Beer Sheva, Israel

SLDMOL: A tool for the structural characterization of thermally disordered membrane proteins

J. E. Curtis,¹ H. Zhang,² and H. Nanda^{1,3}

Membrane proteins that interact peripherally or that dwell inside the lipid membranes of our cells are essential to many biological functions, from our ability to detect light, to our immune system recognizing the difference between native cells and foreign invaders, to the regulation of cell division which if unchecked can lead to cancer. X-ray and neutron reflectivity have emerged as powerful tools to study the complex molecular architecture of biological membranes, filling a pressing need for techniques that can characterize proteins in physiological lipid environments. Typical analysis methods of measured specular reflection provide a 1-D scattering length density (SLD) profile normal to the membrane plane that represents the distribution of protein atoms projected along the membrane normal vector. An important advancement in reflectivity analysis has been the integration of high-resolution structural data (e.g. from crystallography or NMR) with reflectivity to yield a 3-D view of how proteins are situated on the membrane [1]. However, for many proteins only partial structural information is available due to large flexible and disordered domains that are not resolved by traditional structural techniques.

We recently developed the SLDMOL [2] program as a tool to facilitate the molecular interpretation of reflectivity results for full-length proteins consisting of structured as well as intrinsically disordered regions. SLDMOL can function either as a fitting utility to determine the ensemble of conformational states that best represents the reflectivity data or as a modeling utility to help design experiments based on selective deuteration and H_2O/D_2O contrast variation. In addition, the incorporation of SLDMOL as a module in the SASSIE [3] software package provides extended capabilities to generate ensembles of proteins structures and filter them based on various structural criteria.

As an example of the fitting module we show its application to NR data collected for the retroviral assembly protein HIV-1 Gag bound to a solid supported tethered lipid membrane [4]. HIV-1 Gag is the single critical factor that drives the formation of new viral particles and is a highly flexible molecule consisting of three structured domains – the matrix (MA), capsid (CA) and nucleocapsid (NC) – joined by unstructured linkers. Fig. 1A shows the experimentally derived SLD profile and the weighted fit using SLDMOL. A density plot of all 100,000 Gag configurations sampled as well as the best-fit subset is shown in Fig. 1B and 1C. The subset of configurations shown in Fig. 1C gave the best fit to the NR data by restricting SLDMOL to use only configurations with $R_g < 70$ Å. Trial deuteration schemes of Gag with either the MA or CA domains labeled can be modeled as shown in

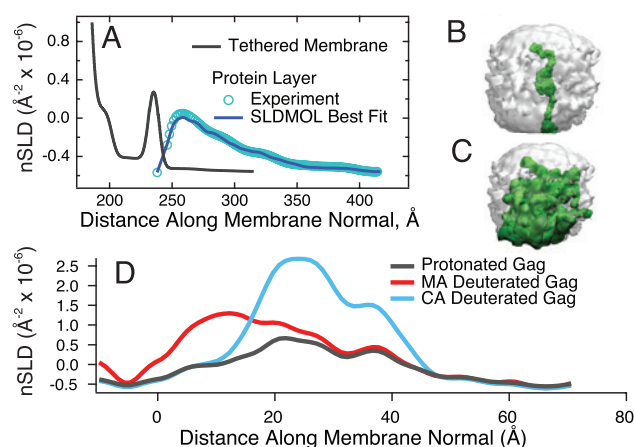


FIGURE 1: Modeling HIV-1 Gag protein bound to a solid supported tethered bilayer. (A): NR experiments were used to determine the 1-D structure of the tethered bilayer (gray line) and the SLD profile of Gag on the membrane (blue circles). SASSIE was used to generate 100,000 independent structures of the Gag protein by varying the backbone dihedrals of the flexible amino acid regions. An average SLD profile using a Monte-Carlo optimization to weight the structures provided a best fit to the data (blue lines). (B) and (C): Overlay of the 3-D density distribution from the entire conformations ensemble of Gag (grey density) with a single extended protein structure (B) and with Gag conformations that best fit to the NR data (C), shown as green density. (D): Modeling deuteration schemes of a compact Gag structure with either the MA or CA domain labeled.

Fig. 1D. The significant difference in the SLD profiles suggests that such a measurement would be able to distinguish the location of each domain along the membrane normal direction.

The SLDMOL program has been developed to fit NR data with detailed 3-D molecular structures of proteins. SLDMOL can easily be used to refine reflectivity measurements of protein structure at any surface or interface. In addition, the modeling facilities of SLDMOL can perform virtual selective deuteration allowing for optimization of experiment design.

References

- [1] H. Nanda *et al.*, Biophys. J. **99**, 2516 (2010).
- [2] J. E. Curtis *et al.*, Comput. Phys. Commun. **183**, 382 (2012).
- [3] J. E. Curtis *et al.*, Comput. Phys. Commun. *in press* (2014).
- [4] S. A. K. Datta *et al.*, J. Mol. Biol. **406**, 205 (2011).

¹ NIST Center for Neutron Research, National Institute of Standards and Technology, Gaithersburg, MD 20899

² California Institute of Technology, Pasadena, CA 91125

³ Carnegie Mellon University, Pittsburgh, PA 15213

Neutron Source Operations

The NCNR neutron source, the 20 MW test reactor (NBSR), operated for 218 days in FY 2014 with a reliability of 93 %. Reliability, as defined by the NCNR, is the ability to deliver neutrons and experimental access for the scientific users on the day scheduled. The NCNR has historically started the facility on schedule and has typically only missed a few days per year of the scheduled experimental cycles due to equipment or other problems. The government-wide shutdown did not have a direct impact on facility operation for experiments because the experimental cycle 613 ended on September 30, 2013 and the government shutdown began the next day. Unfortunately, non-essential reactor maintenance had to be postponed until October 16, which delayed the start of the normal two week maintenance period that must occur between experimental cycles. During the two-week maintenance period, a mechanical problem with the NBSR fuel transfer system prevented loading sufficient reactor fuel for a full 39-day experimental cycle. After a full safety review to consider the off-normal fuel loading, the NBSR was started on October 28 to permit user experiments and to repair the fuel transfer system during the next shutdown period. Repairs to the fuel transfer system were completed in late December, which allowed the NBSR to return to a normal schedule, by February.

During 2014, Reactor Operations and Engineering (ROE) continued the NBSR life extension program by replacing or upgrading older equipment and systems to position the facility to receive an additional 20-year facility license in 2029. One such system was the reactor emergency electrical power systems. The NCNR and NIST are supplied by fairly reliable commercial power, but the NBSR requires backup electrical systems in the event off-site power is lost. Large batteries supply one portion of that backup system and diesel generators supply another portion of the system. The designed reliability and redundancy (two independent battery systems and two independent diesel generators) assure the NBSR critical systems will continue to operate during an unplanned shutdown caused by a loss of site power.



FIGURE 1: NCNR Director Rob Dimeo (left) participating in the IPPAS kick-off meeting along with William Ostendorf (NRC) and Denis Flory (IAEA).

The NCNR participated in an International Physical Protection Advisory Service (IPPAS) assessment in FY 2014. The IPPAS is a program within the IAEA (International Atomic Energy Agency). The IPPAS team reviews and compares security regulations and nuclear facility physical protection systems with international guidelines and best practices. The Nuclear Regulatory Commission and NIST requested the IPPAS assessment, and the NCNR agreed to host a site visit and security posture evaluation. Experts in nuclear facility security from eight member states of the IAEA visited the NCNR and found the facility met or exceeded NRC security requirements and international guidance.

A new project began this year within ROE to consider a possible design for a replacement of the NBSR. Planning continues to relicense the NBSR for another 20 years in 2029, but NCNR management is considering an eventual replacement of the NBSR. The new reactor would be designed to operate using low enriched uranium (LEU) fuel and be optimized for the production of cold neutrons.

Facility Development

Two major relocation projects were completed within the Facility's primary Instrument Development program.

First, the **Neutron Spin Echo** instrument has been relocated from NG-5 to the recently installed NG-A guide. Its location in the new guide hall provides a magnetically quieter experimental area; thus the instrument is now less susceptible to stray magnetic fields. With the move came major investment, upgrading to all new power supplies and a new polarizing cavity, improving both the reliability and sensitivity of the instrument. The instrument has also migrated to the Facility's new data acquisition and instrument control software, NICE, which marks a significant step in the roll-out of this new code. Following a rigorous commissioning program for the new power supplies the instrument is now back in the user program with substantial gains in performance.

Second, one of the **30 m SANS** instruments has also been moved from its long-standing location on NG-3 and reinstalled in the new guide hall. The instrument is now situated on NG-B_{upper}, next to the 10 m SANS, on the second of two low-divergence 50 mm × 50 mm cross-section guides on the new guide network dedicated to the SANS program. Following detailed planning and capitalizing on an extended early-Spring shutdown required for building infrastructure work, the move was completed with minimal impact to the SANS user program. The move has also resulted in significant performance gains for the instrument by virtue of the new guide and from the opportunity to re-align guides in the pre-sample vessel.

The 30 m SANS relocation marked the first step toward installation of the 40 m very Small Angle Neutron Scattering (**vSANS**) instrument at the now vacant NG-3 position. vSANS is one of two new neutron scattering instruments currently under construction at the Facility and will be a highly versatile and unique instrument offering an extended Q -range ($2.0 \times 10^{-4} < Q(\text{\AA}^{-1}) < 0.7$) thus bridging the gap between conventional SANS and uSANS instruments. The design includes both multiple converging pinhole and multiple converging slit geometries and is optimized to take advantage of the current large neutron guide at NG-3, thus offering appropriate intensity for the measurements. A control network has now been established at NG-3 for alignment of the vSANS pre-sample flight path components. The velocity selector bunker and pre-sample vessels are on site and ready for pre-assembly and installation in the coming months.

The second of NCNR's new instruments under development is the white-beam reflectometer **CANDoR**. The instrument will



FIGURE 1: The Neutron Spin Echo spectrometer in its new location on NG-A in the guide hall extension. (Photo credit: Yiming Qiu)



FIGURE 2: Riggers maneuver the 30 m SANS detector vessel from NG-3 to its new location on NG-Bu in the guide hall extension. (Photo credit: Yiming Qiu)

occupy the NG-1 beam line and all pre-sample components have completed designs and are now out for manufacture. CANDoR promises major performance gains by utilizing a polychromatic incident beam of neutrons and an energy analyzing bank of detectors to measure a complete reflectivity curve with only a few settings of the spectrometer. Accordingly the Facility has an on-going scintillator detector development program dedicated to the CANDoR project. Recent developments in this program are described in a highlight earlier in this report.

Neutron Spin Filters

The NCNR supports an active program, operated in collaboration with the Physical Measurement Laboratory at NIST, to provide and develop ^3He neutron spin filters (NSFs) to support measurement capabilities using polarized neutrons. Polarized beam experiments are routinely carried out on the BT-7 thermal neutron triple-axis spectrometer and the small-angle neutron scattering instruments. During the past year, the NCNR's spin filter program serviced 29 user experiments, for a total of 104 days of beam time and 79 bar-liters of polarized ^3He gas.

^3He gas is polarized by spin-exchange optical pumping (SEOP), in which alkali-metal atoms are polarized by optical pumping and the resulting electronic polarization is transferred to ^3He nuclei in spin-exchange collisions. Alkali vapor is produced by heating a boron-free aluminosilicate glass cell containing ^3He , N_2 and a Rb-K mixture metal to 220 °C and illuminating it with near-infrared laser light provided by two or three 100 W diode lasers. Each laser is spectrally narrowed with feedback from a chirped volume holographic grating (VHG). The goal, as always, is to continually improve polarized neutron performance and recent achievements include: fabrication of several large high-pressure cells to meet demands of polarized inelastic experiments on BT-7 with an energy transfer up to 35 meV; fabrication and operation of a large diameter SANS cell that allows users to access magnetic features at higher momentum transfer Q ; successful operation of wide-angle cells for use on the Multi-Axis Crystal Spectrometer (MACS). The success of the wide-angle cells is also highlighted earlier in this report.

Refurbishment of the new ^3He spin filter laboratory has finally been completed and this has enabled an additional SEOP system (SEOP C) to be implemented in the new lab. Motivated by the need to polarize wide-angle analyzer cells for MACS, the new system is equipped with a larger oven and three diode lasers. The system has been commissioned and the higher laser power now enables full polarization of most large-volume cells within a day. This new capability permits more efficient support (about 50 % faster) and better performance of polarized beam experiments. The two existing SEOP systems (SEOP A and SEOP B) will be upgraded to offer a similar capability in the near future.

Data Acquisition Software

The New Instrument Control Environment software package (**NICE**) has been deployed across the suite of reflectometers – MAGIK, PBR, and most recently on the horizontal sample geometry reflectometer on NG-7. A significant project milestone has been achieved with the roll out of NICE on the neutron spin echo spectrometer to meet the complex control requirements of the spectrometer's new power supply system that could not be operated by the legacy software system deployed previously.

NICE is a Java-based package that incorporates a highly versatile scripting capability to enable end user adaptations to be coded under all the major scientific programming languages. Beta-testing of the new code has started on 10 m SANS and on BT-4 in its triple-axis spectrometer configuration.

Data Analysis Software

The Facility is a contributor to the international SANS team working to develop the DANSE/**SASview** software package. SASview utilizes the *bumps* fitting engine that now includes an entropy calculator as a new feature and general developments to the package include uncertainly analysis and support for general-purpose computing on graphics processing units.

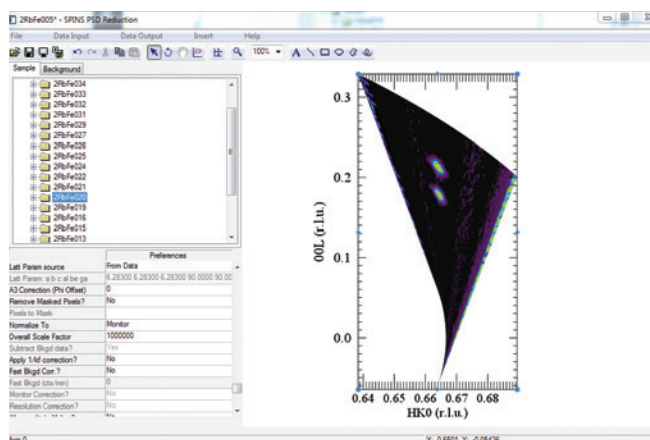


FIGURE 3: The main interface for SPINS PSD Reduction in DAVE. The display window shows a single dataset portraying the intensity as a function of wavevector transfer in the scattering plane defined by the sample orientation vectors.

Development activity continues on the reflectometry analysis package **Ref1d** that originated from the DANSE (Distributed Data Analysis for Neutron Scattering Experiments) project. This package is used by many of our external users to fit their more complicated reflectometry models and a rudimentary graphical user interface has been added to facilitate the input and building of these models.

Facility users of the inelastic neutron scattering instruments at the NCNR require an effective means of quickly reducing, visualizing and analyzing their experiment data. For the last dozen years the Data Analysis and Visualization Environment (**DAVE**) software suite has served as the primary platform through which a large toolset of programs have been compiled and distributed freely to users. The suite is actively maintained in response to feedback from the user community, updated regularly with new functionality and modified as needed to accommodate improvements to neutron scattering instrumentation.

One component that has recently received a major overhaul is the data reduction module for the Spin Polarized Inelastic Neutron Spectrometer (SPINS). This instrument can be operated in several modes. The conventional triple axis mode using a single detector is already handled in the generic Triple Axis Reduction component in DAVE. The new module – SPINS PSD Reduction – handles data taken using the flat but vertically focused multi-crystal analyzer and with the two-dimensional position sensitive detector (PSD). In this mode, the 20 cm x 25 cm PSD detector captures data with 256 individual pixels horizontally while integrating along the vertical direction. Multiple datasets can be reduced simultaneously and the resulting volumetric data can then be manipulated (2D planar slices and 1D cuts) further using Mslice and analyzed using the Peak Fitting module, PAN. The PSD on SPINS is currently underutilized, in part due to a lack of suitable software for interpreting the data. It is hoped that with this addition to DAVE, more users will capitalize on the increased count rate available when SPINS is operated in this mode.

Serving the Science and Technology Community

The mission of the NIST Center for Neutron Research is to assure the availability of neutron measurement capabilities to meet the needs of U.S. researchers from industry, academia and other U.S. government agencies. To carry out this mission, the NCNR uses several different mechanisms to work with participants from outside NIST, including a competitive proposal process, instrument partnerships, and collaborative research with NIST.

Proposal System

Most of the beam time on NCNR instruments is made available through a competitive, peer-review proposal process. The NCNR issues calls for proposals approximately twice a year. Proposals are reviewed at several different levels. First, expert external referees evaluate each proposal on merit and provide us with written comments and ratings. This is a very thorough process where several different referees review each proposal. Second, the proposals are evaluated on technical feasibility and safety by NCNR staff. Third, we convene our Beam Time Allocation Committee (BTAC) to assess the reviews and to allocate the available instrument time. Using the results of the external peer review and their own judgment, the BTAC makes recommendations to the NCNR Director on the amount of beam time to allocate to each approved experiment. Approved experiments are scheduled by NCNR staff members in consultation with the experimenters.

The current BTAC members are:

- Andrew Allen (NIST Ceramics Division)
- Jeffrey Allen (Michigan Technological University)
- Collin Broholm (The Johns Hopkins University)
- Leslie Butler (Louisiana State University)
- Kushol Gupta (University of Pennsylvania)
- Hye-Jung Kang (Clemson University)
- Ramanan Krishnamoorti (University of Houston)
- Valery Kiryukhin (Rutgers University)
- Jennifer Lee (National Institutes of Health)
- Raul Lobo (University of Delaware)
- Janna Maranas (The Pennsylvania State University)
- Steven May (Drexel University)
- Alan Nakatani (Dow Chemical Company)

- Lilo Pozzo (University of Washington)
- Stephan Rosenkranz (Argonne National Laboratory)
- Gila Stein (University of Houston)

Partnerships

The NCNR may form partnerships with other institutions to fund the development and operation of selected instruments. These partnerships, or “Participating Research Teams”, may have access to as much as 75 % of the available beam time on the instrument, depending on the share of total costs borne by the team. A minimum of 25 % of the available beam time is always made available through the NCNR proposal program to all users. Partnerships are negotiated for a fixed period (usually three years) and may be renewed if there is mutual interest and a continued need. These partnerships have proven to be an important and effective way to expand the research community’s access to NCNR capabilities.

Collaboration with NIST

Some time on all instruments is available to NIST staff in support of our mission. This time is used to work on NIST research needs, instrument development, and promoting the widespread use of neutron measurements in important research areas, particularly by new users. As a result of these objectives, a significant fraction of the time available to NIST staff is used collaboratively by external users, who often take the lead in the research. Access through such collaborations is managed through written beam time requests. In contrast to proposals, beam time requests are reviewed and approved internally by NCNR staff. We encourage users interested in exploring collaborative research opportunities to contact an appropriate NCNR staff member.

Research Participation and Productivity

The NCNR continued its strong record of serving the U.S. research community this year. Over the 2014 reporting year, 2271 research participants benefited from use of the NCNR. (Research participants include users who come to the NCNR to use the facility as well as active collaborators, including co-proposers of approved experiments, and co-authors of publications resulting from work performed at the NCNR.) As the number of participants has grown, the number of publications per year has increased in proportion. The quality of the publications has been maintained at a very high level. The trend of the past few

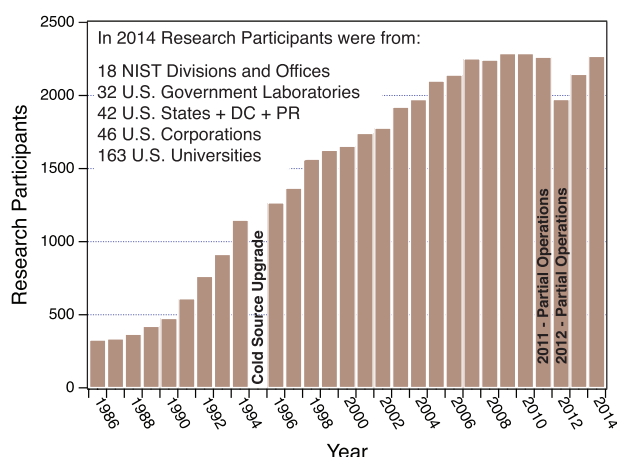


FIGURE 1: Research participants at the NCNR 1986 - 2014.

years, however, suggests that the number of participants and publications is beginning to saturate, as one might expect as the capacity of the facility is reached. Completion of instruments associated with the Expansion Initiative that has taken place over the past few years promises increasing activity and productivity.

2014 NCNR Proposal Program

In response to the last two calls for proposals for instrument time, we received 667 proposals, of which 386 were approved and received beam time. The oversubscription, *i.e.*, the ratio of days requested on all proposals to the days available, was 2.0 on average, but as high as 3.1 for specific instruments. Proposal demand has grown constantly since the NCNR first began accepting proposals in 1991, and has doubled in the past decade. The following table shows the data for several instrument classes.

Instrument class	Proposals	Days requested	Days allocated
SANS and USANS	263	964	461
Reflectometers	97	583	348
Spectrometers	257	1701	761
Diffraction	20	77	56
Imaging	30	146	100
Total	667	3471	1726

Users Group

The NCNR Users Group (NUG) provides an independent forum for all facility users to raise issues to NCNR management, working through its executive officers to carry out this function. The current members of the NUG Executive Committee are Despina Louca (University of Virginia, chair), Kate Gurnon (University of Delaware, student/postdoc member), John Katsaras (Oak Ridge National Laboratory), Michael Mackay (University of Delaware), Alan Nakatani (Dow Chemical), Megan Robertson (University of Houston), and Dale Schaefer (University of Cincinnati).

Panel of Assessment

The major organizational components of NIST are evaluated annually for quality and effectiveness by the National Research Council (NRC), the principal operating agency of both the National Academy of Sciences and the National Academy of Engineering. A panel appointed by the NRC last reported on the NIST Center of Neutron Research in July 2013. The findings are summarized in a document that may be viewed online at <http://www.nist.gov/director/nrc/upload/ncnr-final-report-2013.pdf>. The panel members included Paul Fleury (Yale University), Peter Green (University of Michigan), Laura Greene (University of Illinois), Andrew Harrison (Institut Laue-Langevin), Alan Hurd (U.S. Department of State), Dale Klein (University of Texas), Wade Konze (Dow Chemical Company), Roger Alan Leach (DuPont Central Research and Development), Brian Maple (University of California, San Diego), V. Adrian Parseghian (University of Massachusetts), and David Weitz (Harvard University).

The Center for High Resolution Neutron Scattering (CHRNS)

CHRNS is a national user facility that is jointly funded by the National Science Foundation and the NCNR. Its primary goal is to maximize access to state-of-the-art neutron scattering instrumentation for the research community. It operates six neutron scattering instruments at the NCNR, enabling users from around the nation to observe dynamical phenomena involving energies from ≈ 30 neV to ≈ 100 meV, and to obtain structural information on length scales from ≈ 1 nm to ≈ 10 μ m. A more detailed account of CHRNS activities may be found on pp 61 of this report.

Partnerships for Specific Instruments

NG-7 SANS Consortium

A consortium that includes NIST, the ExxonMobil Research and Engineering Company, and the Industrial Partnership for Research in Interfacial and Materials Engineering (IPRIME) led by the University of Minnesota, operates, maintains, and conducts research at the NG-7 30 m SANS instrument. The consortium uses 57 % of the beam time on this instrument, with the remaining 43 % allocated to the general scientific community through the NCNR's proposal system. Consortium members conduct independent research programs primarily in the area of large-scale structure in soft matter. For example, ExxonMobil has used this instrument to deepen their understanding of the underlying nature of ExxonMobil's products and processes, especially in the fields of polymers, complex fluids, and petroleum mixtures.

The nSoft Consortium

Formed in August 2012, the nSoft Consortium allows member companies to participate with NIST in the development of advanced measurements of materials and manufacturing processes, and develop their own expertise in state-of-the-art

measurement technologies to include in their analytical research programs. nSoft develops new neutron-based measurement science for manufacturers of soft materials including plastics, composites, protein solutions, surfactants, and colloidal fluids. Members receive access to leading expertise and training support in neutron technology and soft materials science at NIST. Contact: Ron Jones, nSoft Director, rljones@nist.gov, 301-975-4624.

NIST / General Motors – Neutron Imaging

An ongoing partnership and collaboration between General Motors and NIST that now includes Honda Motors through GM's partnership with Honda continues to yield exciting results using neutron imaging. Neutron imaging has been employed to visualize the operation of fuel cells for automotive vehicle applications. Neutron imaging is an ideal method for visualizing hydrogen, the fuel of electric vehicle engines. These unique, fundamental measurements provide valuable material characterizations that will help improve the performance, increase the reliability, and reduce the time to market introduction of the next generation electric car engines. 25 % of the time on the BT-2 Neutron Imaging Facility is made available to the general scientific community through peer-reviewed proposals.

Interagency Collaborations

The Smithsonian Institution's Nuclear Laboratory for Archaeological Research is part of the Anthropology Department at the National Museum of Natural History. It has had a productive 35 year partnership with the NCTR, during which time it has chemically analyzed over 43,100 archaeological artifacts by Instrumental Neutron Activation Analysis (INAA), drawing extensively on the collections of the Smithsonian, as well as on those of many other institutions in this country and abroad. Such chemical analyses provide a means of linking these diverse collections together in order to study continuity and change involved in the production of ceramic and other artifacts.

The Center for Food Safety and Applied Nutrition, U.S. Food and Drug Administration (FDA), maintains laboratory facilities at the NCTR providing agency-wide analytical support for food safety and food defense programs. Neutron activation and low-level gamma-ray detection techniques yield multi-element and radiological information about foods and related materials and provide a metrological foundation for FDA's field investigations and for radiological emergency response planning. Current studies include development and validation of swordfish and cocoa powder in-house reference materials, and emergency response/recovery work focuses on measuring cesium levels in soil to study cesium uptake behavior into food products.

Neutron Workshop

The instruments currently under development at the NCNR are nearing completion so planning has begun for the next decade of instrument development. As part of this process, NIST and the University of Maryland co-hosted a workshop on “Neutron Measurements for Materials Design & Characterization” held on August 21st and 22nd, 2014 at the Bolger Center in Potomac, Maryland. More than 100 attendees employed their expertise and experience to help map out the future directions for NCNR instrument development.

This workshop largely built upon the success of the “NCNR Expansion Initiative Workshop” held in July of 2006. Based in part upon the input from the attendees, the NCNR initiated an instrument development plan that addressed the identified research needs of the scientific community at that time. The NCNR will shortly commission the last two instruments identified in this plan: vSANS, a new small-angle neutron scattering instrument that will permit measurements over a very broad range of length scales; and CANDoR, a broad bandwidth reflectometer using energy dispersive detectors enabling high-throughput. After commissioning these instruments there will still be two vacant end positions and possibly two side positions available for additional instruments. The attendees of the recent August workshop were thus tasked with the goals of determining:

- New research opportunities that can be addressed by new capabilities in the NCNR Expansion.
- Neutron measurement capabilities that would open new research opportunities.

To achieve these targets, the attendees were divided into nine breakout groups based on their scientific expertise. Each group provided an oral report at the end of the workshop and a written report shortly thereafter. Rob Briber from the University of Maryland and Collin Broholm from Johns Hopkins University then condensed the various contributions into an executive summary.

This report highlighted the important contributions that neutron scattering has played and continues to play in the development and characterization of new materials that enhance our quality of life. It also called for fully instrumenting the NCNR. To quote the Executive Summary:

With the development of vSANS and CANDoR, the promise of a new D₂ cold source, improvements in many other instruments and new detector technologies, the NCNR will remain one of a small number of leading neutron scattering facilities in the world. There are still open end positions available (one served with thermal neutrons and one with cold neutrons). These



FIGURE 1: Attendees at the August workshop listen attentively to one of the plenary speakers.



FIGURE 2: Members of the Nanostructured Hard Materials breakout group take a brief break from their deliberations.

positions are quite valuable and new instruments should be built at each after a careful evaluation of proposed instrumentation is carried out.

The summary then highlighted several possible choices for instrumenting these open positions including a high throughput powder diffractometer, a new cold triple axis instrument employing the revolutionary detector developed for CANDoR, a new SANS instrument for biological systems, and a substantially upgraded neutron spin echo instrument.

In addition to the improvement in detector technology that will be employed on CANDoR mentioned above, the report also called for concerted efforts: 1) to develop new neutron optics (focusing optics and Wolter optics) to provide high flux neutron beams for all instruments; 2) to continue developing neutron polarization techniques through the use of spin filters based on polarized ^3He and to expand their use to more instruments; 3) to engage the

scientific community in identifying and developing new sample environment systems that extend the variety and range of the fields that can be applied to samples while performing neutron measurements; and to 4) continue to improve the quality of the scientific support infrastructure in terms of lab space for sample preparation, ancillary characterization tools, and high quality data collection, visualization, and analysis software.

The participants at the workshop clearly believe that the NCNR is poised to continue its record of scientific excellence well into the future stating in the conclusion of the Executive Summary:

Through the implementation of the on-going and planned upgrades to the facility and new instrumentation and by following the science outlined by the participants at this workshop, the NCNR will remain a world leader in neutron science for the next decade and beyond.

The Center for High Resolution Neutron Scattering (CHRNA)

The Center for High Resolution Neutron Scattering is a national user facility that is jointly funded by the National Science Foundation through its Division of Materials Research (grant number DMR-0944772) and by the NCNR. The primary purpose of this partnership is to maximize access to state-of-the-art neutron scattering instrumentation for the research community using the NCNR's proposal system. Proposals to use the CHRNA instruments are critically reviewed on the basis of scientific merit and/or technological importance. The core mission of CHRNA is fourfold: (i) to develop and operate neutron scattering instrumentation, with broad application in materials research, for use by the general scientific community; (ii) to promote the effective use of the CHRNA instruments by having an identifiable staff whose primary function is to assist users; (iii) to conduct research that advances the capabilities and utilization of CHRNA facilities; and (iv) to contribute to the development of human resources through educational and outreach efforts.

Scattering Instruments and Research

During FY 2014, CHRNA supported operation of the following instruments: the NG-3 30 m Small Angle Neutron Scattering (SANS) instrument, the Ultra-Small Angle Neutron Scattering (USANS) instrument, the Multi-Angle Crystal Spectrometer (MACS), the Disk Chopper Spectrometer (DCS), the High Flux Backscattering Spectrometer (HFBS), and the Neutron Spin-Echo (NSE) spectrometer. The small angle scattering instruments together provide structural information over length scales from ≈ 1 nm to ≈ 10 μ m. The spectrometers collectively yield dynamical information over time scales from $\approx 3 \times 10^{-14}$ s to $\approx 10^{-7}$ s (energy scales from ≈ 100 meV to ≈ 30 neV). CHRNA users also have access to full polarization-analyzed SANS capabilities via the new double-V SANS polarizer (99 % polarization efficiency) used in conjunction with a radio frequency spin flipper and ^3He spin analyzer cells. These wide ranges of capabilities support a very diverse scientific program, allowing researchers in materials science, chemistry, biology, and condensed matter physics to investigate materials such as polymers, metals, ceramics, magnetic materials, porous media, fluids and gels, and biological molecules.

In the most recent Call for Proposals (call 31), 219 proposals requested CHRNA instruments, and 125 of these proposals received beam time. Of the 1079 days requested for the CHRNA instruments, 551 were awarded. Approximately two-thirds of all proposals received by the NCNR request CHRNA instruments. Publications resulting from experiments on these instruments over the current one-year period are identified in the "Publications"

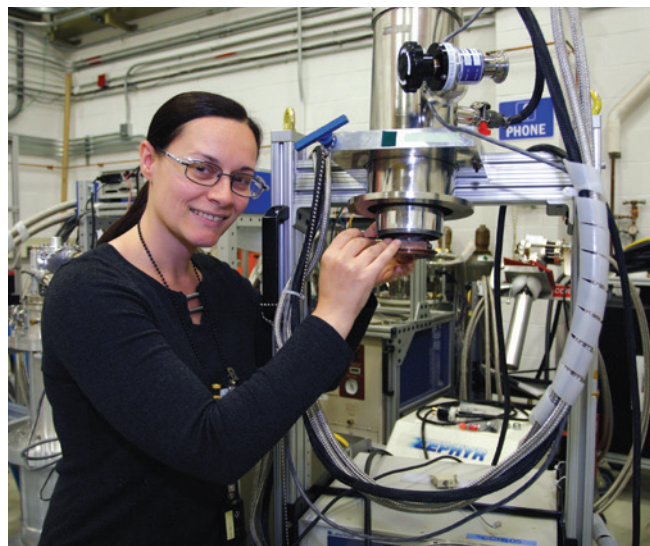


FIGURE 1: Sample Environment Team member Tanya Dax prepares one of the closed cycle refrigerators for a user.

section (p. 66). This report also contains several highlights of CHRNA publications. See the labeled highlights in the table of contents.

Scientific Support Services

CHRNA offers scientific support to our users in two critical areas: sample environment and chemical laboratories.

The laboratory staff ensures that users in our six user laboratories have the equipment and supplies they need for a successful experiment. Moreover, they advise and assist users with sample preparation. During the past year, Stacey Cochiara replaced Kim Tomasi as the primary laboratory support staff. Stacey is continuing the CHRNA tradition of working closely with our users to provide them with the items they need so that they can concentrate on their science rather than instrumental details.

The majority of CHRNA users apply external fields to their samples. The CHRNA Sample Environment team operates and maintains the equipment needed to make neutron measurements under conditions of temperature, pressure, magnetic and electric fields, and fluid flow. This year we commissioned two high-temperature closed-cycle refrigerators (CCR). The new CCRs' temperature range extends from 15 K to 800 K, a wider range than previously available.



FIGURE 2: Participants and instructors in the NCNR 2014 Summer School “Methods and Applications of Small Angle Neutron Scattering and Neutron Reflectometry.”

Education and Outreach

This year the Center for High Resolution Neutron Scattering sponsored a variety of educational programs and activities tailored to specific age groups and professions. The annual summer school, held on July 13 - 18, 2014 was entitled “Methods and Applications of Small Angle Neutron Scattering and Neutron Reflectometry.” Thirty-five graduate and postdoctoral students from 29 universities participated in the school. Course evaluations and student feedback was very positive.

As part of its education and outreach effort, CHRS offers to university-based research groups with BTAC-approved proposals the opportunity to request travel support for an additional graduate student to participate in the experiment. Announcements of this program are sent to all of the university groups whose experimental proposals receive beam time from the BTAC. The program is also advertised on the NCNR’s website at <http://www.ncnr.nist.gov/outreach.html>.

For more than a year we have been fortunate to host Prof. Kimani Stancil at the NCNR via a cooperative research agreement with Howard University in Washington, DC. Prof. Stancil and his students spend their summers at the NCNR performing research on the structure of soft matter using SANS. They continue to work on these projects during the school year, as time permits. The success of this arrangement lays the groundwork for similar arrangements with professors from other minority serving institutions.

As in previous years, CHRS participated in NIST’s Summer Undergraduate Research Fellowship (SURF) program. In 2014 CHRS hosted 15 SURF students. The students made considerable contributions on research projects such as rheological flow of micelles and surfactants, magnetic ground state determination for thin-film industrial sensors, dynamics of methanol/water mixtures, gas adsorption in metal-organic frameworks, enhanced fitting engines for diffraction data refinement, and reactor control systems development. Students presented the results of their research at the NIST SURF colloquium in early August 2014.



FIGURE 3: The 2014 SURF students with NCNR director Rob Dimeo (right), CHRS director Dan Neumann (second from left), and chief of reactor operations Sean O’Kelly (left).



FIGURE 4: The 2014 high school interns with CHRNS director Dan Neumann (fourth from right).

Elementary, Middle, and High School Activities

The Summer High School Intern Program (SHIP) has been a very successful, competitive NIST-wide program for students who are interested in performing scientific research during the summer. This year, the NCNR staff hosted seven high school interns. The students participated on research projects such as developing methodologies for imaging thin-film batteries and fuel cells, Monte Carlo simulation for anti-neutrino detector shielding, web-based data fitting, and model analysis of two-dimensional SANS data. The results of the students' summer investigations were highlighted in a NIST-wide poster session in early August, as well as in an oral symposium at the NCNR. The success of the high school students is exemplified by the accomplishments of one of the 2013 SHIP students, André Guzmán from Poolesville High School, who received 2nd place in high school physics at the Montgomery County Science Fair as well as the Robert H. Herndon Award that is intended to encourage minority students to pursue careers in science and engineering.

The NCNR initiated a Research Experiences for Teachers (RET) program in the summer of 2010. Northwest High School teacher Richard Menendez (Montgomery County, MD) was selected

for the program for the summer of 2014. He collaborated with NCNR's Chris Bertrand and Koty McAllister, an undergraduate from the University of Delaware, on a project involving reversible colloidal aggregation in a near critical binary mixture.

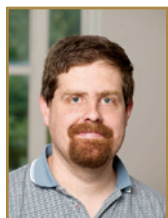
The annual Summer Institute for Middle School Science Teachers brings middle school science teachers from across the United States (and for the first time, from American Samoa) to NIST for two weeks. Each year, CHRNS hosts the teachers for a one-day introduction to neutron scattering. Having toured the neutron guide hall and having seen several neutron instruments, the teachers learn about the types of experiments performed at the NCNR. To bring home projects suitable for middle school students, teachers then learn how to grow crystals of alum (hydrated aluminum potassium sulfate). Throughout the day and at lunchtime, the teachers have the opportunity to interact with NCNR staff.

CHRNS also hosts a variety of other educational activities for K-12 students including tours (more than 20 in the last year), "Take Your Daughters and Sons to Work Day", and "Adventures in Science", a hands-on science program for middle school students.

2014 Awards



Prof. Peter Dowding from Infineum UK Limited has received the **Inspiration and Industry Award** for 2014 from the Royal Society of Chemistry, "For his contribution to enthusing university students about research and colloid science." Peter is a frequent NCNR user.



Tyrel M. McQueen Assistant Professor of Chemistry, Johns Hopkins University has been awarded a **Cottrell Scholar Award** from the Research Corporation for Science Advancement for his research "Superconductivity: From Discovery to Rational Design." Tyrel often uses the NCNR facility for his work.



Kate Gurnon won a **poster session award** at the 9th Annual European Rheology Conference, April 2014, held in Karlsruhe, Germany for her poster titled: "Spatiotemporal stress and microstructure evolution in dynamically sheared wormlike micellar solutions using rheo- and flow-SANS."



At the ACNS meeting in Knoxville, TN, June 2014, **Doug Godfrin** won an **ACNS student prize** for his poster entitled: "Scattering study of reversible cluster formation in concentrated monoclonal antibody formulations" Doug is a graduate student at the University of Delaware stationed at the NCNR.



Thomas H. Epps, III of the University of Delaware received **Sigma Xi's Young Investigator Award** for 2014 at their Annual Meeting held in Arizona, November 2014. He is the Thomas and Kipp Gutshall Associate Professor of Chemical and Biomolecular Engineering with a joint appointment in Materials Science. Thomas was recognized for his growing influence in the field of polymer physics where he designs, synthesizes, and characterizes new polymeric materials. Thomas has been a frequent NCNR facility user during his research.



Chetan Dital of Boston College received the 2013-2014 **Outstanding Dissertation in Magnetism Award** from the APS Topical Group on Magnetism and its Applications (GMAG) for his dissertation: "Electronic Phase Separation and Magnetic Phase Behavior in the Ru-doped Spin-Orbit Mott Insulator $\text{Sr}_3\text{Ir}_2\text{O}_7$." These awards recognize students who have conducted outstanding research leading to their dissertation.



Kate Ross of the NCNR has been awarded the 2014 **NSSA Prize for Outstanding Student Research** by the Neutron Scattering Society of America. Kate was recognized "For seminal neutron scattering studies of exotic ground states, ground state selection, and spin excitations in XY pyrochlore magnets."



Sushil Satija of the NCNR has been named as an **NSSA Fellow** for 2014 for "significant contributions to the advancement of the understanding of the physics of polymers at surfaces and interfaces through the development and innovative application of neutron reflectometry."



The NCNR's **Jeffrey Lynn** has been listed as one of the "**World's Most Influential Scientific Minds**" by Thomson Reuters, the publisher of the Web of Science. This recognition is based on Thomson Reuters' analysis of citations over the decade 2002-2012. Jeff is one of 144 scientists listed in the category of Physics. In addition, more than 40 of the scientists on the various lists have participated in research at the NCNR over the past five years.

Jeff Lynn has also been awarded the 2014 **NSSA Sustained Research Prize** by the Neutron Scattering Society of America. The award recognizes his "seminal studies of the colossal magneto-resistance effect and profound contributions to our understanding of the interplay of magnetism and superconductivity."



Wan Si Tang of the NCNR won a **student poster award** for her poster titled: "Altering the Structural Properties of $A_2B_{12}H_{12}$ Compounds via Cation and Anion Modifications" presented at the 14th International Symposium on Metal-Hydrogen Systems held in Manchester, UK, in July 2014.



NCNR's **Yun Liu** received the 2014 NIST-Sigma Xi **Katharine B. Gebbie Young Investigator Award**. Yun is being recognized "For the discovery of dynamic cluster ordering in complex colloidal systems."



NCNR's **Daniel Hughes** received the **NIST Bronze Medal** in December 2013. Dan was recognized "For outstanding oversight and coordination of all operational activities associated with the facility outage during the NCNR expansion project."



Rana Ashkar of the NCNR and the University of Maryland has been selected as the winner of the **Esther L. Kinsley Ph.D. Dissertation Award** for 2013-2014 for her dissertation, "Dynamical Theory Applications to Neutron Scattering from Periodic Nanostructures" This is the highest honor for research that Indiana University bestows upon its graduate students.



A **NIST Bronze Medal** was awarded to the NCNR's **Paul Liposky** in December 2013. Paul was recognized "For his innovative design and management of the NIST reactor spent-fuel storage pool refurbishment project."



The NCNR's **Shannon Watson** won the **best poster award** at the Polarized Neutrons for Condensed Matter Investigations conference. Her poster was titled "Magnetostatic cavity advancements for ^3He spin filters at the NCNR." The conference was held in September 2014 in Sydney, Australia.



NCNR's **Rachel Pollock** received the award for "**Most Outstanding Poster**" in the category of Materials for her poster titled "Kinetic Trapping of D_2 in Mil-53(Al) Observed Using Neutron Scattering" at the annual Sigma Xi Post-doc poster presentation.



The **Samuel Wesley Stratton Award** has been presented to the NCNR's **Qingzhen Huang, Jeffrey Lynn, and Taner Yildirim**. The group is recognized "for their unusually significant research contributions concerning the origins of superconductivity in the new iron-based superconducting materials. Arguably the most important question in all of materials physics today concerns the origin of the electron pairing mechanism in high-TC superconductors." The Samuel Wesley Stratton Award, first presented in 1962, is granted for outstanding scientific or engineering achievements in support of NIST objectives.



Andrew Yue of NIST's Radiation Physics Division received the award for "**Most Outstanding Poster**" in the category of Physics for his poster titled "Improved Determination of the Neutron Lifetime" at the annual Sigma Xi Post-doc poster presentation.



Charles Majkrzak of the NCNR has received the **Allen V. Astin Award**. The award citation (in part) recognizes Chuck for "his numerous and seminal contributions to the measurement science and applications of neutron reflectivity. He has pioneered the exploration of many issues in "interface" science using this powerful technique, which has driven enormous advances in a huge range of scientific and technological areas." The Allen V. Astin Measurement Science Award, first presented in 1984, is granted for outstanding achievement in the advancement of measurement science or in the delivery of measurement services.

Publications: August 1, 2013 to July 31, 2014

- Abakumov, A.M., Tsirlin, A.A., Bakaimi, I., Van Tendeloo, G., Lappas, A., "Multiple Twinning as a Structure Directing Mechanism in Layered Rock-Salt-Type Oxides: NaMnO_2 Polymorphism, Redox Potentials, and Magnetism," *Chem. Mater.* **26**, 3306 (2014).
- Ahart, M., DeVreugd, C., Li, J., Viehland, D., Gehring, P.M., Hemley, R.J., "X-ray Diffraction Study of the Pressure-Induced bcc-to-hcp Phase Transition in the Highly Magnetostrictive $\text{Fe}_{0.81}\text{Ga}_{0.19}$ Alloy," *Phys. Rev. B* **88**(18), 184102 (2013).
- Akgun, B., Satija, S., Nanda, H., Pirrone, G.F., Shi, X., Engen, J.R., Kent, M.S., "Conformational Transition of Membrane-Associated Terminally Acylated HIV-1 Nef," *Structure* **21**, 1822 (2013).
- Alberca, A., Nemes, N.M., Mompean, F.J., Fehér, T., Simon, F., Tornos, J., Leon, C., Munuera, C., Kirby, B.J., Fitzsimmons, M.R., Hernando, A., Santamaria, J., Garcia-Hernandez, M., "Magnetoelastic Coupling in $\text{La}_{0.7}\text{Ca}_{0.3}\text{MnO}_3/\text{BaTiO}_3$ Ultrathin Films," *Phys. Rev. B* **88**(13), 134410 (2013).
- Alberca, A., Azpeitia-Urkia, J., Tornos, J., Munuera, C., Mompean, F.J., Nemes, N.M., Leon, C., Hernando, A., Fehér, T., Simon, F., Kirby, B.J., Fitzsimmons, M.R., Santamaria, J., Garcia-Hernandez, M., "Magnetoelastic Coupling in Strained $\text{La}_{0.7}\text{Ca}_{0.3}\text{MnO}_3/\text{BaTiO}_3$ Thin Films," *Mater. Res. Soc. Symp. P.* **1587** (2013).
- Alsmadi, A.M., Choi, Y., Keavney, D.J., Eid, K.F., Kirby, B.J., Liu, X., Leiner, J., Tivakornsasithorn, K., Dobrowolska, M., Furdyna, J.K., "Interfacial Exchange Coupling in $\text{Fe}(\text{Ga,Mn})\text{As}$ Bilayers," *Phys. Rev. B* **89**(22), 224409 (2014).
- Alves, L.M.S., de Lima, B.S., dos Santos, C.A.M., Rabello, A., Masunaga, S.H., Neumeier, J.J., Leão, J.B., "Phase Transitions in K-Doped MoO_2 ," *J. Appl. Phys.* **115**(20), 204912 (2014).
- Asada, M., Jiang, N., Sendogdular, L., Sokolov, J., Endoh, M.K., Koga, T., Fukuto, M., Yang, L., Akgun, B., Dimitriou, M., Satija, S., "Melt Crystallization/Dewetting of Ultrathin PEO Films via Carbon Dioxide Annealing: the Effects of Polymer Adsorbed Layers," *Soft Matter*, in press.
- Bakaimi, I., Abakumov, A., Green, M.A., Lappas, A., "Crystal, Magnetic and Dielectric Studies of the 2D Antiferromagnet: $\beta\text{-NaMnO}_2$," in "Proc. of SPIE," edited by Teherani, F.H., Look, D.C., Rogers, D. J., (Oxide-based Materials and Devices V, January 2014, San Francisco, CA) **8987**, 898716 (2014).
- Baldasseroni, C., Pålsson, G.K., Bordel, C., Valencia, S., Unal, A.A., Kronast, F., Nemsak, S., Fadley, C.S., Borchers, J.A., Maranville, B.B., Hellman, F., "Effect of Capping Material on Interfacial Ferromagnetism in FeRh Thin Films," *J. Appl. Phys.* **115**(4), 043919 (2014).
- Bañuelos, J.L., Feng, G., Fulvio, P.F., Li, S., Rother, G., Arend, N., Faraone, A., Dai, S., Cummings, P.T., Wesolowski, D.J., "The Influence of a Hierarchical Porous Carbon Network on the Coherent Dynamics of a Nanoconfined Room Temperature Ionic Liquid: A Neutron Spin Echo and Atomistic Simulation Investigation," *Carbon*, in press. [CHNRN]
- Barin, G., Krungleviciute, V., Gomez-Gualdrón, D.A., Sarjeant, A.A., Snurr, R.Q., Hupp, J.T., Yildirim, T., Farha, O.K., "Isorecticular Series of (3,24)-Connected Metal-Organic Frameworks: Facile Synthesis and High Methane Uptake Properties," *Chem. Mater.* **26**, 1912 (2014).
- Barin, G., Krungleviciute, V., Gutov, O., Hupp, J.T., Yildirim, T., Farha, O.K., "Defect Creation by Linker Fragmentation in Metal-Organic Frameworks and Its Effects on Gas Uptake Properties," *Inorg. Chem.* **53**, 6914 (2014).
- Baroudi, K., Yim, C., Wu, H., Huang, Q., Roudebush, J.H., Vavilova, E., Grafe, H.-J., Kataev, V., Buechner, B., Ji, H., Kuo, C., Hu, Z., Pi, T.-W., Pao, C., Lee, J., Mikhailova, D., Tjeng, L.H., Cava, R.J., "Structure and Properties of $\alpha\text{-NaFeO}_2$ -Type Ternary Sodium Iridates," *J. Solid State Chem.* **210**, 195 (2014).
- Basavaraj, M.G., McFarlane, N.L., Lynch, M.L., Wagner, N.J., "Nanovesicle Formation and Microstructure in Aqueous Ditalloethylesterdimethylammonium Chloride (DEEDMAC) Solutions," *J. Colloid Interf. Sci.*, in press. [CHNRN]
- Basden, M., Eldridge, R.B., Farone, J., Feng, E., Hussey, D.S., Jacobson, D.L., "Liquid Holdup Profiles in Structured Packing Determined via Neutron Radiography," *Ind. Eng. Chem. Res.* **52**, 17263 (2013).

- Beers, K.M., Wong, D.T., Jackson, A.J., Wang, X., Pople, J.A., Hexemer, A., Balsara, N.P., "Effect of Crystallization on Proton Transport in Model Polymer Electrolyte Membranes," *Macromolecules* **47**, 4330 (2014).
- Beers, K.M., Yakovlev, S., Jackson, A., Wang, X., Hexemer, A., Downing, K.H., Balsara, N.P., "Absence of Schroeder's Paradox in a Nanostructured Block Copolymer Electrolyte Membrane," *J. Phys. Chem. B* **118**, 6785 (2014).
- Berk, N.F., "Determination of the Effect Transverse Coherence of the Neutron Wave Packet as Employed in Reflectivity Investigations of Condensed-Matter Structures. II. Analysis of Elastic Scattering using Energy-Gated Wave Packets with an Application to Neutron Reflection from Ruled Gratings," *Phys. Rev. A* **89**(3), 033852 (2014).
- Bishop, R.L., "Instrumental Approaches to Understanding Mesoamerican Economy: Elusive Promises," *Ancient Mesoamerica* **25**(1), 251 (2014).
- Blanco, M.A., Perevozchikova, T., Martorana, V., Manno, M., Roberts, C.J., "Protein-Protein Interactions in Dilute to Concentrated Solutions: α -Chymotrypsinogen in Acidic Conditions," *J. Phys. Chem. B* **118**(22), 5817 (2014).
- Bloch, E.D., Hudson, M.R., Mason, J.A., Chavan, S., Crocellà, V., Howe, J.D., Lee, K., Dzubak, A.L., Queen, W.L., Zadrozny, J.M., Geier, S.J., Lin, L.-C., Gagliardi, L., Smit, B., Neaton, J.B., Bordiga, S., Brown, C.M., Long, J.R., "Reversible CO Binding Enables Tunable Co/H₂ and CO/N₂ Separations in Metal-Organic Frameworks with Exposed Divalent Metal Cations," *J. Am. Chem. Soc.* **136**, 10752 (2014).
- Brand, P.C., Norbedo, A.J., Sprenger, G.S., "NIST Reactor Solves Operational Nuisance Problem using Novel Application of Vacuum Transfer Technology," in "IGORR 15," (IGORR 15, September 2013, Daejeon, Korea) (2013).
- Brown, C.M., Ramirez-Cuesta, A.J., Johnson, M.R., García Sakai, V., "Chemical Spectroscopy using Neutrons," *Chem. Phys.* **427**, 1 (2013).
- Brown, C.M., Ramirez-Cuesta, A.J., Her, J.-H., Wheatley, P.S., Morris, R.E., "Structure and Spectroscopy of Hydrogen Adsorbed in a Nickel Metal-Organic Framework," *Chem. Phys.* **427**, 3 (2013).
- Brown, P., Wasbrough, M.J., Gurkan, B.E., Hatton, T.A., "CO₂-Responsive Microemulsions Based on Reactive Ionic Liquids," *Langmuir* **30**, 4267 (2014). [CHRS]
- Buss, H.L., Brantley, S.L., Scatena, F.N., Bazilievskaya, E.A., Blum, A., Schulz, M., Jiménez, R., White, A.F., Rother, G., Cole, D., "Probing the Deep Critical Zone Beneath the Luquillo Experimental Forest, Puerto Rico," *Earth Surf. Proc. Land.* **38**(10), 1170 (2013). [CHRS]
- Cabrera, I., Thompson, J.D., Coldea, R., Prabhakaran, D., Bewley, R.I., Guidi, T., Rodriguez-Rivera, J.A., Stock, C., "Excitations in the Quantum Paramagnetic Phase of the Quasi-One-Dimensional Ising Magnet CoNb₂O₆ in a Transverse Field: Geometric Frustration and Quantum Renormalization Effects," *Phys. Rev. B* **90**(1), 014418 (2014). [CHRS]
- Cai, J., Rao, X., He, Y., Yu, J., Wu, C., Zhou, W., Yildirim, T., Chen, B., Qian, G., "A Highly Porous NbO Type Metal-Organic Framework Constructed from an Expanded Tetracarboxylate," *Chem. Commun.* **50**, 1552 (2014).
- Cardiel, J.J., Tonggu, L., de la Iglesia, P., Zhao, Y., Pozzo, D.C., Wang, L., Shen, A.Q., "Flow-Induced Structured Phase in Nonionic Micellar Solutions," *Langmuir* **29**, 15485 (2013). [CHRS]
- Cardiel, J.J., Tonggu, L., Dohnalkova, A.C., de la Iglesia, P., Pozzo, D.C., Wang, L., Shen, A.Q., "Worming Their Way into Shape: Toroidal Formations in Micellar Solutions," *ACS Nano* **7**(11), 9704 (2013). [CHRS]
- Carioni, V.M.O., Nomura, C.S., Yu, L.L., Zeisler, R., "Use of Neutron Activation Analysis and LC-ICP-MS in the Development of Candidate Reference Materials for As Species Determination," *J. Radioanal. Nucl. Chem.* **299**, 241 (2014).
- Carlson, A.D., Pronyaev, V.G., Capote, R., Hamsch, F.-J., Käppeler, F., Lederer, C., Mannhart, W., Mengoni, A., Nelson, R.O., Plompen, A.J.M., Schillebeeckx, P., Simakov, S., Talou, P., Tagesen, S., Vonach, H., Vorobyev, A., Wallner, A., "Improvements and Extensions of the Neutron Cross Section and Fluence Standards," *Nucl. Data Sheets* **118**, 126 (2014).
- Carr, S.V., Louca, D., Siewenie, J., Huang, Q., Wang, A., Chen, X., Dai, P., "Structure and Composition of the Superconducting Phase in Alkali Iron Selenide K_yFe_{1.6+x}Se₂," *Phys. Rev. B* **89**(13), 134509 (2014).
- Castellanos, M.M., Pathak, J.A., Leach, W., Bishop, S.M., Colby, R.H., "Explaining the Non-Newtonian Character of Aggregating Monoclonal Antibody Solutions using Small-Angle Neutron Scattering," *Biophys. J.* **107**, 469 (2014).
- Chapman, K.W., Chupas, P.J., Long, G.G., Bendersky, L.A., Levine, L.E., Mompou, F., Stalick, J.K., Cahn, J.W., "An Ordered Metallic Glass Solid Solution Phase that Grows from the Melt like a Crystal," *Acta Mater.* **62**, 58 (2014).
- Chatterjee, T., Nakatani, A.I., Van Dyk, A.K., "Shear-Dependent Interactions in Hydrophobically Modified Ethylene Oxide Urethane (HEUR) Based Rheology Modifier-Latex Suspensions: Part 1. Molecular Microstructure," *Macromolecules* **47**, 1155 (2014).

- Chen, H., Hsiao, Y.-C., Hu, B., Dadmun, M., "Control of Morphology and Function of Low Band Gap Polymer-Bis-Fullerene Mixed Heterojunctions in Organic Photovoltaics with Selective Solvent Vapor Annealing," *J. Mater. Chem. A* **2**, 9883 (2014). [CHNRNS]
- Chen, H., Hsiao, Y.-C., Hu, B., Dadmun, M., "Tuning the Morphology and Performance of Low Bandgap Polymer: Fullerene Heterojunctions via Solvent Annealing in Selective Solvents," *Adv. Funct. Mater.*, in press. [CHNRNS]
- Chen, J., Wang, F., Huang, Q., Hu, L., Song, X., Deng, J., Yu, R., Xing, X., "Effectively Control Negative Thermal Expansion of Single-Phase Ferroelectrics of PbTiO_3 -(Bi,La) FeO_3 over a Giant Range," *Sci. Rep.* **3**, 2458 (2013).
- Chen, J., Wu, H., Wu, G., Xiong, Z., Wang, R., Fan, H., Zhou, W., Liu, B., Chua, Y., Ju, X., Chen, P., "Lithiated Primary Amine-A New Material for Hydrogen Storage," *Chem.-Eur. J.* **20**, 6632 (2014).
- Chen, W.C., Gentile, T.R., Erwin, R., Watson, S., Ye, Q., Krycka, K.L., Maranville, B.B., " ^3He Spin Filter Based Polarized Neutron Capability at the NIST Center for Neutron Research," in "Journal of Physics: Conference Series," edited by Ioffe, A., (International Workshop on Neutron Optics and Detectors, June 2013, Munich, Germany) **528**, 012014 (2014). [CHNRNS]
- Chen, W.C., Gentile, T.R., Ye, Q., Walker, T.G., Babcock, E., "On the Limits of Spin-Exchange Optical Pumping of ^3He ," *J. Appl. Phys.* **116**(1), 014903 (2014).
- Cheng, G., Hammouda, B., Perahia, D., "Polystyrene-Block-Polyisoprene Diblock-Copolymer Micelles: Coupled Pressure and Temperature Effects," *Macromol. Chem. Phys.* **215**(8), 776 (2014). [CHNRNS]
- Cheng, G., Hammouda, B., Perahia, D., "Effects of Intermicellar Interactions on the Dissociation of Block Copolymer Micelles: SANS and NMR Studies," *Macromol. Chem. Phys.* **215**(4), 341 (2014). [CHNRNS]
- Chiang, N., Cicerone, M.T., Zhong, Q.N., Liu, M., Pikal, M.J., "Characterization of Dynamics in Complex Lyophilized Formulations: II. Analysis of Density Variations in Terms of Glass Dynamics and Comparisons with Global Mobility, Fast Dynamics, and Positron Annihilation Lifetime Spectroscopy (PALS)," *Eur. J. Pharm. Biopharm.* **85**, 197 (2013). [CHNRNS]
- Choi, J., Hore, M.J.A., Clarke, N., Winey, K.I., Composto, R.J., "Nanoparticle Brush Architecture Controls Polymer Diffusion in Nanocomposites," *Macromolecules* **47**, 2404 (2014).
- Chua, Y.S., Pei, Q., Ju, X., Zhou, W., Udovic, T.J., Wu, G., Xiong, Z., Chen, P., Wu, H., "Alkali Metal Hydride Modification on Hydrazine Borane for Improved Dehydrogenation," *J. Phys. Chem. C* **118**, 11244 (2014).
- Chung, J.-H., Song, Y.-S., Kim, J.-H., Suzuki, T., Katsufuji, T., Matsuda, M., Lee, S.-H., "Dynamic Spin Correlations in the Frustrated Cubic Phase of MnV_2O_4 ," *Phys. Rev. B* **88**(9), 094430 (2013).
- Clark, N.J., Raththagala, M., Wright, N.T., Buenger, E.A., Schilbach, J.F., Krueger, S., Curtis, J.E., "Structures of Tral in Solution," *J. Mol. Model.* **20**, 23208 (2014). [CHNRNS]
- Clark, N.J., Zhang, H., Krueger, S., Lee, H.J., Ketchum, R.R., Kerwin, B., Kanapuram, S.R., Treuheit, M.J., McAuley, A., Curtis, J.E., "Small-Angle Neutron Scattering Study of a Monoclonal Antibody using Free-Energy Constraints," *J. Phys. Chem. B* **117**, 14029 (2013). [CHNRNS]
- Coakley, K.J., Vecchia, D.F., Hussey, D.S., Jacobson, D.L., "Neutron Tomography of a Fuel Cell: Statistical Learning Implementation of a Penalized Likelihood Method," *IEEE T. Nucl. Sci.* **60**(5), 3945 (2013).
- Cook, J.C., "Concepts and Engineering Aspects of a Neutron Resonance Spin-Echo Spectrometer for the National Institute of Standards and Technology Center for Neutron Research," *J. Res. Natl. Inst. Stan.* **119**, 55 (2014).
- Couet, A., Motta, A.T., Comstock, R.J., "Hydrogen Pickup Measurements in Zirconium Alloys: Relation to Oxidation Kinetics," *J. Nucl. Mater.*, in press.
- Crawford, B.E., Anderson, E., Barrón-Palos, L., Bass, C.D., Bass, T.D., Fry, J., Gan, K., Haddock, C., Heckel, B.R., Luo, D., Malone, R.C., Markoff, D.M., Micherdzinska, A.M., Mumm, H.P., Nico, J.S., Oppen, A.K., Penn, S., Santra, S., Sarsour, M., Sharapov, E.I., Snow, W.M., Swanson, H.E., Van Sciver, S., Walbridge, S.B., Yan, H., Zhumabekova, V., "Parity-Violating Neutron Spin-Rotation Measurements at NIST," in "International Seminar on Interactions with Nuclei," (International Seminar on Interactions with Nuclei, May 2013, Alushta, Ukraine), in press.
- Creuziger, A., Hu, L., Gnäupel-Herold, T., Rollett, A.D., "Crystallographic Texture Evolution in 1008 Steel Sheet during Multi-Axial Tensile Strain Paths," *Integr. Mater. Manuf. Innov.* **3**(1), 1 (2014).
- Creuziger, A., Syed, K., Gnäupel-Herold, T., "Measurement of Uncertainty in Orientation Distribution Function Calculations," *Scripta Mater.* **72-73**, 55 (2014).
- Cui, J., Choi, J.P., Li, G., Polikarpov, E., Darsell, J., Overman, N., Olszta, M., Schreiber, D., Bowden, M., Droubay, T., Kramer, M.J., Zarkevich, N.A., Wang, L.L., Johnson, D.D., Marinescu, M., Takeuchi, I., Huang, Q.Z., Wu, H., Reeve, H., Vuong, N.V., Liu, J.P., "Thermal Stability of MnBi Magnetic Materials," *J. Phys.-Condens. Mat.* **26**, 064212 (2014).

- Cui, J., Choi, J.P., Polikarpov, E., Darsell, J., Kramer, M.J., Zarkevich, N.A., Wang, L.L., Johnson, D.D., Marinescu, M., Huang, Q.Z., Wu, H., Vuong, N.V., Liu, J.P., "Development of MnBi Permanent Magnet: Neutron Diffraction of MnBi Powder," *J. Appl. Phys.* **115**(17), 17A743 (2014).
- Cunningham, N., Wu, Y., Klingensmith, D., Odette, G.R., "On the Remarkable Thermal Stability of Nanostructured Ferritic Alloys," *Mater. Sci. Eng. A-Struct.*, in press.
- Cunningham, N.J., Wu, Y., Etienne, A., Haney, E.M., Odette, G.R., Stergar, E., Hoelzer, D.T., Kim, Y.D., Wirth, B.D., Maloy, S.A., "Effect of Bulk Oxygen on 14YWT Nanostructured Ferritic Alloys," *J. Nucl. Mater.* **444**, 35 (2014).
- Cunningham, W.C., "Use of Water Activity Characteristics Enables a Simplified Approach for Defining the Reference Moisture Condition for FDA Cocoa Powder In-House Reference Material," *Anal. Bioanal. Chem.* **405**(26), 8615 (2013).
- Curtis, J.E., Zhang, H., Nanda, H., "SLDMOL: A Tool for the Structural Characterization of Thermally Disordered Membrane Proteins," *Comput. Phys. Commun.*, in press.
- D'Ortenzio, R.M., Dabkowska, H.A., Dunsiger, S.R., Gaulin, B.D., Gingras, M.J.P., Goko, T., Kycia, J.B., Liu, L., Medina, T., Munsie, T.J., Pomaranski, D., Ross, K.A., Uemura, Y.J., Williams, T.J., Luke, G.M., "Unconventional Magnetic Ground State in $\text{Yb}_2\text{Ti}_2\text{O}_7$," *Phys. Rev. B* **88**(13), 134428 (2013).
- Danial, M., Tran, C.M.-N., Jolliffe, K.A., Perrier, S., "Thermal Gating in Lipid Membranes using Thermoresponsive Cyclic Peptide-Polymer Conjugates," *J. Am. Chem. Soc.* **136**(22), 8018 (2014). [CHNRNS]
- DeCaluwe, S.C., Kienzle, P.A., Bhargava, P., Baker, A.M., Dura, J.A., "Phase Segregation of Sulfonate Groups in Nafion Interface Lamellae, Quantified via Neutron Reflectometry Fitting Techniques for Multi-Layered Structures," *Soft Matter*, in press.
- de la Iglesia, P., Pozzo, D.C., "Effects of Supersturation on the Structure and Properties of Poly(9,9-Dioctyl Fluorene) Organogels," *Soft Matter* **9**, 11214 (2013). [CHNRNS]
- Dhital, C., Hogan, T., Zhou, W., Chen, X., Ren, Z., Pokharel, M., Okada, Y., Heine, M., Tian, W., Yamani, Z., Opeil, C., Helton, J.S., Lynn, J.W., Wang, Z., Madhavan, V., Wilson, S.D., "Carrier Localization and Electronic Phase Separation in a Doped Spin-Orbit-Driven Mott Phase in $\text{Sr}_3(\text{Ir}_{1-x}\text{Ru}_x)_2\text{O}_7$," *Nat. Commun.* **5**(3377), 1 (2014).
- Dimeo, R.M., "The NIST Center for Neutron Research," *HANARO Report* **71**, 18 (2013).
- Dimeo, R.M., "Wave Packet Scattering from Time-Varying Potential Barriers in One Dimension," *Am. J. Phys.* **82**(2), 142 (2014).
- Ding, C., Gong, X., Man, H., Zhi, G., Guo, S., Zhao, Y., Wang, H., Chen, B., Ning, F.L., "The Suppression of Curie Temperature by Sr Doping in Diluted Ferromagnetic Semiconductor $(\text{La}_{1-x}\text{Sr}_x)(\text{Zn}_{1-y}\text{Mn}_y)\text{AsO}_4$," *Europhys. Lett.* **107**, 17004 (2014).
- Disseler, S.M., "Direct Evidence for the All-In/All-Out Magnetic Structure in the Pyrochlore Iridates from Muon Spin Relaxation," *Phys. Rev. B* **89**(14), 140413 (2014).
- Downing, R.G., "NIST Neutron Depth Profiling Facility: 2013, Invited," *T. Am. Nucl. Soc.* **109**, 527 (2013).
- Downing, R.G., "Enhanced Reaction Rates in NDP Analysis with Neutron Scattering," *Rev. Sci. Instrum.* **85**(4), 045109 (2014).
- Du, W., Yuan, G., Wang, M., Han, C.C., Satija, S.K., Akgun, B., "Initial Stages of Interdiffusion between Asymmetrical Polymeric Layers: Glassy Polycarbonate and Melt Poly(Methyl Methacrylate) Interface Studied by Neutron Reflectometry," *Macromolecules* **47**, 713 (2014).
- Eberle, A.P.R., Martys, N.N., Porcar, L., Kline, S.R., George, W.L., Kim, J.M., Butler, P.D., Wagner, N.J., "Shear Viscosity and Structural Scalings in Model Adhesive Hard-Sphere Gels," *Phys. Rev. E* **89**(5), 050302 (2014). [CHNRNS]
- Edmonds, M.T., Hellerstedt, J.T., Tadich, A., Schenk, A., O'Donnell, K.M., Tosado, J., Butch, N.P., Syers, P., Paglione, J., Fuhrer, M.S., "Air-Stable Electron Depletion of Bi_2Se_3 using Molybdenum Trioxide into the Topological Regime," *ACS Nano* **8**(6), 6400 (2014).
- Ehlers, G., Podlesnyak, A.A., Frontzek, M., Freitas, R.S., Ghivelder, L., Gardner, J.S., Shiryaev, S.V., Barilo, S., "A Detailed Study of the Magnetic Phase Transition in CuCrO_2 ," *J. Phys.: Condens. Matter* **25**, 496009 (2013). [CHNRNS]
- Eriksson, S.M., Mackey, E.A., Lindstrom, R.M., Lamaze, G.P., Grogan, K.P., Brady, D.E., "Delayed-Neutron Activation Analysis at NIST," *J. Radioanal. Nucl. Chem.* **298**, 1819 (2013).
- Erlkamp, M., Grobelny, S., Faraone, A., Czeslik, C., Winter, R., "Solvent Effects on the Dynamics of Amyloidogenic Insulin Revealed by Neutron Spin Echo Spectroscopy," *J. Phys. Chem. B* **118**, 3310 (2014). [CHNRNS]
- Fairweather, J.D., Spornjak, D., Spendelow, J., Mukundan, R., Hussey, D., Jacobson, D., Borup, R.L., "Evaluation of Transient Water Content during PEMFC Operational Cycles by Stroboscopic Neutron Imaging," *ECS Transactions* **58**(1), 301 (2013).

- Fajalia, A.I., Tsianou, M., "Charging and Un-Charging a Neutral Polymer in Solution: A Small-Angle Neutron Scattering Investigation," *J. Phys. Chem. B*, in press. [CHNRNS]
- Faraone, A., Fratini, E., Garai, S., Müller, A., Tyagi, M., Jenkins, T., Mamontov, E., Paul, R.L., Copley, J.R.D., Baglioni, P., "Incoherent Quasielastic Neutron Scattering Study of the Relaxation Dynamics in Molybdenum-Oxide Keplerate-Type Nanocages," *J. Phys. Chem. C* **118**, 13300 (2014). [CHNRNS]
- Ferguson, P.P., Le, D.-B., Todd, A.D.W., Martine, M.L., Trussler, S., Obrovac, M.N., Dahn, J.R., "Nanostructured $\text{Sn}_{30}\text{Co}_{30}\text{C}_{40}$ Alloys for Lithium-Ion Battery Negative Electrodes Prepared by Horizontal Roller Milling," *J. Alloy Compd.* **595**, 138 (2014).
- Ferguson, P.P., Todd, A.D.W., Martine, M.L., Dahn, J.R., "Structure and Performance of Tin-Cobalt-Carbon Alloys Prepared by Attriting, Roller Milling and Sputtering," *J. Electrochem. Soc.* **161**(3), A342 (2014).
- Ferrier, Jr., R.C., Lee, H.-S., Hore, M.J.A., Caporizzo, M., Eckmann, D.M., Compasto, R.J., "Gold Nanorod Linking to Control Plasmonic Properties in Solution and Polymer Nanocomposites," *Langmuir* **30**, 1906 (2014).
- Fobes, D., Zaliznyak, I.A., Xu, Z., Zhong, R., Gu, G., Tranquada, J.M., Harriger, L., Singh, D., Ovidiu Garlea, V., Lumsden, M., Winn, B., "Ferro-Orbital Ordering Transition in Iron Telluride Fe_{1+y}Te ," *Phys. Rev. Lett.* **112**(18), 187202 (2014).
- Fritsch, K., Kermarrec, E., Ross, K.A., Qiu, Y., Copley, J.R.D., Pomaranski, D., Kycia, J.B., Dabkowska, H.A., Gaulin, B.D., "Temperature and Magnetic Field Dependence of Spin-Ice Correlations in the Pyrochlore Magnet $\text{Tb}_2\text{Ti}_2\text{O}_7$," *Phys. Rev. B* **90**(1), 014429 (2014). [CHNRNS]
- Furukawa, H., Gándara, F., Zhang, Y.-B., Jiang, J., Queen, W.L., Hudson, M.R., Yaghi, O.M., "Water Adsorption in Porous Metal-Organic Frameworks and Related Materials," *J. Am. Chem. Soc.* **136**, 4369 (2014).
- Gadipelli, S., Travis, W., Zhou, W., Guo, Z., "A Thermally Derived and Optimized Structure from ZIF-8 with Giant Enhancement in CO_2 Uptake," *Energ. Environ. Sci.* **7**, 2232 (2014).
- Gamża, M.B., Tomczak, J.M., Brown, C., Puri, A., Kotliar, G., Aronson, M.C., "Electronic Correlations in FeGa_3 and the Effect of Hole Doping on its Magnetic Properties," *Phys. Rev. B* **89**(19), 195102 (2014).
- Ganapatibhotla, L.V.N.R., Maranas, J.K., "Interplay of Surface Chemistry and Ion Content in Nanoparticle-Filled Solid Polymer Electrolytes," *Macromolecules* **47**, 3625 (2014). [CHNRNS]
- Gao, J., Chen, W., Dou, L., Chen, C.-C., Chang, W.-H., Liu, Y., Li, G., Yang, Y., "Elucidating Double Aggregation Mechanisms in the Morphology Optimization of Diketopyrrolopyrrole-Based Narrow Bandgap Polymer Solar Cells," *Adv. Mater.* **26**, 3142 (2014).
- Gao, W.-Y., Cai, R., Meng, L., Wojtas, L., Zhou, W., Yildirim, T., Shi, X., Ma, S., "Quest for a Highly Connected Robust Porous Metal-Organic Framework on the Basis of a Bifunctional Linear Linker and a Rare Heptanuclear Zinc Cluster," *Chem. Commun.* **49**, 10516 (2013).
- Gao, Y., Nieuwendaal, R., Hammouda, B., Berciu, C., Nicastro, D., Douglas, J., Xu, B., Horkay, F., "Supramolecular Self-Assembly Inside Living Mammalian Cells," *Mater. Res. Soc. Symp. P.* **1622**, 85 (2014). [CHNRNS]
- Ge, W., Devreugd, C.P., Phelan, D., Zhang, Q., Ahart, M., Li, J., Luo, H., Boatner, L.A., Viehland, D., Gehring, P.M., "Lead-Free and Lead-Based ABO_3 Perovskite Relaxors with Mixed-Valence A-Site and B-Site Disorder: Comparative Neutron Scattering Structural Study of $(\text{Na}_{1/2}\text{Bi}_{1/2})\text{TiO}_3$ and $\text{Pb}(\text{Mg}_{1/3}\text{Nb}_{2/3})\text{O}_3$," *Phys. Rev. B* **88**(17), 174115 (2013).
- Gentile, L., Behrens, M.A., Porcar, L., Butler, P., Wagner, N.J., Olsson, U., "Multilamellar Vesicle Formation from a Planar Lamellar Phase under Shear Flow," *Langmuir* **30**, 8316 (2014). [CHNRNS]
- Gentile, T.R., Chen, W.C., "Polarized ^3He Spin Filters for Neutron Science," in "Proceedings of Science," (XVth International Workshop on Polarized Sources, and Polarimetry, August 2013, Charlottesville, VA), 1 (2014).
- Gericke, A., Leslie, N.R., Lösche, M., Ross, A.H., "PI(4,5) P_2 -Mediated Cell Signaling: Emerging Principles and PTEN as a Paradigm for Regulatory Mechanism," in "Advances in Experimental Medicine and Biology," (Springer, Netherlands, Netherlands, Netherlands) 85 (2013).
- Gilliam, D.M., Yue, A.T., "Improvements in the Characterization of Actinide Targets by Low Solid-Angle Counting," *J. Radioanal. Nucl. Chem.* **299**, 1061 (2014).
- Glassman, M.J., Olsen, B.D., "Structure and Mechanical Response of Protein Hydrogels Reinforced by Block Copolymer Self-Assembly," *Soft Matter* **9**, 6814 (2013).
- Gnäupel-Herold, T., Iadicola, M.A., Creuziger, A.A., Foecke, T., Hu, L., "Interpretation of Diffraction Data from In-Situ Stress Measurements during Biaxial Sheet Metal Forming," *Mater. Sci. Forum* **768-769**, 441 (2013).
- Gnäupel-Herold, T., Green, D.E., Foecke, T., Iadicola, M.A., "Through-Thickness Stresses in Automotive Sheet Metal after Plane Strain Channel Draw," *Mater. Sci. Forum* **768-769**, 433 (2013).

- Gnäupel-Herold, T., Slotwinski, J., Moylan, S., "Neutron Measurements of Stresses in a Test Artifact Produced by Laser-Based Additive Manufacturing," AIP Conf. Proc. **1581**, 1205 (2014).
- Godfrin, P.D., Castañeda-Priego, R., Liu, Y., Wagner, N.J., "Intermediate Range Order and Structure in Colloidal Dispersions with Competing Interactions," J. Chem. Phys. **139**(15), 154904 (2013).
- Godfrin, P.D., Valadez-Pérez, N.E., Castañeda-Priego, R., Wagner, N.J., Liu, Y., "Generalized Phase Behavior of Cluster Formation in Colloidal Dispersions with Competing Interactions," Soft Matter **10**, 5061 (2014).
- Greene, P.K., Kirby, B.J., Lau, J.W., Borchers, J.A., Fitzsimmons, M.R., Liu, K., "Deposition Order Dependent Magnetization Reversal in Pressure Graded Co/Pd Films," Appl. Phys. Lett. **104**(15), 152401 (2014).
- Gressier, V., Bonaldi, A.C., Dewey, M.S., Gilliam, D.M., Harano, H., Masuda, A., Matsumoto, T., Moiseev, N., Nico, J.S., Nolte, R., Oberstedt, S., Roberts, N.J., Röttger, S., Thomas, D.J., "International Key Comparison of Neutron Fluence Measurements in Monoenergetic Neutron Fields - CCRI(III)-K11," Metrologia, in press.
- Grogan, K.P., O'Kelly, D.J., "Analytical Applications of Delayed and Instrumental Neutron Activation Analysis," J. Radioanal. Nucl. Chem. **299**, 543 (2014).
- Grutter, A.J., Yang, H., Kirby, B.J., Fitzsimmons, M.R., Aguiar, J.A., Browning, N.D., Jenkins, C.A., Arenholz, E., Mehta, V.V., Alaan, U.S., Suzuki, Y., "Interfacial Ferromagnetism in $\text{LaNiO}_3/\text{CaMnO}_3$ Superlattices," Phys. Rev. Lett. **111**(8), 087202 (2013).
- Gurnon, A.K., Godfrin, P.D., Wagner, N.J., Eberle, A.P.R., Butler, P., Porcar, L., "Measuring Material Microstructure under Flow using 1-2 Plane Flow-Small Angle Neutron Scattering," J. Vis. Exp. (84), e51068 (2014).
- Gurnon, A.K., López-Barrón, C., Eberle, A.P.R., Porcar, L., Wagner, N.J., "Spatiotemporal Stress and Structure Evolution in Dynamically Sheared Polymer-Like Micellar Solutions," Soft Matter **10**, 2889 (2014).
- Gurnon, A.K., López-Barrón, C., Wasbrough, M.J., Porcar, L., Wagner, N.J., "Spatially Resolved Concentration and Segmental Flow Alignment in a Shear-Banding Solution of Polymer-Like Micelles," ACS Macro Lett. **3**, 276 (2014). [CHRS]
- Gutov, O.V., Bury, W., Gomez-Gualdrón, D.A., Krungleviciute, V., Fairen-Jimenez, D., Mondloch, J.E., Sarjeant, A.A., Al-Juaid, S.S., Snurr, R.Q., Hupp, J.T., Yildirim, T., Farha, O.K., "Water-Stable Zirconium-Based Metal-Organic Framework Material with High-Surface Area and Gas-Storage Capacities," Chem.-Eur. J., in press.
- Hammouda, B., "Are Bragg Peaks Gaussian?," J. Res. Natl. Inst. Stan. **119**, 15 (2014). [CHRS]
- Hammouda, B., Mildner, D.F.R., Brûlet, A., Desert, S., "Insight into Neutron Focusing: the Out-of-Focus Condition," J. Appl. Crystallogr. **46**, 1361 (2013). [CHRS]
- Harris, A.B., Yildirim, T., "Spin Dynamics of Trimers on a Distorted Kagome Lattice," Phys. Rev. B **88**(1), 014411, (2013).
- He, Y., Zhou, W., Yildirim, T., Chen, B., "A Series of Metal-Organic Frameworks with High Methane Uptake and an Empirical Equation for Predicting Methane Storage Capacity," Energ. Environ. Sci. **6**(9), 2735 (2013).
- He, Y., Guo, Z., Xiang, S., Zhang, Z., Zhou, W., Fronczek, F.R., Parkin, S., Hyde, S.T., O'Keeffe, M., Chen, B., "Metastable Interwoven Mesoporous Metal-Organic Frameworks," Inorg. Chem. **52**, 11580 (2013).
- He, Y., Zhou, W., Qian, G., Chen, B., "Methane Storage in Metal-Organic Frameworks," Chem. Soc. Rev., in press.
- Heinrich, F., Nanda, H., Go, H.Z., Bachert, C., Lösche, M., Linstedt, A.D., "Myristoylation Restricts Orientation of the GRASP Domain on Membranes and Promotes Membrane Tethering," J. Biol. Chem. **289**(14), 9683 (2014).
- Heinrich, F., Lösche, M., "Zooming in on Disordered Systems: Neutron Reflection Studies of Proteins Associated with Fluid Membranes," BBA-Biomembranes, in press.
- Helgeson, M.E., Gao, Y., Moran, S.E., Lee, J., Godfrin, M., Tripathi, A., Bose, A., Doyle, P.S., "Homogeneous Percolation Versus Arrested Phase Separation in Attractively-Driven Nanoemulsion Colloidal Gels," Soft Matter **10**, 3122 (2014). [CHRS]
- Heller, W.T., Urban, V.S., Lynn, G.W., Weiss, K.L., O'Neill, H.M., Pingali, S.V., Qian, S., Littrell, K.C., Melnichenko, Y.B., Buchanan, M.V., Selby, D.L., Wignall, G.D., Butler, P.D., Myles, D.A., "The Bio-SANS Instrument at the High Flux Isotope Reactor of Oak Ridge National Laboratory," J. Appl. Crystallogr., in press.
- Hellsing, M.S., Kwaambwa, H.M., Nermark, F.M., Nkoane, B.B.M., Jackson, A.J., Wasbrough, M.J., Berts, I., Porcar, L., Rennie, A.R., "Structure of Flocs of Latex Particles Formed by Addition of Protein from Moringa Seeds," Colloid Surface. A, in press. [CHRS]
- Heuser, B.J., Trinkle, D.R., Jalarvo, N., Serio, J., Schiavone, E.J., Mamontov, E., Tyagi, M., "Direct Measurement of Hydrogen Dislocation Pipe Diffusion in Deformed Polycrystalline Pd Using Quasielastic Neutron Scattering," Phys. Rev. Lett. **113**(2), 025504 (2014). [CHRS]

- Hoarfrost, M.L., He, Y., Lodge, T.P., "Lower Critical Solution Temperature Phase Behavior of Poly(*n*-Butyl Methacrylate) in Ionic Liquid Mixtures," *Macromolecules* **46**, 9464 (2013).
- Hong, T., Schmidt, K.P., Coester, K., Awwadi, F.F., Turnbull, M.M., Qiu, Y., Rodriguez-Rivera, J.A., Zhu, M., Ke, X., Aoyama, C.P., Takano, Y., Cao, H., Tian, W., Ma, J., Custelcean, R., Zhou, H.D., Matsuda, M., "Magnetic Ordering Induced by Interladder Coupling in the Spin-1/2 Heisenberg Two-Leg Ladder Antiferromagnet $C_9H_{18}N_2CuBr_4$," *Phys. Rev. B* **89**(17), 174432 (2014). [CHNRNS]
- Hore, M.J.A., Ford, J., Ohno, K., Composto, R.J., Hammouda, B., "Direct Measurements of Polymer Brush Conformation using Small-Angle Neutron Scattering (SANS) from Highly Grafted Iron Oxide Nanoparticles in Homopolymer Melts," *Macromolecules* **46**, 9341 (2013). [CHNRNS]
- Hore, M.J.A., Composto, R.J., "Functional Polymer Nanocomposites Enhanced by Nanorods," *Macromolecules* **47**, 875 (2014). [CHNRNS]
- Hore, M.J.A., Hammouda, B., Li, Y., Cheng, H., "Co-Nonsolvency of Poly(*n*-isopropylacrylamide) in Deuterated Water/Ethanol Mixtures," *Macromolecules* **46**, 7894 (2013). [CHNRNS]
- Horkay, F., "Ion Polymer Interactions in DNA Solutions and Gels," *Macromol. Symp.* **329**, 19 (2013). [CHNRNS]
- Horkay, F., Bassar, P.J., Hecht, A.-M., Geissler, E., "Structure and Interactions in Hyaluronic Acid Solutions," *Polym. Mater. Sci. Eng.* **108**, 111 (2013). [CHNRNS]
- Hulvey, Z., Lawler, K.V., Qiao, Z., Zhou, J., Fairen-Jimenez, D., Snurr, R.Q., Ushakov, S.V., Navrotsky, A., Brown, C. M., Forster, P.M., "Noble Gas Adsorption in Copper Trimesate, HKUST-1: An Experimental and Computational Study," *J. Phys. Chem. C* **117**, 20116 (2013).
- Hussey, D.S., Coakley, K.J., Baltic, E., Jacobson, D.L., "Improving Quantitative Neutron Radiography through Image Restoration," *Nucl. Instrum. Meth. A* **729**, 316 (2013).
- Hussey, D.S., Spornjak, D., Wu, G., Jacobson, D.L., Liu, D., Khaykovich, B., Gubarev, M.V., Fairweather, J., Mukundan, R., Lujan, R., Zelenay, P., Borup, R.L., "Neutron Imaging of Water Transport in Polymer-Electrolyte Membranes and Membrane-Electrode Assemblies," *ECS Transactions* **58**(1), 293 (2013).
- Inceoglu, S., Young, N.P., Jackson, A.J., Kline, S.R., Costeux, S., Balsara, N.P., "Effect of Supercritical Carbon Dioxide on the Thermodynamics of Model Blends of Styrene-Acrylonitrile Copolymer and Poly(Methyl Methacrylate) Studied by Small-Angle Neutron Scattering," *Macromolecules* **46**, 6345 (2013). [CHNRNS]
- Jain, N., Liu, C.K., Hawkett, B.S., Warr, G.G., Hamilton, W.A., "Application of Small-Angle Neutron Scattering to the Study of Forces between Magnetically Chained Monodisperse Ferrofluid Emulsion Droplets," *J. Appl. Crystallogr.* **47**, 41 (2014). [CHNRNS]
- Jalarvo, N., Gourdon, O., Ehlers, G., Tyagi, M., Kumar, S.K., Dobbs, K.D., Smalley, R.J., Guise, W.E., Ramirez-Cuesta, A., Wildgruber, C., Crawford, M.K., "Structure and Dynamics of Octamethyl-POSS Nanoparticles," *J. Phys. Chem. C* **118**, 5579 (2014). [CHNRNS]
- Jeong, Y., Gnäupel-Herold, T., Barlat, F., Iadicola, M., Creuziger, A., Lee, M.-G., "Evaluation of Biaxial Flow Stress Based on Elasto-Viscoplastic Self-Consistent Analysis of X-ray Diffraction Measurements," *Int. J. Plasticity*, in press.
- Jiao, Y., Parra, J., Akcora, P., "Effect of Ionic Groups on Polymer-Grafted Magnetic Nanoparticle Assemblies," *Macromolecules* **47**, 2030 (2014). [CHNRNS]
- Jin, L., Mathur, R., Rother, G., Cole, D., Bazilevskaya, E., Williams, J., Carone, A., Brantley, S., "Evolution of Porosity and Geochemistry in Marcellus Formation Black Shale during Weathering," *Chem. Geol.* **356**, 50 (2013). [CHNRNS]
- Jones, R., "Specimen Name: NIST nSoft Consortium," *Adv. Mater. Processes* **172**, 48 (2014).
- Kamazawa, K., Harada, M., Araki, T., Matsuo, Y., Tyagi, M., Sugiyama, J., "Interrelationship between Number of Mobile Protons, Diffusion Coefficient, and AC Conductivity in Superprotonic Conductors, $CsHSO_4$ and $Rb_3H(SeO_4)_2$," *J. Phys. Soc. Jpn.* **83**, 074604 (2014). [CHNRNS]
- Kandlakunta, P., Cao, L.R., "Neutron Conversion Efficiency and Gamma Interference with Gadolinium," *J. Radioanal. Nucl. Chem.* **300**, 953 (2014).
- Karabiyik, U., Mao, M., Satija, S.K., Esker, A.R., "Determination of Thicknesses and Refractive Indices of Polymer Thin Films by Multiple Incident Media Ellipsometry," *Thin Solid Films*, in press.
- Ke, X., Birol, T., Misra, R., Lee, J.-H., Kirby, B.J., Schlom, D.G., Fennie, C.J., Freeland, J.W., "Structural Control of Magnetic Anisotropy in a Strain-Driven Multiferroic $EuTiO_3$ Thin Film," *Phys. Rev. B* **88**(9), 094434 (2013).
- Kelley, E.G., Murphy, R.P., Seppala, J.E., Smart, T.P., Hann, S.D., Sullivan, M.O., Epps, T.H., "Size Evolution of Highly Amphiphilic Macromolecular Solution Assemblies via a Distinct Bimodal Pathway," *Nat. Commun.* **5**, 3599 (2014).

- Kennedy, R.D., Krungleviciute, V., Clingerman, D.J., Mondloch, J.E., Peng, Y., Wilmer, C.E., Sarjeant, A.A., Snurr, R.Q., Hupp, J.T., Yildirim, T., Farha, O.K., Mirkin, C.A., "Carborane-Based Metal-Organic Framework with High Methane and Hydrogen Storage Capacities," *Chem. Mater.* **25**, 3539 (2013).
- Khodadadi, S., Clark, N.J., McAuley, A., Cristiglio, V., Curtis, J.E., Shalae, E.Y., Krueger, S., "Influence of Sorbitol on Protein Crowding in Solution and Freeze-Concentrated Phases," *Soft Matter* **10**, 4056 (2014). [CHNRNS]
- Kim, D., Syers, P., Butch, N.P., Paglione, J., Fuhrer, M.S., "Ambipolar Surface State Thermoelectric Power of Topological Insulator Bi_2Se_3 ," *Nano Lett.* **14**, 1701 (2014).
- Kim, J., Gao, Y., Hebebrand, C., Peirtsegeale, E., Helgeson, M.E., "Polymer-Surfactant Complexation as a Generic Route to Responsive Viscoelastic Nanoemulsions," *Soft Matter* **9**, 6897 (2013).
- Kim, M.D., Dergunov, S.A., Richter, A.G., Durbin, J., Shmakov, S.N., Jia, Y., Kenbeilova, S., Orazbekuly, Y., Kengpeil, A., Lindner, E., Pingali, S.V., Urban, V.S., Weigand, S., Pinkhassik, E., "Facile Directed Assembly of Hollow Polymer Nanocapsules within Spontaneously Formed Catanionic Surfactant Vesicles," *Langmuir* **30**, 7061 (2014).
- Kim, S.Y., Zukoski, C.F., "Molecular Weight Effects on Particle and Polymer Microstructure in Concentrated Polymer Solutions," *Macromolecules* **46**, 6634 (2013).
- Kizilay, E., Dinsmore, A.D., Hoagland, D.A., Sun, L., Dubin, P.L., "Evolution of Hierarchical Structures in Polyelectrolyte-Micelle Coacervates," *Soft Matter* **9**(30), 7320 (2013). [CHNRNS]
- Kline, S.R., "2013 NCNR Annual Report," *NIST SP* **1168**, (2014).
- Kofu, M., Kajiwar, T., Gardner, J.S., Simeoni, G.G., Tyagi, M., Faraone, A., Nakajima, K., Ohira-Kawamura, S., Nakano, M., Yamamuro, O., "Magnetic Relaxations in a Tb-Based Single Molecule Magnet Studied by Quasielastic Neutron Scattering," *Chem. Phys.* **427**, 147 (2013). [CHNRNS]
- Kong, G.-Q., Han, Z.-D., He, Y., Ou, S., Zhou, W., Yildirim, T., Krishna, R., Zou, C., Chen, B., Wu, C.-D., "Expanded Organic Building Units for the Construction of Highly Porous Metal-Organic Frameworks," *Chem.-Eur. J.* **19**, 14886 (2013).
- Kotaka, T., Tabuchi, Y., Pasaogullari, U., Wang, C.-Y., "The Influence of Liquid Water Interaction between Channel, GDL and CL on Cell Performance," *ECS Transactions* **58**(1), 1033 (2013).
- Krayer, L., Lau, J.W., Kirby, B.J., "Structural and Magnetic Etch Damage in CoFeB ," *J. Appl. Phys.* **115**(17), 17B751 (2014).
- Krueger, S., Shin, J.-H., Curtis, J.E., Robinson, K.A., Kelman, Z., "The Solution Structure of Full-length Dodecameric MCM by SANS and Molecular Modeling," *Proteins*, in press. [CHNRNS]
- Kruk, I.I., Zajdel, P., "Single Crystal Growth and Structural Characterization of Iron Telluride Doped with Chromium and Zinc," *J. Cryst. Growth*, in press.
- Kumari, H., Kline, S.R., Fowler, D.A., Mossine, A.V., Deakyne, C.A., Atwood, J.L., "Solution Superstructures: Truncated Cubeoctahedron Structures of Pyrogallol[4]arene Nanoassemblies," *Chem. Commun.* **50**, 109 (2014).
- Kumari, H., Kline, S.R., Atwood, J.L., "Aqueous Solubilization of Hydrophobic Supramolecular Metal-Organic Nanocapsules," *Chem. Sci.* **5**, 2554 (2014). [CHNRNS]
- LaManna, J.M., Chakraborty, S., Gagliardo, J.J., Mench, M.M., "Isolation of Transport Mechanisms in PEFCs using High Resolution Neutron Imaging," *Int. J. Hydrogen Energ.* **39**, 3387 (2014).
- Lavelle, C.M., Deacon, R.M., Hussey, D.S., Coplan, M., Clark, C.W., "Characterization of Boron Coated Vitreous Carbon Foam for Neutron Detection," *Nucl. Instrum. Meth. A* **729**, 346 (2013).
- Lee, C.L., Dowding, P.J., Doyle, A.R., Bakker, K.M., Lam, S.S., Rogers, S.E., Routh, A.F., "The Structures of Salicylate Surfactants with Long Alkyl Chains in Non-Aqueous Media," *Langmuir* **29**, 14763 (2013). [CHNRNS]
- Lee, J.S., Richardella, A., Rench, D.W., Fraleigh, R.D., Flanagan, T.C., Borchers, J.A., Tao, J., Samarth, N., "Ferromagnetism and Spin-Dependent Transport in *n*-type Mn-Doped Bismuth Telluride Thin Films," *Phys. Rev. B* **89**(17), 174425 (2014).
- Lee, K., Isley, III, W.C., Dzubak, A.L., Verma, P., Stoneburner, S.J., Lin, L.-C., Howe, J.D., Bloch, E.D., Reed, D.A., Hudson, M.R., Brown, C.M., Long, J.R., Neaton, J.B., Smit, B., Cramer, C.J., Truhlar, D.G., Gagliardi, L., "Design of a Metal-Organic Framework with Enhanced Back Bonding for the Separation of N_2 and CH_4 ," *J. Am. Chem. Soc.* **136**, 698 (2014).
- Lehnert, R., Snow, W.M., Yan, H., "A First Experimental Limit on In-Matter Torsion from Neutron Spin Rotation in Liquid ^4He ," *Phys. Lett. B* **730**, 353 (2014).
- Leiner, J., Kirby, B.J., Fitzsimmons, M.R., Tivakornasithorn, K., Liu, X., Furdyna, J.K., Dobrowolska, M., "Magnetic Depth Profile in GaMnAs Layers with Vertically Graded Mn Concentrations," *J. Magn. Magn. Mater.* **350**, 135 (2014).
- Leiner, J., Thampy, V., Christianson, A.D., Abernathy, D.L., Stone, M.B., Lumsden, M.D., Sefat, A.S., Sales, B.C., Hu, J., Mao, Z., Bao, W., Broholm, C., "Modified Magnetism within the Coherence Volume of Superconducting $\text{Fe}_{1+\delta}\text{Se}_x\text{Te}_{1-x}$," *Phys. Rev. B*, in press. [CHNRNS]

- Leys, J., Subramanian, D., Rodezno, E., Hammouda, B., Anisimov, M.A., "Mesoscale Phenomena in Solutions of 3-Methylpyridine, Heavy Water, and an Antagonistic Salt," *Soft Matter* **9**, 9326 (2013). [CHNRS]
- Li, B., Wen, H.-M., Wang, H., Wu, H., Tyagi, M., Yildirim, T., Zhou, W., Chen, B., "A Porous Metal-Organic Framework with Dynamic Pyrimidine Groups Exhibiting Record High Methane Storage Working Capacity," *J. Am. Chem. Soc.* **136**, 6207 (2014). [CHNRS]
- Li, F., Parnell, S.R., Hamilton, W.A., Maranville, B.B., Wang, T., Semerad, R., Baxter, D.V., Cremer, J.T., Pynn, R., "Superconducting Magnetic Wollaston Prism for Neutron Spin Encoding," *Rev. Sci. Instrum.* **85**(5), 053303 (2014).
- Li, G.-N., Rao, G.-H., Huang, Q.-Z., Gao, Q.-Q., Luo, J., Liu, G.-Y., Li, J.-B., Liang, J.-K., "Phase Separation in Sr Doped BiMnO₃," *Chinese Phys. B* **23**(3), 036401 (2014).
- Li, X., ShamsiJazeyi, H., Pesek, S.L., Agrawal, A., Hammouda, B., Verduzco, R., "Thermoresponsive PNIPAA Bottlebrush Polymers with Tailored Side-Chain Length and End-Group Structure," *Soft Matter* **10**, 2008 (2014). [CHNRS]
- Li, X., Porcar, L., Sánchez-Díaz, L.E., Do, C., Liu, Y., Kim, T.-H., Smith, G.S., Hamilton, W.A., Hong, K., Chen, W.-R., "Influence of Molecular Solvation on the Conformation of Star Polymers," *ACS Macro Lett.* **3**(5), 458 (2014).
- Li, X., Ma, X., Su, D., Liu, L., Chisnell, R., Ong, S.P., Chen, H., Toumar, A., Idrobo, J.-C., Lei, Y., Bai, J., Wang, F., Lynn, J.W., Lee, Y.S., Ceder, G., "Direct Visualization of the Jahn-Teller Effect Coupled to Na Ordering in Na_{5/8}MnO₂," *Nat. Mater.* **13**, 586 (2014).
- Lin, K., Wu, H., Wang, F., Rong, Y., Chen, J., Deng, J., Yu, R., Fang, L., Huang, Q., Xing, X., "Structure and Thermal Expansion of the Tungsten Bronze Pb₂KNb₅O₁₅," *Dalton T.* **43**, 7037 (2014).
- Lin, K., Rong, Y., Wu, H., Huang, Q., You, L., Ren, Y., Fan, L., Chen, J., Xing, X., "Ordered Structure and Thermal Expansion in Tungsten Bronze Pb₂K_{0.5}Li_{0.5}Nb₅O₁₅," *Inorg. Chem.*, in press.
- Lindstrom, R.M., "The Half-Lives of ^{90m}Y and ⁹⁷Ru," *J. Radioanal. Nucl. Chem.* **299**, 897 (2014).
- Lindstrom, R.M., "The Half-Life of ^{111m}Pd," *J. Radioanal. Nucl. Chem.* **300**, 605 (2014).
- Liu, D., Hussey, D.S., Gubarev, M.V., Ramsey, B.D., Jacobson, D., Arif, M., Moncton, D.E., Khaykovich, B., "Response to 'Comment on 'Demonstration of Achromatic Cold-Neutron Microscope Utilizing Axisymmetric Focusing mirrors,'" *Appl. Phys. Lett.* **103**, 236101 (2013).
- Liu, D.X., Wang, J., Pan, K., Qiu, J., Canova, M., Cao, L.R., Co, A.C., "In Situ Quantification and Visualization of Lithium Transport with Neutrons," *Angew. Chem. Int. Ed.*, in press.
- Liu, X., Majzoub, E.H., Stavila, V., Bhakta, R.K., Allendorf, M.D., Shane, D.T., Conradi, M.S., Verdal, N., Udovic, T.J., Hwang, S.-J., "Probing the Unusual Anion Mobility of LiBH₄ Confined in Highly Ordered Nanoporous Carbon Frameworks via Solid State NMR and Quasielastic Neutron Scattering," *J. Mater. Chem. A* **1**, 9935 (2013). [CHNRS]
- Liu, X., Trabold, T.A., Gagliardo, J.J., Jacobson, D.L., Hussey, D.S., "Neutron Imaging of Water Accumulation in the Active Area and Channel-to-Manifold Transitions of a PEMFC," in "Proceedings of the ASME 2013 11th Fuel Cell Science," (Engineering and Technology Conference, June 2013, Minneapolis, MN) (2013).
- Liu, Y., "Colloidal Systems with Both a Short-Range Attraction and a Long-Range Repulsion," *Chem. Eng. Process*, **1**(2), 1010 (2013). [CHNRS]
- Livingston, R.A., Al-Sheikhly, M., Grissom, C., Aloiz, E., Paul, R., "Feasibility Study of Prompt Gamma Neutron Activation for NDT Measurement of Moisture in Stone and Brick," *AIP Conf. Proc.* **1581**, 828 (2014).
- Lopes, T., Sansiñena, J.-M., Mukundan, R., Hussey, D.S., Jacobson, D.L., Garzon, F.H., "Diagnosing the Effects of Ammonia Exposure on PEFC Cathodes," *J. Electrochem. Soc.* **161**(6), F703 (2014).
- López-Barrón, C.R., Gurnon, A.K., Eberle, A.P.R., Porcar, L., Wagner, N.J., "Microstructural Evolution of a Model, Shear-Banding Micellar Solution during Shear Startup and Cessation," *Phys. Rev. E* **89**(4), 042301 (2014).
- Lott, J.R., McAllister, J.W., Wasbrough, M.J., Sammler, R.L., Bates, F.S., Lodge, T.P., "Fibrillar Structure in Aqueous Methylcellulose Solutions and Gels," *Macromolecules* **46**, 9760 (2013). [CHNRS]
- Lott, J.R., McAllister, J.W., Arvidson, S.A., Bates, F.S., Lodge, T.P., "Fibrillar Structure of Methylcellulose Hydrogels," *Biomacromolecules* **14**, 2484 (2013).
- Lu, X., Tam, D.W., Zhang, C., Luo, H., Wang, M., Zhang, R., Harriger, L.W., Keller, T., Keimer, B., Regnault, L.-P., Maier, T.A., Dai, P., "Short-Range Cluster Spin Glass near Optimal Superconductivity in BaFe_{2-x}Ni_xAs₂," *Phys. Rev. B* **90**(2), 024509 (2014).
- Lu, Z., Waldecker, J., Xie, X., Lai, M.-C., Hussey, D.S., Jacobson, D.L., "Investigation of Water Transport in Perforated Gas Diffusion Layer by Neutron Radiography," *ECS Transactions* **58**(1), 315 (2013).

- Luo, X., Ögüt, S., Yildirim, T., "Giant Charge Fluctuations with Se Height and Fe-Vacancy Formation in $M_x\text{Fe}_{2-y}\text{Se}_2$," *Phys. Rev. B* **89**(5), 054519 (2014).
- Majkrzak, C.F., Metting, C., Maranville, B.B., Dura, J.A., Satija, S., Udovic, T., Berk, N.F., "Determination of the Effective Transverse Coherence of the Neutron Wave Packet as Employed in Reflectivity Investigations of Condensed-Matter Structures. I. Measurements," *Phys. Rev. A* **89**(3), 033851 (2014).
- Majkrzak, C.F., Krycka, K., Krueger, S., Berk, N.F., Kienzle, P., Maranville, B., "Phase-Sensitive Small-Angle Neutron Scattering," *J. Appl. Crystallogr.* **47**, 780 (2014).
- Mang, J.T., Francois, E.G., Hagelberg, S.I., "Compaction Properties of Diaminoazoxy Furazan (DAAF): A Small-Angle Neutron Scattering Study," *Int. J. Energetic Materials Chem. Prop.* **12**(5), 411 (2013). [CHRNS]
- Mang, J.T., Hjelm, R.P., "Fractal Networks of Inter-Granular Voids in Pressed TATB," *Propell. Explos. Pyrot.* **38**(6), 831 (2013). [CHRNS]
- Manley, M.E., Jeffries, J.R., Lee, H., Butch, N.P., Zabalegui, A., Abernathy, D.L., "Multiple High-Temperature Transitions Driven by Dynamical Structures in NaI ," *Phys. Rev. B* **89**(22), 224106 (2014).
- Manley, M.E., Lynn, J.W., Abernathy, D.L., Specht, E.D., Delaire, O., Bishop, A.R., Sahul, R., Budai, J.D., "Phonon Localization Drives Polar Nanoregions in a Relaxor Ferroelectric," *Nat. Commun.* **5**, 3683 (2014).
- Matan, K., Nambu, Y., Zhao, Y., Sato, T.J., Fukumoto, Y., Ono, T., Tanaka, H., Broholm, C., Podlesnyak, A., Ehlers, G., "Ghost Modes and Continuum Scattering in the Dimerized Distorted Kagome Lattice Antiferromagnet $\text{Rb}_2\text{Cu}_3\text{SnF}_{12}$," *Phys. Rev. B* **89**(2), 024414 (2014).
- McCabe, E.E., Stock, C., Rodriguez, E.E., Wills, A.S., Taylor, J.W., Evans, J.S.O., "Weak Spin Interactions in Mott Insulating $\text{La}_2\text{O}_2\text{Fe}_2\text{OSe}_2$," *Phys. Rev. B* **89**(10), 100402 (2014). [CHRNS]
- McComb, J.C., Coplan, M.A., Al-Sheikhly, M., Thompson, A.K., Vest, R.E., Clark, C.W., "Noble Gas Excimer Scintillation Following Neutron Capture in Boron Thin Films," *J. Appl. Phys.* **115**(14), 144504 (2014).
- Menéndez, E., Dias, T., Geshev, J., Lopez-Barbera, J.F., Nogués, J., Steitz, R., Kirby, B.J., Borchers, J.A., Pereira, L.M.C., Vantomme, A., Temst, K., "Interdependence between Training and Magnetization Reversal in Granular Co-CoO Exchange Bias Systems," *Phys. Rev. B* **89**(14), 144407 (2014).
- Mildner, D.F.R., "Resolution of Small-Angle Neutron Scattering with a Reflective Focusing Optic," *J. Appl. Crystallogr.*, in press. [CHRNS]
- Miller, C.W., Belyea, D.D., Kirby, B.J., "Magnetocaloric Effect in Nanoscale Thin Films and Heterostructures," *J. Vac. Sci. Technol. A* **32**(4), 040802 (2014).
- Miskowiec, A., Buck, Z.N., Brown, M.C., Kaiser, H., Hansen, F.Y., King, G.M., Taub, H., Jiji, R., Cooley, J.W., Tyagi, M., Diallo, S.O., Mamontov, E., Herwig, K.W., "On the Freezing Behavior and Diffusion of Water in Proximity to Single-Supported Zwitterionic and Anionic Bilayer Lipid Membranes," *Europhys. Lett.* **107**, 28008 (2014). [CHRNS]
- Mitkus, R.J., Powell, J.L., Zeisler, R., Squibb, K.S., "Comparative Physicochemical and Biological Characterization of NIST Interim Reference Material $\text{PM}_{2.5}$ and SRM 1648 in Human A549 and Mouse RAW264.7 Cells," *Toxicol. in Vitro* **27**, 2289 (2013).
- Miyatsu, S., Kofu, M., Nagoe, A., Yamada, T., Sadakiyo, M., Yamada, T., Kitagawa, H., Tyagi, M., García Sakai, V., Yamamuro, O., "Proton Dynamics of Two-Dimensional Oxalate-Bridged Coordination Polymers," *Phys. Chem. Chem. Phys.*, in press. [CHRNS]
- Monroe, J.G., Thompson, S.M., Aspin, Z.S., Jacobson, D., Hussey, D., "Neutron Imaging of an Unbalanced Flat-Plate Oscillating Heat Pipe," in "52nd Aerospace Sciences Meeting," (52nd Aerospace Sciences Meeting, January 2014, National Harbor, Maryland) (2014).
- Moon, E.J., Balachandran, P.V., Kirby, B.J., Keavney, D.J., Sichel-Tissot, R.J., Schlepütz, C.M., Karapetrova, E., Cheng, X.M., Rondinelli, J.M., May, S.J., "Effect of Interfacial Octahedral Behavior in Ultrathin Manganite Films," *Nano Lett.* **14**, 2509 (2014).
- Mourigal, M., Fuhrman, W.T., Sheckelton, J.P., Wartelle, A., Rodriguez-Rivera, J.A., Abernathy, D.L., McQueen, T.M., Broholm, C.L., "Molecular Quantum Magnetism in $\text{LiZn}_2\text{Mo}_3\text{O}_8$," *Phys. Rev. Lett.* **112**(2), 027202 (2014). [CHRNS]
- Nagaraja, A.R., Stone, K.H., Toney, M.F., Peng, H., Lany, S., Mason, T.O., "Experimental Characterization of a Theoretically Designed Candidate p-Type Transparent Conducting Oxide: Li-Doped Cr_2MnO_4 ," *Chem. Mater.*, in press.
- Nagpure, S.C., Mulligan, P., Canova, M., Cao, L.R., "Neutron Depth Profiling of Li-Ion Cell Electrodes with a Gas-Controlled Environment," *J. Power Sources* **248**, 489 (2014).
- Nagpure, S.C., Bhushan, B., Babu, S.S., "Multi-Scale Characterization Studies of Aged Li-Ion Large Format Cells for Improved Performance: An Overview," *J. Electrochem. Soc.* **160**(11), A2111 (2013).

- Nelson, A.R.J., "Towards a Detailed Resolution Smearing Kernel for Time-of-Flight Neutron Reflectometers," *J. Appl. Crystallogr.* **46**, 1338 (2013).
- Newman, C., Zhou, X., Goundie, B., Ghampson, I.T., Pollock, R.A., Ross, Z., Wheeler, M.C., Meulenberg, R.W., Austin, R.N., Frederick, B.G., "Effects of Support Identity and Metal Dispersion in Supported Ruthenium Hydrodeoxygenation Catalysts," *Appl. Catal. A-Gen.* **477**, 64 (2014).
- Nickels, J.D., "Instrumental Resolution Effects in Neutron Scattering Studies of Protein Dynamics," *Chem. Phys.* **424**, 7 (2013). [CHNRNS]
- Nickels, J.D., García Sakai, V., Sokolov, A.P., "Dynamics in Protein Powders on the Nanosecond-Picosecond Time Scale are Dominated by Localized Motions," *J. Phys. Chem. B* **117**, 11548 (2013). [CHNRNS]
- Nozaki, Y., Nakano, K., Yajima, T., Kageyama, H., Frandsen, B., Liu, L., Cheung, S., Goko, T., Uemura, Y.J., Munsie, T.S.J., Medina, T., Luke, G.M., Munevar, J., Nishio-Hamane, D., Brown, C.M., "Muon Spin Relaxation and Electron/Neutron Diffraction Studies of $\text{BaTi}_2(\text{As}_{1-x}\text{Sb}_x)_2\text{O}$: Absence of Static Magnetism and Superlattice Reflections," *Phys. Rev. B* **88**(21), 214506 (2013).
- Olsson, A., Hellsing, M.S., Rennie, A.R., "A Holder to Rotate Sample Cells to Avoid Sedimentation in Small-Angle Neutron Scattering and Ultra Small-Angle Neutron Scattering Experiments," *Meas. Sci. Technol.* **24**, 105901 (2013). [CHNRNS]
- Owejan, J.P., Trabold, T.A., Mench, M.M., "Oxygen Transport Resistance Correlated to Liquid Water Saturation in the Gas Diffusion Layer of PEM Fuel Cells," *Int. J. Heat. Mass Tran.* **71**, 585 (2014).
- Page, K.A., Rowe, B.W., Masser, K.A., Faraone, A., "The Effect of Water Content on Chain Dynamics in Nafion Membranes Measured by Neutron Spin Echo and Dielectric Spectroscopy," *J. Polym. Sci. Pol. Phys.* **52**, 624 (2014). [CHNRNS]
- Pajerowski, D.M., Ravel, B., Li, C.H., Dumont, M.F., Talham, D.R., "X-ray Absorption Study of Structural Coupling in Photomagnetic Prussian Blue Analogue Core@Shell Particles," *Chem. Mater.* **26**, 2586 (2014).
- Pajerowski, D.M., Li, Q., Hyun, J., Dennis, C.L., Phelan, D., Yan, P., Chen, P., Li, G., "Chloride-Bridged, Defect-Dicubane $\{\text{Ln}_4\}$ Core Clusters: Syntheses, Crystal Structures and Magnetic Properties," *Dalton T.*, in press.
- Pang, D., Nico, J.S., Karam, L., Timofeeva, O., Blakely, W.F., Dritschilo, A., Dizdaroglu, M., Jaruga, P., "Significant Disparity in Base and Sugar Damage in DNA Resulting from Neutron and Electron Irradiation," *J. Radiat. Res.*, in press.
- Pangelis, S., Olsen, S.R., Scherschligt, J., Leão, J.B., Pullen, S.A., Dender, D., Hester, J.R., Imperia, P., "Safety Interlock and Vent System to Alleviate Potentially Dangerous Ice Blockage of Top-loading Cryostat Sample Sticks," *J. Appl. Crystallogr.* **46**(4), 1236 (2013). [CHNRNS]
- Parshall, D., Heid, R., Niedziela, J.L., Wolf, Th., Stone, M.B., Abernathy, D.L., Reznik, D., "Phonon Spectrum of SrFe_2As_2 Determined using Multizone Phonon Refinement," *Phys. Rev. B* **89**(6), 064310 (2014).
- Parsons, M.S., "SiDecSo, A Simple Analytic Software for Neutron Depth Profiling, Invited," in "Transactions of the American Nuclear Society," (Developments and Applications of Neutron Beam Techniques, November 2013, Washington, D.C.) **109**, 525 (2013).
- Patterson, J.P., Kelley, E.G., Murphy, R.P., Moughton, A.O., Robin, M.P., Lu, A., Colombani, O., Chassenieux, C., Cheung, D., Sullivan, M.O., Epps, III, T.H., O'Reilly, R.K., "Structural Characterization of Amphiphilic Homopolymer Micelles using Light Scattering, SANS, and Cryo-TEM," *Macromolecules* **46**, 6319 (2013).
- Paul, R.L., Davis, W.C., Yu, L., Murphy, K.E., Guthrie, W.F., Leber, D.D., Bryan, C.E., Vetter, T.W., Shakirova, G., Mitchell, G., Kyle, D.J., Jarrett, J.M., Caldwell, K.L., Jones, R.L., Eckdahl, S., Wermers, M., Maras, M., Palmer, C.D., Verostek, M.F., Geraghty, C.M., Steuerwald, A.J., Parsons, P.J., "Certification of Total Arsenic in Blood and Urine Standard Reference Materials by Radiochemical Neutron Activation Analysis and Inductively Coupled Plasma-Mass Spectrometry," *J. Radioanal. Nucl. Chem.* **299**, 1555 (2014).
- Paul, R.L., "Determination of Arsenic in Food and Dietary Supplement Standard Reference Materials by Neutron Activation Analysis," *J. Radioanal. Nucl. Chem.* **297**, 365 (2013).
- Pena-Francesch, A., Akgun, B., Miserez, A., Zhu, W., Gao, H., Demirel, M.C., "Pressure Sensitive Adhesion of an Elastomeric Protein Complex Extracted from Squid Ring Teeth," *Adv. Funct. Mater.*, in press.
- Peng, Y., Krungleviciute, V., Eryazici, I., Hupp, J.T., Farha, O.K., Yildirim, T., "Methane Storage in Metal-Organic Frameworks: Current Records, Surprise Findings, and Challenges," *J. Am. Chem. Soc.* **135**(32), 11887 (2013).
- Pesek, S.L., Li, X., Hammouda, B., Hong, K., Verduzco, R., "Small-Angle Neutron Scattering Analysis of Bottlebrush Polymers Prepared via Grafting-Through Polymerization," *Macromolecules* **46**, 6998 (2013). [CHNRNS]
- Phelan, D., Bhatti, K.P., Taylor, M., Wang, S., Leighton, C., "Magnetically Inhomogeneous Ground State Below the First-Order Valence Transition in $(\text{Pr}_{1-y}\text{Y}_y)_{0.7}\text{Ca}_{0.3}\text{CoO}_{3-\delta}$," *Phys. Rev. B* **89**(18), 184427 (2014). [CHNRNS]

- Phelan, D., Suzuki, Y., Wang, S., Huq, A., Leighton, C., "Structural, Transport, and Magnetic Properties of Narrow Bandwidth $\text{Nd}_{1-x}\text{Ca}_x\text{CoO}_{3-\delta}$ and Comparisons to $\text{Pr}_{1-x}\text{Ca}_x\text{CoO}_{3-\delta}$ " *Phys. Rev. B* **88**(7), 075119 (2013). [CHNRNS]
- Phelan, D., "Constraints on the Possible Long-Range Orbital Ordering in LaCoO_3 ," *J. Magn. Magn. Mater.* **350**, 183 (2014).
- Phelan, D., Stock, C., Rodriguez-Rivera, J.A., Chi, S., Leão, J., Long, X., Xie, Y., Bokov, A.A., Ye, Z.-G., Ganesh, P., Gehring, P.M., "Role of Random Electric Fields in Relaxors," *P. Natl. A. Sci. USA* **111**(5), 1754 (2014). [CHNRNS]
- Pintschovius, L., Reznik, D., Weber, F., Bourges, P., Parshall, D., Mittal, R., Chaplot, S.L., Heid, R., Wolf, T., Lamago, D., Lynn, J.W., "Spurious Peaks Arising from Multiple Scattering Events Involving the Sample Environment in Inelastic Neutron Scattering," *J. Appl. Crystallogr.*, in press.
- Pollock, R.A., Her, J.-H., Brown, C.M., Liu, Y., Dailly, A., "Kinetic Trapping of D_2 in MIL-53(Al) Observed using Neutron Scattering," *J. Phys. Chem. C*, in press.
- Pulido, R., Baker, S.J., Barata, J.T., Carracedo, A., Cid, V.J., Chin-Sang, I.D., Davé, V., den Hertog, J., Devreotes, P., Eickholt, B.J., Eng, C., Furnari, F.B., Georgescu, M.-M., Gericke, A., Hopkins, B., Jiang, X., Lee, S.-R., Lösche, M., Malaney, P., Matias-Guiu, X., Molina, M., Pandolfi, P.P., Parsons, R., Pinton, P., Rivas, C., Rocha, R.M., Rodríguez, M.S., Ross, A.H., Serrano, M., Stambolic, V., Stiles, B., Suzuki, A., Tan, S.-S., Tonks, N.K., Trotman, L.C., Wolff, N., Woscholski, R., Wu, H., Leslie, N.R., "A Unified Nomenclature and Amino Acid Numbering for Human PTEN," *Science Signaling* **7**(332), pe15 (2014).
- Queen, W.L., Lee, J., Gonzalez, M., Geier, S.J., Mason, J.A., Long, J.R., Brown, C.M., Hudson, M.R., Teat, S.J., "Correlations between Structure and Gas-Adsorption/Separation Properties of Metal-Organic Frameworks," *T. Am. Crystallogr. Assn.* **44**, 120 (2014).
- Quinn, G.D., Zilcha, O., Rowe, J.M., Pierce, D.J., "Failure Analysis of a 41-m Long Neutron Beam Line Guide," *J. Eur. Ceram. Soc.*, in press.
- Quiquandon, M., Gratiás, D., "About the Atomic Structures of Icosahedral Quasicrystals," *C. R. Phys.* **15**, 18 (2014).
- Rao, X., Cai, J., Yu, J., He, Y., Wu, C., Zhou, W., Yildirim, T., Chen, B., Qian, G., "A Microporous Metal-Organic Framework with Both Open Metal and Lewis Basic Pyridyl Sites for High C_2H_2 and CH_4 Storage at Room Temperature," *Chem. Commun.* **49**(60), 6719 (2013).
- Ratcliff, II, W., "Reflections on the Magnetic Pair Distribution Function," *Acta Crystallogr. A* **A70**, 1 (2014).
- Rennie, A.R., Hellsing, M.S., Wood, K., Gilbert, E.P., Porcar, L., Schweins, R., Dewhurst, C.D., Lindner, P., Heenan, R.K., Rogers, S.E., Butler, P.D., Krzywon, J.R., Ghosh, R.E., Jackson, A.J., Malfois, M., "Learning about SANS Instruments and Data Reduction from Round Robin Measurements on Samples of Polystyrene Latex," *J. Appl. Crystallogr.* **46**, 1289 (2013).
- Richards, J.J., Whittle, C.L., Shao, G., Pozzo, L.D., "Correlating Structure and Photocurrent for Composite Semiconducting Nanoparticles with Contrast Variation Small-Angle Neutron Scattering and Photoconductive Atomic Force Microscopy," *ACS Nano* **8**(5), 4313 (2014). [CHNRNS]
- Rodriguez, E.E., Sokolov, D.A., Stock, C., Green, M.A., Sobolev, O., Rodriguez-Rivera, J.A., Cao, H., Daoud-Aladine, A., "Magnetic and Structural Properties near the Lifshitz Point in Fe_{1+x}Te ," *Phys. Rev. B* **88**(16), 165110 (2013). [CHNRNS]
- Roh, J.H., Tyagi, M., Hogan, T.E., Roland, C.M., "Effect of Binding to Carbon Black on the Dynamics of 1,4-Polybutadiene," *J. Chem. Phys.* **139**(13), 134905 (2013). [CHNRNS]
- Roh, J.H., Tyagi, M., Hogan, T.E., Roland, C.M., "Space-Dependent Dynamics in 1,4-Polybutadiene Nanocomposite," *Macromolecules* **46**, 6667 (2013). [CHNRNS]
- Ross, K.A., Qiu, Y., Copley, J.R.D., Dabkowska, H.A., Gaulin, B.D., "Order by Disorder Spin Wave Gap in the XY Pyrochlore Magnet $\text{Er}_2\text{Ti}_2\text{O}_7$," *Phys. Rev. Lett.* **112**(5), 057201 (2014). [CHNRNS]
- Ross, K.A., Harriger, L., Yamani, Z., Buyers, W.J.L., Garrett, J.D., Menovsky, A.A., Mydosh, J.A., Broholm, C.L., "Strict Limit on In-Plane Ordered Magnetic Dipole Moment in URu_2Si_2 ," *Phys. Rev. B* **89**(15), 155122 (2014).
- Rubinson, K.A., "Small-Angle Neutron Scattering of Aqueous SrI_2 Suggests a Mechanism for Ion Transport in Molecular Water," *J. Solution Chem.* **43**, 453 (2014). [CHNRNS]
- Sadakane, K., Nagao, M., Endo, H., Seto, H., "Membrane Formation by Preferential Solvation of Ions in Mixture of Water, 3-Methylpyridine, and Sodium Tetraphenylborate," *J. Chem. Phys.* **139**(23), 234905 (2013). [CHNRNS]
- Saffer, E.M., Lackey, M.A., Griffin, D.M., Kishore, S., Tew, G.N., Bhatia, S.R., "SANS Study of Highly Resilient Poly(Ethylene Glycol) Hydrogels," *Soft Matter* **10**, 1905 (2014).
- Saha, S.R., Drye, T., Goh, S.K., Klintberg, L.E., Silver, J.M., Grosche, F.M., Sutherland, M., Munsie, T.J.S., Luke, G.M., Pratt, D.K., Lynn, J.W., Paglione, J., "Segregation of Antiferromagnetism and High-Temperature Superconductivity in $\text{Ca}_{1-x}\text{La}_x\text{Fe}_2\text{As}_2$," *Phys. Rev. B* **89**(13), 134516 (2014).

- Şahin, D., Radulović, V., Lindstrom, R.M., Trkov, A., "Reevaluation of Neutron Flux Characterization Parameters for NIST RT-2 Facility," *J. Radioanal. Nucl. Chem.* **300**, 499 (2014).
- Saparov, B., Cantoni, C., Pan, M., Hogan, T.C., Ratcliff, II, W., Wilson, S.D., Fritsch, K., Gaulin, B.D., Sefat, A.S., "Complex Structures of Different CaFe_2As_2 Samples," *Sci. Rep.* **4**, 4120 (2014).
- Sarachan, K.L., Curtis, J.E., Krueger, S., "Small-Angle Scattering Contrast Calculator for Protein and Nucleic Acid Complexes in Solution," *J. Appl. Crystallogr.* **46**, 1889 (2013).
- Seibel, E.M., Roudebush, J.H., Wu, H., Huang, Q., Ali, M.N., Ji, H., Cava, R.J., "Structure and Magnetic Properties of the $\alpha\text{-NaFeO}_2$ -Type Honeycomb Compound $\text{Na}_3\text{Ni}_2\text{BiO}_6$," *Inorg. Chem.* **52**, 13605 (2013).
- Shen, H., Zhang, W., Mackay, M.E., "Dual Length Morphological Model for Bulk-Heterojunction Polymer-Based Solar Cells," *J. Polym. Sci. Pol. Phys.* **52**, 387 (2014). [CHNRS]
- Silverstein, H.J., Fritsch, K., Flicker, F., Hallas, A.M., Gardner, J.S., Qiu, Y., Ehlers, G., Savici, A.T., Yamani, Z., Ross, K.A., Gaulin, B.D., Gingras, M.J.P., Paddison, J.A.M., Foyevtsova, K., Valenti, R., Hawthorne, F., Wiebe, C.R., Zhou, H.D., "Liquidlike Correlations in Single-Crystalline $\text{Y}_2\text{Mo}_2\text{O}_7$: An Unconventional Spin Glass," *Phys. Rev. B* **89**(5), 054433 (2014). [CHNRS]
- Simmons, J.M., Cook, J.C., Ibberson, R.M., Majkrzak, C.F., Neumann, D.A., "Polychromatic Energy-Dispersive Neutron Diffraction at a Continuous Source," *J. Appl. Crystallogr.* **46**, 1347 (2013).
- Singh, D.K., "Interplay of Spin Gap and Nanoscopic Quantum Fluctuations in Intermetallic CeCu_2Ge_2 ," *Phys. Lett. A* **378**, 1906 (2014).
- Sinha, K., Maranas, J., "Does Ion Aggregation Impact Polymer Dynamics and Conductivity in PEO-Based Single Ion Conductors?" *Macromolecules* **47**, 2718 (2014). [CHNRS]
- Skowronek, R.K., Blackman, M.J., Bishop, R.L., "Ceramic Production in Early Hispanic California", (University Press of Florida, Gainesville, Florida) (2014).
- Skowronek, R.K., Blackman, M.J., Bishop, R.L., "Ceramic Production in Early Hispanic California: Craft, Economy, and Trade on the Frontier of New Spain," in press.
- Skipov, A.V., Paul-Bancour, V., Udovic, T.J., Rush, J.J., "Hydrogen Dynamics in Laves-Phase Hydride $\text{YFe}_2\text{H}_{2.6}$: Inelastic and Quasielastic Neutron Scattering Studies," *J. Alloy Compd.* **595**, 28 (2014). [CHNRS]
- Skipov, A.V., Babanova, O.A., Soloninin, A.V., Stavila, V., Verdal, N., Udovic, T.J., Rush, J.J., "Nuclear Magnetic Resonance Study of Atomic Motions in $\text{A}_2\text{B}_{12}\text{H}_{12}$ ($\text{A} = \text{Na, K, Rb, Cs}$): Anion Reorientations and Na^+ Mobility," *J. Phys. Chem. C* **117**, 25961 (2013).
- Smoot, C.D., Ma, H.B., Winholtz, R.A., Jacobson, D.L., Hussey, D.S., "Thermal and Visual Observation of a Hybrid Heat Pipe," *Heat Transf. Res.* **44**(1), 31 (2013).
- Soh, J.H., Tucker, G.S., Pratt, D.K., Abernathy, D.L., Stone, M.B., Ran, S., Bud'Ko, S.L., Canfield, P.C., Kreyssig, A., McQueeney, R.J., Goldman, A.I., "Inelastic Neutron Scattering Study of a Nonmagnetic Collapsed Tetragonal Phase in Nonsuperconducting CaFe_2As_2 : Evidence of the Impact of Spin Fluctuations on Superconductivity in the Iron-Arsenide Compounds," *Phys. Rev. Lett.* **111**(22), 227002 (2013).
- Sokolov, D.A., Aronson, M.C., Wu, L., Zhu, Y., Nelson, C., Mansfield, J.F., Sun, K., Erwin, R., Lynn, J.W., Lumsden, M., Nagler, S.E., "Neutron, Electron, and X-ray Scattering Investigation of $\text{Cr}_{1-x}\text{V}_x$ Near Quantum Criticality," *Phys. Rev. B* **90**(3), 035139 (2014).
- Srinivas, G., Krungleviciute, V., Guo, Z.-X., Yildirim, T., "Exceptional CO_2 Capture in a Hierarchically Porous Carbon with Simultaneous High Surface Area and Pore Volume," *Energ. Environ. Sci.* **7**, 335 (2014).
- Stalick, J.K., Waterstrat, R.M., "The Hafnium-Platinum Phase Diagram," *J. Phase Equilib. Diff.* **35**(1), 15 (2014).
- Subramanian, D., Boughter, C.T., Klauda, J.B., Hammouda, B., Anisimov, M.A., "Mesoscale Inhomogeneities in Aqueous Solutions of Small Amphiphilic Molecules," *Faraday Discuss.* **167**, 217 (2013). [CHNRS]
- Swain, M., Singh, S., Basu, S., Gupta, M., "Effect of Interface Morphology on Intermetallics Formation Upon Annealing of Al-Ni Multilayer," *J. Alloy Compd.* **576**, 257 (2013).
- Takatsu, H., Nénert, G., Kadowaki, H., Yoshizawa, H., Enderle, M., Yonezawa, S., Maeno, Y., Kim, J., Tsuji, N., Takata, M., Zhao, Y., Green, M., Broholm, C., "Magnetic Structure of the Conductive Triangular-Lattice Antiferromagnet PdCrO_2 ," *Phys. Rev. B* **89**(10), 104408 (2014).
- Tao, R., Du, E., Tang, H., Xu, X., "Neutron Scattering Studies of Crude Oil Viscosity Reduction with Electric Field," *Fuel*, in press.
- Tassel, C., Goto, Y., Kuno, Y., Hester, J., Green, M., Kobayashi, Y., Kageyama, H., "Direct Synthesis of Chromium Perovskite Oxyhydride with a High Magnetic-Transition Temperature," *Angew. Chem. Int. Ed.*, in Press.

- Thomas, J.J., Musso, S., Prestini, I., "Kinetics and Activation Energy of Magnesium Oxide Hydration," *J. Am. Ceram. Soc.* **97**(1), 275 (2014). [CHRSN]
- Thomas, J.J., Valenza, II, J.J., Craddock, P.R., Bake, K.D., Pomerantz, A.E., "The Neutron Scattering Length Density of Kerogen and Coal as Determined by $\text{CH}_3\text{OH}/\text{CD}_3\text{OH}$ Exchange," *Fuel* **117**, 801 (2014).
- Turk, G.C., Sharpless, K.E., Cleveland, D., Jongsma, C., Mackey, E.A., Marlow, A.F., Oflaz, R., Paul, R.L., Sieber, J.R., Thompson, R.Q., Wood, L.J., Yu, L.L., Zeisler, R., Wise, S.A., Yen, J.H., Christopher, S.J., Day, R.D., Long, S.E., Greene, E., Harnly, J., Ho, I.-P., Betz, J.M., "Certification of Elements in and Use of Standard Reference Material 3280 Multivitamin/Multielement Tablets," *J. AOAC Int.* **96**(6), 1281 (2013).
- Turkoglu, D., Glover, S., Spitz, H., Cao, L., "Applying Method of Integral Thermal Neutron Cross-Section Measurement using Activated Prompt Gamma Rays to Non-1/v Isotopes," *T. Am. Nucl. Soc.* **109**, 118 (2013).
- Udovic, T.J., Verdal, N., Rush, J.J., De Vries, D.J., Hartman, M.R., Vajo, J.J., Gross, A.F., Skripov, A.V., "Mapping Trends in the Reorientational Mobilities of Tetrahydroborate Anions via Neutron-Scattering Fixed-Window Scans," *J. Alloy Compd.* **580**, S47 (2013). [CHRSN]
- Udovic, T.J., Matsuo, M., Unemoto, A., Verdal, N., Stavila, V., Skripov, A.V., Rush, J.J., Takamura, H., Orimo, S.-I., "Sodium Superionic Conduction in $\text{Na}_2\text{B}_{12}\text{H}_{12}$," *Chem. Commun.* **50**, 3750 (2014).
- Ueland, B.G., Kreyssig, A., Prokeš, K., Lynn, J.W., Harriger, L.W., Pratt, D.K., Singh, D.K., Heitmann, T.W., Sauerbrei, S., Saunders, S.M., Mun, E.D., Bud'ko, S.L., McQueeney, R.J., Canfield, P.C., Goldman, A.I., "Fragile Antiferromagnetism in the Heavy-Fermion Compound YbBiPt ," *Phys. Rev. B* **89**(18), 180403 (2014).
- Vaish, A., Vanderah, D.J., Vierling, R., Crawshaw, F., Gallagher, D.T., Walker, M.L., "Membrane Protein Resistance of Oligo(ethylene oxide) Self-Assembled Monolayers," *Colloid Surface. B*, in press.
- Valadez-Pérez, N.E., Castañeda-Priego, R., Liu, Y., "Percolation in Colloidal Systems with Competing Interactions: The Role of Long-Range Repulsion," *RSC Adv.* **3**, 25110 (2013).
- Valadez-Pérez, N.E., Liu, Y., Eberle, A.P.R., Wagner, N.J., Castañeda-Priego, R., "Dynamical Arrest in Adhesive Hard-Sphere Dispersions Driven by Rigidity Percolation," *Phys. Rev. E* **88**(6), 060302 (2013).
- Verdal, N., Udovic, T.J., Stavila, V., Tang, W.S., Rush, J.J., Skripov, A.V., "Anion Reorientations in the Superionic Conducting Phase of $\text{Na}_2\text{B}_{12}\text{H}_{12}$," *J. Phys. Chem. C*, in press. [CHRSN]
- Verdal, N., Udovic, T.J., Rush, J.J., Liu, X., Majzoub, E.H., Vajo, J.J., Gross, A.F., "Dynamical Perturbations of Tetrahydroborate Anions in LiBH_4 due to Nanoconfinement in Controlled-Pore Carbon Scaffolds," *J. Phys. Chem. C* **117**, 17983 (2013). [CHRSN]
- Verdal, N., Her, J.-H., Stavila, V., Soloninin, A.V., Babanova, O.A., Skripov, A.V., Udovic, T.J., Rush, J.J., "Complex High-Temperature Phase Transitions in $\text{Li}_2\text{B}_{12}\text{H}_{12}$ and $\text{Na}_2\text{B}_{12}\text{H}_{12}$," *J. Solid State Chem.* **212**, 81 (2014). [CHRSN]
- Verploegen, E., Sokolov, A.N., Akgun, B., Satija, S.K., Wei, P., Kim, D., Kapelewski, M.T., Bao, Z., Toney, M.F., "Swelling of Polymer Dielectric Thin Films for Organic-Transistor-Based Aqueous Sensing Applications," *Chem. Mater.* **25**, 5018 (2013).
- von Bardeleben, H.J., Cantin, J.L., Zhang, D.M., Richardella, A., Rench, D.W., Samarth, N., "Ferromagnetism in Bi_2Se_3 : Mn Epitaxial Layers," *Phys. Rev. B* **88**(7), 075149 (2013).
- Wallace, D.C., Brown, C.M., McQueen, T.M., "Evolution of Magnetism in the $\text{Na}_{3-x}(\text{Na}_{1-x}\text{Mg}_x)\text{Ir}_2\text{O}_6$ Series of Honeycomb Iridates," *J. Solid State Chem.*, in press.
- Wang, C.-W., Lee, C.-H., Li, C.-Y., Wu, C.-M., Li, W.-H., Chou, C.-C., Yang, H.-D., Lynn, J.W., Huang, Q., Harris, A.B., Berger, H., "Complex Magnetic Couplings in Co_3TeO_6 ," *Phys. Rev. B* **88**(18), 184427 (2013).
- Wang, D., Hore, M.J.A., Ye, X., Zheng, C., Murray, C.B., Composto, R.J., "Gold Nanorod Length Controls Dispersion, Local Ordering, and Optical Absorption in Polymer Nanocomposite Films," *Soft Matter* **10**, 3404 (2014).
- Wang, H.-W., Anovitz, L.M., Burg, A., Cole, D.R., Allard, L.F., Jackson, A.J., Stack, A.G., Rother, G., "Multi-scale Characterization of Pore Evolution in a Combustion Metamorphic Complex, Hatrurim Basin, Israel: Combining (ultra) Small-Angle Neutron Scattering and Image Analysis," *Geochim. Cosmochim. Ac.* **121**, 339 (2013). [CHRSN]
- Wang, J., Liu, D.X., Canova, M., Downing, R.G., Cao, L.R., Co, A.C., "Profiling Lithium Distribution in Sn Anode for Lithium-ion Batteries with Neutrons," *J. Radioanal. Nucl. Chem.* **301**, 277 (2014).
- Wang, S.-F., Yang, S., Lee, J., Akgun, B., Wu, D.T., Foster, M.D., "Anomalous Surface Relaxations of Branched-Polymer Melts," *Phys. Rev. Lett.* **111**(6), 068303 (2013).
- Wang, Z., Liu, K.-H., Le, P., Li, M., Chiang, W.-S., Leão, J.B., Copley, J.R.D., Tyagi, M., Podlesnyak, A., Kolesnikov, A.I., Mou, C.-Y., Chen, S.-H., "Boson Peak in Deeply Cooled Confined Water: A Possible Way to Explore the Existence of the Liquid-to-Liquid Transition in Water," *Phys. Rev. Lett.* **112**(23), 237802 (2014). [CHRSN]

- Wang, Z., Liu, K.-H., Harriger, L., Leão, J.B., Chen, S.-H., "Evidence of the Existence of the High-Density and Low-Density Phases in Deeply-Cooled Confined Heavy Water under High Pressures," *J. Chem. Phys.* **141**(1), 014501 (2014).
- Watson, M.C., Curtis, J.E., "Rapid and Accurate Calculation of Small-Angle Scattering Profiles using the Golden Ratio," *J. Appl. Crystallogr.* **46**(4), 1171 (2013).
- Watson, M.C., Morriss-Andrews, A., Welch, P.M., Brown, F.L.H., "Thermal Fluctuations in Shape, Thickness, and Molecular Orientation in Lipid Bilayers. II. Finite Surface Tensions," *J. Chem. Phys.* **139**(8), 084706 (2013).
- Watson, M.C., Curtis, J.E., "Probing the Average Local Structures of Biomolecules using Small-Angle Scattering and Scaling Laws," *Biophys. J.* **106**, 2474 (2014).
- Weinrich, M., Worcester, D.L., "Xenon and Other Volatile Anesthetics Change Domain Structure in Model Lipid Raft Membranes," *J. Phys. Chem. B* **117**, 16141 (2013).
- Wen, H.-M., Li, B., Yuan, D., Wang, H., Yildirim, T., Zhou, W., Chen, B., "A Porous Metal-Organic Framework with an Elongated Anthracene Derivative Exhibiting a High Working Capacity for the Storage of Methane," *J. of Mater. Chem. A* **2**, 11516 (2014).
- White, J.S., Niedermayer, Ch., Gasparovic, G., Broholm, C., Park, J.M.S., Shapiro, A.Ya., Demianets, L., Kenzelmann, M., "Multiferroicity in the Generic Easy-Plane Triangular Lattice Antiferromagnet $\text{RbFe}(\text{MoO}_4)_2$," *Phys. Rev. B* **88**(6), 060409 (2013).
- Wietfeldt, F.E., Darius, G., Dewey, M.S., Fomin, N., Greene, G.L., Mulholland, J., Snow, W.M., Yue, A.T., "A Path to a 0.1 s Neutron Lifetime Measurement using the Beam Method," *Physics Procedia* **51**, 54 (2014).
- Wong-Ng, W., Laws, W., Talley, K.R., Huang, Q., Yan, Y., Martin, J., Kaduk, J.A., "Phase Equilibria and Crystal Chemistry of the $\text{CaO-1/2 Nd}_2\text{O}_3\text{-CoO}_2$ system at 885 °C in Air," *J. Solid State Chem.* **215**, 128 (2014).
- Wood, B.M., Ham, K., Hussey, D.S., Jacobson, D.L., Faridani, A., Kaestner, A., Vajo, J.J., Liu, P., Dobbins, T.A., Butler, L.G., "Real-Time Observation of Hydrogen Absorption by LaNi_5 with Quasi-Dynamic Neutron Tomography," *Nucl. Instrum. Meth. B* **324**, 95 (2014).
- Wu, M., Wang, C., Sun, Y., Chu, L., Yan, J., Chen, D., Huang, Q., Lynn, J.W., "Magnetic Structure and Lattice Contraction in Mn_3NiN ," *J. Appl. Phys.* **114**(12), 123902 (2013).
- Xiao, D.J., Bloch, E.D., Mason, J.A., Queen, W.L., Hudson, M.R., Planas, N., Borycz, J., Dzubak, A.L., Verma, P., Lee, K., Bonino, F., Crocellà, V., Yano, J., Bordiga, S., Truhlar, D.G., Gagliardi, L., Brown, C.M., Long, J.R., "Oxidation of Ethane to Ethanol by N_2O in a Metal-Organic Framework with Coordinatively Unsaturated Iron(II) Sites," *Nat. Chem.* **6**, 590 (2014).
- Xu, J., Yang, B., Hammouda, B., "Thermophysical Properties and Pool Boiling Characteristics of Water-in-Polyalphaolefin Nanoemulsion Fluids," *J. Heat Transf.* **135**, 091303 (2013). [CHRS]
- Xu, J., Wang, X., Fu, H., Brown, C.M., Jing, X., Liao, F., Lu, F., Li, X., Kuang, X., Wu, M., "Solid-State ^{29}Si NMR and Neutron-Diffraction Studies of $\text{Sr}_{0.7}\text{K}_{0.3}\text{SiO}_{2.85}$ Oxide Ion Conductors," *Inorg. Chem.* **53**, 6962 (2014).
- Yajima, T., Takeiri, F., Nozaki, Y., Li, Z., Tohyama, T., Green, M.A., Kobayashi, Y., Kageyama, H., "Superconductivity in the Hypervalent Compound $\text{Ba}_2\text{Bi}(\text{Sb}_{1-x}\text{Bi}_x)_2$ with a Square-Honeycomb Lattice," *J. Phys. Soc. Jpn.* **83**, 073705 (2014).
- Yamada, T., Yamada, T., Tyagi, M., Nagao, M., Kitagawa, H., Yamamuro, O., "Phase Transition and Dynamics of Water Confined in Hydroxyethyl Copper Rubinate Hydrate," *J. Phys. Soc. Jpn.* **82**, SA010 (2013). [CHRS]
- Yan, J., Sun, Y., Wu, H., Huang, Q., Wang, C., Shi, Z., Deng, S., Shi, K., Lu, H., Chu, L., "Phase Transitions and Magnetocaloric Effect in $\text{Mn}_3\text{Cu}_{0.89}\text{N}_{0.96}$," *Acta Mater.*, in press.
- Yan, J., Sun, Y., Wen, Y., Chu, L., Wu, M., Huang, Q., Wang, C., Lynn, J.W., Chen, Y., "Relationship between Spin Ordering, Entropy, and Anomalous Lattice Variation in $\text{Mn}_3\text{Sn}_{1-\epsilon}\text{Si}_{\epsilon}\text{C}_{1-\delta}$ Compounds," *Inorg. Chem.* **53**, 2317 (2014).
- Yang, K., Tyagi, M., Moore, J.S., Zhang, Y., "Odd-Even Glass Transition Temperatures in Network-Forming Ionic Glass Homologue," *J. Am. Chem. Soc.* **136**, 1268 (2014). [CHRS]
- Yang, X., Downing, R.G., Wang, G.-B., Qian, D.-Z., Liu, H.-G., Wang, K., "A Monte Carlo Code to Get Response Spectrum of Ions for Neutron Depth Profiling," *J. Radioanal. Nucl. Chem.* **301**(1), 213 (2014).
- Yang, Y., Liu, Y., Wu, H., Zhou, W., Gao, M., Pan, H., "An Ammonia-Stabilized Mixed-Cation Borohydride: Synthesis, Structure and Thermal Decomposition Behavior," *Phys. Chem. Chem. Phys.* **16**, 135 (2014).
- Yano, S.-I., Louca, D., Chi, S., Matsuda, M., Qiu, Y., Copley, J.R.D., Cheong, S.-W., "Intertwining of Frustration with Magneto-Elastic Coupling in the Multiferroic LuMnO_3 ," *J. Phys. Soc. Jpn.* **83**, 024601 (2013). [CHRS]

- Yearley, E.J., Zarraga, I.E., Shire, S.J., Scherer, T.M., Gokarn, Y., Wagner, N.J., Liu, Y., "Small-Angle Neutron Scattering Characterization of Monoclonal Antibody Conformations and Interactions at High Concentrations," *Biophys. J.* **105**, 720 (2013). [CHNRNS]
- Yearley, E.J., Godfrin, P.D., Perevozchikova, T., Zhang, H., Falus, P., Porcar, L., Nagao, M., Curtis, J.E., Gawande, P., Taing, R., Zarraga, I.E., Wagner, N.J., Liu, Y., "Observation of Small Cluster Formation in Concentrated Monoclonal Antibody Solutions and Its Implications to Solution Viscosity," *Biophys. J.* **106**, 1763 (2014). [CHNRNS]
- Yu, J., Phelan, D., Rodriguez-Rivera, J.A., Podlesnyak, A., Louca, D., "Magneto-Polaron Formation and Field-Induced Effects with Dilute Doping in $\text{LaCo}_{1-y}\text{Ni}_y\text{O}_3$," *J. Supercond. Nov. Magn.* **26**(8), 2627 (2013). [CHNRNS]
- Yue, A.T., Dewey, M.S., Gilliam, D.M., Greene, G.L., Laptev, A.B., Nico, J.S., Snow, W.M., Wietfeldt, F.E., "Improved Determination of the Neutron Lifetime," *Phys. Rev. Lett.* **111**, 222501 (2013).
- Zhang, C., Li, H.-F., Song, Y., Su, Y., Tan, G., Netherton, T., Redding, C., Carr, S.V., Sobolev, O., Schneidewind, A., Faulhaber, E., Harriger, L.W., Li, S., Lu, X., Yao, D.-X., Das, T., Balatsky, A.V., Brückel, Th., Lynn, J.W., Dai, P., "Distinguishing s^\pm and s^{++} Electron Pairing Symmetries by Neutron Spin Resonance in Superconducting $\text{NaFe}_{0.935}\text{Co}_{0.045}\text{As}$," *Phys. Rev. B* **88**(6), 064504 (2013).
- Zhang, C., Harriger, L.W., Yin, Z., Lv, W., Wang, M., Tan, G., Song, Y., Abernathy, D.L., Tian, W., Egami, T., Haule, K., Kotliar, G., Dai, P., "Effect of Pnictogen Height on Spin Waves in Iron Pnictides," *Phys. Rev. Lett.* **112**(21), 217202 (2014).
- Zhang, H., Khodadadi, S., Fiedler, S.L., Curtis, J.E., "Role of Water and Ions on the Dynamical Transition of RNA," *J. Phys. Chem. Lett.* **4**, 3325 (2013).
- Zhang, R., Singh, G., Dang, A., Dai, L., Bockstaller, M.R., Akgun, B., Satija, S., Karim, A., "Nanoparticle-Driven Orientation Transition and Soft-Shear Alignment in Diblock Copolymer Films via Dynamic Thermal Gradient Field," *Macromol. Rapid Commun.* **34**, 1642 (2013).
- Zhao, J., Shen, Y., Birgeneau, R.J., Gao, M., Lu, Z.-Y., Lee, D.-H., Lu, X.Z., Xiang, H.J., Abernathy, D.L., Zhao, Y., "Neutron Scattering Measurements of Spatially Anisotropic Magnetic Exchange Interactions in Semiconducting $\text{K}_{0.85}\text{Fe}_{1.54}\text{Se}_2$ ($T_N = 280$ K)," *Phys. Rev. Lett.* **112**(17), 177002 (2014).
- Zhou, S., Zhang, J., Liu, D., Hu, Q., Huang, Q., "The Effect of Samarium Doping on Structure and Enhanced Thermionic Emission Properties of Lanthanum Hexaboride Fabricated by Spark Plasma Sintering," *Phys. Status Solidi A* **211**(3), 555 (2014).
- Zhou, Z., Hollingsworth, J.V., Hong, S., Wei, G., Shi, Y., Lu, X., Cheng, H., Han, C.C., "Effects of Particle Softness on Shear Thickening of Microgel Suspensions," *Soft Matter*, in press. [CHNRNS]
- Zhu, Z.-H., Nicolaou, A., Levy, G., Butch, N.P., Syers, P., Wang, X.F., Paglione, J., Sawatzky, G.A., Elfimov, I.S., Damascelli, A., "Polarity-Driven Surface Metallicity in SmB_6 ," *Phys. Rev. Lett.* **111**(21), 216402 (2013).
- Zorko, A., Adamopoulos, O., Komelj, M., Arčon, D., Lappas, A., "Frustration-Induced Nanometre-Scale Inhomogeneity in a Triangular Antiferromagnet," *Nat. Commun.* **5**, 3222 (2014).

Instruments and Contacts

(name, tel. 301-975-xxxx, email)

High resolution powder diffractometer (BT-1):

- J. K. Stalick, 6223, judith.stalick@nist.gov
- H. Wu, 2387, hui.wu@nist.gov
- Q. Z. Huang, 6164, qing.huang@nist.gov
- C. M. Brown, 5134, craig.brown@nist.gov

Residual stress diffractometer (BT-8):

- T. Gnaeupel-Herold, 5380, thomas.gnaeupel-herold@nist.gov

30-m SANS instrument (NG-7):

- Y. Liu, 6235, yun.liu@nist.gov
- P. D. Butler, 2028, paul.butler@nist.gov
- J. R. Krzywon, 6650, jkrzywon@nist.gov

30-m SANS instrument (NG-B 30m) (CHRS):

- B. Hammouda, 3961, hammouda@nist.gov
- S. Krueger, 6734, susan.krueger@nist.gov
- C. Gagnon, 2020, cedric.gagnon@nist.gov

10-m SANS instrument (NG-B) (nSoft):

- R. Jones, 4624, ronald.jones@nist.gov
- K. Weigandt, 8396, kathleen.weigandt@nist.gov

USANS, Perfect Crystal SANS (BT-5) (CHRS):

- D. F. R. Mildner, 6366, david.mildner@nist.gov
- P. D. Butler, 2028, paul.butler@nist.gov

Polarized Beam Reflectometer/Diffractometer (NG-D):

- B. J. Kirby, 8395, brian.kirby@nist.gov
- J. A. Borchers, 6597, julie.borchers@nist.gov
- C. F. Majkrzak, 5251, cmajkrzak@nist.gov

MAGIK, Off-Specular Reflectometer (NG-D):

- B. B. Maranville, 6034, brian.maranville@nist.gov
- J. A. Dura, 6251, joseph.dura@nist.gov

Neutron reflectometer-horizontal sample (NG-7):

- S. K. Satija, 5250, satija@nist.gov

Double-focusing triple-axis Spectrometer (BT-7):

- Y. Zhao, 2164, yang.zhao@nist.gov
- D. Parshall, 8097, daniel.parshall@nist.gov
- J. W. Lynn, 6246, jeff.lynn@nist.gov

SPINS, Spin-polarized triple-axis spectrometer (NG-5):

- L. Harriger, 8360, leland.harriger@nist.gov

Triple-axis spectrometer (BT-4):

- W. Ratcliff, 4316, william.ratcliff@nist.gov

FANS, Filter-analyzer neutron spectrometer (BT-4):

- T. J. Udovic, 6241, udovic@nist.gov

DCS, Disk-chopper time-of-flight spectrometer (NG-4) (CHRS):

- J. R. D. Copley, 5133, jcopley@nist.gov
- N. Butch, 4863, nicholas.butch@nist.gov
- C. M. Brown, 5134, craig.brown@nist.gov

HFBS, High-flux backscattering spectrometer (NG-2) (CHRS):

- M. Tyagi, 2046, madhusudan.tyagi@nist.gov
- W. Zhou, 8169, wei.zhou@nist.gov

NSE, Neutron spin echo spectrometer (NG-5) (CHRS):

- A. Faraone, 5254, antonio.faraone@nist.gov
- M. Nagao, 5505, michihiro.nagao@nist.gov

MACS, Multi-angle crystal spectrometer (BT-9) (CHRS):

- J. A. Rodriguez-Rivera, 6019, jose.rodriguez@nist.gov
- Y. Qiu, 3274, yiming.qiu@nist.gov

Cold-neutron prompt-gamma neutron activation analysis (NG-D):

- R. L. Paul, 6287, rpaul@nist.gov
- D. J. O'Kelly, 8793, donna.okelly@nist.gov

Thermal-neutron prompt-gamma activation analysis (VT-5):

- R. G. Downing, 3782, gregory.downing@nist.gov

Other activation analysis facilities:

- D. J. O'Kelly, 8793, donna.okelly@nist.gov

Cold neutron depth profiling (NG-1):

- R. G. Downing, 3782, gregory.downing@nist.gov

Neutron Imaging Station (BT-2):

- D. Jacobson, 6207, david.jacobson@nist.gov
- D. Hussey, 6465, daniel.hussey@nist.gov
- M. Arif, 6303, muhammad.arif@nist.gov

Neutron interferometer (NG-7):

- M. Arif, 6303, muhammad.arif@nist.gov
- D. Jacobson, 6207, david.jacobson@nist.gov
- D. Hussey, 6465, daniel.hussey@nist.gov

Fundamental neutron physics station (NG-C):

- J. Nico, 4663, nico@nist.gov

Fundamental neutron physics station (NG-6):

- NG-6M: M. S. Dewey, 4843, mdewey@nist.gov
- NG-6U: H. P. Mumm, 8355, pieter.mumm@nist.gov
- NG-6: J. Nico, 4663, nico@nist.gov

Theory and modeling:

- J. E. Curtis, 3959, joseph.curtis@nist.gov
- T. Yildirim, 6228, taner@nist.gov

Instruments under development:

vSANS instrument:

- J. G. Barker, 6732, john.barker@nist.gov
- C. J. Glinka, 6242, charles.glinka@nist.gov

CANDOR, White-beam reflectometer/diffractometer:

- F. Heinrich, 4507, frank.heinrich@nist.gov
- C. F. Majkrzak, 5251, charles.majkrzak@nist.gov

NIST Center for Neutron Research Contacts

Copies of annual reports, facility information, user information, and research proposal guidelines are available electronically.

Please visit our website: <http://www.ncnr.nist.gov>

For a paper copy of this report:

Steve Kline
301-975-6243
steven.kline@nist.gov

For general information on the facility:

Rob Dimeo
301-975-6210
robert.dimeo@nist.gov

Dan Neumann
301-975-5252
dan.neumann@nist.gov

For information on visiting the facility and/or user access questions:

Julie Keyser
301-975-8200
julie.keyser@nist.gov

Mary Ann FitzGerald
301-975-8200
maryann.fitzgerald@nist.gov

For information on performing research at the facility:

Bill Kamitakahara
301-975-6878
william.kamitakahara@nist.gov

Facility address:

NIST Center for Neutron Research
National Institute of Standards and Technology
100 Bureau Drive, Mail Stop 6100
Gaithersburg, MD 20899-6100 USA

NIST CENTER FOR NEUTRON RESEARCH

National Institute of Standards and Technology

100 Bureau Drive, MS 6100

Gaithersburg, MD 20899-6100

www.ncnr.nist.gov